



**MONASH** University

***Investigation of the Subsurface Structural Behaviour in the Surat  
Basin using SAR Interferometry Deformation Maps***

*By*

*Negin Fouladi Moghaddam*

Submitted in fulfilment of the requirements for the degree of  
Master of Engineering Science (Research)

18 December 2015

Department of Civil Engineering

Monash University

To **Nahid** that taught me going after my dreams and make them materialize

To **Naser** who taught me not to lose sight and fight for my dreams

To **Mamani, Negar** and **Hossein** for their ongoing support

## **Copyright notice**

© Negin Fouladi Moghaddam (2016). Except as provided in the Copyright Act 1968, this thesis may not be reproduced in any form without the written permission of the author.

I certify that I have made all reasonable efforts to secure copyright permissions for third-party content included in this thesis and have not knowingly added copyright content to my work without the owner's permission.

# Table of Contents

|                                                         |            |
|---------------------------------------------------------|------------|
| <b>Table of Contents</b> .....                          | iv         |
| <b>Synopsis</b> .....                                   | vii        |
| <b>Declaration</b> .....                                | ix         |
| <b>Acknowledgment</b> .....                             | x          |
| <b>List of Symbols</b> .....                            | xii        |
| <b>List of Abbreviations</b> .....                      | xiii       |
| <b>List of Figures</b> .....                            | xv         |
| <b>List of Tables</b> .....                             | xix        |
| <br>                                                    |            |
| <b>1 Introduction</b> .....                             | <b>1-1</b> |
| 1.2 Statement of Problem.....                           | 1-1        |
| 1.3 Objectives and Scope .....                          | 1-3        |
| 1.4 Outline of Approach .....                           | 1-3        |
| 1.5 Structure of Thesis .....                           | 1-4        |
| <b>2 Literature Review</b> .....                        | <b>2-1</b> |
| 2.1 Background.....                                     | 2-1        |
| 2.1.1 Surface Deformation.....                          | 2-2        |
| 2.1.2 Subsurface Structural Behaviour .....             | 2-3        |
| 2.2 Modelling surface deformation.....                  | 2-3        |
| 2.2.1 Analytical Inverse Modelling.....                 | 2-6        |
| 2.2.2 Numerical Inverse Modelling .....                 | 2-7        |
| 2.3 Monitoring surface deformation .....                | 2-9        |
| 2.3.1 In situ Monitoring .....                          | 2-9        |
| 2.3.2 Remote Sensing Monitoring and Photogrammetry..... | 2-10       |
| 2.4 SAR for Surface Deformation.....                    | 2-11       |
| 2.4.1 Principles of SAR and Interferometric SAR.....    | 2-11       |
| 2.4.2 Interferometric SAR Processing Techniques .....   | 2-18       |
| 2.5 Proposed Methodology .....                          | 2-22       |
| 2.6 Chapter Summary .....                               | 2-22       |
| <b>3 Study Area and Available Data</b> .....            | <b>3-1</b> |
| 3.1 Background.....                                     | 3-1        |
| 3.2 Geology of the Surat Basin.....                     | 3-3        |
| 3.2.1 Geomorphology .....                               | 3-3        |
| 3.2.2 Surface Geology.....                              | 3-5        |

|                                                                            |            |
|----------------------------------------------------------------------------|------------|
| 3.2.3. Basin Evolution and Stratigraphy .....                              | 3-7        |
| 3.2.4 Subsurface Geology .....                                             | 3-12       |
| 3.2.5 Petrophysical View .....                                             | 3-12       |
| 3.3 Underground Resources and Regional Deformation Records .....           | 3-13       |
| 3.3.1 Groundwater Aquifers.....                                            | 3-13       |
| 3.3.2 Hydrocarbon Resources .....                                          | 3-17       |
| 3.3.3 CO <sub>2</sub> injection in the Surat Basin.....                    | 3-19       |
| 3.3.4 Underground Coal Gasification .....                                  | 3-20       |
| 3.3.5 Potential for Subsidence and Uplift .....                            | 3-21       |
| 3.4 Geophysics and Geodesy of the Surat Basin.....                         | 3-21       |
| 3.4.1 Seismic and Electromagnetic surveys.....                             | 3-21       |
| 3.4.2 Subsurface monitoring boreholes.....                                 | 3-24       |
| 3.4.3 Geodetic Observations (Levelling and GPS Measurements).....          | 3-26       |
| 3.4.4 Satellite Imagery (ERS1-2, ENVISAT, ALOS PALSAR and RADARSAT-2)..... | 3-29       |
| 3.5 Chapter Summary .....                                                  | 3-30       |
| <b>4 Advanced Interferometric SAR Processing .....</b>                     | <b>4-1</b> |
| 4.1 Background.....                                                        | 4-1        |
| 4.2 Methodology .....                                                      | 4-3        |
| 4.2.1 Interferometric Analysis .....                                       | 4-4        |
| 4.2.2 Stacking Method for Interferometric Analysis .....                   | 4-4        |
| 4.2.3 Small Baseline Subset (SBAS) for Interferometric Analysis.....       | 4-5        |
| 4.3 Data Processing.....                                                   | 4-7        |
| 4.4 Results.....                                                           | 4-13       |
| 4.5 Discussion.....                                                        | 4-18       |
| 4.6 Chapter Summary .....                                                  | 4-19       |
| <b>5 Subsurface Structural Behaviour .....</b>                             | <b>5-1</b> |
| 5.1 Background.....                                                        | 5-1        |
| 5.2 Data Resources.....                                                    | 5-2        |
| 5.2.1 Seismic Data .....                                                   | 5-3        |
| 5.2.2 Wire-line logs.....                                                  | 5-4        |
| 5.3 Methodology .....                                                      | 5-5        |
| 5.3.1 Subsurface Structural Modelling .....                                | 5-5        |
| 5.3.2 DInSAR Geophysical Inverse Modelling .....                           | 5-13       |
| 5.4 Results.....                                                           | 5-16       |
| 5.4.1 Subsurface Structural Modelling .....                                | 5-16       |
| 5.4.2 DInSAR Geophysical Inverse Modelling .....                           | 5-28       |

|                                                                             |            |
|-----------------------------------------------------------------------------|------------|
| 5.5 Discussion on Modelling Results.....                                    | 5-36       |
| 5.6 Chapter Summary .....                                                   | 5-40       |
| <b>6 Conclusions and Future Work.....</b>                                   | <b>6-1</b> |
| 6.1 Remote Sensing of Surface Deformation.....                              | 6-1        |
| 6.1.1 Surface Deformation Retrieval from SAR.....                           | 6-2        |
| 6.1.2 Interpretation of Remotely Sensed Deformation Maps.....               | 6-3        |
| 6.2 Subsurface Modelling .....                                              | 6-4        |
| 6.2.1 Subsurface Model Retrieval from in-situ Measurements .....            | 6-4        |
| 6.2.2 Interpretation of Subsurface Modelling and Sensitivity Analysis ..... | 6-5        |
| 6.3 Conclusion .....                                                        | 6-6        |
| 6.4 Future Directions .....                                                 | 6-6        |
| <b>References .....</b>                                                     | <b>1</b>   |
| <b>Appendix A1.....</b>                                                     | <b>A-1</b> |
| <b>Appendix A2.....</b>                                                     | <b>A-7</b> |

## Synopsis

Mapping subsurface structural behaviour and volume change in the underlying reservoir due to resource extraction are of prime importance in both conventional and unconventional hydrocarbon reservoirs. The structurally fractured or faulted zones that often occur around collapsed features are permeable zones for hydrocarbon accumulations and weak zones for infrastructure development. Therefore, knowledge of subsurface structural behaviour is a key priority for both geoscientists and reservoir engineers.

In-situ geophysical observations such as seismic testing and well-logging are the most commonly used methods for determining subsurface structure, by marrying time and depth measurements of seismic surveys and wells. Volumetric techniques are also able to indirectly estimate the hydrocarbon in place based on a geological model, but due to technical limitations such as sparse sampling in time and a need for detailed down-hole information, enhanced mapping of subsurface behaviour requires costly data and software, and expertise in geological modelling and interpretation.

Interferometric SAR remote sensing provides a non-contact observation technique for monitoring large hydrocarbon basins with much higher spatial/temporal coverage and lower cost than traditional methods. While it allows for measuring the ground surface deformation with high vertical accuracy, it does not give any direct information on subsurface structure. Consequently, this thesis investigates the novel idea of using InSAR deformation maps, complemented with geological modelling to extract reservoir volume change and to infer the structural behaviour of the subsurface for an unconventional hydrocarbon field with no access to a dynamic model.

This study first presents the outcome of two different InSAR processing algorithms using a unique combination of satellite acquisitions to detect and analyse ground surface deformation due to man-made interactions in an operational hydrocarbon extraction basin located in eastern Australian. For the last five years, the north-eastern part of this basin, containing coal seam gas mining operations and accompanied groundwater extraction, has drawn the attention of local operating companies and water commissions for its gradual depressurization and subsequent land surface deformation. Contrary to a previous study, which used a different interferometric technique, three regions above coal seam gas mining districts were identified as having an ongoing downward motion. As a proof-of-concept study, the sub-basin with a maximum settlement risk and limited seismic measurements was selected for evaluating its subsurface structural behaviour and reservoir volume change.

This research presents a unique approach to comprehensively assess the viscoelastic multi-layer source model for the selected area with significant deformation overlaying an unconventional reservoir. This model was previously tested on conventional hydrocarbon resources with no access to 3D geological modelling. Tuning elastic properties of underlying formations in a stratified coal seam gas reservoir with more than approximately 300m thickness of overburden and several fresh-water

aquifers was conducted by integrating down-hole logs and seismic interpretation through property modelling and source inversion.

The outcomes of the inverse modelling in this coal seam gas reservoir include the retrieval of stress components and fractional volume change. Analysing volume change results revealed that the dense network of extraction wells was the main cause for ground surface deformation and subsequent volume change. Moreover, the two-lobe pattern and NW-SE trend of volumetric change were found to be the controlling effect of an underlying structure, such as an aperture or a fault that affects subsurface behaviour and was not identified in the 3D geological model due to the absence of seismic acquisition in this area.

## **Declaration**

This thesis contains no material which has been accepted for the award of any other degree or diploma at any university or equivalent institution and that, to the best of my knowledge and belief, this thesis contains no material previously published or written by another person, except where due reference is made in the text of the thesis.

*Negin Fouladi Moghaddam*

## Acknowledgements

This research was financially supported by the Australian Government International Postgraduate Research Scholarship and the Australian Postgraduate Award and was accomplished at the Civil Engineering Department, Monash University. The satellite observation dataset was provided through the Space Agency (ESA) Cat-1 project (P13196), the Japan Aerospace Exploration Agency (JAXA) project (P1338002) and the Canadian Space Agency (CSA). Moreover, I gratefully acknowledge the support from the Geological Survey of Queensland, the Department of Natural Resource and Mines (DNRM), and Geoscience Australia for having provided access to in-situ measurements and technical supports. I take this opportunity to express my gratitude to everyone who supported me throughout this course of research.

I would like to express my sincere gratitude to my main advisor, Dr. Christoph Rüdiger, for the continuous support of my study and related research at Monash University, and for his patience and immense knowledge. His guidance helped me in my research and in the writing of my thesis. I would also like to thank the rest of my project committee: Dr. Sergey Samsonov, Prof. Mike Hall, and Prof. Jeffery P. Walker, for their insightful comments and encouragement, but also for their valuable input on each stage of my study. I extend my special thanks to Dr. Samsonov for his patience, punctuality and willingness to answer all my questions.

My sincere thanks also go to Prof. Kim Lowell, Dr. Mihai Tanase, and Ms. Wendy Jackson at CRC for Spatial Science who provided me an opportunity to join their team, and who gave me access to the laboratory and image processing facilities. I would also like to express my heartfelt gratitude to 3D-geo directors and staff - especially Mr. Hadi Nourollah, Mr. Keven Asquith and Dr. Jeffery Keetley who always provided me with inspiring advice during my study. I have gained a lot of knowledge and working skills from them. Without their precious support it would not have been possible to accomplish this research.

My deepest thanks go to Dr. Donald Vasco in Lawrence Berkeley National Laboratory for his assistance with geophysical inverse modelling and for his comments that greatly improved the outcome of my investigation. Also I thank Prof. Daniele Perissin at Purdue University for training me on using his processing software for my initial monitoring results. I am also immensely grateful to Mr. Kedar Nadkarni for his insights on an earlier version of this manuscript.

I am using this opportunity to thank Ms. Jenny Manson for her invaluable guidance and friendly advice during this project. I am sincerely grateful to her for sharing truthful and illuminating views on a number of issues related to the project. I also thank my fellow lab mates- Arezou, Mei Sun, Juri, Zeinab, Sabah, Mohammad, Ashley, and Ashkan for the stimulating discussions, and for all the fun we have had in the last couple of years.

Last but not least, I would like to thank my family for their loving support and for having great confidence in me all through these years. I would finally like to thank one of my best friends in

Melbourne, Sam, who was always helping me out of difficulties and supporting me without a word of complaint. Thank you for always being around when I needed your help and advice.

## List of symbols

| Symbols          | Unit                 | Definition                                      |
|------------------|----------------------|-------------------------------------------------|
| $d$              | -----                | Vector of deformation values                    |
| $P$              | -----                | Vector of pressure changes                      |
| $n$              | -----                | Number of observation points                    |
| $s$              | -----                | Number of reservoir blocks                      |
| $\alpha^2$       | -----                | Damping factor                                  |
| $\beta^2$        | -----                | Penalty for smoothing constraint                |
| $\Delta R_{min}$ | [m]                  | SAR sensor resolution                           |
| $r$              | [m]                  | Range direction (sensor-target distance)        |
| $T_p$            | [t]                  | Pulse duration                                  |
| $\Delta r$       | [m]                  | Distance between two objects in range direction |
| $C$              | [m/sec]              | Light speed                                     |
| $BW$             | [Hz]                 | Band Width                                      |
| $f_s$            | [Hz]                 | Sampling rate                                   |
| $\theta$         | [° Degree]           | Look angle                                      |
| $\sigma^0$       | -----                | Radar backscatter coefficient                   |
| $\phi$           | [rad]                | Phase value                                     |
| $\varphi$        | [rad]                | Reflectivity phase                              |
| $\rho$           | -----                | Coherence                                       |
| $h_a$            | [m]                  | Altitude of ambiguity                           |
| $Z$              | -----                | SAR image                                       |
| $B_n$            | [m]                  | Normal baseline                                 |
| $\pi$            | -----                | Pi                                              |
| $\phi_{obs}^k$   | $[-\pi, \pi]$        | Each interferogram                              |
| $\Phi_{def}^k$   | $[-\pi, \pi]$        | Sum of deformation                              |
| $\Phi_{topo}^k$  | $[-\pi, \pi]$        | Residual topographic                            |
| $\Phi_{atm}^k$   | $[-\pi, \pi]$        | Atmospheric component                           |
| $\sigma$         | -----                | Standard deviation                              |
| $V_p$            | [m/sec]              | Compressional velocity                          |
| $V_s$            | [m/sec]              | Shear velocity                                  |
| $\rho$           | [g/cm <sup>3</sup> ] | Rock density                                    |
| $V_{Int}$        | [m/sec]              | Interval velocity                               |
| $\sigma_1$       | -----                | Principal stress component                      |
| $R_w$            | MΩ·cm                | Water resistivity                               |

## List of Abbreviations

|                 |                                                              |
|-----------------|--------------------------------------------------------------|
| AHD             | Australian Height Datum                                      |
| AI              | Acoustic Impedance                                           |
| ALOS            | Advanced Land Observing Satellite                            |
| AOI             | Area of Interest                                             |
| API             | American Petroleum Institute                                 |
| BRS             | Bureau of Rural Sciences                                     |
| CBM             | Coal Bed Methane                                             |
| CCRA            | Central Condamine River Alluvium                             |
| CCS             | Carbon Capture and Storage                                   |
| CGPS            | Continuous GPS                                               |
| CLVD            | Compensated Linear Vertical Dipole                           |
| CO <sub>2</sub> | Carbon Dioxide                                               |
| CORS            | Continuously Operating Reference Station                     |
| CSA             | Canada Space Agency                                          |
| CSG             | Coal Seam Gas                                                |
| CSIRO           | Commonwealth Scientific and Industrial Research Organisation |
| CSS             | Cyclic Steam Simulation                                      |
| DEM             | Digital Elevation Model                                      |
| DFIT            | Diagnostic Fracture Injection Testing                        |
| DNRM            | Department of Natural Resources and Mines                    |
| DS              | Distributed Scatterers                                       |
| DST             | Drill Stem Test                                              |
| DTM             | Digital Terrain Model                                        |
| ENVISAT         | ENVironmental SATellite                                      |
| EOR             | Enhanced Oil Recovery                                        |
| EPBC            | Environment Protection and Biodiversity Conservation         |
| ERS             | European Remote Sensing                                      |
| ESA             | European Space Agency                                        |
| FBD             | Fine Beam Double                                             |
| FBS             | Fine Beam Single                                             |
| FEM             | Finite Element Modelling                                     |
| FFT             | Fast Fourier Transform                                       |
| GA              | Genetic Algorithm                                            |
| GAB             | Great Artesian Basin                                         |
| GABHYD          | Great Artesian Basin hydraulic model                         |
| GABSIM          | Great Artesian Basin simulation model                        |
| GADDS           | Geophysical Archive Data Delivery System                     |
| GHG             | Green House Gas                                              |
| GL              | Giga Litre                                                   |
| GNSS            | Global Navigation Satellite System                           |
| GPS             | Global Positioning System                                    |
| GR              | Gamma Ray                                                    |
| GRFS            | Gaussian Random Function Simulation                          |
| HH              | Horizontal- horizontal polarization                          |
| HV              | Horizontal-vertical polarization                             |
| IAA             | Immediately Affected Area                                    |
| InSAR           | Interferometric Synthetic Aperture Radar                     |
| JAXA            | Japan Aerospace Exploration Agency                           |
| kPa             | KiloPascal                                                   |
| LAA             | Long-term Affected Area                                      |
| LIDAR           | Light Detection And Ranging                                  |

|                     |                                                               |
|---------------------|---------------------------------------------------------------|
| LNG-EIS             | Liquefied National Gas Environmental Impact Statement         |
| LOS                 | Line Of Sight                                                 |
| mD                  | MilliDarcy                                                    |
| m/d                 | Meter per day                                                 |
| MDT                 | Modular Formation Dynamic Tester                              |
| Msec                | Microsecond                                                   |
| MSBAS               | Multidimensional Small BAseLine Subset                        |
| Msm <sup>3</sup> /d | Mega Standard Cubic Metres per Day                            |
| Mt/y                | Million Ton per year                                          |
| m/a                 | Meter per Annual                                              |
| mV                  | Millivolt                                                     |
| NPOR                | Neutron Porosity                                              |
| PALSAR              | Phased-Array L-band Synthetic Aperture Radar                  |
| PJ                  | Petajoule                                                     |
| PS                  | Permanent Scatterer                                           |
| PSCMP               | Post Seismic Composite Model                                  |
| PSGRN               | Post Seismic Green Function                                   |
| PSInSARTM           | Permanent Scatterers Interferometric Synthetic Aperture Radar |
| PU                  | Porosity Unit                                                 |
| QGC                 | Queensland Gas Company                                        |
| QWC                 | Queensland Water Commission                                   |
| RC                  | Reflection Coefficient                                        |
| RCS                 | Radar Cross Section                                           |
| RINEX               | Receiver Independent Exchange Format                          |
| SA                  | Simulated Annealing                                           |
| SAR                 | Synthetic Aperture Radar                                      |
| SBAS                | Small BAseLine Subset                                         |
| SC                  | Statistical Competency                                        |
| SLC                 | Single Look Complex                                           |
| SNR                 | Signal to Noise Ratio                                         |
| SP                  | Spontaneous Potential                                         |
| SRS                 | Seismic Reference Survey                                      |
| SRTM                | Shuttle Radar Topography Mission                              |
| SVD                 | Single Value Decomposition                                    |
| TMI                 | Total Magnetic Intensity                                      |
| TVD                 | True Vertical Depth                                           |
| TWT                 | Two –way Time                                                 |
| UAVSAR              | Uninhabited Aerial Vehicle SAR                                |
| UCG                 | Underground Coal Gasification                                 |
| USA                 | United States of America                                      |
| VH                  | Vertical-horizontal polarization                              |
| VV                  | Vertical-vertical polarization                                |
| VSP                 | Vertical Seismic Profile                                      |
| WCM                 | Walloon Coal Measures                                         |

# List of Figures

**Figure 2-1:** (a) amplitude and (b) phase components of ENVISAT ASAR image. Phase shows the change in sensor-target distance while amplitude represents backscattered values for each resolution cell or image pixel .....2-13

**Figure 2-2:** Schematic of along-track SAR interferometry observation with geometric parameters. The flight paths, which are pointing into the page, are not shown. T1 represents the first ground observation and T2 shows the second, with the time interval  $\Delta T$  between two observations giving the  $\Delta R$  displacement in range direction (r).....2-16

**Figure 3-1:** The green square shows the location of the study area in the Surat Basin (yellow) in Queensland, Australia over the extent of Great Artesian Basin (blue).....3-2

**Figure 3-2:** Distribution of soil types in the Surat Basin including the location of the previously mapped faults.....3-4

**Figure 3-3:** Land use map of the study area, showing the various types of land cover with different kinds of land use available in the Surat Basin.....3-5

**Figure 3-4:** Surface geology map of the Surat Basin, including the location of the previously mapped faults.....3-6

**Figure 3-5:** The location of the superimposed Surat and Bowen Basin along with other related Mesozoic basins. The structure of the Surat Basin and the extent of the Walloon Coal Measures are also highlighted.....3-8

**Figure 3-6:** Stratigraphic column of the Jurassic- Cretaceous units in the Surat Basin.....3-8

**Figure 3-7:** Normal-polarity seismic section (BMR84-14), which passes across the southern part of the Surat Basin, shows a sequence of sedimentary rocks. The vertical scale is in milliseconds seismic two way travel time.....3-11

**Figure 3-8:** Detailed subsurface layers including the aquifers and aquitards in the Great Artesian Basin including the Surat Basin .....3-14

**Figure 3-9:** The procedure for underground coal gasification (UCG).....3-20

**Figure 3-10:** Overview of the location of seismic lines and petroleum wells over the study area in the Surat Basin (the inlet image). Two selected seismic lines in yellow colour are shown in the background image. The right-hand side line is called OW05-103 and the left-hand side line is called MS87B-37 to show the stratigraphic horizons identified in this region using Petrel Schlumberger © software.....3-22

**Figure 3-11:** Example of seismic interpretation for seismic line MS87B-37 showing lithological boundaries and structural faults.....3-23

**Figure 3-12:** Total Magnetic Intensity (TMI) survey conducted in the study area part extracted from the Geoscience Australia database (Geophysical Archive Data Delivery System (GADDS)). The magnetic intensity is higher in the western part of the area compared to the eastern part. The boundary between magnetic high and magnetic low anomalies indicates the magnetic body location or geological boundaries such as faults.....3-23

**Figure 3-13:** The distribution of the resource extraction wells, including petroleum, coal seam gas and groundwater, in this part of the Surat Basin. The majority of the petroleum wells (red) are located in the eastern part of the area while coal seam gas extraction wells (green) lie in an elongated area from northwest to southeast. Groundwater extraction wells (blue) are spread over a larger area, but more densely concentrated in the eastern part. For the 2D seismic lines, there is a lack of data in the eastern part with very old seismic surveys, while the western part has a fair distribution of the poor to good quality seismic lines. As already noted there are no 3D seismic surveys in this part of the Surat Basin. Near Kogan, there are also two opal mining districts.....3-24

**Figure 3-14:** (a) Distribution of the geodetic measurements, including levelling, Doppler GPS, and continuous GPS (CGPS) over the study area of the Surat Basin that is being extracted for different resources by various companies in their specific exploration and excavation permits. (b) Distribution of 65 new geodetic sites in the Surat Basin (background grey shade) including 40 co-located survey marks and corner reflectors as yellow dots.....**3-27**

**Figure 3-15:** Time series analysis of ground surface movement at (a) Dalby, (b) Eidsvold, (c) Mitchell (d) Toowoomba CGPS station between 2010 and 2016. The green lines show 3 times of the weighted RMS values and the red lines indicate uncertainty of velocity estimates in each epoch that the calculation was performed .....**3-28**

**Figure 3-16 :** Location map of the study area between Miles and Dalby in the Surat Basin showing C-band (ERS1/2, ENVISAT, RADARSAT-2) and L-band (ALOS-PALSAR) satellite footprints in image mode over the 90 m SRTM Digital Elevation Model. Two scenes of ERS/ENVISAT (pink squares), four scenes of ALOS PALSAR (grey squares), and two scenes of RADARSAT-2 (white squares) cover the region of interest (blue circle) for the space-borne observation period (1992-2014).....**3-29**

**Figure 4-1:** Location map of the study area in the Surat Basin showing C-band (ERS/ENVISAT, RADARSAT-2) and L-band (ALOS-PALSAR) satellite footprints in image mode over the 90 m SRTM Digital Elevation Model. Four scenes of ALOS PALSAR (grey squares) and two scenes of RADARSAT-2 (white squares), both in ascending paths, cover the region of interest for 2006-2011 and 2012-2014 respectively. ENVISAT coverage in two scenes is in descending paths. The fault traces are shown in red and the triangle marks the location of reported gas leakage.....**4-3**

**Figure 4-2:** Flow chart diagram of the code used for time series calculation and mean or linear deformation rate estimation in both ALOS PALSAR and RADARSAT-2 satellite observations. Flags (\_FLAG) specified in a header file are used for controlling processing flow..... **4-6**

**Figure 4-3:** The mean deformation rate in ENVISAT both descending tracks a) T488-F4149 and b) T216-F4149) derived from stacking method in centimetre per year scale. Highlighted location A is the area with likely deformation signals.....**4-8**

**Figure 4-4:** Line of Sight deformation rates (in cm/year) from stacking of ALOS PALSAR ascending scenes: a) T366-F6640; b) T365-F6640; c) T366-F6630; d) T365-F6630 between 2006 and 2011. Based on the processing results, among four ALOS scenes, significant phase delay responses were detected in a and d, but the other two scenes show no signal of ground movement. Locations S1, S2, and S3 are candidate sites with downward motion, closely aligned to the areas with CSG mining.....**4-9**

**Figure 4-5:** SBAS analysis results for T366-F6640 with 22 ALOS PALSAR FBS-FBD imagery a) The rate of deformation (cm/year) in LOS direction b) The frequency distribution of deformation rate for the best reference point (R in 5a) after implementing Gaussian filtering in time domain. c – d) Selected points (P1, P2, and P3) for time series analysis over the areas with downward and adjacent upward motion in candidate region S1. e) Time series of ground surface deformation for selected points relative to the assigned reference in LOS direction before Gaussian filtering (UPx) and after filtering (Px).....**4-11**

**Figure 4-6:** SBAS analysis results for T365-F6630 with 20 ALOS PALSAR FBS-FBD imagery a) The rate of deformation (cm/year) in LOS direction b) The frequency distribution of deformation rate for the best reference point (R in 6a) after implementing Gaussian filtering in time domain. c – d) Selected points (P1, P2, and P3) for time series analysis over the areas with downward motion in candidate regions S2 and S3. e) Time series of ground surface deformation for selected points relative to the assigned reference in LOS direction before Gaussian filtering (UPx) and after filtering (Px).....**4-12**

**Figure 4-7:** SBAS analysis results for RADARSAT-2. a and b) The rate of deformation (cm/year) in LOS direction for RADARSAT-2 left and right in Figure 4-1 respectively. c and d) The frequency distribution of deformation rate for the best reference points (R in a and b) after implementing Gaussian filtering in time domain. e) Graph illustrates the time series of ground surface deformation for selected points relative to the assigned reference for RADARSAT-2 right.....**4-14**

**Figure 4-8:** Graphs of the CSG and groundwater extraction rates versus ground surface displacement in selected regions S1, S2 and S3. a) Daandine b) Tipton West c) Berwyndale South and d) Kogan North CSG mining districts.....**4-16**

|                                                                                                                                                                                                                                                                                                                                                                                                                                                                                                                              |             |
|------------------------------------------------------------------------------------------------------------------------------------------------------------------------------------------------------------------------------------------------------------------------------------------------------------------------------------------------------------------------------------------------------------------------------------------------------------------------------------------------------------------------------|-------------|
| <b>Figure 5-1:</b> Outline of the area for which the 3D geological modelling and inverse modelling were undertaken (black outline), showing the available seismic dataset (green and red lines). The green seismic lines were in good quality for seismic interpretation but the red ones were in poor quality. The black dot points show the location of petroleum wells with velocity check shots.....                                                                                                                     | <b>5-4</b>  |
| <b>Figure 5-2:</b> A composite line between XM86-9 and XM86-14 seismic lines as shown in small image on the lower left-hand corner. By overall reviewing of significant events in seismic lines and using SRSs in Mackie_1, stratigraphic levels and structural features were identified and traced. The image in the background, shows tying Mackie_1 with seismic and horizon picks. The colourful lines show the traced stratigraphic levels while the black lines are normal and reverse faults both in time domain..... | <b>5-7</b>  |
| <b>Figure 5-3:</b> The workflow for interpretation and modelling in the proposed geological modelling package.....                                                                                                                                                                                                                                                                                                                                                                                                           | <b>5-8</b>  |
| <b>Figure 5-4:</b> The time-depth plot used to extract the velocity model and to convert horizons in seismic time domain into depth domain. These results based on observed interval velocity of four wells with check shots i.e. Bulwer_1, Coloomoola_1, Picurda_1, and Xylex_1 with equal weight in distribution.....                                                                                                                                                                                                      | <b>5-10</b> |
| <b>Figure 5-5:</b> Flowchart of major subroutines in PSEGRN program.....                                                                                                                                                                                                                                                                                                                                                                                                                                                     | <b>5-15</b> |
| <b>Figure 5-6:</b> The flowchart of major subroutines in PSCMP program.....                                                                                                                                                                                                                                                                                                                                                                                                                                                  | <b>5-15</b> |
| <b>Figure 5-7(a):</b> Vertical depth map of the Gubberamunda Sandstone formation in the study area.<br>This map was extracted from seismic interpretation and velocity modelling steps.....                                                                                                                                                                                                                                                                                                                                  | <b>5-17</b> |
| <b>Figure 5-7(b):</b> Isopach map for the Gubberamunda Sandstone and Westbourne Formation in the study area. This map is extracted from seismic depth conversion.....                                                                                                                                                                                                                                                                                                                                                        | <b>5-18</b> |
| <b>Figure 5-8:</b> Three-dimensional view of the entire region with structural faults (black colour) that were traced on seismic sections.....                                                                                                                                                                                                                                                                                                                                                                               | <b>5-19</b> |
| <b>Figure 5-9:</b> 3D view of eight horizons in depth domain converted by using the velocity model and well-bores that were involved for subsurface down-hole information.....                                                                                                                                                                                                                                                                                                                                               | <b>5-20</b> |
| <b>Figure 5-10:</b> Three-dimensional view of the structural model based on available seismic interpretation and well log data trended with stratigraphic well tops in depth domain.....                                                                                                                                                                                                                                                                                                                                     | <b>5-20</b> |
| <b>Figure 5-11:</b> Spatial distribution of compressional velocity over the entire modelling region within the Walloon Coal Measures layer. As it is shown the compressional velocity has the lowest value in the south-western part of the study area, but over the deformation area the values are quite high.....                                                                                                                                                                                                         | <b>5-22</b> |
| <b>Figure 5-12:</b> Spatial distribution of sonic log over the entire region within the Walloon Coal Measures layer. As it is shown the values are the lowest in the proximity of the deformation region and change abruptly from south to north.....                                                                                                                                                                                                                                                                        | <b>5-22</b> |
| <b>Figure 5-13:</b> Spatial distribution of neutral porosity over the entire outline for geological modelling. While the majority of study area covered with medium neutral porosity formations, the area with deformation signal shows both high and medium porous formations.....                                                                                                                                                                                                                                          | <b>5-23</b> |
| <b>Figure 5-14:</b> Spatial distribution of gamma ray response in three-dimensional view. It is shown that the GR values in area with deformation vary between 60 and 100 gAPI.....                                                                                                                                                                                                                                                                                                                                          | <b>5-24</b> |
| <b>Figure 5-15:</b> Spatial distribution of density over the modelling area at Walloon Coal Measures depth (~ -400m) in g/cm <sup>3</sup> upscaled for the well-bore column in the subsurface model.....                                                                                                                                                                                                                                                                                                                     | <b>5-25</b> |
| <b>Figure 5-16:</b> Spatial distribution of Spontaneous Potential (SP) over the outline of modelling with the highest values in the proximity of Condabri_8, Picurda_1, and Talinga_121 within the Walloon Coal Measures.....                                                                                                                                                                                                                                                                                                | <b>5-26</b> |
| <b>Figure 5-17:</b> Pressure – Depth gradient plot for 31 petroleum wells available in the entire Surat Basin (solid purple line) and its comparison with standard hydrostatic pressure and lithostatic pressure gradients in a reservoir.....                                                                                                                                                                                                                                                                               | <b>5-27</b> |

**Figure 5-18:** Flowchart of the inverse and forward modelling packages to estimate the synthetic data and to calculate the fractional volume change.....5-30

**Figure 5-19:** The impact of different depths of Walloon Coal Measures (CSG reservoir) on the rate of surface deformation recovery. Range change data is surface deformation observation by SAR interferometry (truth) while others are the outcomes of forward modelling (simulated).....5-31

**Figure 5-20:** The impact of different formation density of Walloon Coal Measures (CSG reservoir) on the rate of surface deformation recovery. Range change data is surface deformation observation by SAR interferometry (truth) while others are the outcomes of forward modelling (simulated).....5-32

**Figure 5-21:** Residual values between synthetic deformation maps at different depths of Walloon Coal Measure source layer. Based on seismic interpretation and 3D modelling, Walloon Coal Measure is located at 380m.....5-33

**Figure 5-22:** Residual values between synthetic deformation maps for different densities of Walloon Coal Measure source layer. Based on seismic interpretation and 3D modelling, density of Walloon Coal Measure changes between 1526(kg/m<sup>3</sup>) and 1885.8 (kg/m<sup>3</sup>).....5-34

**Figure 5-23:** Result of modelling as a fractional volume change (equates to change in volume over initial volume) represents the source as a grid that undergoes variable volume changes. As it is shown changing in the depth of reservoir (Walloon Coal Seam) from 0.38 km to 0.78 km did not impact on the amount of volume flux significantly.....5-38

**Figure 5-24:** (a) Location map of structural faults intersected with Walloon Coal Measure reservoir layer at approximately 400 m depth. (b) The result of geophysical inverse modelling using InSAR surface observation superimposed on the Walloon Coal Measure depth map in (a).....5-39

## List of Tables

|                                                                                                                                                                                                                                         |             |
|-----------------------------------------------------------------------------------------------------------------------------------------------------------------------------------------------------------------------------------------|-------------|
| <b>Table 2-1:</b> Analytical models, their major assumptions for inverse modelling and their free parameters .....                                                                                                                      | <b>2-5</b>  |
| <b>Table 2-2:</b> Optimization methods with different geoscience application.....                                                                                                                                                       | <b>2-5</b>  |
| <b>Table 2-3:</b> Space-borne SAR sensors characteristics for monitoring purposes.....                                                                                                                                                  | <b>2-12</b> |
| <b>Table 2-4:</b> Different procedures to remove or mitigate phase contaminations in interferometric results .....                                                                                                                      | <b>2-19</b> |
| <b>Table 2-5:</b> Interferometric SAR processing algorithms with their specific characteristics and outcomes .....                                                                                                                      | <b>2-21</b> |
| <b>Table 3-1:</b> The two different categories of groundwater discharge in aquifer system in the Surat Basin .....                                                                                                                      | <b>3-15</b> |
| <b>Table 3-2:</b> Major geological and hydrological factors affecting coal seam gas reserves in the Surat basin in different levels.....                                                                                                | <b>3-19</b> |
| <b>Table 3-3:</b> List of seismic surveys conducted in the Surat Basin proposed area since 1976.....                                                                                                                                    | <b>3-22</b> |
| <b>Table 3-4:</b> Hydraulic properties of the GAB aquifers.....                                                                                                                                                                         | <b>3-26</b> |
| <b>Table 4-1:</b> SAR data used for DInSAR processing in this work: time span (in YYYYMMDD format), azimuth $\theta$ and incidence angles $\phi$ , number of available SAR images $N$ and number of calculated interferograms $M$ ..... | <b>4-7</b>  |
| <b>Table 4-2:</b> Correlation coefficient estimation for each resources extraction site with displacement.....                                                                                                                          | <b>4-17</b> |
| <b>Table 5-1:</b> List of in-situ measurements for 3D geological modelling for the proposed area in the Surat Basin. These data sources are publically available in different scales.....                                               | <b>5-5</b>  |
| <b>Table 5-2:</b> Interval velocity for each formation unit estimated based on averaging the down-hole interval velocity measured for the four selected wells.....                                                                      | <b>5-10</b> |
| <b>Table 5-3:</b> The input box for creating velocity model – this input box includes different horizons that are trended with well tops and modelled by selective interval velocity (Petrel Schlumberger ©).....                       | <b>5-11</b> |
| <b>Table 5-4:</b> Setting up variogram analysis for petrophysical modelling.....                                                                                                                                                        | <b>5-13</b> |

# 1 Introduction

This thesis presents the application of microwave remote sensing satellite observations for evaluation of ground deformation and of subsurface structural behaviour. One of the main applications of interferometric SAR processing algorithms is the retrieval of accurate deformation maps on a regional-scale, to define the geometries of the deformation source. There has been a long history of radar data spanning the past two decades, with the most extensive ones including ERS-1/2, ENVISAT, RADARSAT-2 in C-band, and ALOS-PALSAR in L-band. All of those have been collected separately by different space agencies for the historical analysis of ground surface deformation. Collecting numerous SAR datasets in different wavelengths and different geometries has the advantage of providing an essential spatial and temporal coverage that is required for the reliable monitoring of ground displacements with sub-centimeter accuracy. A comprehensive study was conducted in this thesis that includes primary and advanced interferometric SAR analysis to estimate the rate of downward or upward motions. More emphasis was then laid on the area with maximum subsidence rate for subsequent subsurface structural modelling using geophysical in situ measurements. Source properties and changes in reservoir volume due to resource extraction were then estimated by inverting surface deformation information and elastic properties of the subsurface.

## 1.2 Statement of Problem

The long-term exploitation of conventional (i.e. oil and gas) and unconventional (i.e. CSG) hydrocarbon resources, along with farming and infrastructure development has put a number of regions under significant land surface deformation risk due to subsequent compaction of the geological units. The accumulated small amounts of failure in geological units may result in suddenly occurring sink holes or gradually as a subsidence. In either case, there is an instant need to detect the location and estimate the intensity of the surface deformation in a timely manner with high accuracy. On the other hand, depleted reservoirs or deep saline groundwater supplies (i.e. aquifers) could be a target for the injection of environmental contaminants or CO<sub>2</sub> storage on a basin scale. Therefore, mapping surface deformation patterns and their gradual spatial and temporal evolution can be a valuable tool for operational risk assessment in production and field development.

Although in situ geodetic measurements such as tilt meter, optical levelling, and Global Positioning System (GPS) are traditional methods to measure vertical inclination and the geodetic height of a given point relative to pre-assigned datum, respectively, their need for conducting multiple point-based measurements across large geodetic networks results in significant cost for basin-wide monitoring. Moreover, common geophysical surveys such as seismic and well logging provide

valuable information about the subsurface structural framework and reservoir properties, but even when available, these measurements are often spatially or temporally too sparse to be used for land surface deformation studies or volume change estimation.

To address the limited and sparse data sampling problem of in situ geodetic observations, and to enhance mapping subsurface geological behaviour in a field under persistent hydrocarbon extraction, Interferometric SAR (or InSAR) is used as an optimal non in situ geodetic technique. In addition, deformation patterns on the surface might be an indication for subsurface structures such as concealed faults [Amelung *et al.*, 1999]. The role of these geological features to control the trend and pattern of deformation signals has been suggested in Anderssohn *et al.* [2009] and Vasco *et al.* [2010], but has never been examined with subsurface structural modelling using seismic interpretation.

InSAR-based historical analysis of surface deformation can also be used as a constraint for geophysical source models. According to mathematical source models constrained by advanced interferometric observations, the circular shape of deformation (i.e. uplift or subsidence) pattern indicates that the causative source is a localized volume at a particular depth [Samsonov *et al.*, 2014]. For the quantitative interpretation of the underground source that is responsible for the ground displacement, an inversion scenario with an idealized earth structure to simplify the subsurface in a Coal Bed Methane (CBM) reservoir is required.

One of the primary data resources to build a comprehensive image of the subsurface is to conduct two-dimensional seismic surveys accompanied by well-bore information. These static measurements are normally sparse and limited to a few locations across the basin, but they can approximate the subsurface stratigraphy and formation properties such as depth, density and porosity. Moreover, extracting a snapshot of reservoir volume change due to a variation in pressure or production using in situ geophysical measurements needs complementary information such as drawn from a dynamic model of the reservoir. Conversely, the geophysical inversion of high-resolution deformation patterns along with subsurface properties of the soil can translated into the ongoing volume changes at the depth of the reservoir to better understand the subsurface behaviour in terms of gradual compaction or potential for fluid storage. The volume change estimation then might be crosschecked with production rates for any essential revision on field development plans.

Different interferometric SAR processing techniques have been proposed for monitoring surface deformation and subsequently tested for conventional hydrocarbon resources, such as oil and gas fields or open pit mining districts. However, it is essential to examine this remotely geodetic technology for subsidence measurements in Coal Seam Gas (CSG) supplies associated with shallow depth aquifers to evaluate the nature and propagation of resource extraction at depth. Therefore, interferometric SAR as a highly accurate monitoring scheme will be used in this thesis. The work will be based on archived and new satellite acquisitions to address the scientific requirements pertinent to ground surface deformation and subsequent volume changes occurring at depth as a result of CSG extraction. The outcome of this research may be of interest to both mining companies and the

government by providing detailed and accurate information on how the CSG operations are progressing in near real time.

### 1.3 Objectives and Scope

A previous geodetic study [[Dura et al., 2012](#)] using an interferometric processing technique based on permanent scatterers is relatively sparse in spatial resolution for the whole CSG basin that is located in a non-urban region and is in contradiction with several reports for an ongoing groundwater depressurization and subsequent methane leakage into the fresh water supplies. Hence, the main objective of this thesis is to thoroughly evaluate the performance of further processing algorithm called Small BAseline Subset (SBAS) [[Berardino et al., 2002](#)] for similar satellite datasets covering the same basin. Contrary to the previous method, the proposed processing algorithm is independent from persistent scatterers that are sparse or are not available in the proposed remote CSG field.

The second objective of this research is to evaluate the possibility of using surface deformation maps to extract subsurface structural behaviour for an area in which limited geophysical acquisitions are available and long-term surface deformation is present. In order to achieve this objective, surface deformation mapping will be conducted in a CSG prone Basin in Australia, and will be followed by static 3D structural mapping and geophysical inverse modelling to find the best subsurface parameters for a given source that is responsible for detected ground surface deformation.

### 1.4 Outline of Approach

The approach in this thesis includes three main parts: i) collecting available SAR datasets and interferometric processing for surface deformation map retrieval ii) seismic interpretation tied to wire-line down-hole information for 3D subsurface structural modelling and property analysis iii) geophysical inverse modelling for estimating the source properties and variations in reservoir volume to define the subsurface structural behaviour.

The current research is undertaken across the Surat Basin, Queensland, Australia. For the nature of agricultural and CSG mining operations, as well as of geological conditions of this area, the surface deformation of the region between Chinchilla and Dalby has been reported [[QWC, 2012](#)]. These in situ observations were the starting point for using multi-temporal and high resolution monitoring techniques for various SAR satellite datasets acquired at C-band (ERS-1/2, ENVISAT and RADARSAT-2) and L-band (ALOS-PALSAR) in their descending and ascending orbits. Those data come with different looking angles to thoroughly monitor the long-term behaviour of the ground surface in response to ongoing anthropogenic activities. The primary interferometric processing results were obtained with SARPROZ [[Perissin et al., 2011](#)] as discussed in [[Fouladi Moghaddam et al., 2013](#)]. Those results gave a general overview about deformation in the Surat Basin indicating that

among the four major ENVISAT tracks, only two adjacent tracks contained temporally consistent deformation signals. On the contrary, other scenes were ruled out from further processing due to lack of coherent signals over time. Using preliminary monitoring results based on the stacking method, the focus was put on the two most likely ENVISAT scenes to order and process archived L-band ALOS-PALSAR and C-band RADARSAT-2 SAR images to increase the temporal coverage and accuracy of the measurement. Conversely to stacking, re-processing these datasets with an advanced interferometric algorithm called Small Baseline Subset (SBAS) by using a cluster of SAR acquisitions with small baseline length for each SAR pairs to create a more accurate time series of deformation for each measurement points with reduced atmospheric, orbital and thermal noises from 2006 to 2014. Additionally, stacks of ALOS-PALSAR and RADARSAT-2 images both in ascending path ruled out the need for Multi-dimensional SBAS (MSBAS) as an advanced type of SBAS algorithm that was proposed at an initial stage of this research, and indicated the need for both descending and ascending acquisition geometries.

Based on the provided deformation signals by the InSAR processing, the subsurface structural simulation using geological characteristics, in situ well logging observations and 2D seismic interpretation, will be provided as the true model. Modelling subsurface structure and its properties will be considered as a guideline for inverse modelling initial conditions. The principal objective for solving such an inverse problem is to find a suitable estimated earth model which would be able to project the properties of shallow depth geological structures (e.g. thrust faults, folds), as well as the strain history in relation to controlling structures and sequence stratigraphy. All being well, it is expected that marginal changes in coal layer volumetric properties and stress components can be estimated for the CSG reservoir using ground surface remote observations.

### 1.5 Structure of Thesis

This thesis is divided into 6 chapters. **Chapter 2** is an extensive review of literature pertaining to the need for ground surface deformation measurement and the available ground surface monitoring and modelling techniques. **Chapter 3** is a description of the major data sets including the introduction of the study area for this research in the locality of Chinchilla, in the Surat Basin, Australia, and the collection of geological and geophysical in situ sampling and remote sensing microwave satellite observations. **Chapter 4** presents advanced interferometric SAR processing results with their geological interpretation, and points out three hotspots with significant downward motion situated over CSG mining districts. According to the processing outcomes in **Chapter 4** and focusing on one of the settlement regions with the highest rate and lowest field seismic acquisitions, **Chapter 5** develops the process of simulating the 3D subsurface geological model using seismic interpretation and alternative geophysical field measurements. Based on the simulated geo-model, the geophysical

inverse model is tested for the CSG reservoir in the second part of **Chapter 5**. The conclusion and future work are discussed in **Chapter 6**.

**Chapter 4** of this thesis is based on all of the following publications:

- Fouladi Moghaddam, N., S. Samsonov, C. Rüdiger, J.P. Walker, and M. Hall (2016), Multi-Temporal SAR Observations For Deformation Scenario Evaluation Associated with Man-made Interactions, *Environmental Earth Sciences*, *Environ Earth Sci* 75(4):281-296.
- Moghaddam, F.N., C. Rüdiger, S. Samsonov, J.P. Walker, and M. Hall (2013), An Assessment of DInSAR Potential for Simulating Geological Subsurface Structure. In Piantadosi, J., Anderssen, R.S., and Boland J. (eds) MODSIM2013, 20th International Congress on Modelling and Simulation. Modelling and Simulation Society of Australia and New Zealand, Adelaide, December 2013, pp. 3099-3105.

## 2 Literature Review

This chapter outlines the importance of mapping surface deformation for reservoir source modelling and the need for a better understanding of the subsurface structural behaviour. This is followed by a discussion of the methods for both modelling and monitoring of surface deformation, particularly the methods focused on geophysical inverse modelling using observations from microwave SAR remote sensing. The strengths and limitations of these techniques along with their gradual advances are then discussed. Finally, the proposed methodology for surface deformation observation and estimating the reservoir volume changes in a geological basin associated with CSG mining through space-borne SAR observation and geophysical modelling will be presented. The knowledge gap in extracting subsurface structural properties such as the location of faults by using the inverse modelling of surface deformation map is then identified.

### 2.1 Background

Any reduction in fluid pressure due to resource extraction may result in compaction of the geological units. In mining operations for coal seam gas extraction, compaction occurs when groundwater is removed from the pores of saturated, high porosity layers such as clays and silts that cannot maintain the increased vertical stress. The amount of ground deformation is dependent on the depth and thickness of the layer that experienced depressurisation, and the properties of the overlying formations [*Commonwealth-of-Australia, 2014*]. However, compaction in some formations could be elastic, such that the land subsidence could be reversed and to some degree recovered naturally or after injecting some fluids into the reservoir to maintain the pressure decline [*Sansosti et al., 2010*]. In the case of injection, similar to what is happening in Enhanced Oil Recovery (EOR) and Carbon Capture and Storage (CCS), there is the possibility for ground heave, triggering fault reactivation and threatening well integrity. Therefore, surface deformation mapping provides unique data for observing the performance of producing reservoirs [*Ferretti et al., 2011b*].

To measure surface deformation, several geodetic techniques have been developed. These can be categorized into two different groups: in situ monitoring and remote sensing surveys. These two groups can be compared for their cost and extent of monitoring scales. While multiple readings from a large network are required for deformation monitoring relative to a reference using in situ measurement, remote sensing techniques can provide a complete and consistent deformation map of the Earth's surface over large areas with sub-centimetre accuracy within days [*IESC, 2014*].

Collecting optical and microwave satellite images to observe, analyse, and assess natural resources globally has been done for more than two decades. Compared to optical satellites, microwave satellites do not rely on sunlight to collect the images. Moreover, they use a specific portion of the

electromagnetic spectrum that can penetrate thick clouds, fog and dust during any weather conditions due to lower levels of atmospheric attenuation. Synthetic Aperture Radar (SAR) is one of the microwave remote sensing tools used widely for measuring regional-scale land subsidence, thus providing support to field surveying and computer modelling [Ramirez and Foxall, 2014; Sambridge, 1999]. SAR in general and interferometric SAR in particular have been used to quantify the surface response to reservoir depletion in different locations such as Wyoming [Grigg, 2012], the San Juan Basin of Colorado and New Mexico [Katzenstein, 2012] in the USA, and the Gippsland Basin [Ge and Li, 2014] in Australia. Defining the source of the land surface deformation in order to mitigate or prevent the associated risk is one objective of using the surface deformation observations. High-resolution mapping of spatio-temporal deformation fields can provide important information about source geometries and associated physical processes [Anderssohn et al., 2009]. Changes in volumes due to fluid production, injection and thermal processes result in patterns of surface deformation which will propagate from the underground source and be projected on the Earth's surface, such that they can be measured by interferometric SAR sub-centimetre scale observations [Fialko and Simons, 2000].

The following presents a brief overview of the surface deformation problem and its potential link to subsurface structural behaviour. In order to define the source of deformation, various geophysical inverse modelling solutions have been proposed; these will be discussed in the first part of this chapter. This is followed by a review of different surface deformation monitoring techniques. These include the space-borne SAR remote sensing capabilities and the InSAR processing techniques. Lastly, the chapter emphasizes the proposed approach that could be tested for the rest of this research to answer the prior hypotheses and to address the knowledge gap.

### 2.1.1 Surface Deformation

Surface deformation can be caused by a natural or anthropogenic source, and occur over a wide range of temporal scales, from almost instantaneous settlement (i.e. earthquake, volcanic, and glacier movement) to a gradual gentle displacement (i.e. resource extraction). Moreover, it can be localized or large-scale. The most immediate impact of local surface deformation may involve crucial surface infrastructure and their sustainable development [Bakon et al., 2014; Hooper et al., 2004; Normand and Heggy, 2015; Poland and Davis, 1969]. However, regional ground settlement contributes to an increased risk of flooding in coastal areas; seawater intrusion; changes in groundwater systems or regional faults reactivation [Nagel, 2001; Zektser et al., 2005]. Therefore, measuring and monitoring ground surface deformation is crucial for current and future planning of developments.

Various techniques are used to assess and predict the surface deformation, its magnitude, direction, and causes [Galloway and Burbey, 2011]. Mapping relative changes in the elevation or inclination of the ground surface are usually conducted through either ground-based or remotely-sensed geodetic

surveys such as tilt meter, GPS, levelling, InSAR and LIDAR [*Densmore et al., 2010; King et al., 2007; Leva et al., 2003; Massonnet and Feigl, 1998*].

### 2.1.2 Subsurface Structural Behaviour

Fluid flow and pressure evolution together with stress-strain changes are associated with reservoir exploitation. Geomechanical processes along with reservoir development are of primary interest since they can change the reservoir behaviour and impact on the productive layers in the form of compaction and land subsidence. Compaction in a reservoir may alter the rock permeability and reduce the well rates with subsequent delay in recovery from compaction [*Ostermeier, 1995*]. For the above mentioned reasons, a promising understanding of subsurface structure is essential for optimized reservoir management and for well casing design [*Bruno and Bovberg, 1992; Da Silva et al., 1990*].

To analyse the subsurface structure, a priori knowledge about the sequence and thickness of the stratigraphic layers and their relationship with controlling structures such as faults is essential for three-dimensional modelling. Static or dynamic modelling of geological units (i.e. Geo-modelling) consists of the rock matrix and/or the fluid flowing in its pore spaces [*Hosseini et al., 2013*]. The static model is a detailed reconstruction of the geological structure of the reservoir (e.g. the shape of the layers and the trend of the faults), including definition of the geological zones and the petro-physical parameters (initial porosity and density) as a function of the location. Therefore, the result of a static study of reservoir and its surrounding region consists all geological, lithological, stratigraphical and petrophysical aspects [*Adeoti et al., 2014*]. Dynamic models take all the information from the static model and add parameters corresponding to the fluid, rock and well system for dynamic reserve evaluation and production profile estimation. Initial values of porosity and permeability, the evolution of the fluid pressure as a function of space and time, as well as the grid discretization of the reservoir and of the surrounding areas are the output of dynamic model which can be used for the geomechanical finite element simulation [*Cunha, 2004*]. Having access to the dynamic model integrated with surface deformation rates is essential to extract viscoelastic properties of subsurface medium; however, in most cases, these models are confidential or limited to a few production wells for field development purposes. Consequently, static geological modelling for subsurface structure is the common approach and will be examined in this research.

## 2.2 Modelling surface deformation

Scientists and engineers have been using variable source models to determine the best-fit estimate of dislocation source for seismic faults originating from earthquakes [*Massonnet et al., 1993; Segall, 2010*], volume changes in the magma chamber [*Pritchard and Simons, 2004*], and/or characterizing the size and orientation of an induced fracture in a reservoir [*Vasco et al., 2008*]. For the latter,

accurate surface deformation measurements over a reservoir have been inverted to retrieve different source parameters at depth. By using both horizontal and vertical components of the surface displacement field, volumetric strains in the reservoir can be estimated and then converted to stress variations by using proper elastic parameters [Ferretti, 2014].

For inversion, the discrete Green's function,  $G$ , [Segall, 1992] represents the surface deformation at a specified location due to a pressure change in a reservoir block. The surface deformation might include both vertical and horizontal components. The relation between surface deformation and the reservoir pressure change is given by:

$$d = G p, \quad (2.1)$$

where  $d$  is a vector of deformation values with dimension  $n$ , and  $p$  is an unknown vector of pressure changes with dimension  $s$  [Du and Olson, 2001]. The best estimation of the pressure change distribution that minimizes the objective function is the key in this inverse problem. Accordingly, the objective function  $F_p(p)$  proposed by Du et al. [1992] is commonly defined as:

$$F_p(p) = \|Gp - d\|^2 + \alpha^2 \|p - p_0\|^2 + \beta^2 \|Hp - d_0\|^2, \quad (2.2)$$

where  $p$  is the pressure change in reservoir blocks that needs to be mapped. Parameters in this model have several constraints that are imposed by the smoothness ( $Hp - d_0$ ) and the initial pressure ( $p_0$ ). The initial model can be based on pressure front simulations and depletion predictions. The  $\|Gp - d\|^2$  term represents the square of the norm of residuals and  $\alpha^2$  is a damping factor that defines the weight of the initial model. For the initial conditions,  $d_0$  is set to zero, with  $H$  being the finite difference approximation of the Laplacian operator to impose smoothness on the pressure change distribution and  $\beta^2$  is the penalty factor for smooth constraint. To increase the understanding of the underlying processes correspondent to surface deformation, the InSAR data are usually inverted to provide constraints on model parameters [Hooper and Wright, 2009]. There are two common types of models for analyzing surface deformation signals and theoretically reproducing them for extracting specific characteristics of the subsurface source such as its location and its volume or pressure changes. These geophysical models (Table 2-1) for solving the inverse problems are categorized as analytical and numerical models [Anderssohn et al., 2009] and will be discussed in the following two sections. To find a proper set of model parameters for a given dataset (i.e. interferometric SAR observations) and solving an inverse problem, parameterization or parameter identification is an essential stage for the model. From a mathematical point of view, there are a number of tools for minimizing functions that can be used in inverse problem solution to estimate geophysical parameters.

**Table 2-1: Analytical models, their major assumptions for inverse modelling and their free parameters**

| Analytical model    | Assumption                      | Free parameters                                                                                                                              |
|---------------------|---------------------------------|----------------------------------------------------------------------------------------------------------------------------------------------|
| Spherical Source    | An infinite spherical chamber   | Spherical centre coordinates, source volume                                                                                                  |
| Ellipsoidal Source  | Finite prolate spheroid chamber | Ellipsoidal centre coordinates, source excess pressure, major axis, minor axes, strike of major axis, dip of the major axis, Poisson's ratio |
| Penny-shaped source | Symmetric disk reservoir        | Disk centre coordinates, disk thickness, disk radius, reservoir pressure change, Biot coefficient, Poisson's ration(if unknown)              |

**Table 2-2: Optimization methods with different geoscience application after [Shirzaei and Walter, 2009]**

| Method                               | Main idea                                                                   | Application                                                                                          | Advantage                         | Disadvantage                                                                                                                                                                  |
|--------------------------------------|-----------------------------------------------------------------------------|------------------------------------------------------------------------------------------------------|-----------------------------------|-------------------------------------------------------------------------------------------------------------------------------------------------------------------------------|
| Least Squares                        | Gradient based                                                              | Lundgren et al., 2001<br>Jonsson et al., 2002<br>Battaglia et al., 2003, 2006<br>Lanari et al., 2004 | Very fast and convex search space | May get trapped in local minima                                                                                                                                               |
| Monte Carlo                          | Randomly samples the parameters space                                       | Keilis-Borok and Yanovskaja(1967)                                                                    | Gradient free                     | Slow, may miss the global solution                                                                                                                                            |
| Neighbourhood Algorithm <sup>a</sup> | Generate new samples with density function related to previous step samples | Sambridge (1998,1999a,1999b)<br>Amoruso et al., 2007                                                 | Gradient free                     | Slows down very significantly when the number of parameters increases                                                                                                         |
| Simulated Annealing <sup>a</sup>     | Motivated by analogy between annealing in solids and optimization problems  | Cervelli et al., 2001b<br>Chevrot, 2002<br>Jonsson et al., 2002<br>Amelung et al., 2007              | Gradient free, fast               | Slows down very significantly when the number of parameters increases.<br>Success depends on the cooling schedule. May find a solution in the vicinity of the global solution |
| Genetic Algorithm <sup>a</sup>       | Motivated by analogy between biological evolution and optimization problems | Currenti et al., 2005<br>Gottsmann et al. 2006<br>Carbone et al., 2008                               | Gradient free, fast               | Slows down when the number of parameters increase. May find a solution in the vicinity of the global solution                                                                 |
| Statistical Competency               | Iterative approach with no down sampling for observations                   | Shirzaei and Walter , 2009                                                                           | Gradient free, fast               | Improved quality of the results by avoiding local traps                                                                                                                       |

As shown in [Table 2-2](#), there are a number of optimization methods among which the least square adjustment is the most popular for solving the linear inversion equation. For this purpose, interferograms are observations and the corresponding coherence-dependent phase variations are the weights used in a least square adjustment [[Anderssohn et al., 2009](#)]. To find the least-square best fit solution for the model parameters given the data and the simulated noise, non-linear inversion techniques such as Simulated Annealing (SA) [[Cervelli et al., 2001](#); [Faegh-Lashgary et al., 2012](#); [Rothman, 1985](#); [T Wright et al., 2001](#)] or Bayesian [[Hooper, 2010](#)] can be used. With no constraints on the model parameters the result of both inversion methods are similar for real and synthetic InSAR data. While SA needs many model runs to be performed for each realization of the posterior distribution (in the order of  $10^5$ ), the Bayesian approach generates a realization on every forward model run to characterize the probability distribution for the model parameters [[Hooper and Wright, 2009](#)]. In order to find the best fit for the model parameters, Genetic Algorithm (GA) is another method which is based on selection, pairing, mating, and mutation of operators to modify the population and explore the solution space [[Holland, 1973](#)]. The degree of success for this method depends on the freedom of search operator in exploring the vicinity of the optimum solution [[Shirzaei and Walter, 2009](#)].

In comparison to other optimization techniques, SA and GA have been shown to be excellent methods for finding global solutions and optimizations in geophysical fields [[Sambridge and Mosegaard, 2002](#)]. However, according to the evaluation conducted by Shirzaei and Walter [[2009](#)] for balance of robustness and efficiency in sophisticated inversion techniques, GA in general and SA in particular may get trapped or converged in local minima because of limited random search space and minor chance of finding global minimum. Therefore, they suggested a new iterative approach called statistical competency test (SC) to avoid local traps and to estimate the reliability of the solution, thus improving the quality of the result. Conversely to other sampling approaches, the SC algorithm improves the effectiveness and speed of computation without down-sampling the observation field, which results in losing some important data [[Jonsson et al., 2002](#)].

### 2.2.1 Analytical Inverse Modelling

In order to understand the surface deformation due to reservoir depletion, one of the simplest but most efficient approaches are analytical inversion methods. As shown in [Table 2-1](#), there are three types of analytical source models to estimate the position and the geometry of sources responsible for the deformation observed on the surface. These models are categorized as spherical, ellipsoidal and disk-shaped source models based on the initial assumption source's shape [[Fokker et al., 2012](#)].

The primary analytical source models were employed in investigating magmatic sources of Japanese volcanoes to demonstrate the relationship between surface deformation measured by in situ geodetic tools and an inflating point source in an elastic half-space [[Mogi, 1958](#)]. The Mogi model is a

representation of a volcanic source in spherical shape to explain its expansion and compression with regards to vertical and horizontal displacement. Using this model to find the best fit for deformation leaves a donut shape residual by overestimation of the subsidence in the centre and underestimation of the subsidence on the flanks of a volcano [Biggs *et al.*, 2009]. To close the gaps of the Mogi model in determining the shape and dynamic parameters of a deformation source, a non-spherical source model in the homogenous half-space was proposed [Davis, 1986]. This research paved the way for other analytical expressions such as a finite sphere in half-space [McTigue and Segall, 1988] and a pressurized dipping ellipsoidal source [Yang *et al.*, 1988]. Later a horizontal penny-shaped source model in a homogenous elastic half-space was introduced [Fialko *et al.*, 2001] as an analytical expression suitable for intrusion sources with a radius as much as five times greater than its depth. This type of source may give rise to a more localized pattern of surface deformation compared to the Mogi source model at the same depth [Battaglia *et al.*, 2013].

For earthquake source simulations with rectangular dislocation elements, such as faults that cause surface deformation in an elastic half-space, Okada [1985] introduced an analytical source model. In this model, the source is treated as a finite rectangular fault with either opening or strike and dip-slip motions. Based on the concept of the Okada model, Wang *et al.* [2006] proposed two sets of modifications to simulate the volcanic source and to represent ground surface deformation and gravity changes resulting from an expansion source in a layered viscoelastic half-space [Zhu *et al.*, 2008].

Despite their simplicity, the analytical models are valid to explain the deformation signals over volcanic and tectonic regions and to define the shape and properties of the underlying source [Dzurisin, 2007]. While the depth of deformation source is well presented by using the Mogi Model, the ellipsoidal and penny-shaped source models overestimate the source depth up to 200m to 350m, respectively. The penny-shaped model also estimates greater source pressure changes with smaller relative uncertainty compared to the ellipsoidal source model [Liu, 2012]. However, the optimized ellipsoidal model shows a better overall fit to interferometric observations than the spherical Mogi source with smaller error variance when there is no added noise for both models [Fialko and Simons, 2000].

### 2.2.2 Numerical Inverse Modelling

Compared to analytical methods, the numerical source models can handle complex material rheology, reservoir geometry, and medium heterogeneity with overlying layers to solve an inverse problem for reservoir compaction and subsequent surface deformation [Abdulraheem *et al.*, 1993; Chin *et al.*, 1993; Plischke, 1994]. Most of the common numerical source models are based on the Finite Element Modelling (FEM) approach. A FEM-based model is suitable to describe the geomechanical behaviour of a depleting reservoir and its surrounding materials, but developing stable mesh attributes by adequately characterizing the complex media is its major drawback. In some cases

the uncertainties in rock and fluid properties measurement and the computation cost might limit the quality of the results or make the repetitive calculations in inverse modelling impractical [Du and Olson, 2001].

An FEM-based model can be compared with the analytical Okada's model for a rectangular dislocation source in a homogeneous and isotropic half-space for which the misfit index will demonstrate the discrepancies between the two models. The accuracy of the solution depends on the number of observation points and number of parameters to be extracted. In other words, for a reliable and precise source inversion with adequate sensitivity, good coverage including both near- and far-field InSAR data is necessary [Currenti et al., 2010].

Most of the commercial FEM-based models such as ADINA<sup>TM</sup>, ABAQUS<sup>TM</sup>, and ANSYS<sup>TM</sup> are common for surface deformation and reservoir compaction analysis [Bruno and Bovberg, 1992; Hamilton et al., 1992]. ABAQUS<sup>TM</sup>, with its flow simulator ECLIPSE [Schlumberger, 2005] can be used for studying the geomechanical behaviour of reservoirs and for realistically simulating complex structures at both field and well scale. By transferring pore pressure depletion data from ECLIPSE into ABAQUS, the underlying surface subsidence mechanism can be simulated, in order to forecast and prevent well failures and adverse environmental impacts [Capasso and Mantica, 2006].

Another numerical model that can be used for the computation of the crust response to resource extraction in a multi-layer half-space consists of two interrelated programs: PSGRN and PSCMP [Wang et al., 2006]. This model is a viscoelastic-gravitational version of the EDGRN/EDCMP numerical codes [Bell, 2008]. PSGRN prepares the time-dependent Green's functions to describe four fundamental dislocation sources at different depths as a database for the PSCMP program. Using this database, PSCMP computes the transient deformation changes in the geoid and gravity field induced by finite fault planes. The computation in this model is more complex than those models which are only a function of the layers and the observation locations, but the estimation time is relatively short, which makes it suitable for inversion problems [Vasco, 2008]. In this model, the fractional volume change associated with each cell is unknown while roughness and model norm penalty terms are included in the inversion. There is also a term to penalize volume change as a function of distance from the injection well [Vasco et al., 2001]. Due to the fact that the inverse problem is linear, this model can measure overburden deformation that can also be used for extracting flow properties such as permeability in different layers of the reservoir [Vasco et al., 2008].

As there is no unique solution for inverse problems, properly understanding the problem and determining a physically adequate deformation model by using available geological and geophysical information is essential. Time series of deformation signals in the proposed area show viscoelastic patterns in a region with flat Earth and stratified subsurface formations without particular geometrical shape for the source. Accordingly, for the case study in this research, a multi-layer viscoelastic source model [Vasco et al., 2008] will be applied as a numerical geophysical inversion method. This inversion technique is an approach that integrates both mathematical and physical principles for a

particular problem in a coal-rich area. The constraints used come from the physics of the problem in a multi-layer stratified medium with more than 350m thickness of overburden sediments. These constraints will play the most important role in inversion process and dictate a particular inversion technique. They can be either hidden behind the inversion method such as slip distribution for shallow features or can add more convenience to the modelling procedure such as smoothing [Du *et al.*, 1992].

### 2.3 Monitoring surface deformation

Ground surface deformation refers to any change in shape, dimension and position of a deformable body, and might include natural or man-made features. Moreover, these ground movements could be the result of natural processes or anthropogenic activities and measuring them is crucial for safety assessments and future disaster prevention. Either shallow impacts such as swelling and shrinkage of clay soils or landslides, or deeper features such as earthquakes, fluid abstraction, and mining operations and can be the cause of ground surface deformation [Duncan *et al.*, 2010].

In situ geodetic measurements such as levelling, or remote surveys (e.g. digital photogrammetry and remote sensing techniques) are two types of monitoring techniques that can be used for intense mining sites. In underground mining sites, the establishment of a ground control network and the measurement of deformation in different epochs that cover the desired time span are required for monitoring the ground behaviour and for determining the vertical displacement using in situ techniques. Combining both geodetic and geotechnical observations could also be used to obtain a detailed pattern of the ground displacement [Telioni, 2006].

#### 2.3.1 In situ Monitoring

Soil under expansion or compression can cause significant economic damage. Using traditional laboratory testing is difficult to accurately measure the in situ behaviour of a clay deposit, because it will depend on both environmental factors such as hydrological cycle, and the soil properties (i.e. clay mineralogy) [Lu and Likos, 2004]. In addition, these pointwise historical measurements show limited spatial coverage [Garner and Coffman, 2014]. Multiple types of static deformation monitoring for the surface such as tilt meter, optical levelling and differential GPS (or GNSS), ground-based radar interferometry and LIDAR, or combinations of these four can be used to define the dislocation vectors.

Since the early 1990s, tilt meters have been used along with micro-seismic surveys to monitor hydraulic fracturing operations at more than 3km depth in the Cyclic Steam Stimulation (CSS) projects of North America [Williams *et al.*, 1998]. Tilt meters provide continuous and precise local mapping of deformation gradients with two vertical derivatives, but long-term drift and its installation (i.e. at least 3-4m below the surface) significantly impact on its set-up and operational costs. GPS

stations can measure ground motion in three dimensions with relatively low accuracy in the vertical direction. Comparable to tilt meters, a large network of GPS receiver stations can cover the entire monitoring area providing point measurements, but this would be an extremely expensive solution for obtaining accurate displacement observations. Contrary to GPS, optical levelling provides high vertical accuracy for surface deformation of a set of distributed benchmarks. In levelling, the measurement accuracy relies on the height differences between each observation point and the reference point that can be affected by temperature variation over long time periods [Ferretti, 2014].

Deformation and volume change mapping of compacted clay can also be performed using a portable radar interferometer or a LIDAR. Both of these technologies are capable of detecting small ground motions. However, the effectiveness of these instruments is limited by several system drawbacks. Data collection, data processing, and data reduction are potential error sources in this type of imaging [Garner and Coffman, 2014].

### 2.3.2 Remote Sensing Monitoring and Photogrammetry

Frequent and large-scale observations of surface deformation with centimetre-scale vertical accuracy have been achieved using air-borne or space-borne interferometric SAR to retrieve valuable information about the ground surface behaviour and its long-term analysis [Amelung et al., 1999; Baer et al., 2002; Carnec and Delacourt, 2000; Cigna et al., 2012; Galloway et al., 1998; Liu, 2012; Wright and Stow, 1999]. Having access to adequate SAR dataset acquisitions, processing, and analysis for surface deformation consists of two complementary stages which will also reduce the time and cost of analysis: stage one is low-cost screening over large areas with high spatial extent but low spatial resolution SAR images such as C-band to detect unknown deformation spots. Following this primary observation, the next stage is a more localized interferometric analysis by using a higher resolution SAR dataset such as X-band [Crosetto et al., 2005]. Moving from low spatial resolution C-band towards high spatial resolution X-band, L-band SAR satellite offers a medium resolution with greater penetration in vegetation. Accordingly, using a two-stage screening strategy is common for interferometric monitoring of areas for different application purposes or challenging surface conditions, such as densely vegetated areas or non-urban and mountainous regions. Implementing advanced processing algorithms provides more reliable results because of their reduced sensitivity to foliage [Colesanti et al., 2005; Perski et al., 2009]. Recent investigations by NASA's airborne interferometric SAR (UAVSAR) team also raised the possibility that InSAR could provide a way to predict the location of sinkholes by detecting horizontal surface deformation as an early-warning signature [Buis and Harrington, 2014].

## 2.4 SAR for Surface Deformation

Space-borne imaging Synthetic Aperture Radar (SAR) systems are active sensors operating at microwave wavelengths, which can monitor the surface under any weather conditions with no need for solar illumination. They can measure amplitude and phase simultaneously, from which phase values are related to the sensor-target distance. SAR images over topographically rough terrains are distorted by atmospheric artefacts or geometric effects; the latter can be improved by looking at the same location from different acquisition geometries. The following section presents the fundamental concepts of SAR as an imaging tool, and interferometric SAR as a technology to extract ground surface deformation rate from SAR images.

### 2.4.1 Principles of SAR and Interferometric SAR

SAR is a specific form of imaging radar that measures the return of an actively emitted microwave signal from a target. Due to the nature of microwave energy as an illuminating source in radar sensors, this imaging technology does not rely on solar irradiation, making it more versatile than traditional passive optical and spectral sensor technologies. The radar signals are unaffected by darkness or by clouds in terms of visibility of the land surface, and are therefore capable of obtaining information largely irrespective of the surface and atmospheric conditions.

Imaging radar sensors emit signals over a specific portion of the electromagnetic spectrum that is generally based on their mission purposes. They operate in different microwave frequencies and wavelengths including X-band (9.6GHz, ~ 3cm), C-band (5.3GHz, ~5.6cm), L-band (1.3GHz, 23.6cm), and P-band (0.4GHz, 74cm) (Table 2-3) with typically higher spatial resolution in X-band and greater penetration power in P-band [Ferretti *et al.*, 2011a]. Accordingly, X-band operating systems are suitable for surveillance purposes while P-band is the preferred choice for biomass mapping and hydrological monitoring due to its potential to recover the forest height and its resistance to temporal decorrelation [Le Toan *et al.*, 2011; Neeff *et al.*, 2005].

SAR can generate an electromagnetic field with a fixed phase relationship between the electric field values at different locations and at different times. It also has the potential to record amplitude and phase information simultaneously for a ground target [Ferretti, 2014]. The on-board integration of backscattered signals is represented by a matrix of complex numbers containing both the amplitude and phase information of ground scattering elements illuminated by the radar pulse. While the amplitude data depends on the amount of returned energy from each resolution cell or image pixel, the phase information depends on the distance between the phase centres of the radar antenna to the terrestrial target (Figure 2-1).

**Table 2-3: Air-borne and Space-borne SAR sensors characteristics for monitoring purposes**

| Type                         | Platform              | Organization | Operation Time | Altitude (km) | Revisit Time (day) | Incidence Angle (degree) | Normal Looking Direction | Image size (km <sup>2</sup> ) | Swath Width (km) | Normal Spatial Resolution (m)  | Beam Mode | Polarization |
|------------------------------|-----------------------|--------------|----------------|---------------|--------------------|--------------------------|--------------------------|-------------------------------|------------------|--------------------------------|-----------|--------------|
| X band<br>(3.0 cm ~ 9.6GHz)  | TerraSAR-X            | DLR          | 2006-Present   | 515           | 11                 | 20-55                    | Right                    | 30 × 50                       | 10 to 100        | 1 to 6                         | Multi     | SP+DP        |
|                              | CSK SAR Constellation | ASI          | 2007-Present   | 619           | 12hrs              | 20-60                    | Left/Right               | 40 × 40                       | 10 to 200        | <1 to 100                      |           |              |
| C band<br>(5.6cm ~ 5.3GHz)   | ERS1-ERS2             | ESA          | 1991- 1995     | 782           | 35                 | 23.8                     | Right                    | 80×80                         | 5 to 500         | 30                             | Single    | SP           |
|                              | RADARSAT-1            | CSA          | 1995-2007      | 800           | 24                 | 20-59                    | Right                    | 50 ×50<br>100 ×100            | 50 to 500        | 8 to 100                       | Multi     | SP           |
|                              | RADARSAT-2            | CSA          | 2007-Present   | 798           | 24                 | 18-50                    | Left/Right               | 8 ×18 to<br>300 ×300          | 20 to 50         | 3 to 100                       | Multi     | SP+DP+FP     |
|                              | ENVISAT-ASAR          | ESA          | 2002-2011      | 790           | 35                 | 15-45                    | Right                    | 100 ×100                      | 58 to 110        | 30 to 150                      | Multi     | SP           |
|                              | Sentinel-1            | ESA          | 2014-Present   | 693           | 6 - 12             | 20-45                    | Right                    | > 80 × 80<br>> 250 × 250      | 20 to 400        | 5 to 40                        | Multi     | SP+DP        |
| L band<br>(23.6 cm ~ 1.3GHz) | JERS-1                | JAXA         | 1992-1998      | 570           | 44                 | 32-38                    | Right                    | 80 × 75                       | 75               | 18                             | Single    | SP           |
|                              | ALOS-PALSAR           | JAXA         | 2006-2011      | 692           | 46                 | 8-60                     | Right                    | 70 ×70                        | 20 to 350        | 7 to 100                       | Multi     | SP+DP+FP     |
|                              | ALOS-2                | JAXA         | 2014-Present   | 628           | 14                 | 8-70                     | Left/Right               | 48 ×48                        | 25 to 450        | 1 to 100                       | Multi     | SP+DP+FP     |
| P-band<br>(74.0 cm ~ 0.4GHz) | UAVSAR AIRMOSS        | NASA         | 2012-Present   | 12.5          | 2-3 times per year | 25-45                    | N/A                      | 25 to 100                     | 7                | Range: 7m<br>Azimuth :<br>0.8m | Single    | SP+DP+FP     |

\*Estimated accuracy for interferograms resulted from each satellite images is about quarter of wavelength or 0.5 Fringe.

SP (Single Polarization): HH or VV or HV

DP (Double Polarization): HH+VV or VV+VH

FP (Full Polarization): HH+HV+VH+VV

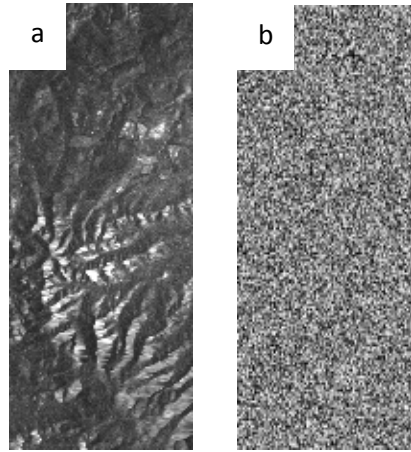


**Figure 2-1: (a) amplitude and (b) phase components of ENVISAT ASAR image. Phase shows the change in sensor-target distance while amplitude represents backscattered values for each resolution cell or image pixel.**

For a SAR sensor, the resolution ( $\Delta R_{min}$ ) in range direction ( $r$ ) depends on the pulse duration ( $T_p$ ). The shorter the pulse, the better the resolution in terms of being able to distinguish between two nearby objects when their distance in range direction ( $\Delta r$ ) satisfies the relationship:

$$\Delta R_{min} = \Delta r \geq \frac{c}{2} T_p, \quad (2.3)$$

Based on this relationship, the two-way travel path of the microwave signal and the propagation speed of the pulse are equal to the speed of light ( $c \sim 300,000$  km/sec). Radar systems use a linear frequency modulated pulse called chirp to compress the rectangular pulse in range direction and to generate short pulses with good Signal-To-Noise ratio (SNR). By sending a chirp and applying matched filtering for returning signals, the Equation 2.3 can be reshaped as follows:

$$\Delta R_{min} = \Delta r \geq \frac{c}{2BW}, \quad (2.4)$$

where  $BW$  is the bandwidth of the radar corresponding to the range of frequencies spanned by the chirp. Therefore, it can be assumed that the radar emits very short sinc-shaped (i.e.  $\frac{\sin(x)}{x}$ ) pulses and SAR image resolution in the range direction depends on the signal bandwidth ( $BW$ ) rather than on the sampling rate ( $f_s$ ) for the antenna which is not immutable [Ferretti, 2014].

Moreover, SAR data can be recorded in different polarizations (i.e. temporal variation or oscillation) of the electric field associated with each radar pulse in a specific plane. The polarization can be in linear-single or dual-pol modes, or more sophisticated full-polarimetric modes. While single polarization SAR transmits and receives polarized radiation vertically (VV) or horizontally (HH), the dual polarization is designed to generate two linear polarization combinations (HH, HV) or (VH, VV). Recently available full-polarization systems have been designed to transmit two orthogonal polarizations and record both received polarizations (HH, HV, VH, and VV) [Cloude, 2009; Van Zyl and Kim, 2010]. In comparison with classical single or dual polarization, SAR systems that are

equipped with full-polarization can provide a complete scattering matrix to extract substantial information from the image and to separate surface scattering from dihedral scattering in more vegetated areas [Shirvany, 2012].

The coordinates of each pixel in a SAR image according to range and azimuth directions are related to the acquisition geometry. While range direction is orthogonal to the moving platform path, azimuth direction refers to the path. The inclination of the radar antenna with respect to the nadir is called off-nadir or look-angle ( $\theta$ ) which is never zero but ranges from about 20 to 50 degrees. The ability of SAR systems to change the off-nadir angle is important for their adjustment to mountainous terrain, which is a potential barrier to InSAR. The direction along the sensor Line of Sight (LOS) is usually called slant-range direction and SAR acquisitions are collected in this direction [Ferretti, 2014]. Over rough topography, SAR images can be geometrically distorted due to three types of effects: foreshortening, layover and shadow effects. Slopes facing the sensor are affected by foreshortening and layover. In foreshortening, a radar beam reaches the base of a tall feature before it reaches the top, while for the layover case a radar beam touches the top of feature before its base. When a radar beam is not able to illuminate the ground surface, the image is distorted by the so-called shadow effect and spatial sampling is shrunk to a few meters [Lillesand et al., 2008]. This normally occurs behind vertical features or steep slopes.

In SAR imagery brighter pixels represent stronger backscatter with high amplitude values, whereas the phase value for each pixel is related to the sensor-target distance and the signal-target interaction. Accordingly, subtle ground motions in the radar LOS direction would result in a slight increase or decrease in sensor-target distance and offsets in phase that can be detected and measured by interferometric techniques [Engelbrecht and Inggis, 2013]. Conversely, variations in imaging conditions such as acquisition geometry, surface roughness and orientation, dielectric constant (in particular moisture content), wavelength and polarization can affect the visibility of the ground scatterer by changing its Radar Cross Section (RCS) values and backscatter coefficient. The radar backscatter coefficient  $\sigma^0$  can vary between -40dB and +5dB or even more, from *near-range* to *far-range* pixels as a function of the local incidence angle [Ferretti, 2014].

The near-polar orbit of SAR satellites - in combination with the Earth's east-west rotation - theoretically allows observing the same area from two different looking angles on satellite orbits i.e. ascending (S-N) and descending (N-S), or left and right-looking geometries with different incidence angles. This observation is conducted based on the orbiting schedule of each individual satellite, which varies from 46 days down to 11 days (Table 2-3). Combining these observations not only mitigates the problems due to the acquisition geometry and the uneven sampling on hilly terrain areas, but can also distinguish between vertical and east-west motions [Ferretti et al., 2007]. In other words, the use of data acquired by satellites in both ascending and descending orbits makes it possible to compute the true vertical movement and the east-west component of horizontal movement.

Since phase varies in SAR image acquisitions over the same area at different times, this can be used to retrieve ground motion over large remote regions with little or no regular access for ground-based observations [Bürgmann *et al.*, 2000]. For this purpose, InSAR, as one of the major applications of SAR imagery, is based on the superposition of two images to generate a new image which shows topography and changes in ground levels with precision to the millimetre, as well as random orbital error, and weather and background noise interferences [Duro *et al.*, 2013; Massonnet and Feigl, 1998].

The basic idea behind SAR interferometry for phase measurements lies in the following equation which can model the phase value ( $\phi$ ) of a pixel  $P$  in a SAR image as a mixture of four different components  $\varphi, r, a, v$ :

$$\phi(P) = \varphi + \frac{4\pi}{\lambda}r + a + v + 2\pi, \quad (2.5)$$

where  $\varphi$  is the phase of the coherent sum of the contributions of all scattering objects in a resolution cell associated with pixel  $P$ ,  $r$  is the sensor-target distance,  $\frac{4\pi}{\lambda}r$  represents the centre of a resolution cell, while  $a$  is an additive phase contribution representing the random effects of both ionospheric and tropospheric disturbances (i.e. clouds, water vapour, rain, fog) on the speed of the microwave signal propagation that have a negative impact on the quality of retrieval results from conventional InSAR [Hanssen, 2001]. The last component ( $v$ ) represents any extra noise sources such as thermal noise due to the SNR level, radar system internal noise, or noise related to the power of the received signal. Moreover,  $v$  contains the phase component due to the distribution and backscattering characteristics of the scatterers contributing the pixel's signal. By computing the difference in phase values of pixel  $P$  in two co-registered (re-sampled) SAR images, an interferogram can be generated providing:

$$\Delta\phi(P) = \Delta\varphi + \frac{4\pi}{\lambda}\Delta r + \Delta a + \Delta v, \quad (2.6)$$

More precisely, an interferogram is a result of multiplying the complex values of the first SAR image (Master image) by the complex conjugate of the second SAR image (Slave image) [Ferretti *et al.*, 2007] according to:

$$I = Z_M Z_S^* = A_M A_S e^{j(\phi_M - \phi_S)}, \quad (2.7)$$

Rather than measuring absolute range values, accurate differential measurements can be calculated if pixels with very high SNR ratio are selected in both acquisitions. Equation 2.6 is then converted to Equation 2.8 for ground surface deformation calculations; although, at this stage  $\Delta r$  is not only the deformation component but also includes topography:

$$\Delta\phi(P) = \frac{4\pi}{\lambda}\Delta r, \quad (2.8)$$

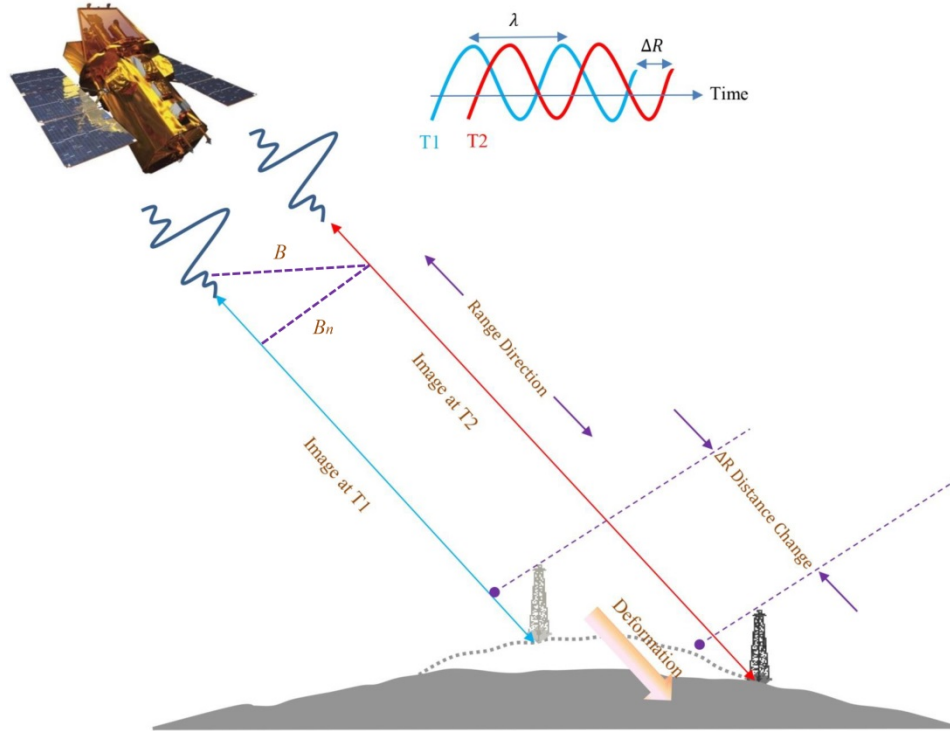


**Figure 2-2: Schematic of along-track SAR interferometry observation with geometric parameters. The flight paths, which are pointing into the page, are not shown. T1 represents the first ground observation and T2 shows the second, with the time interval  $\Delta T$  between two observations giving the  $\Delta R$  displacement in range direction ( $r$ ).**

To initialize the interferometric processing, an interferometric pair needs to be selected based on two main criteria: a) coherence ( $\rho$ ), and (b) altitude of ambiguity ( $h_a$ ). Coherence or degree of decorrelation is a local information computed across small windows among two SAR images that can vary between 0 and 1. According to:

$$\rho = \frac{|\sum_{i=1}^N \sum_{j=1}^M Z_1 Z_2^*|}{\sqrt{\sum_{i=1}^N \sum_{j=1}^M Z_1 Z_1^*} \sqrt{\sum_{i=1}^N \sum_{j=1}^M Z_2 Z_2^*}} \quad (2.9)$$

in which  $Z_1$  and  $Z_2$  represent the master and slave images (i.e. the satellite orbit positions),  $N$  and  $M$  are the number of pixels in the range ( $i$ ) and the azimuth ( $j$ ) directions, respectively. High coherence values (above 0.5) indicate low interferometric phase noise, while low values are associated with a low phase quality.

A coherent interferogram with coherence values close to 1 will appear as an image with smooth fringe-pattern, while areas with low coherence show noisy fringe patterns with the values close to zero [Hanssen, 2005]. Coherence in interferometric pairs depends on the surface conditions. Urban areas and exposed rocks remain coherent over time, as they are relatively stable targets, while vegetated areas or places with strong variations in surface conditions impose a rapid loss of

coherence. Such decorrelation is mainly caused by volume scattering due to vegetation growth or soil humidity variation [Jung *et al.*, 2007; Liu, 2012 ; Perski and Jura, 2003; Raucoules *et al.*, 2003; Teatini *et al.*, 2012]. Moreover, coherence ( $\rho$ ) can be easily lost when the time interval between acquisitions increases (*temporal decorrelation*) or there are substantial traces of atmospheric perturbations, thermal noise, and non-overlapping Doppler spectral energy [Massonnet and Feigl, 1998; Rosen *et al.*, 2000; Zebker and Villasenor, 1992].

The second criterion in InSAR pair selection and using the Digital Elevation Model (DEM) is the altitude of ambiguity, which by definition is an artificial fringe that may be caused by the orbital separation between two acquisitions, and is inversely proportional to the normal baseline ( $B_n$ ):

$$h_a = \frac{\lambda r \sin \theta}{2B_n}, \quad (2.10)$$

In case that the phase noise is equivalent to a smaller altitude noise, the larger normal baseline indicates the more accurate altitude measurement; however, there is an upper limit to the normal baseline for each individual SAR sensor, over which the interferometric signals are decorrelated and no fringes can be generated. The topographic component is dependent on  $h_a$  and for the same phase change rate, the topographic change is  $\frac{r \sin \theta}{B_n}$  times the change in range. Conversely, since  $\frac{r \sin \theta}{B_n} \gg 1$  the interferometric phase is much more sensitive to range change than to topographic variation, and thus the accuracy of InSAR is higher in displacement mapping [Zebker *et al.*, 1994].

Although InSAR technology has been proven to be an outstanding technology to detect and measure ground surface motion with sub-centimetre accuracy, sometimes its competency can be constrained by reduced phase coherence, limited number of SAR imagery for a specific area and strong atmospheric phase distortion. Reduced phase coherence and phase discontinuities can be removed by phase unwrapping techniques [Yague-Martinez *et al.*, 2012] on the assumption that the phase difference between any two adjacent pixels in the interferogram should be less than one half cycle (i.e.  $\pi$  rad) [Chen and Zebker, 2002]. Linear combination of interferograms from dual-frequency sensors (L- and C-band satellite images) [Zhang *et al.*, 2010] or signal decomposition using a combination of various interferometric techniques [Perski *et al.*, 2009] can minimize the phase ambiguity. Atmospheric artefacts usually manifest themselves in SAR imagery as ionospheric path delay or tropospheric path delay, and due to the fact that they often correlate with surface topography, their patterns resemble surface inflation signals. Ionospheric path delay is a consequence of variations in the total electron content along the transmission path on the global scale. However, tropospheric path delay is more common in interferometric misinterpretation. This artefact is caused by local changes in the atmospheric water vapour content, as well as pressure and temperature, all degrading the quality of the phase pattern in the final interferogram [Gens and Van Genderen, 1996]. Accordingly, a 20 percent change in atmospheric relative humidity leads to 10 cm deformation error

[Zebker et al., 1997]. For atmospheric phase delay correction, different procedures can be used (as indicated in Table 2-4) to reduce the artefacts to 50-60 % from their original value. Gradual developments in SAR remote sensing platforms and the need to produce more accurate deformation maps with less spatial or temporal decorrelation has resulted in advanced InSAR processing algorithms, generally using multiple SAR datasets that will be discussed in the following section.

#### 2.4.2 Interferometric SAR Processing Techniques

As previously mentioned, interferometric SAR emerged as an approach to accurately measure ground deformation [Gabriel et al., 1989; Massonnet and Feigl, 1998; Rosen et al., 2000]. Comparing the phase of two or more SAR images with zero-baseline condition which are typically acquired from the same flight track but at different times is the main principal in this technique. In the zero-baseline condition the phase information would only be related to the LOS displacement, while in reality a certain baseline is always present, and thus makes the interferogram sensitive to the topography. By using an external DEM, the topographic phase contribution (Equation 2.10) is subtracted from the interferogram, leading to *Differential* SAR Interferometry (DInSAR) that can be used to detect subtle elevation changes in range distance between two acquisitions [Fujiwara et al., 1998; Goldstein, 1995; Zebker et al., 1997].

For interferogram generation, two Single Look Complex (SLC) images, which are the focused version of SAR raw data, are required. The two SLC images, referred to as master (reference image) and slave should have a suitable temporal and spatial baseline according to the image selection criteria (i.e. coherence and altitude of ambiguity) that was explained in advance [Ferretti et al., 2007]. Focusing is one of the initial signal processing stages; it builds a new image by aggregating the phase response histories and replacing it with the pixel value at each target location [McCandless and Jackson, 2004]. The sampling product of SAR interferometry from physical quantity of the surface is an absolute phase that is wrapped into the  $(-\pi, \pi)$  interval. In order to quantify the physical properties, the hidden and continuous phase information should be extracted from the wrapped phase. Two-dimensional phase unwrapping is the process for extracting unwrapped information from ambiguous wrapped phase [Gens, 2003].

Conventional DInSAR processing with discrete interferograms is highly prone to decorrelation effects and atmospheric artefacts that limit the number of useful differential pairs and impose a phase unwrapping deficiency in rough areas or for complex field movements [Zebker and Villasenor, 1992]. Over the past two decades, different scenarios have been suggested to overcome these processing problems, including multi-image InSAR processing techniques that have been categorized in two main groups [Sansosti et al., 2010]: (i) techniques that work on localized targets, referred to as Persistent Scatterers Interferometry (PSI) methods [Ferretti et al., 2011a; Ferretti et al., 2001; Kampes and Hanssen, 2004] and (ii) techniques that utilize distributed targets referred to as SBAS

Table 2-4: Different procedures to remove or mitigate phase contaminations in interferometric results.

| Type of phase contamination | Methods                                                                                                                                                                                                                                                                                                 | Previous studies                                                                  |
|-----------------------------|---------------------------------------------------------------------------------------------------------------------------------------------------------------------------------------------------------------------------------------------------------------------------------------------------------|-----------------------------------------------------------------------------------|
| Atmospheric                 | <ul style="list-style-type: none"> <li>• High resolution Numerical Weather Prediction (NWP) model</li> <li>• Variance-covariance model</li> <li>• Adaptive atmospheric phase filter</li> <li>• Using Joint atmospheric data such as MERIS, MODIS, GPS</li> <li>• Power Law Correction Method</li> </ul> | <p>Yague-Martinez et al.,2012;</p> <p>Bekaert et al., 2015</p>                    |
| Volume Scattering           | <ul style="list-style-type: none"> <li>• Adaptive Filtering</li> <li>• Short-term interferogram</li> <li>• Different polarization or multi-frequency SAR</li> </ul>                                                                                                                                     | <p>Goldstein et al., 1998;</p> <p>Shimada, 1999;</p> <p>Perski and Jura, 2003</p> |

methods [Berardino *et al.*, 2002; Casu *et al.*, 2008]. Recently, a few solutions that incorporate both the PSI and the SBAS approaches have also been proposed, known as Hybrid methods [Hooper *et al.*, 2012]. These two methods have proven to be the most useful for mapping various sources of ground deformation, including seismic and volcanic displacements, subsidence due to fluid extraction, and many other natural and anthropogenic phenomena [Samsonov and d'Oreye, 2012].

While stacking fails to be an effective DInSAR technique because the noise in interferograms is generally not normally distributed, more advanced multi-temporal interferometric techniques should be implied [Williams *et al.*, 1998; Zebker *et al.*, 1997]. In particular, the accuracy of LOS velocity measurements using various interferometric SAR techniques is strongly dependent on the number of SAR acquisitions. However, in areas like agricultural or mining fields, low accuracies may result due to the small number of man-made structures and thus a very low Permanent Scatterer (PS) density [Perski *et al.*, 2009]. The PSI method uses a stack of images to generate differential interferograms with respect to one common master. All combinations are included, even those exceeding the critical baseline, but only the coherent pixels are considered. Conversely, the SBAS technique relies on an optimized set of differential interferograms created by using SAR image pairs that are characterized by small baseline separation and reduced temporal decorrelation. Moreover, compared to PSI, the SBAS algorithm requires fewer SAR images with several master images to achieve the same accuracy [Lauknes, 2004]. When the observation area is homogenous and several interferograms are available, the use of phase unwrapping allows SBAS to identify coherent point-wise scatterers, but at the cost of spatial resolution [Berardino *et al.*, 2002; Hooper, 2008; Lanari *et al.*, 2004; Prati *et al.*, 2010; Samsonov *et al.*, 2011].

Unlike the standard SBAS, which separately solves descending and ascending data from different satellites, MSBAS does not introduce any interpolation errors. However, interpolation errors may become significant, especially in the case of temporarily sparse data sets [Samsonov and d'Oreye, 2012]. Compared to other advanced processing methods, statistical characterization and DS covariance matrix definition are the most significant improvements in SqueeSAR if the computational costs involved can be compensated [Ferretti *et al.*, 2011a].

According to the characteristics and requirements of each advanced interferometric processing method discussed, for the region at hand with a sparse number of coherent scatterers to extract, and limited number of SAR images available, a dense PS network could not be achieved. For this reason, the advanced DInSAR techniques such as PSI and its sub-categories that relies on several SAR acquisitions and high spatial density of PS ( $\sim 5$  PSs per km<sup>2</sup>) or Distributed Scatterers (DS) will not be suitable for the area of interest, being characterized with non-vegetated surfaces, rock outcrops, and limited man-made structures.

**Table 2-5: Interferometric SAR processing algorithms with their specific characteristics and outcomes**

| Category            | Method                                 | Condition                                          | How it works                                                                                                                                                     | Outcome                                                                                                                                                                                      | Comments                                                                                                  | References                                                                                                                                                |                                                                                            |
|---------------------|----------------------------------------|----------------------------------------------------|------------------------------------------------------------------------------------------------------------------------------------------------------------------|----------------------------------------------------------------------------------------------------------------------------------------------------------------------------------------------|-----------------------------------------------------------------------------------------------------------|-----------------------------------------------------------------------------------------------------------------------------------------------------------|--------------------------------------------------------------------------------------------|
| Conventional DInSAR | Stacking                               | Presence of random noise with normal distribution  | -Assigning weights based on interferogram corresponding time span<br>-Measuring weighted average of all the deformation velocities within a single interferogram | Mean deformation rate for each pixel                                                                                                                                                         | Averaged interferogram with less noise but reduced amplitude                                              | Zebker et al., 1997; Sandwell and Price, 1998; Sansosti et al., 2010                                                                                      |                                                                                            |
| Advanced DInSAR     | Methods based on Permanent Scatterers  | PSI                                                | -Presence of at least 15- 20 SAR images<br>-Single master base processing algorithm                                                                              | -Searching for pixels with stable amplitude and coherent phase throughout every image in dataset<br>-Identification and exploitation of Permanent Scatterers (SAR reflectors) within a pixel | Rate of elevation change with up to 1mm/yr accuracy                                                       | -Using all available SAR images regardless of their geometrical baseline<br>-Suitable for urban areas with some difficulty in natural environment regions | Ferretti et al., 2001; Hooper et al., 2007; Jung et al., 2007; Hooper et al., 2012;        |
|                     |                                        | Coherent Pixels Technique (CPT)                    | -PSI based conditions<br>-Deformation phase consists of linear and non-linear components                                                                         | - Identification of sufficient pixels based on their amplitude<br>-Does not require unwrapping                                                                                               | -Extracting low and high pass components of non-linear movements<br>-Extracting atmospheric perturbation  | -Underestimate abrupt non-linear deformation<br>-Suitable for urban areas                                                                                 | Mora et al., 2003; Blanco et al., 2005; Herrera et al., 2007; Blanco-Sanchez et al., 2008; |
|                     |                                        | Quasi Coherent Targets (Q-CTs)                     | -PSI based conditions<br>-Weighted coherent targets                                                                                                              | -Using classification information and coherence properties of ground targets                                                                                                                 | Deformation estimation in both urban and non-urban areas                                                  | -Significant improvement in coherence and target selection in non-urban areas                                                                             | Tao et al., 2012                                                                           |
|                     | Methods based on Small Baseline Subset | SBAS                                               | -No isolate image cluster<br>-Producing large number of small baseline multi-reference interferograms                                                            | -Increasing in number of ground points<br>-Reducing the spatial baseline length for each image pair                                                                                          | -Extracting linear and non-linear components of deformation field                                         | -Several master images<br>-Optimal set of interferograms<br>-Smallest spatial and temporal decorrelation                                                  | Berardino et al., 2002; Hooper, 2008; Wu et al., 2012                                      |
|                     |                                        | Multi-dimensional SBAS (MSBAS)                     | -SBAS based conditions<br>-Combining SAR data with different acquisition parameters, temporal and spatial resolution and polarization                            | -Using multi SAR image acquisitions including different satellites in ascending and descending modes                                                                                         | -Compute ground deformation rate<br>- Reconstruct 2D or 3D time series of deformation                     | -Improved temporal resolution<br>-relatively uninterrupted coverage<br>-Average noise sources during the processing                                       | Samsonov and d'Oreye, 2012                                                                 |
|                     | Hybrid Based                           | Stanford Method for Persistent Scatterers (StaMPS) | -Combining PSI and SBAS concepts<br>-Less than 25 SAR images<br>-Single master base processing algorithm<br>-Full resolution small baseline                      | -Using phase spatial correlation instead of amplitude analysis to identify PS pixels<br>-Trusts on the spatial correlation of deformation rather than its temporal dependence                | -High resolution deformation signals<br>-Extracting linear and non-linear components of deformation field | -Increase spatial sampling rate in regions with limited corner reflectors<br>-More reliable phase unwrapping                                              | Ketelaar, 2009; Hooper et al., 2007; Hooper et al., 2012                                   |
|                     |                                        | SqueeSAR™                                          | -Joint processing of Permanent Scatterers (PS) and Distributed Scatterers (DS)                                                                                   | -Using statistical behaviour patterns of both PS and DS                                                                                                                                      | -High resolution deformation signals with drastic increase in measurement points in km <sup>2</sup>       | -Improved density and quality of interferometric measurement points over non-urban areas                                                                  | Ferretti et al., 2011; Tao et al., 2012; Kuzuoko et al., 2013                              |

## 2.5 Proposed Methodology

Reviewing the available literature to identify the strengths and weaknesses of each monitoring techniques for surface deformation and inverse modelling of its probable source, a methodology can be proposed to extract high-resolution deformation maps from a historical analysis of SAR observations over a barren area located in the inland of Australia. Since accurate surface deformation measurements over a CSG reservoir in a large basin with no access to previous in situ geodetic observations is essential for current reservoir surveillance and future seismic acquisitions, interferometric SAR is suggested as a reliable and cost-efficient non in situ geodetic observation to fill the gap for constraining geophysical source models. Amongst the advanced SAR processing algorithms mentioned in this chapter, the standard SBAS algorithm is the most promising approach, not only due to its suitability for remote barren landscapes, but because of its potential to identify the optimal set of interferograms with the smallest spatial and temporal decorrelation, in case only a limited number of SAR acquisitions are available. Moreover, SBAS-based deformation maps rely less on auxiliary information such as dense networks of PS, DS or corner reflectors.

Consequently, based on the review of various source modelling approaches and their limitations, the PSGRN/PSCMP multi-layer viscoelastic model will be tested for the CSG reservoir in this research. Using the ground movement in satellite line of sight direction in the proposed CSG field, as extracted from InSAR historical analysis, and elastic parameters extracted from down-hole geophysical surveys, volumetric changes in the reservoir will be estimated. This model represents a valuable tool to demonstrate the simple multi-layer stratified subsurface medium of the study area and to calculate the relative changes in volume and stress components. Then, the resilience of this source model to variations in properties of the reservoir layers extracted from seismic observations will be evaluated. Ultimately, the outcome of the geophysical inverse modelling will be discussed in detail with the aim of extracting subsurface structural features that were not captured with seismic field measurements.

## 2.6 Chapter Summary

This chapter has provided a background on the importance of surface deformation and subsurface structural behaviour in resource management and development. This background is then followed by a review of currently available geophysical inverse modelling approaches that can be solved analytically or numerically to infer the responsible underground source of deformation. A description of surface deformation monitoring using in situ and remote sensing techniques to provide the required parameters needed to constrain the source model is also presented.

Since in situ geodetic observations such as levelling and GPS are not available or very sparse in the proposed area, InSAR historical and non in situ observations will be used to map the ground surface deformation patterns and its locations. Using SBAS algorithm, available SAR images covering the proposed region will be processed and then will be used to identify the optimal set of interferograms to extract ground surface deformation rate map. This rate map will then constrain a multi-layer viscoelastic model for a CSG reservoir to estimate volumetric changes in the reservoir level and to examine the resilience of the source model to variations in the properties of the reservoir layers.

Subsequently, Chapter 3 will present an overview of the study area and available in situ data set including geology, geophysics and geodetic observations in the Surat Basin region. This is followed by a brief overview of the available satellite image data sets that cover the proposed area in the basin during observation time.

### **3 Study Area and Available Data**

This chapter presents an overview of the study area, including a description of its surface and subsurface geology, including aspects of its stratigraphy and petrophysical properties. This field-based information along with subsurface geophysical observations is used to model the subsurface geological framework and to extract petrophysical maps for simulating elastic medium properties. In situ geodetic surveys conducted in the Surat Basin are also reviewed for validation purposes of the deformation signals extracted from satellite imagery. For the interpretation of source modelling results, various underground resources that are present in the Surat Basin along with their contributions to formation pressure change and subsequent ground surface subsidence or uplift were also reviewed.

#### **3.1 Background**

The Jurassic - Cretaceous Surat Basin is one of three sub-basins in the Great Artesian Basin (GAB). It is a vast underground water resource that underlies one fifth of the Australian landmass, extending across the states of Queensland, northern New South Wales, the Northern Territory and northern South Australia. The Surat Basin itself ([Figure 3-1](#)) covers approximately 300,000km<sup>2</sup> of southeastern Queensland and northern New South Wales, and is delineated by the Nebine and Kumbarilla Ridges. In the South, the Surat Basin is bounded by the Central West Fold Belt and the New England Fold Belt, while in the North it has been eroded and overlies the Triassic and Permian sediments of the Bowen Basin [[Exon, 1974](#)].

The Surat Basin is a wedge-shaped basin with a gradually increasing sediment thickness from the western margin to the axis of the Mimosa Syncline, thinning more sharply towards the east to the Kumbarella Ridge [[Power and Devine, 1970](#)]. During the Late Triassic to Early Cretaceous periods, up to 2,500m of sedimentary rocks, dominated by fluvio-lacustrine deposits, were deposited in the Surat Basin. The basin is composed of different geological layers, including sandstone, mudstone and siltstone, with the thicknesses ranging from less than 100m to more than 600m. Some of these layers, such as those of the sandstone, are permeable aquifers and allow water to percolate. Others on the other hand, including mudstone and siltstone, are relatively impermeable aquitards and do not allow water to pass through them easily. There are many aquitards with significant thicknesses that separate the lower formations from the most commonly used groundwater aquifer supplies. Aquifers are naturally recharged at the edges of the basin where areas of sandstone are exposed, and rainfall and stream flow over these rocks soak into the system. Due to limited interconnectivity between layers, as well as the slow rate of natural recharge (i.e. one and five meters per year), there is the potential for a

drop in pressure in some aquifers as water slowly makes its way through aquitards towards the lower formations. The structure of the Surat Basin is relatively simple, with the maximum deposition in the Mimosa Syncline overlying the Permian-Triassic rocks of the Taroom Trough in the Bowen Basin [Green et al., 1997; Hoffmann et al., 2009].

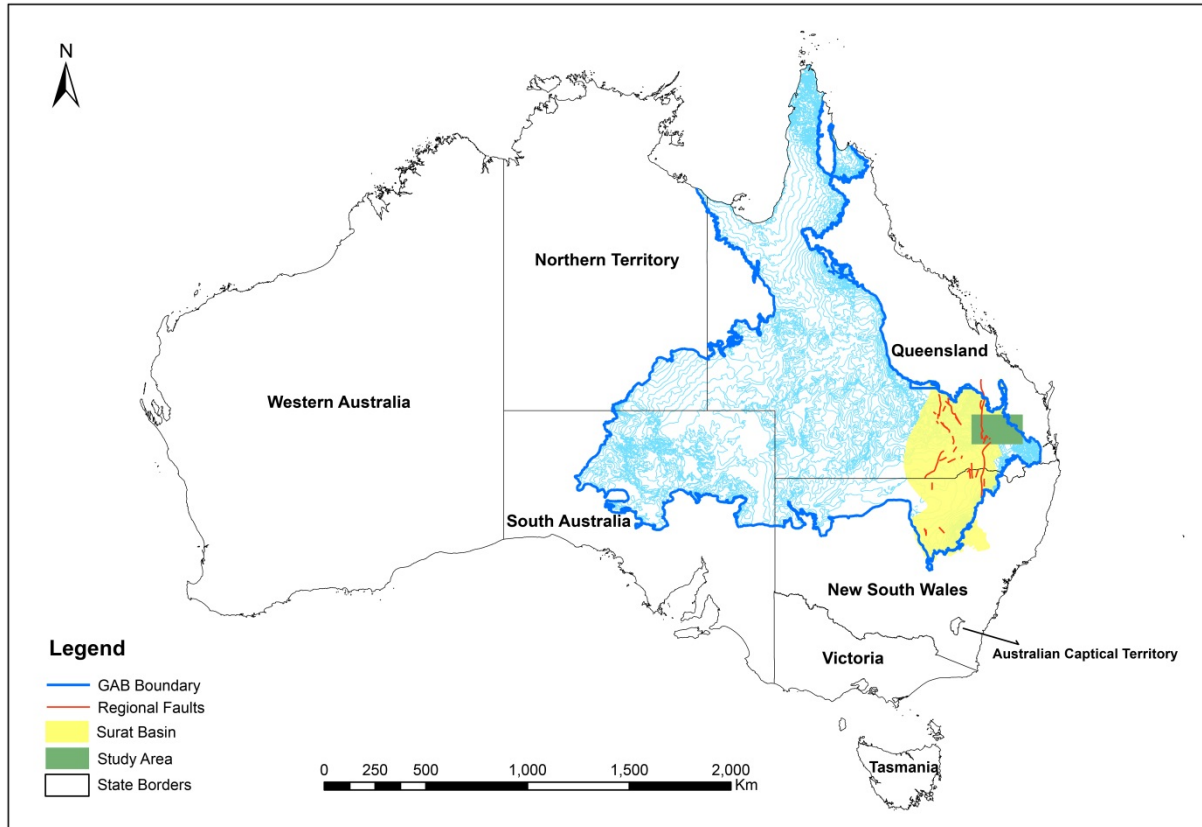


**Figure 3-1: The green square shows the location of the study area in the Surat Basin (yellow) in Queensland, Australia over the extent of Great Artesian Basin (blue).**

The Mimosa Syncline is the predominant tectonic element in the Surat Basin with a north-south trend in the central region. The fault systems in the eastern and western margins of the Surat Basin impose minor deformation caused by the Moonie-Goondiwindi, Burunga-Leichhardt and Hutton-Wallumbilla faults [Korsch et al., 2009] with low amplitude anticlines along the eastern margin of the basin. Reactivation of the fault systems have resulted in minor displacements of the overlying Jurassic-Cretaceous sequence. However, there is no reported vertical offset of the regional reservoir and seal units [QCGI, 2009]. The regional faults within the Surat Basin are generally continuations of deeper faults in the underlying Bowen Basin; those deeper faults have less impact on the formations in the Surat Basin. The displacement associated with a number of small faults in the lower formations of the GAB ranges from zero to some tens of meters, with only minor propagation into the younger or shallower units, according to the Geological Survey of Queensland [Hodgkinson et al., 2010; Hodgkinson et al., 2009]. Even though these faults appear close to some of the springs in the region [QWC, 2012], there are different viewpoints about the influence of faults on regional groundwater flows. For example, Golder Associates [2009] stated that the faults reduce hydraulic connectivity

across the structures, while Hodgkinson et al. [2010] believe that the faults penetrate the Hutton Sandstone and that they are unlikely to act as a hydraulic barrier for lateral groundwater flow at a regional scale according to the hydraulic head contours.

### 3.2 Geology of the Surat Basin

An appreciation of the Surat Basin geology is the key to understanding its past and current depositional system, along with controlling factors that demonstrate its long-term regional and local deformation regimes. This section covers in detail the Surat Basin surface and subsurface structure and its gradual evolution throughout time.

#### 3.2.1 Geomorphology

In terms of location and extent, the Surat Basin is an onshore basin that extends from less than 200km from the Pacific Coast (east of Dalby) to 500km inland near the Nebine Ridge. Most of the basin is located in Queensland while the southern boundary extends to the Coonamble Embayment near Dubbo in New South Wales. For the purpose of this research, only the part of the basin located in Queensland will be the focus of this investigation. Primarily, this site was selected for the reported gas leakage in the area between Roma and Dalby [QWC, 2012], and the high density of structural faults and rate of resource extraction in this part of the Basin compared to the part in New South Wales.

The topography in the Surat Basin is mountainous in the east but with gently sloping plains in the west, with elevation ranging from 900m M.S.L in the eastern and northern margins to less than 200m M.S.L in the southwest [Worley-Parson, 2010]. The regional drainage system is dominated by the Condamine River, which originates from the elevated eastern margin of the basin. The river flows northwest to the town of Chinchilla before changing its course towards the west and southwest where it joins the Darling River drainage system [Exon, 1976]. The Condamine River and its tributaries are major parts of the Central Condamine Alluvium in the basin, which is located approximately 200km west of Brisbane and covers an area of about 30,000km<sup>2</sup>. This surface water system comprises the floodplain alluvium (i.e. fine to coarse sand, gravel, silt and clay) with thicknesses ranging from ten meters to a maximum of 134m in the central part south of Dalby [Murphy, 2008]. As part of the Condamine catchment, the Surat Basin contains some of the most fertile soils relative to central Queensland, with basalt the main parent material for soil formation (Figure 3-3). The soil type in this area changes from highly fertile (Ferrosols) in the eastern part to red-brown earths (Chromo sols) and heavy black clays (vert sols) on the floodplains [White et al., 2010].

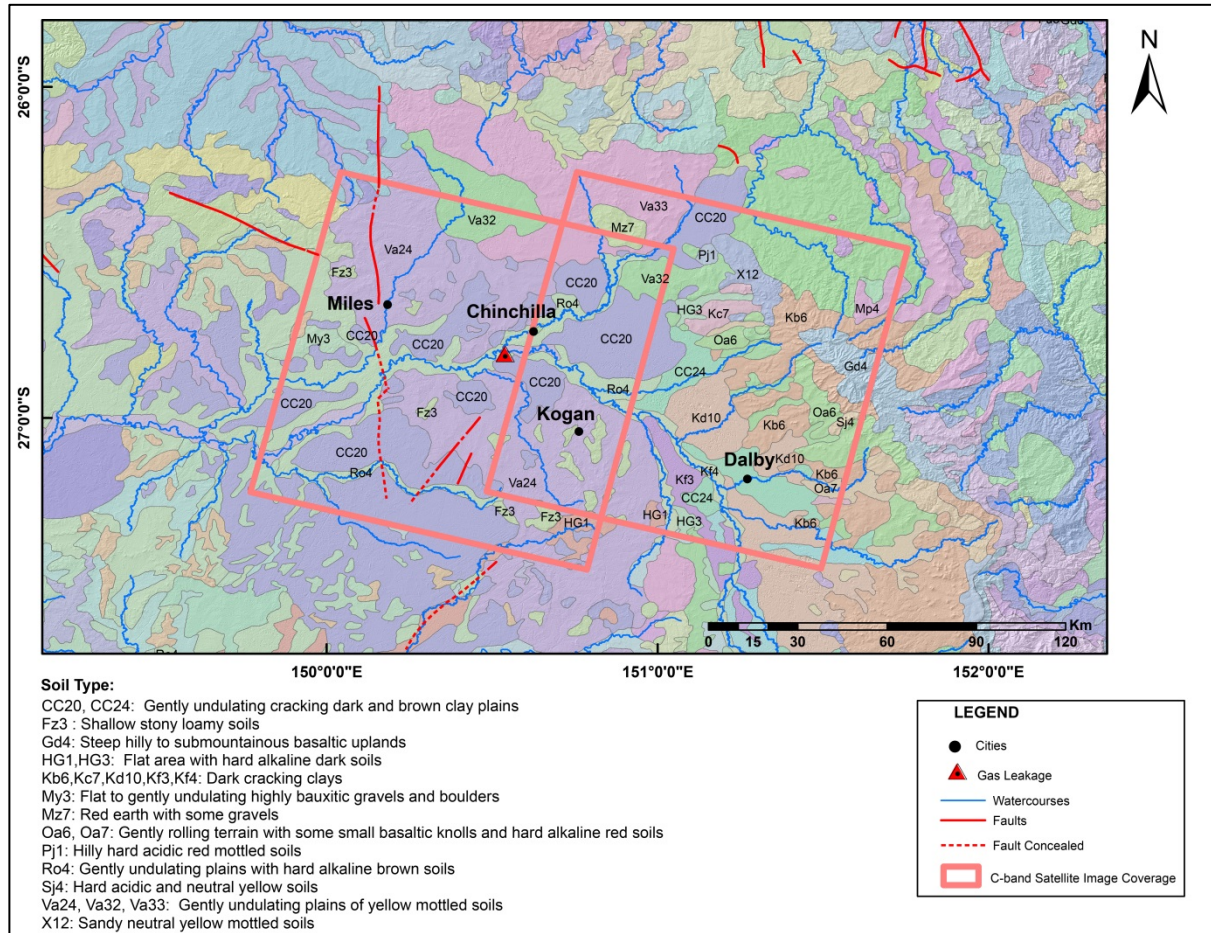


**Figure 3-2: Distribution of soil types in the Surat Basin including the location of the previously mapped faults [Digital Atlas of Australian Soil, Bureau of Rural Sciences (BRS), 2009]**

Bluegrass grasslands and popular box woodlands with brigalow or belah forests are the main natural ecosystems in the Surat Basin, and have been cleared to a vast extent for urban and agricultural developments (Figure 3-3). The annual rainfall in the basin increases with increasing distance from the coastline [Worley-Parson, 2010] with substantial variability across the basin. Peak rainfalls generally occur between October and March [APLNG, 2010]. In the Condamine catchment the annual rainfall ranges from 943mm in Toowoomba to 665mm in Chinchilla, with the seasonal pattern imposing extended periods of drought and low stream flow [Preston et al., 2007]. The rate of average annual evaporation is between 1,800mm/year and 2,400mm/year, which is more than the precipitation received throughout the Basin [APLNG, 2010].

The dominant climate in this area is sub-tropical with warm, wet summer months and cooler, drier winter months. The temperature spans from 0°C to 35°C with an annual average of approximately 20°C [Exon, 1976]. For the period of February 2006 to September 2007, the Condamine region experienced the third worst drought, with only 270mm of rain recorded in Dalby [Clewett et al., 2003]. However, CSIRO [CSIRO, 2008] suggested that the resultant impacts of climate change on temperature, rainfall, evaporation, and dry and wet periods would not be more than 10%, with trivial impact on recharging groundwater resources compared to the impact of groundwater extraction. CSIRO also indicated that

the North Branch and the Oakey Creek tributaries of the Condamine River are largely disconnected from the underlying aquifers, which seems to be the result of large scale groundwater extraction since the late 1960s. The poor recovery of the surface water system results in the depletion of its aquifer storage, while the magnitude depends on the extent and duration of the imbalance. Such imbalance in the reservoir might be projected on the surface as land deformation [White et al., 2010].

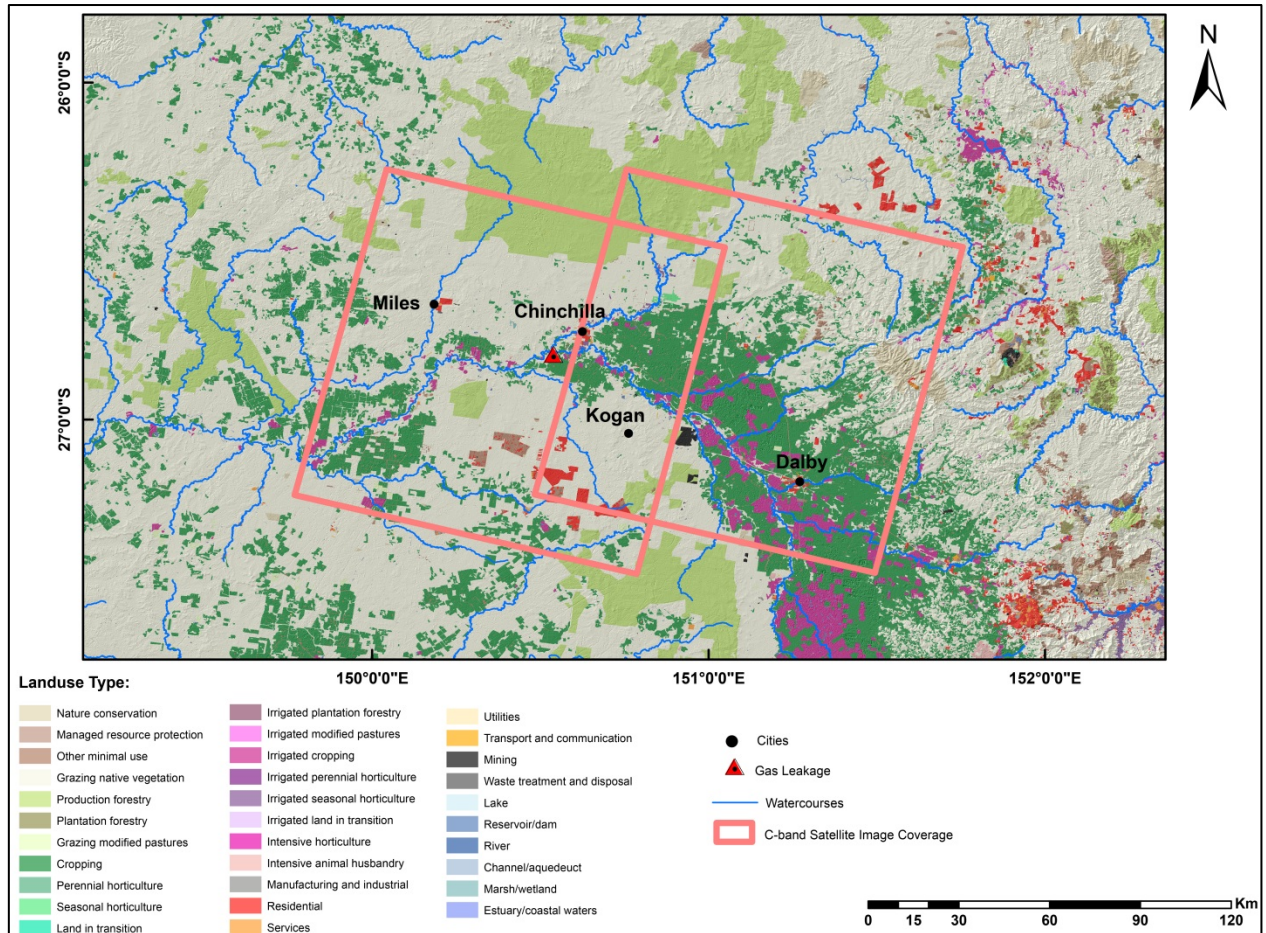


Figure 3-3: Land use map of the study area, showing the various types of land cover with different kinds of land use available in the Surat Basin.

### 3.2.2 Surface Geology

A deep blanket of clay-rich alluvium and colluvium covers a large portion of the study area [Harris et al., 1999]. While most of the stratigraphic sequences do not outcrop, older (Late Jurassic) Kumbarilla Beds, Springbok Sandstone, and Westbourne Formation are unconformably overlain by younger (Early Cretaceous) Gubberamunda Sandstone. Around Chinchilla Late Tertiary (Pliocene) fossil beds are associated with Chinchilla Sands, with extension towards the east and southeast. Figure 3-4 shows that the majority of the area monitored by C-band imagery is covered by Late Jurassic-Early Cretaceous siltstone, mudstone, sandstone and clay ( $J_{kb}$ ), Late Tertiary - Quaternary clay, silt, sand, gravel and soil ( $TQ_e$ ), along with Tertiary Sandstone, mudstone and conglomerate (T1) and a

## Study Area and Available Data

significant coverage of Quaternary sand, silt, mud, and gravel ( $Q_a$ ). These different sedimentary formations within the study area generally have similar geotechnical properties. While most of the major river valleys are covered with Brigalow clay sheets and fine-grained deposits resulting from long-term erosion, gravels and cobbles can be observed along the fringes of the Kumbarilla Ridge. Moreover, between Dalby and Chinchilla, no rock outcrops are reported to be present. Previous site observations by geologists have revealed that weathered and crushed sandstone with medium strength is used as the road sub-base for the entire study area [Ellis and Mather, 2011]. According to Coffey Geotechnic's [2011] site observations and report, slopes within this part of the Surat Basin do not show signs of instability or landslide. Accordingly, based on the rock and soil material properties and the steepness of the slopes, it is unlikely that rock falls or landslides would have occurred during the satellite observation time and therefore contributed a signal.

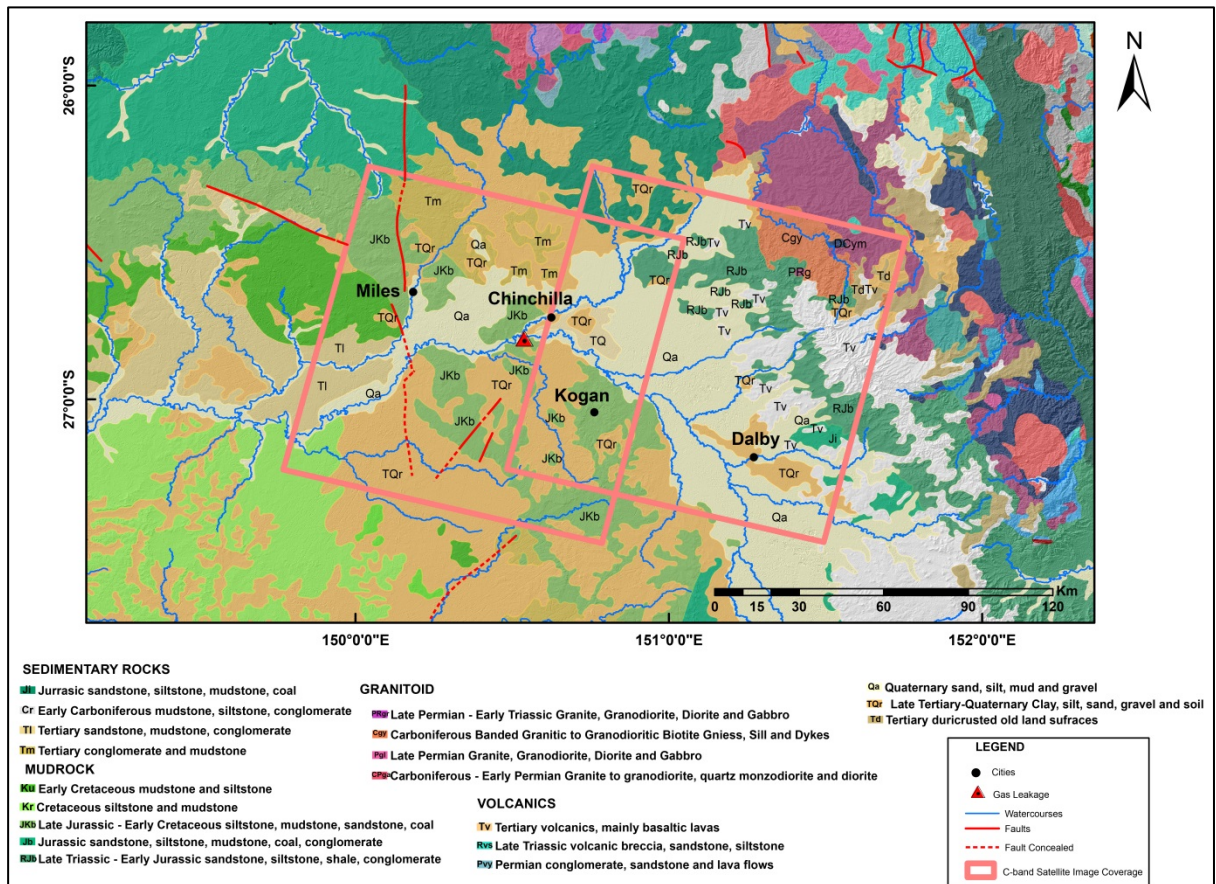


**Figure 3-4: Surface geology map of the Surat Basin, including the location of the previously mapped faults.**

Although the area of interest is stable in terms of rock movements, the particular mineralogy of Vertosols (deep clay soils) over the field can cause shrinking and swelling during the wetting and drying cycles. When the soil dries out, cracking will occur due to shrinkage and the ground can experience deformation after expansion due to re-wetting which is a common feature across the extensive clay plains [Ellis and Mather, 2011].

### 3.2.3. Basin Evolution and Stratigraphy

The structure of the Surat Basin on a regional scale is made up of a collection of several large-scale synclinal structures overlying the Bowen Basin and associated bedrock [Henning, 2005]. The Surat Basin is slightly offset from the depositional and structural axes [Fielding *et al.*, 1990] and significantly less structurally complex than its surrounding basins [Martin *et al.*, 2013]. The axial zone of the Mimosa Syncline is the major depocentre of the Surat Basin and is parallel to and slightly offset from the Taroom Trough axis in the Bowen Basin (Figure 3-5). The Taroom Trough, with its half-graben structure and various depths (i.e. 10,000m to 1,600m) from north to south, is confined by a series of basement thrust faults, named the Burunga-Leichardt and Moonie-Goondiwindi fault zones, on the eastern margin. For those faults on the western margin of the basin, the maximum displacement is between 1,000m in the south and up to 2,000m in the north [Exon, 1974].

Isopachs of the sequences in the Surat Basin are complex but are broadly concentrated around several depocentres, including the Mimosa Syncline. As previously mentioned, renewed subsidence and sediment accumulation characterized Early Jurassic times as the Surat Basin began to form. Subsidence in the Surat Basin was extensive, largely passive, slow and relatively even [Exon, 1976]. Following the accumulation of Jurassic alluvial and lacustrine sequences, and under the influence of flexure along pre-existing fault lines, particularly the Hutton-Wallumbilla fault, mild compressive deformation characterized the structuring of the Surat Basin (Figure 3-5). However, in late Cretaceous times sediment accumulation ceased and the whole area was uplifted via mild structuring during Tertiary times to arrive at its present structural configuration.

The stratigraphy of the Surat Basin (Figure 3-6) has been well described in Green *et al.* [1997] and Hoffmann *et al.* [2009]. After sedimentation, as uplift and erosion occurred over much of the Bowen Basin until the end of the Triassic, the compressional regime from Permian through to Triassic times gave rise to thrust faulting and associated folds. As a result, most structures in the Surat Basin have resulted from either drape over pre-existing basement highs or differential compaction with constant lower relief than those found in the underlying Triassic sections. Early in the Late Cretaceous, there was a contractional deformational event that caused thrust faults to propagate from the underlying section into the Surat Basin sequence. This episode resulted in folding and uplift of the Surat Basin sediments over these deeper reactivated thrust faults.

Throughout the basin, regional subsidence commenced with relatively little reactivation of earlier faulting in the Early Jurassic, and the first sediments to be deposited were the fluvial sandstone called Precipice Sandstone. This was deposited across the basin as a series of fluvial sands in meandering and braided stream environments. The reservoir sandstones of this formation are sealed by a discontinuous shale horizon at the top of the unit, and elsewhere by the overlying Evergreen Formation.

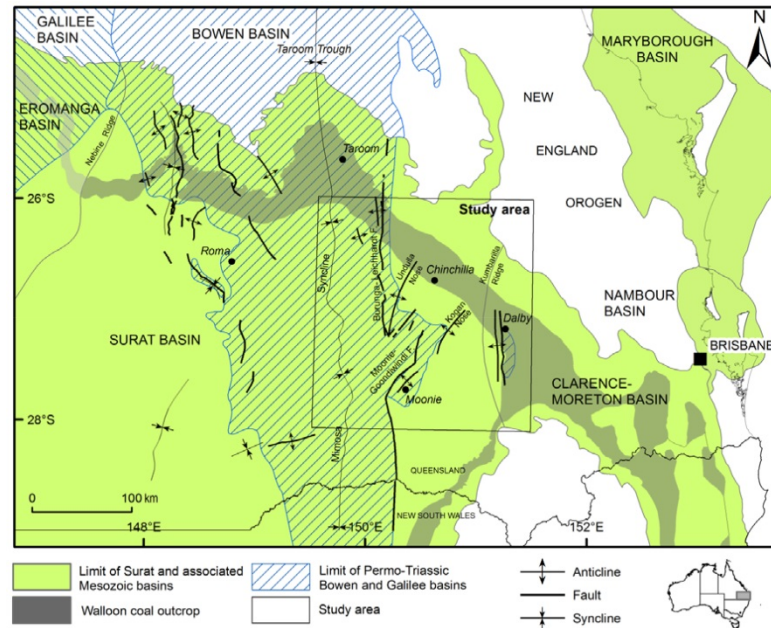


**Figure 3-5: The location of the superimposed Surat and Bowen Basin along with other related Mesozoic basins. The structure of the Surat Basin and the extent of the Walloon Coal Measures are also highlighted after [Hamilton et al., 2013] Queensland Government © 2013 .**

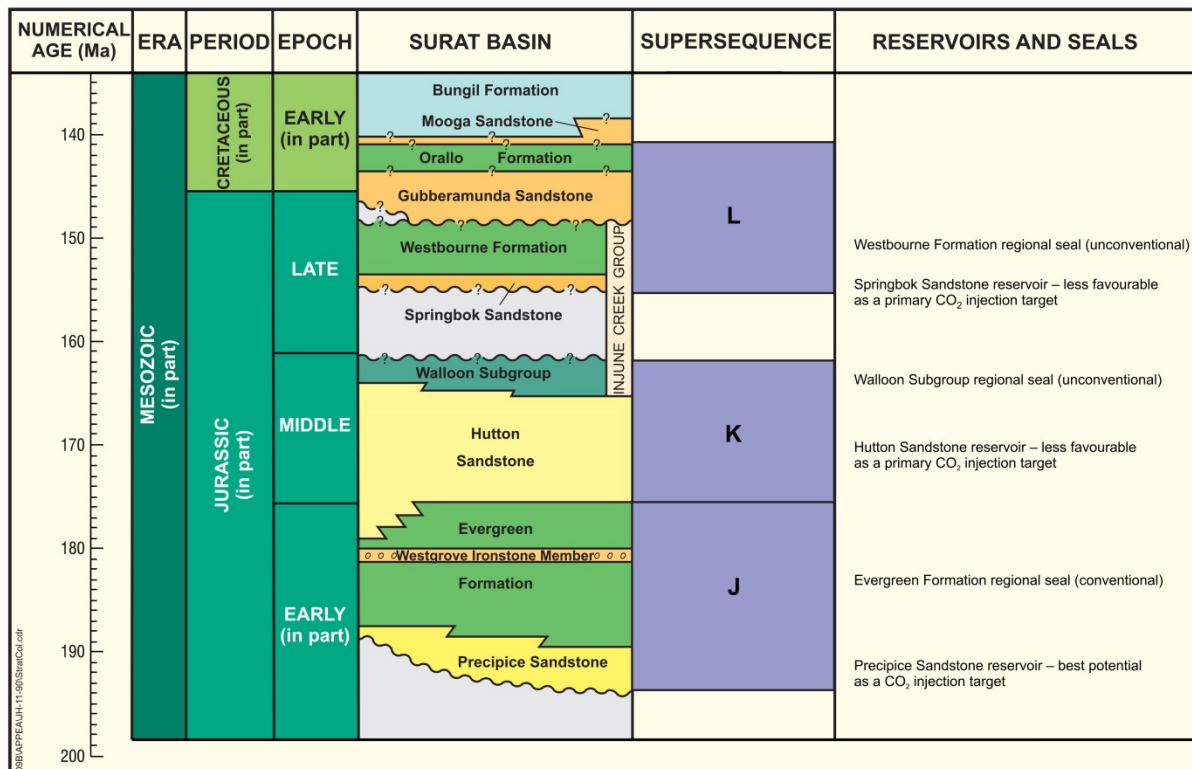


**Figure 3-6: Stratigraphic column of the Jurassic- Cretaceous units in the Surat Basin after [Hodgkinson et al., 2010]**

The Precipice Sandstone has a maximum thickness of at least 120m in the Mimosa Syncline, adjacent to the Chinchilla-Goondiwindi/Moonie Faults, but towards the Roma shelf in the west it is less than 40m thick [Cadman and Pain, 1998]. Throughout the Early Jurassic period, the sediment source for the Precipice Sandstone appears to have been Precambrian rocks bordering the western and south-western margin of the Great Artesian Basin [Martin, 1981].

Overlying directly on Precipice Sandstone is the Evergreen Formation with an Early Jurassic age. Sediments in this formation represent a transgressive phase with basal fluvial sandstones similar to underlying Precipice Sandstone, siltstone, and shale and minor fine grained sandstones deposited in fluvio-lacustrine to marginal marine environments. The more extensive Evergreen Formation thickens both to the north and east into the Mimosa Syncline with maximum thickness of ~ 300m [QCGI, 2009]. The physical properties within the Evergreen Formation are somewhat variable, although porosities are generally good to excellent, ranging between 15% and 25%. Permeability is more variable and ranges from 6 to 475mD [CSIRO, 2011].

After the deposition of the Evergreen Formation, the Hutton Sandstone is the next sequence, with fluvial, deltaic and lacustrine sandstones and minor siltstone and shale. The Hutton Sandstone is a relatively uniform, blanketing sand body ranging in thickness between 150m and 250m. In this formation the porosity generally varies between 15% and 25 %, with permeability around 441.8mD. Both the Hutton Sandstone and the Precipice Sandstone are major aquifers in the shallow regions of the northern Surat Basin, close to the recharge and discharge zones, while in the central part of the basin the Gubberamunda Sandstone and Springbok Sandstone are the main groundwater reservoirs [Hodgkinson et al., 2010].

To the south of the Surat Basin the heterogeneous Walloon Subgroup transgresses the Hutton Sandstone, while in the north they rest conformably on the Eurombah Formation. Rapid sedimentation of the Eurombah Formation below the Walloon Subgroup resulted in a series of fine-grained sequences consisting of interbedded siltstones and mudstone as an aquitard with effective porosity that reaches above 15%. On the other hand, the overlying Walloon Formation above thickens eastward into the Mimosa Syncline and attains a maximum thickness in excess of 400m in the north and east of the basin [QGC, 2013a]. The middle Jurassic Walloon Subgroup is a prolific, low-rank CSG resource in the Surat Basin and can be divided into the Juandah (upper), and Taroom (lower) coal measures, separated by a relatively coal-barren and sandstone-dominated unit called Tangalooma Sandstone [Martin et al., 2013]. The Walloon Subgroup also hosts significant thermal coal with high ash content and is exploited for its CSG resources.

With dominated fluvial conditions over much of the basin towards the end of the Middle Jurassic, the Springbok Sandstone rests conformably on the Walloon Subgroup and comprises fine-grained, lithic sandstones with interbedded, carbonaceous and micaceous siltstone and mudstones. This unit has the maximum thickness of around 200m towards east and has similar properties to the Walloon coal measures, but less abundant coal seams [Bradshaw et al., 2010].

At the beginning of the Late Jurassic, fluvial sediments of the Westbourne Formation were deposited conformably over the Springbok Sandstone, which comprises interbedded shale, fine-grained sandstones and siltstones. This formation can be identified on logs by its high gamma ray and low resistivity response. Porosities exceed 20% but permeability is relatively poor. This formation, with up to 250m thickness in some places, is one of the low permeability aquitards that separate the lower Walloon coal layers from the commonly used groundwater aquifers above.

Towards the end of the Jurassic and in the earliest Cretaceous, a series of fluvial sandstones filled the slowly subsiding Surat Basin (Gubberamunda Sandstone, Orallo Formation and Mooga Sandstone). In the Early Cretaceous marine influences came back to the Surat Basin and the Bungil Formation, which comprises lithic sandstones, mudstones and siltstones, was deposited conformably over the Mooga Sandstone. This marine transgression culminated with mudstones, siltstones and lithic sandstones of the Wallumbilla Formation and Surat Siltstone. Above the Surat Siltstone is the Griman Creek Formation, which was deposited when the seas began to retreat from the Surat Basin towards the end of the Early Cretaceous. This unit comprises thinly interbedded siltstone, fine-grained sandstone and mudstone with more conglomerates towards the top of the sequence. The lower Griman Creek Formation is probably marine, while the upper section grades into transitional and finally freshwater facies.

Early in the Late Cretaceous, a contractional deformational event resulted in folding and uplift of the Surat Basin sediments over reactivated thrust faults from deeper in the section. Erosion over most of the Surat Basin developed in the Late Cretaceous and Early Tertiary; however, epirogenic movements tilted the entire sedimentary section to the southwest during the extrusion of basalts to the north of the basin. To the south, where uplift was much less pronounced, erosion is less evident. Following the tilting event, erosion of the Surat Basin sediments has continued from Tertiary times until the present day, with Cenozoic sedimentation of fluvial sandstones and siltstones as a thin layer.

According to the stratigraphic section of the Surat Basin, predominant aquifers are the Cretaceous sediments, Gubberamunda Sandstone, Springbok Sandstone, Hutton Sandstone and Precipice Sandstone. Formations with aquitard properties are the Westbourne Formation, Evergreen Formation and some basement rocks. The Walloon Subgroup and all aquifer formations have both aquifer and aquitard characteristics. Water bearing horizons are present in Westbourne Formation and Evergreen Formation [[QGC, 2013a](#)].

According to drilling results by Queensland Gas Company (QGC), the stratigraphic subdivision by Jones and Patrick [[1981](#)] is the acceptable representation of the subsurface stratigraphy. Juandah Coal Measures comprises six coal seams, the Kogan, Macalister, Nangram, Wambo, Iona and Argyle Seams in descending stratigraphic order. For the Taroom Coal Measures QGC considered three coal seams, informally referred to as the Auburn, Bulwer, and Condamine Seams.

Within the Walloon Coal Measures lateral variation in coal character is high and precludes regionally agreed coal group or seam correlation. With increasing depth there is a general increase in

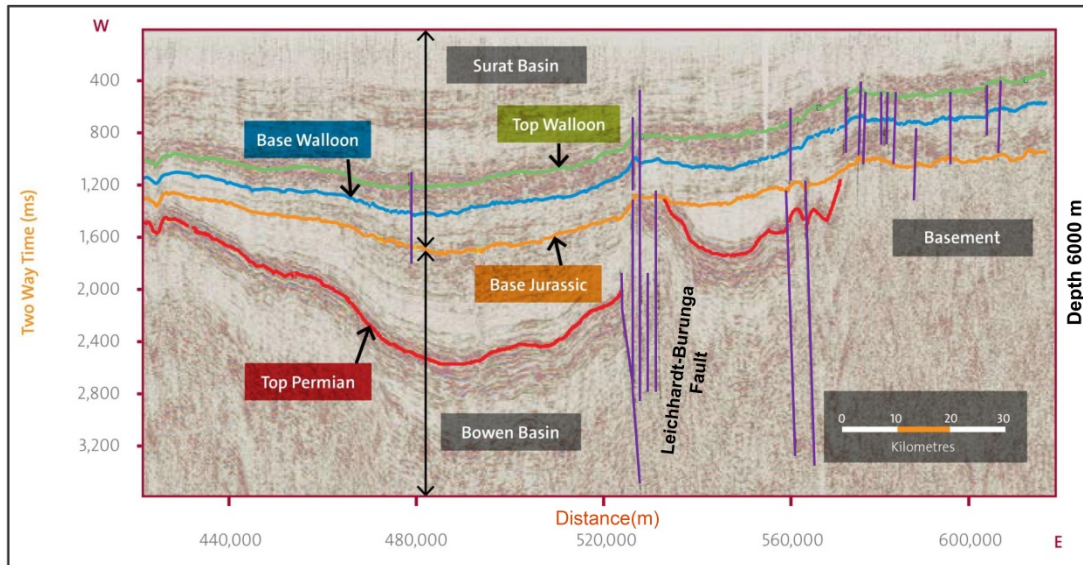


**Figure 3-7: Normal-polarity seismic section (BMR84-14), which passes across the southern part of the Surat Basin, shows a sequence of sedimentary rocks. The vertical scale is in milliseconds seismic two way travel time after [QGC, 2013c] Queensland Government © 2013.**

gas content (dry-ash-free) as a function of hydrostatic pressure but with considerable scatter in the distribution. Gas content follows one of three trends in each individual well in the Walloon Coal Measures: gas content either increases, first increases then decreases or increases with depth, with the second trend (parabolic) being the dominant trend for the majority of the wells. According to the analysis of the well profiles and gas gradients, there is a high gas gradient zone in coals within or above the Tangalooma Sandstone, with possible gas migration from underlying higher rank coals with biogenic and meteoric recharge from above. Significant ethane accumulation in the upper Taroom and Tangalooma coal seams supports such interpretation. There is also another possibility, that the adsorption-desorption cycles due to the burial and uplift events might be responsible for such distribution [Hamilton *et al.*, 2012] .

### 3.2.4 Subsurface Geology

As an elongated basin with up to 2,500m of sediments, the Surat Basin has experienced a series of four depositional cycles during the Jurassic Period followed by transgressive marine sediments deposited during the Cretaceous Period [Henning, 2005]. These sediments inter-lace with sediments of the Eromanga Basin across the Nebine Ridge to the west and Clarence-Moreton Basin across the Kumbarilla Ridge (near Dalby) in the east. In addition, during the Tertiary Period the northern margin of the basin was extensively eroded due to orogenic uplift [Exon, 1976], while the morphology of its base is largely controlled by the underlying basement architecture, Bowen Basin and older rocks [SRK, 2008] .

Basin structural features such as faults can influence aquifer-system deformation in multiple ways: (i) changing the thickness of compressible aquifer materials on each side of the fault and causing

differential displacement, (ii) behaving as a hydraulic boundary to impede propagation of water level declines from pumping across the fault, and (iii) mechanical discontinuity of 3D strain distribution and reducing the migration of vertical and horizontal deformation across the fault [Burbey, 2008].

The structure of the Surat Basin in the proposed study area is dominated by two major fault systems that were active during the Triassic (i.e. Moonie-Goondiwindi and Burunga-Leichhardt thrust faults) [Korsch *et al.*, 2009]. Throughout the deposition of the sediments in the Surat Basin these two faults, with a series of discrete fault segments, were the controlling structures of the depositional architecture [Korsch *et al.*, 1998; Sliwa and Esterle, 2008]. Mild reactivation of the Triassic-style compressional forces caused the region tilt to the south, with normal faulting resulting from sediment loading and isostatic re-adjustment [Rayner, 1987]. Contractional reactivation of these structures in the Late Cretaceous prevented further brittle faulting and folding with structural relief of Wandoan Anticline, Undulla Nose and Kogan Nose [Hamilton *et al.*, 2012].

### 3.2.5 Petrophysical View

Interpretation of petrophysical wire-line log data is one of the useful tools for both hydrogeologists and reservoir engineers to characterize the subsurface framework. The petrophysical properties in any formation are partly a function of depth, and can be used for extracting different parameters such as lithology, porosity, permeability, fluid type and saturation, as well as fracturing. Petrophysical observations of permeability distribution in the rock mass can also be used to estimate the spatial distribution of hydraulic conductivity within a hydro-stratigraphic unit. The geometry and spatial extent of hydro-stratigraphic units and their hydraulic properties can constrain conceptual hydrogeological models.

Conducting local-state formation tests for temperature and pressure over a large number of well points can represent patterns in permeability and porosity over a large basin such as the Surat Basin. Within formations with inflow capacity and subsequent high permeability ( $\sim >300\text{mD}$ ), a Drill Stem Test (DST) is accompanied with pressure testing, while for low permeability formations Flow Rate Tester (FRT) and Modular Formation Dynamic Tester (MDT) are common.

Within the Surat Basin, based on aquifer testing, the Gubberamunda Sandstone aquifer is more permeable than the Springbok Sandstone. These two aquifers are exploited extensively for groundwater supplies in the northern and central Surat Basin [Hodgkinson *et al.*, 2010]. In contrast to the Gubberamunda Sandstone, which has no leakages, the Springbok Sandstone is susceptible to leakages due to pumping from the upper or the lower sand unit [QGC, 2013b].

### 3.3 Underground Resources and Regional Deformation Records

The area studied in the Surat Basin is located in the Western Downs with an administrative centre located in Dalby, 210km west of Brisbane and 84km from Toowoomba, and includes several major towns such as Wandoan, Miles, Chinchilla, Jandowae, and Tara. Recently, with a number of energy generating infrastructures in Chinchilla and Dalby, Western Downs has become known as the “energy capital” of Australia. The major emerging industrial projects form the Surat Basin Energy Province and accommodate the increased investment and demand in the area [*Matusik-Property-Insights, 2011*].

#### 3.3.1 Groundwater Aquifers

As a dynamic entity, groundwater moves under the effect of gravitational force to lower lying formations. The pace of groundwater travel throughout the underlying formations is dependent on the permeability of the formation and on the presence of the geological structures such as faults and fractures [*Fennell et al., 2012*]. The aquifers, as one of the natural groundwater storage places associated with the Surat Basin, are generally not flat but bowl-shaped and slope towards their centre (generally at less than one degree) [*Hodgkinson et al., 2010*]. In addition, they are capped or sealed by impermeable aquitards. The water at the lowest point of the basin is stored under pressure. The higher the water level (i.e. the higher the water reaches up the side of the basin) the more pressure there is. When the aquifer is tapped by a bore, the pressure causes the water to rise towards the ground surface. In the areas under study, most bores are sub-artesian and require pumps to draw water to the surface.

The Mooga and Gubberamunda aquifers, called Kumbarilla Beds in some regions, are the most commonly used aquifers for agricultural and farming purposes in the Surat region. These aquifers are generally located at depths between 50m and 250m. Some industrial bores access the Hutton and Precipice aquifers, which sit at depths between 500m and 1,000m. Key aquifer petrophysical properties (e.g. porosity, horizontal and vertical permeability) are established through pumping tests and standard hydrogeological techniques. Petrophysical properties can be derived from high-quality wire-line logs (i.e. neutron porosity and density) for porosity calculation, along with stratigraphic interpretation.

Groundwater in geological formations flows from areas of higher water level or water pressure to areas of lower water level or water pressure. It should be noted that the permeability of both formations is also critical. At the location of the Great Dividing Range, through the centre of Surat Basin, the groundwater flow direction splits the system into two opposing groundwater flows: (a) groundwater within the northern 'Dawson Rich Catchment' which exists via the Dawson River, and (b) groundwater within the southern 'Balonne-Condamine River Catchment' in the south and southwest. In the case of this study area, groundwater flow follows within the 'Balonne-Condamine River Catchment' and is dominated by local to regional processes that correlates with the surface water drainage flow direction (i.e. south and southwest) over outcrops of predominantly Gubberamunda Sandstone and Cretaceous sediments [APLNG, 2010].

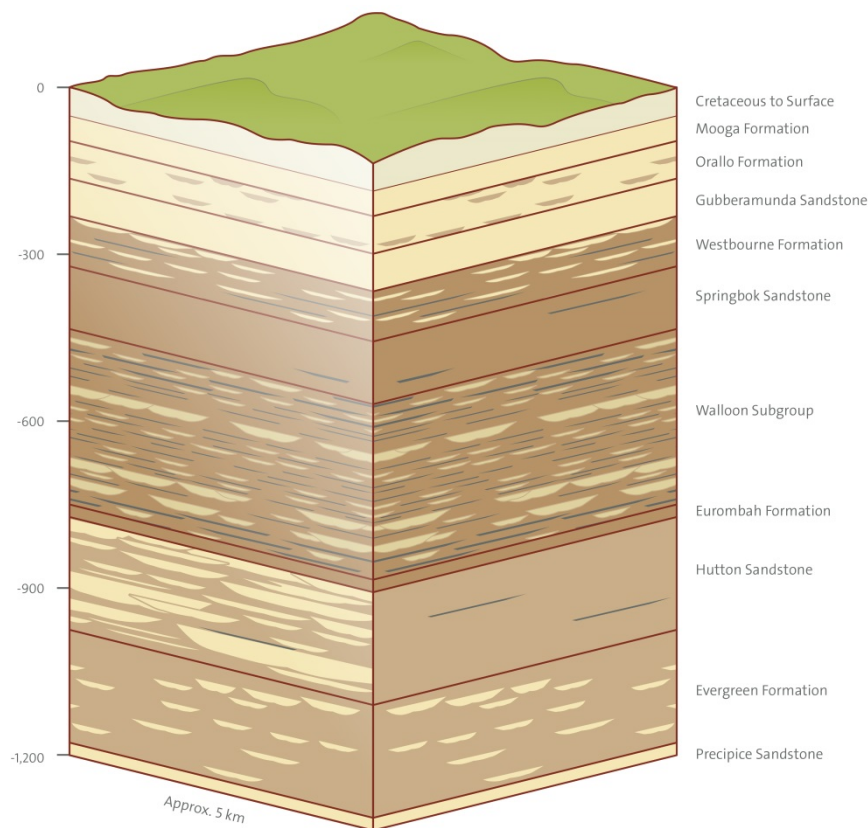


**Figure 3-8: Detailed subsurface layers including the aquifers and aquitards in the Great Artesian Basin including the Surat Basin [QGC, 2013a] Queensland Government © 2013.**

To address aquifer storage values within the Surat Basin derived from bore pumping based on the Queensland Water Commission report [QWC, 2012], estimates of storage in the unconsolidated sediments and alluvium range from less than 0.1% to more than 30%, while within the confined consolidated formations the average is about  $5 \times 10^{-5}\%$ . According to the Australia Pacific Liquefied National Gas Environmental Impact Statement (LNG-EIS) Project, the potentiometric surfaces of aquifers in shallower formations of this region are a reflection of the topography. However, in deep formations the regional-scale groundwater flow system (generally towards the

southwest) can impact on this pattern and contribute to groundwater discharge as local springs, rivers or streams [APLNG, 2010; Worley-Parson, 2010]. Both natural and artificial discharge is occurring in the GAB as described in Table 3-1.

**Table 3-1: The two different categories of groundwater discharge in aquifer system in the Surat Basin.**

| Natural Discharge                                                                                                                          |
|--------------------------------------------------------------------------------------------------------------------------------------------|
| Concentrated outflow from springs accompanied with structural features such as faults, folds and intersecting lineaments [Habermehl, 1982] |
| Base flow contribution to rivers                                                                                                           |
| Vertical upward leakage from the lower formations towards to the regional water table [Woods et al., 1990]                                 |
| Subsurface outflow into neighbouring basins                                                                                                |
| Artificial Discharge                                                                                                                       |
| Free or controlled artesian flow, groundwater abstraction through pumping from confined aquifers                                           |

Conversely, recharge to the Great Artesian Basin is usually expressed as a percentage of average annual rainfall, which has occurred for all aquifers in the Jurassic sequence in the northwest of the basin [Radke et al., 2000]. According to the GAB groundwater flow models (GABSIM and GABHYD) developed by the Bureau of Rural Sciences (BRS), estimates vary between 1 and 3% of total rainfall for the Gubberamunda Sandstone and Hutton Sandstone [GABCC, 2000]. Results of previous studies indicate that recharge rates at 14 sites ranged from 0.5 to 2.0mm/year [BRS and NRM, 2003].

The Great Artesian Basin was in a steady-state condition with natural equilibrium up to the late 1800s. However, agricultural development, with intensive groundwater abstraction significantly reduced the natural discharge from springs in the south-central, southwestern and northern regions [Habermehl, 2002]. Groundwater abstraction in turn has contributed to large-scale lowering of potentiometric surfaces and steepening the hydraulic gradients, resulting in higher rates of recharge to the Basin [Habermehl, 1980].

Regarding to the inter-aquifer flow regime, it is worth mentioning that the predominant groundwater flow in the GAB is horizontal with limited flow in a vertical direction between aquifers. The inter-aquifer flow is generally occurring where intervening aquitards are narrow or where aquifers are connected by faults. For instance, in the Walloon Coal Measures, groundwater flow is from the coal layers into the overlying Condamine river alluvium, while the vertical gradient downstream of Dalby is from alluvial deposits to the Marburg Sandstone [Lane, 1979]. Recent investigations on Surat Basin aquifers for carbon storage, combining the formation pressure dataset and potentiometric head measurements, have indicated that there is a potential connectivity between the Precipice Sandstone and Hutton Sandstone in the Central Surat Basin, and that the Evergreen formation is not an effective seal in this area [Hodgkinson et al., 2010]. The spatial distribution of hydraulic head values in the Precipice Sandstone also suggests that the Burunga-Leichhardt thrust

fault does not act as a barrier to horizontal groundwater flow, while for Evergreen Formation the lack of relevant data precludes any conclusion on the probable influence of faults on fluid flow [QCGI, 2009]. It is also worthwhile mentioning that the inter-basin flow in the Precipice Sandstone aquifer is from the Surat Basin into the Clarence-Moreton Basin, while the Hutton Sandstone aquifer shows the opposite flow direction from the Clarence-Moreton Basin into the Surat Basin with limited vertical communication between these two in the southeast of the Basin [Hodgkinson *et al.*, 2010].

It should be noted that the major influencing factors on depressurization of the Walloon subgroup and its possible impact on adjacent aquifers are the lithological and hydraulic properties of major aquitards and their spatial distribution. In the Surat Basin the three key aquitards are the Eurombah, Westbourne and Evergreen formations. Alternatively, groundwater pressure differences between formations, which can be locally and topographically distinct, along with “layer cake geology” of separate homogenous aquifer and aquitard formations should also be considered as crucial factors in subsurface depressurization [QGC, 2013d].

Within the Surat Basin, alluvial aquifers are associated with various river systems. The most significant and highly developed is the *Condamine Alluvial Aquifer*. Ground water extraction from this aquifer for irrigation and town water supply has caused considerable decline in groundwater levels as extraction exceeds recharge. The Condamine Alluvial Aquifer, in part, overlies the Walloon Measures [Gas-field-Commission, 2013].

More than 21,000 water bores are located within the Surat Basin to extract approximately 215,000 mL/yr for grazing, irrigation, industry and urban consumption. Among these bore holes, 528 are expected to experience a decline in water level of more than the trigger threshold as a result of ground water extraction. For consolidated aquifers (sandstone) the threshold is five meters, while for unconsolidated aquifers (sand) the threshold is around two meters. There are also 498 monitoring points in place to measure the water level and quality. Based on 85 registered water bores in the Surat Basin, water level decline by more than the trigger threshold is predicted within three years in the immediately affected areas [QWC, 2013]. Based on a QGC report in 2013, the drawdown threshold proposed in line with Queensland’s Water Act, are:

- 5m for the Mooga Aquifers (excluding existing trends or oscillations);
- 5m for the Gubberamunda Aquifers (excluding existing trends or oscillations); and
- 5m for the Springbok Aquifers (excluding existing trends or oscillations).

The Surat Cumulative Area divides the aquifers into two major areas: (a) Immediately Affected Area (IAA) and (b) Long-term Affected Area (LAA). In case of IAA, the groundwater resource is extracted more than the trigger threshold (i.e. around 5m in consolidated aquifers such as the GAB sandstones and 2m in unconsolidated aquifers such as the Condamine Alluvium by petroleum tenure holders). However, in the case of LAA, groundwater levels are expected to fall by more than the

trigger threshold due to gas field production at any time in the future. The default drawdown threshold, as a precursor for all aquifers, is 0.2m and is applied for those that are considered as the source aquifers to EPBC listed springs [QGC, 2013b].

Generally, there are two types of bore holes in the Surat Basin that were implemented in two major phases: Phase One was started in 2011 for shallower bores to the Gubberamunda and Springbok aquifers, while Phase Two (2012-2013) is addressing bores to deep and shallow aquifers and aquitards above and below the Walloon Group. A number of monitoring boreholes are targeting multiple levels within the stratigraphic sequence and include the Walloon Subgroup. These sites are typically at the location of CSG appraisal pilots where there is trial pumping to determine porosity, permeability, etc. of the Walloon Subgroup [QGC, 2013b].

### 3.3.2 Hydrocarbon Resources

Conventional (i.e. oil and natural gas) and unconventional (i.e. CSG) hydrocarbons are all valuable resources that have been exploited in the Surat Basin [Bradshaw *et al.*, 2010] since 2000. Common hydrocarbon traps in the Bowen/Surat Basins are generally structural and structural-stratigraphic. The main hydrocarbon production and exploration targets in these basin systems are the Jurassic Precipice and Triassic sandstones sealed by the Evergreen and Moolayember formations respectively [CSIRO, 2011].

While most coal mining operations in the Surat Basin are by open-cut mining, Scott *et al.* [2007] confirmed that extracting gas from the coal seams is considered economically viable. According to Geoscience Australia, over 64% of the 2P (proven and probable) CSG reserves occur in the Surat Basin [Geoscience-Australia, 2010] and contributed around 113PJ to the Queensland energy supply in 2010-2011 [Queensland-Mines-and-Energy, 2012]. The CSG production in these two basins is distributed in six areas that are located in the central Bowen Basin and the Surat Basin, with the four major coal layer targets known as Moranbah, Baralaba, Bandanna, and Walloon seams due to their distinctive depositional and structural settings [Barrett *et al.*, 2008]. CSG in the Surat Basin is produced from multiple coal layers in which the shallow (i.e. 100m to more than 900m depth) low-rank, Middle Jurassic Walloon Subgroup, with high permeability and vast lateral extent, is an attractive target for low-cost CSG development and sustainable microbial regeneration of methane [Scott, 1999; Scott *et al.*, 2007].

As the CSG industry involves lowering water pressure in the subsurface formations, fractures, and rock pores, taking into consideration the potential impacts of its development on water resources is the key aspect in surveillance of CSG projects in the Surat Basin. For the CSG industry, extraction of substantial volumes of poor quality water, and changing the static water level by reducing the water pressure in the formations, are the outcome of CSG extraction. The rate of groundwater extraction in Queensland for recent years was estimated at about 12.6GL/yr with the predicted rate rising to greater

than 100gL/yr because of the expansion of the CSG industry in this region [Barrett *et al.*, 2008]. By converting pressure changes to vertical effective stress changes, and by calculating the potential deformation, the range of maximum water drawdown could be between 0.08m and 0.145m [QGC, 2013c].

The Undulla Nose CSG province (Figure 3-5), which is largely operated by QGC and Origin Energy companies, is a structure encompassing the Berwyndale South, Argyle, Lauren and Talinga gas fields. In addition to the plunging structure, thick coal seams (over 29m net), high gas saturation and enhanced permeability are the outstanding characteristics of the Undulla Nose area. For example, the average gas flow rate of the wells drilled in the Berwyndale South gas field was over  $10^6$  MSm<sup>3</sup>/d, which is considerably higher and atypical when compared to other CBM wells in the Surat Basin. As opposed to structural enrichment, the permeability tends to drop quickly in the Undulla Nose down dip of the central and north Candabri field, which requires stimulation to produce at commercial rates [Johnson and Mazumder, 2014].

Another successful CSG area in the Surat Basin, operated by Arrow Energy Pty. Ltd., is the Daandine gas field located 40km west of Dalby. This field started its production with two wells in 2005 and reached its initial commercial rate by the end of that year. High rate producing Walloon Coal Measures (WCM) wells in the Daandine gas field were drilled after 2007, penetrating coal layers less than 25m thick and with permeability values of 100-200mD. This field as part of Undulla Nose CSG province has an average flow rate of  $3 \times 10^6$  MSm<sup>3</sup>/d [Johnson and Mazumder, 2014].

The Ridgewood area is part of the Chinchilla/Goondiwindi slope project that extends southward to the margins of the Surat Basin. This area was a trial site for an extensive hydraulic fracturing undertaken by QGC to frack thick layers of coals. A comprehensive geomechanical study, including Diagnostic Fracture Injection Testing (DFIT) for stress and permeability, surface deformation tilt meter, and downhole microseismic data, was conducted in this region by QGC [Brooke-Barnett *et al.*, 2013; Megorden *et al.*, 2013].

While gas production from laterally continuous coal beds in the Undulla Nose and Daandine areas has demonstrated high rates due to improved permeability and lower stress, the Chinchilla/Goondiwindi slope remains less developed because the strategy to stimulate this part of the WCM was unsuccessful due to low permeability and higher stress conditions [Johnson and Mazumder, 2014]. In the eastern part of the Surat Basin, the WCM biogenic gas content [Draper and Boreham, 2006] versus depth shows a heterogeneous distribution that does not simply increase with depth or hydrostatic pressure, and is not related to a single controlling factor such as coal type or stratigraphy [Scott *et al.*, 2004; Scott *et al.*, 2007]. According to Scott [2002] the main geological and hydrogeological factors affecting CSG such as gas content, gas saturation, permeability, structure, coal petrology and temperature are interrelated (Table 3-2). Groundwater from the GAB sub-basins such as the Surat Basin is generally suitable for livestock or industrial uses, and less commonly of a quality suitable for human consumption or irrigation due to its high mineral salt content.

**Table 3-2: Major geological and hydrogeological factors affecting coal seam gas reserves in the Surat Basin in different levels.**

| Control                        | Low impact                                                                                                                                                                      | High impact                                                                                                                                                                                     |
|--------------------------------|---------------------------------------------------------------------------------------------------------------------------------------------------------------------------------|-------------------------------------------------------------------------------------------------------------------------------------------------------------------------------------------------|
| Coal Petrology                 | Tentative negative correlation between inertinite and gas content <sup>b</sup>                                                                                                  | Tentative positive correlation between liptinite and gas content <sup>b</sup>                                                                                                                   |
| Formation                      | Upper Juandah Coal Measures-lower gas contents due to gas loss into overlying Springbok Sandstone. Regionally under saturated despite higher adsorptive capacity <sup>b</sup> . | Higher gas contents for coal seam groups within and stratigraphically close to the Tangalooma Sandstone <sup>b</sup>                                                                            |
| Depth below ground level (G.L) | Lower than average gas contents/saturation in wells where the top of the Walloon Subgroup is <250m below G.L <sup>a</sup> .                                                     | No clear relationship; gas content/ saturation and permeability not strictly related to depth <sup>b</sup> ; most production is 250-600m below G.L.                                             |
| Anticlines/'Noses'             | Lower than average gas contents and saturation on large anticlines, incl. Wandoan, Kogan Anticlines; low permeability <sup>a</sup>                                              | Undulla Nose displays high gas contents relative to depth, higher gas saturation and high permeability <sup>a</sup>                                                                             |
| Large-scale faults             | Lower than average gas contents and saturation near Leichhardt, Moonie faults; low permeability <sup>a</sup>                                                                    |                                                                                                                                                                                                 |
| Temperature/ rank              | Lower gas contents on the Kogan Anticline coincide with lower Vitrinite reflectance <sup>c</sup>                                                                                | Undulla Nose- higher gas contents coincide with elevated geothermal gradient <sup>d</sup> . Coals in Undulla Nose wells have a higher rank/ lower moisture content for their depth <sup>b</sup> |

### 3.3.3 CO<sub>2</sub> injection in the Surat Basin

Based on the *Wandoan CCS project* (2017/18) for capture and storage of up to 2.5Mt/yr of CO<sub>2</sub>, and in order to mitigate the adverse environmental impacts of greenhouse gas emissions in the region, the Surat Basin has been identified as a potential geological storage site, although the location of injection wells is still under investigation. Geological and structural assessment of the subsurface by understanding the geomechanics and structural integrity of the geological framework will demonstrate the degree of contamination security in selected storage sites that may be under CO<sub>2</sub> injection. Among different structural targets, depleted oil and gas fields, along with deep saline aquifers, can offer the most suitable targets for CO<sub>2</sub> storage in sedimentary basins such as the Surat Basin [IPCC, 2005]. The exact location of the injection site is unknown at this stage. The main targets for injection are the Precipice Sandstone with the Evergreen Formation as the conventional seal at the regional scale [CSIRO, 2011]. The Precipice Sandstone is a laterally extensive reservoir, with good porosity (maximum 37 %, median 17%) and permeability (maximum 7908mD, median 6.4mD) [Bradshaw et al., 2010]. Moreover, aquifer injection has been proposed as a management option for reducing the impact of CSG extraction in the area at groundwater level under the Queensland Government’s CSG water management policy. Injection into both shallow and deep targets in the Central Condamine

River Alluvium (CCRA) is the most probable options for maintaining the recovery effort [Klohn-Crippen-Berger, 2012].

### 3.3.4 Underground Coal Gasification

Underground Coal Gasification (UCG) is the process of extracting coal from underground without mining it in the traditional sense. In the simplest terms, the coal is heated and gassified in place to produce a synthesis gas (syngas) that is extracted through a well and utilised for power generation or as feedstock in the production of liquid fuels, fertilisers, or other chemical products (Figure 3-9).

Linc Energy was active near Chinchilla (about 300km west of Brisbane) for over 10 years with its UCG technology to produce syngas from CSG in around 60 minutes. The UCG-GTL Linc Energy Chinchilla Demonstration Facility developed and validated a series of models to predict and control the technology in terms of site selection, land subsidence, and groundwater contamination prevention. Although the UCG development in the area was suspended due to potential environmental damages, the Chinchilla Demonstration Facility is still available for research and development and similar commercial operations will be established in South Australia [Bajkowski, 2014; Linc-Energy, 2011].

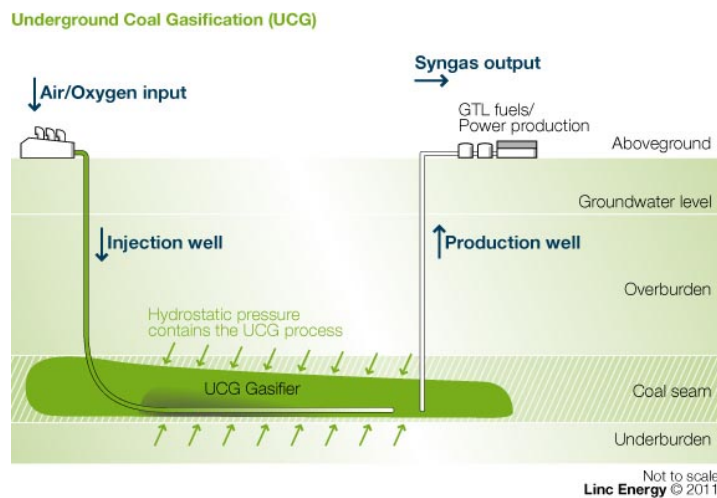


Figure 3-9: The procedure for underground coal gasification (UCG)[Linc-Energy, 2011].

### 3.3.5 Potential for Subsidence and Uplift

Downward ground deformation in the Surat Basin can potentially result from volumetric changes to subsurface formations and adjacent overburden (referred to as matrix volumetric strain) due to groundwater extraction and associated strata compaction. This volumetric decrease can occur due to pore pressure reduction, which increases the stress applied to the rock matrix. Although pore pressure reduction can occur during de-watering, there is documented literature that the magnitude of

subsidence occurring as a result of groundwater extraction should not be particularly significant. However, based on a QGC report in 2013, there is a significant depressurization that started in December 2013 and ground truthing in the form of traditional field surveying will be undertaken in the future to show its magnitude.

### 3.4 Geophysics and Geodesy of the Surat Basin

In order to make a detailed image of underground geology and to evaluate any potential ground surface motion against valid geological structural data, geophysical observations including seismic lines over the proposed area have been identified and uploaded in a geo-modelling package for further analysis. There are also electromagnetic surveys, such as gravity, magnetic and radiometric, which are conducted by Geoscience Australia for the proposed area and are presented in the following section. In addition, conventional and in situ geodetic observations along with non in situ geodetic measurements will be discussed in this section.

#### 3.4.1 Seismic and Electromagnetic surveys

The initial component of hydrocarbon exploration in central and southern Queensland required conducting seismic surveys [QGC, 2013b]. Interpreting seismic lines can indicate the exploration potential of the permit by defining the key scenarios. In the past 40 years, extensive exploration programs were accomplished in the Surat Basin, but it is still categorized as a relatively unexplored region. Between 1976 and 2006 about 893km of seismic reflection data, designated in 12 distinctive surveys, were acquired in the region. These data, which were gathered by different seismic acquisition companies were recorded on the surface from a dynamite source located at around 7m to 30m depth. The high content of unconsolidated sand, weathering and interference of signal from the Walloon Coal Measure contribute significantly to the poor quality of the recorded data. In the study area, the quality of the acquisitions was good enough for uploading and interpreting, and sufficient to distinguish shallow sediments from the basal Jurassic unconformity. Moreover, the presence of several major faults and discontinuous reflections made it difficult to contour the Hutton Sandstone. According to the final reports, the overall quality of the seismic surveys in the study region varies from poor to good with limited potential for structural mapping [Castleden, 1988; Choudhury and Bell, 1984]. The study area is covered by a number of seismic surveys as listed in Table 3-3.

Seismic reflections at each lithological boundary (i.e. seismic reflections) result from changes in Acoustic Impedance (AI) of the travelling seismic wave. AI represents the predictable and characteristic acoustic properties of a rock and is the product of rock density and seismic velocity. In order to investigate rock units in the subsurface, there should be a significant AI contrast [Badley, 1985].

**Table 3-3: List of seismic surveys conducted in the Surat Basin proposed area since 1976.**

| Survey Name       | No. of Seismic Lines | Survey Completion Date | Length of Seismic Lines (Km) |
|-------------------|----------------------|------------------------|------------------------------|
| AT92              | 2                    | 01-MAY-1992            | 96.44                        |
| BENNETT & DETAIL  | 8                    | 31-DEC-1982            | 130.25                       |
| CONDABRI 2D       | 3                    | 16-JAN-2006            | 34.47                        |
| CONDAMINE         | 1                    | 31-DEC-1976            | 10.81                        |
| MILES             | 5                    | 31-DEC-1987            | 49.67                        |
| PERTH             | 1                    | 31-DEC-1983            | 39.67                        |
| ROCKWOOD & EXT    | 14                   | 31-DEC-1981            | 317.49                       |
| SURAT BASIN 79    | 6                    | 31-DEC-1979            | 48.65                        |
| TARA NORTH        | 3                    | 31-DEC-1980            | 24.05                        |
| TRACKERS LAGOON   | 2                    | 31-OCT-1987            | 9.92                         |
| XYLEM             | 12                   | 24-MAR-1986            | 63.89                        |
| XYLEX & EXTENSION | 22                   | 15-MAR-1986            | 67.96                        |
| Total             |                      |                        | <b>893.27</b>                |

Electromagnetic surveys are a traditional type of geophysical measurement, with applications in both ore exploration and the oil industry. These methods, including gravity and magnetic surveys, have been widely used to detect the type of sediments that are less sensitive to the presence of oil than the presence of saline water. Electromagnetic surveys can also be used to map soil types and land drainage systems. As the name implies, these surveys use the principle of electromagnetic induction in order to calculate the electrical conductivity of the subsurface. For successful accomplishment, electromagnetic surveys must be conducted within a few hundred meters of water depth, and relatively shallow (< 2-3km) hydrocarbon accumulations [Bjørlykke, 2015].

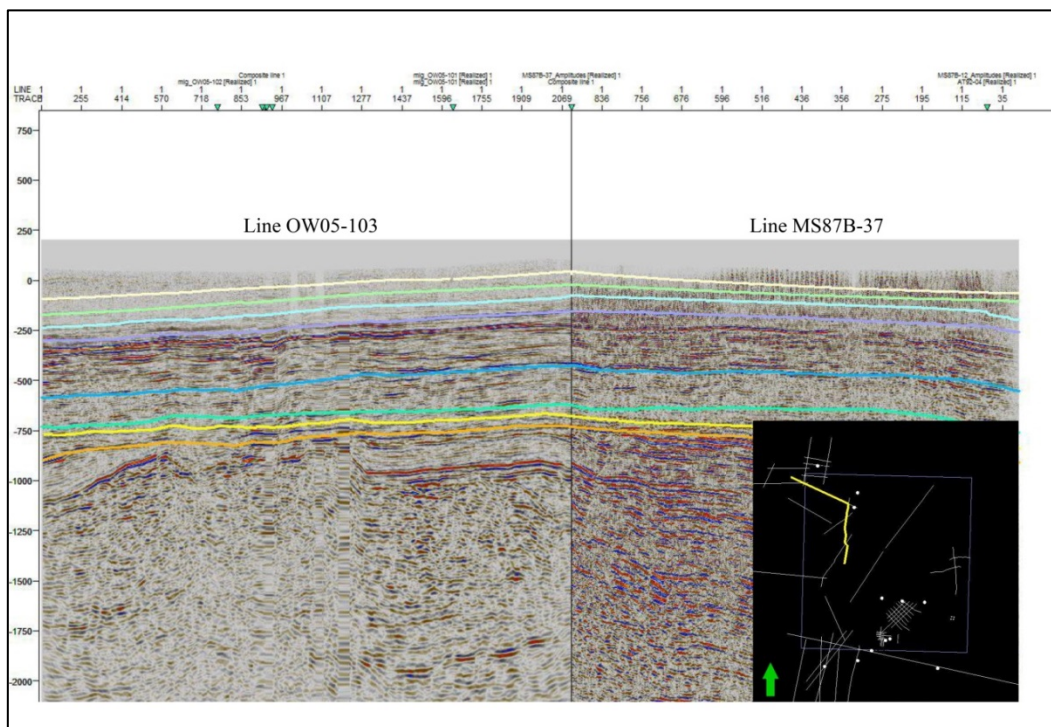


**Figure 3-10: Overview of the location of seismic lines and petroleum wells over the study area in the Surat Basin (the inset image). Two selected seismic lines in yellow colour are shown in the background image. The right-hand side line is called OW05-103 and the left-hand side line is called MS87B-37 to show the stratigraphic horizons identified in this region using Petrel software (Schlumberger©).**

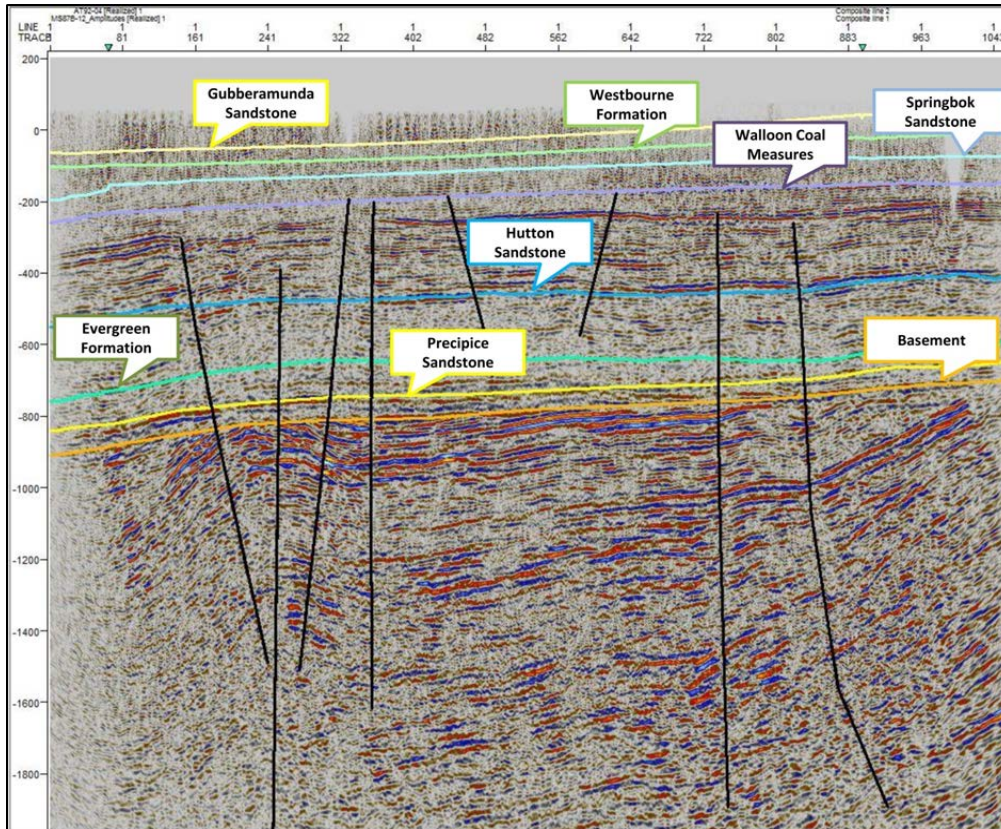


Figure 3-11: Example of seismic interpretation for seismic line MS87B-37 showing lithological boundaries and structural faults.

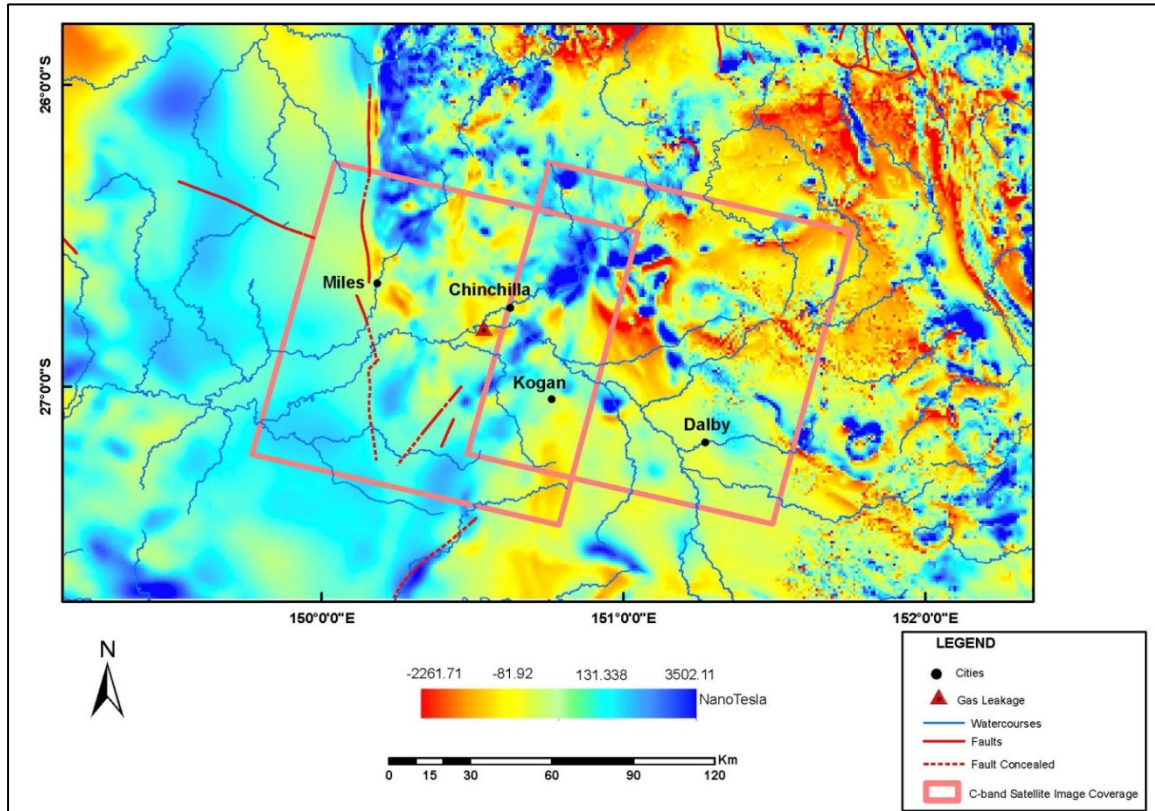
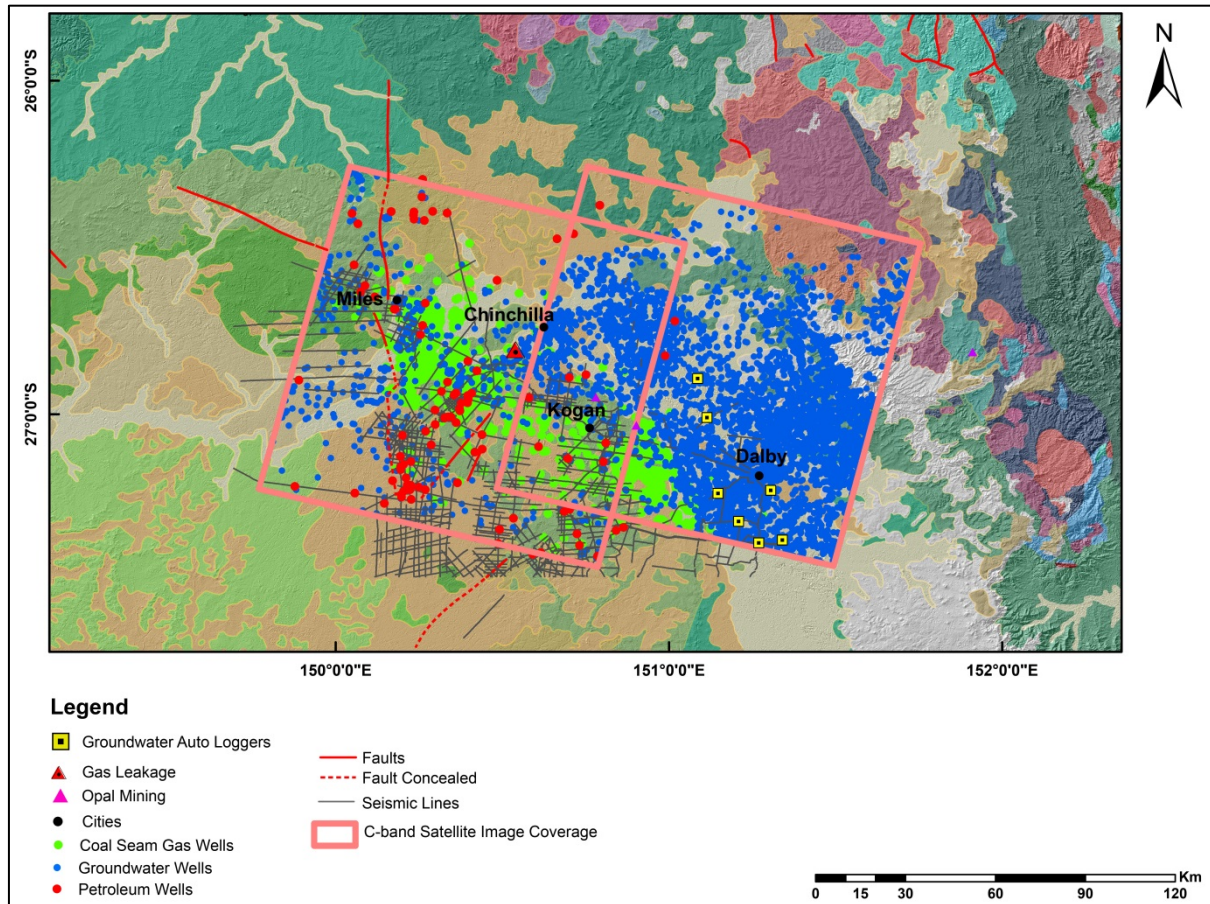


Figure 3-12: Total Magnetic Intensity (TMI) survey conducted in the study area part extracted from the Geoscience Australia database (Geophysical Archive Data Delivery System (GADDs)). The magnetic intensity is higher in the western part of the area compared to the eastern part. The boundary between magnetic high and magnetic low anomalies indicates the magnetic body location or geological boundaries such as faults.

### 3.4.2 Subsurface monitoring boreholes

To establish a static geological model as a representation of the subsurface, consisting of surfaces and layers with assigned reservoir properties, other empirical data acquired from core, wire-line logs, and seismic surveys need to be modelled using statistical approaches. The distribution of petroleum wells in the Surat basin is shown in Figure 3-13.



**Figure 3-13: The distribution of the resource extraction wells, including petroleum, coal seam gas and groundwater, in this part of the Surat Basin. The majority of the petroleum wells (red) are located in the eastern part of the area while coal seam gas extraction wells (green) lie in an elongated area from northwest to southeast. Groundwater extraction wells (blue) are spread over a larger area, but more densely concentrated in the eastern part. For the 2D seismic lines, there is a lack of data in the eastern part with very old seismic surveys, while the western part has a fair distribution of the poor to good quality seismic lines. As already noted there are no 3D seismic surveys in this part of the Surat Basin. Near Kogan, there are also two opal mining districts.**

The majority of these wells were drilled in the western part of this region, with exploration targets down to over 3,000m, but with an average depth of 1,500m. For regional modelling purposes more than 200 conventional and unconventional hydrocarbon (exploration and appraisal) well completion reports and reports for development wells were accessed through the Queensland Government, Department of Natural Resources and Mines website. Based on their location, total depth and the

sequences penetrated, a total of 33 exploration, 19 appraisal, and 330 conventional and unconventional hydrocarbon development wells were chosen and analysed for this study.

The Precipice Sandstone has the most comprehensive petroleum well dataset, with low reliability data commonly distributed in close proximity to data with better reliability. The dataset for the Evergreen Formation is generally quite poor but there is a reasonable amount of reliable data with a basin wide distribution.

Geophysical well-logging methods, ranging from simple electric and radioactive logs to more advanced ones, provide detailed and continuous information through well penetration into the underlying formations. Wire-line logs with both image and digital formats make it possible to interpret the depositional environment, lithological composition and properties of rocks, as well as down-hole bedding and fractures [Bjørlykke, 2015]. Using these down-hole data, the coal rich and coal poor units can be separated in the Walloon Subgroup and its overlying and underlying formations [Esterle et al., 2013].

The wire-line log datasets are available for a number of wells that penetrated to deeper intervals within the study area in the Surat Basin. Properties such as rock density, porosity and compressional/shear velocity can be used for interpretation and assignment of lithofacies to each cell, but determining the spatial heterogeneity of the Walloon Subgroup is difficult using well log correlations. For this reason, the static geological model needs to be simplified into a layer cake model and used for dynamic flow simulation [Esterle et al., 2013]. Consequently, the basic wire-line logs including Density, Gamma Ray, Spontaneous Potential (SP) and Porosity were used in this study.

Within the Surat Basin only a poor spatial coverage of the regional groundwater system is available, but the flow regimes in the deep aquifers can be predicted using data from formation pressure tests with potentiometric head measurements in the petroleum wells. For this study the groundwater database of Queensland government, containing data for 138,534 registered bores, the Geological Survey of Queensland pre-1987 interpretation of water bore data, and the Department of Primary Industries and Resources database were checked. Potentiometric head values for groundwater bores were also collected from the Department of the Environment and Resource Management groundwater database (DERM-GWDB). Throughout the region of interest there are more than 5,000 groundwater observational bores that monitor the rate of water withdrawal from CSG. The rate of withdrawal is about 18,000mL/yr, which is far greater than water extracted during conventional hydrocarbon production [GABCC, 2000]. The number of registered groundwater bores with information about aquifers is 15 for the period 2001-2009. The groundwater movement regime in the GAB aquifers ranges from an average of less than 1m/yr in the centre to 5m/yr close to the recharge zone in the elevated areas. For the aquifers in the GAB the hydraulic conductivity ranges from 0.1m/d to 10m/d, with transmissivity ranging between 1m<sup>2</sup>/d and up to 2,000m<sup>2</sup>/d [Habermehl, 2002]. Additional hydraulic properties of aquifers are listed in Table 3-4.

**Table 3-4: Hydraulic properties of the GAB aquifers**

|                                         |                                                   |
|-----------------------------------------|---------------------------------------------------|
| Storage Coefficients                    | $10^{-4}$ to $10^{-5}$                            |
| Intrinsic permeabilities                | Several tens to several thousands of millidarcies |
| Porosity ( as a fraction of void space) | 10 to 30 %                                        |
| Average vertical hydraulic conductivity | $10^{-1}$ to $10^{-4}$ m/d                        |

Over the study area, well-developed coal seams and associated fracture networks over the Undulla Nose structure are responsible for a high local permeability of 154 mD, while the areas close to the Leichhardt and Moonie regional faults or the shallow depth coal seams are mineral-filled, with low permeability characteristics and averages of 6mD to 43mD, respectively [Scott *et al.*, 2004] .

### 3.4.3 Geodetic Observations (Levelling and GPS Measurements)

Global Positioning System (GPS), as part of Global Navigation Satellite System (GNSS), provides accurate and absolute three-dimensional measurements of surface height which can be used as an absolute and rigid reference frame for other relative geodetic observations, such as interferometric SAR. The coverage of GNSS stations provided by Geoscience Australia is shown in Figure 3-14(a). As illustrated, the Mitchell and Toowoomba GNSS stations are within the Surat Basin, but the only continuous GPS station (CGPS) is located near Dalby (see Figure 3.14-b). As it is shown, there are two pathways to conduct levelling surveys, but one does not include much in the way of satellite data [ICSM, 2014].

The GNSS station in Dalby has been considered operational since 22<sup>nd</sup> of July 2010. Prior to that time (i.e. starting from 17<sup>th</sup> of September 2009) a GNSS antenna and receiver were on the site for testing purposes; however, the reference information in the data stream from this site is less reliable and with larger data gaps. Apart from 30-second data from the National GNSS CORS Campaign website since 17 August 2010 and archived 1-second data for the site from 11 December 2009, there are no data prior to this time. There are also some private GNSS stations in this area, owned and operated by SmartNetAUS and AllDayRTK. As shown in Figure 3-15, Dalby station experiences a seasonal movement in the vertical direction in a range of -20 to 20mm per year. However, for the eastern and northern components there is a gradual downward motion in the modelled residuals based on national AusGeoid model. As illustrated the modelled residuals were calculated after an offset correction using a tectonic plate velocity model for the four CORS stations available in the study area [AUSPOS, 2015].

For precise deformation measurements on a regional scale, having access to a systematic geodetic network and well distributed corner reflectors would be a significant advantage in areas such as the Surat Basin, where no previous regular geodetic observations are available. For this purpose, Geoscience Australia completed the initial phase for the installation of 40 co-located survey markers

and corner reflectors across the Darling Downs region, with a spacing of 10km to 30km in an area of 150 by 150 square kilometers [Garthwaite et al., 2015].

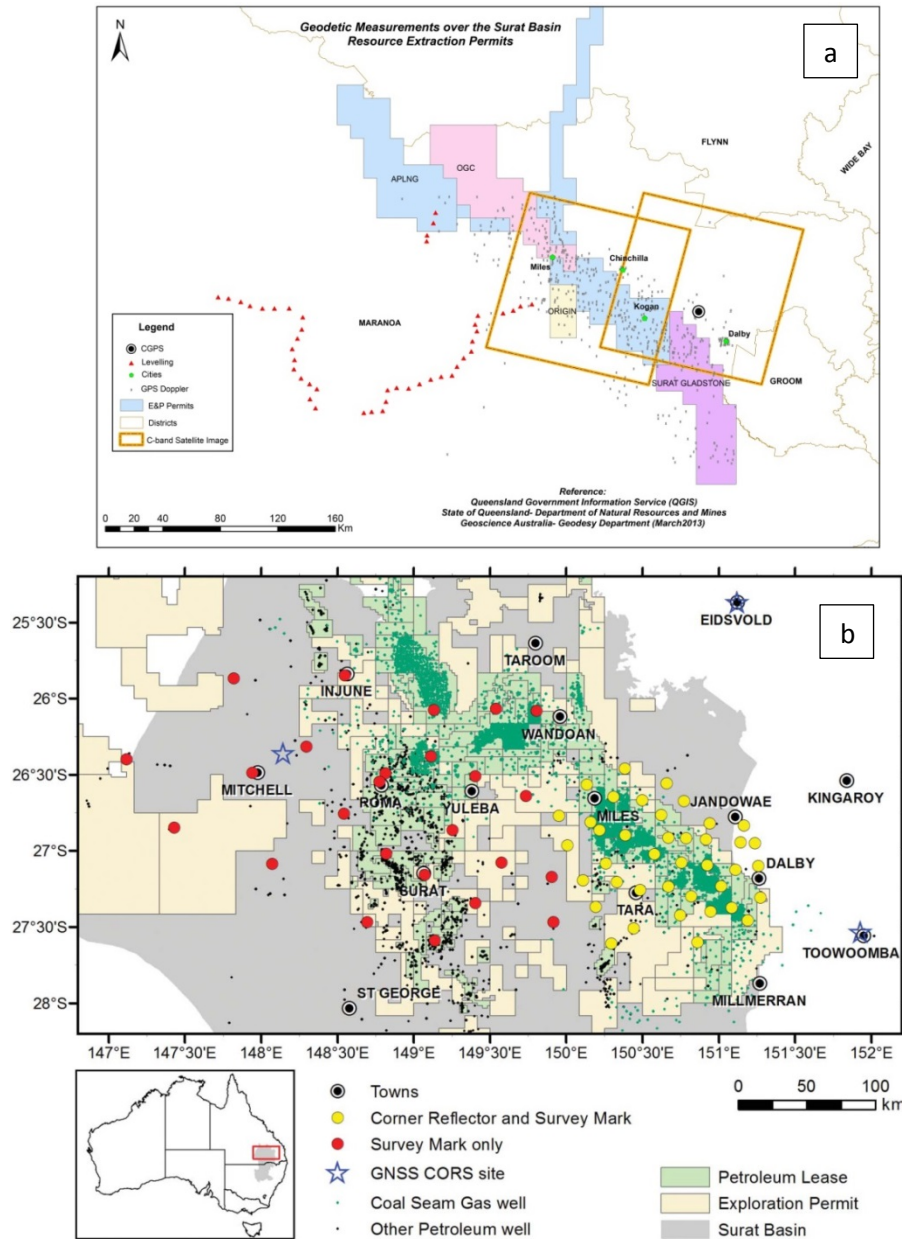


Figure 3-14: (a) Distribution of the geodetic measurements, including levelling, Doppler GPS, and continuous GPS (CGPS) over the study area of the Surat Basin that is being extracted for different resources by various companies in their specific exploration and excavation permits. (b) Distribution of 65 new geodetic sites in the Surat Basin (background grey shade) including 40 co-located survey marks and corner reflectors as yellow dots after [Garthwaite et al., 2015].

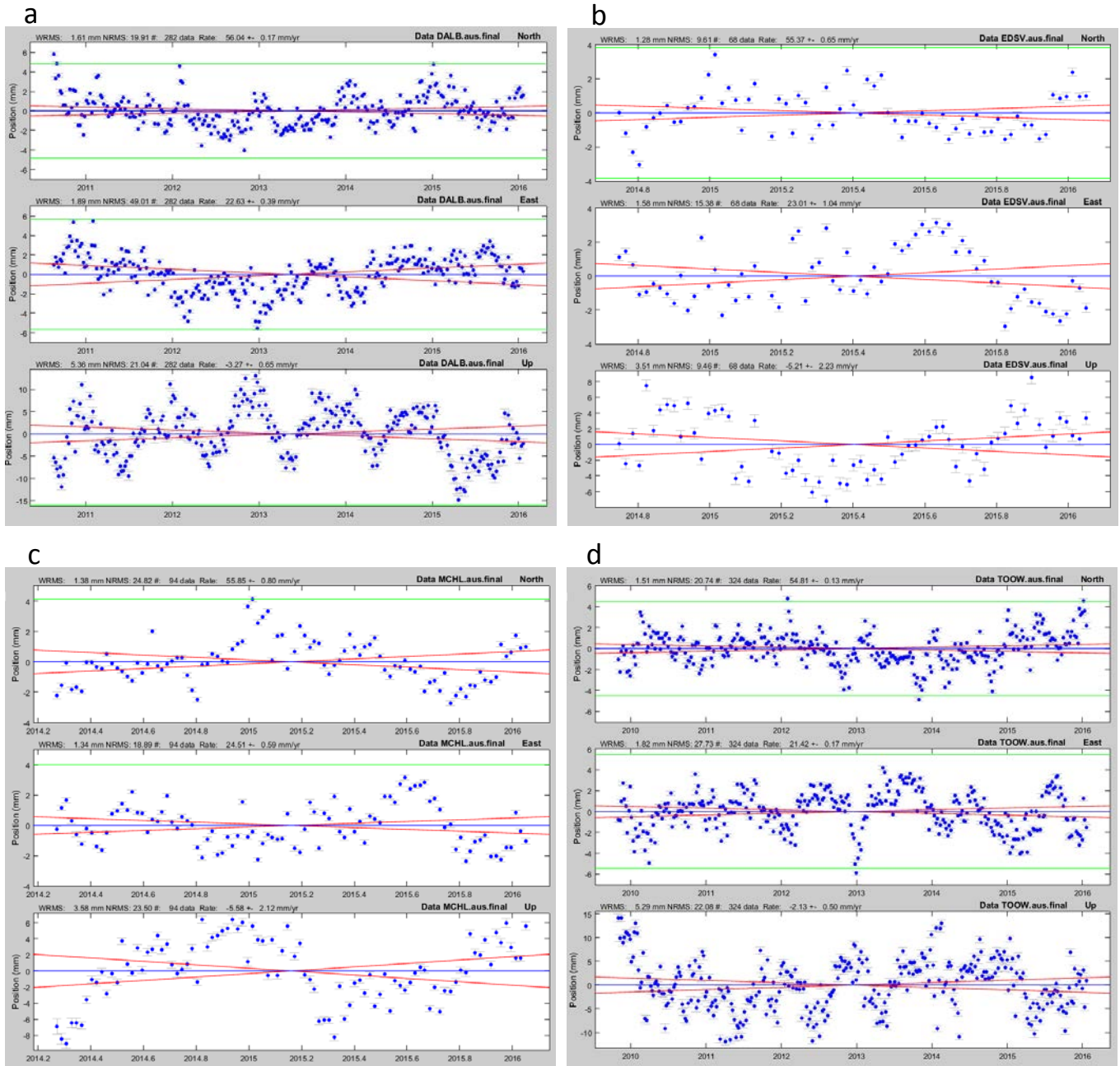
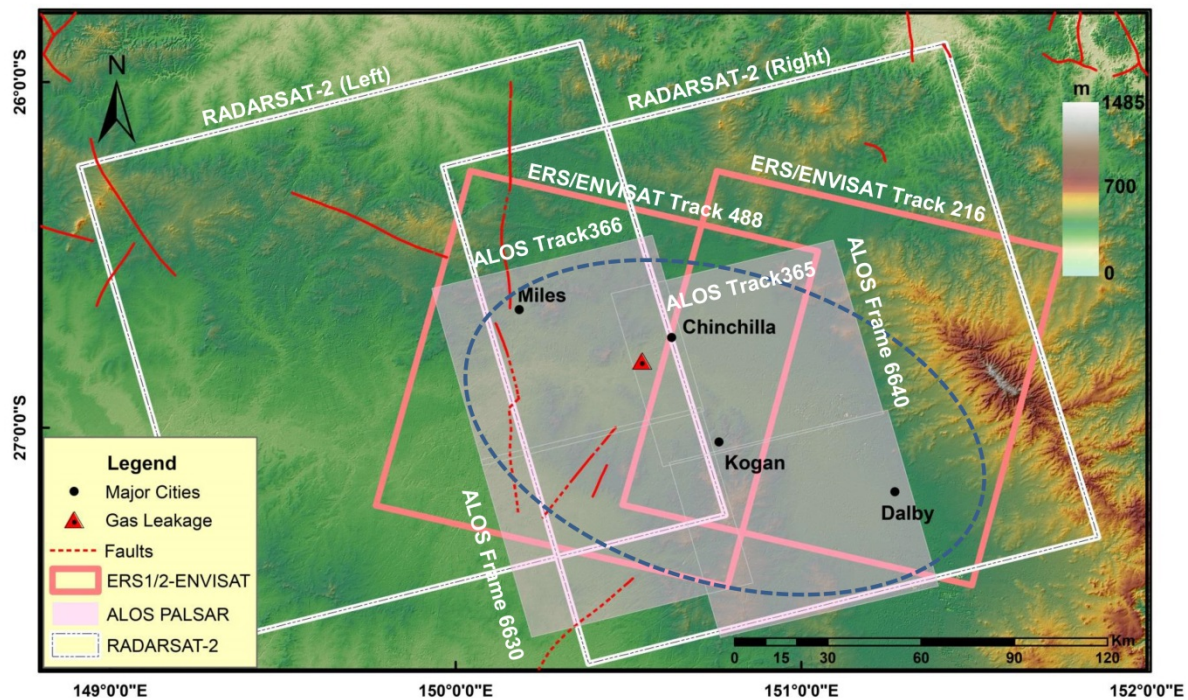


Figure 3-15: Time series analysis of ground surface movement at (a) Dalby, (b) Eidsvold, (c) Mitchell (d) Toowoomba CGPS station between 2010 and 2016. The green lines show 3 times of the weighted RMS values and the red lines indicate uncertainty of velocity estimates in each epoch that the calculation was performed [Geodesy Section, Geoscience Australia, 2016]

### 3.4.4 Satellite Imagery (ERS1-2, ENVISAT, ALOS-PALSAR and RADARSAT-2)

The Area of Interest (AOI) for the current research is located in the northeastern part of the Surat Basin from Miles to Dalby, and was chosen on the basis of reports on gas leakage observed by in situ measurements [DNRM, 2012]. To detect any potential deformation signals in this area, all available and archived SAR images (150 in total) from four different types of imaging satellites were collected and processed:



**Figure 3-16 :** Location map of the study area between Miles and Dalby in the Surat Basin showing C-band (ERS1/2, ENVISAT, RADARSAT-2) and L-band (ALOS-PALSAR) satellite footprints in image mode over the 90 m SRTM Digital Elevation Model. Two scenes of ERS/ENVISAT (pink squares), four scenes of ALOS-PALSAR (grey squares), and two scenes of RADARSAT-2 (white squares) cover the region of interest (blue circle) for the space-borne observation period (1992-2014).

#### **Dataset 1:** European Space Agency ERS-1/2 satellite images

The SAR sensor was operational on board the European ERS-1/2 satellites. It consisted of a C-band system with a wavelength of 5.6cm (i.e. frequency ~5.3GHz) and a revisit time of 35 days. A total of 12 images over two tracks are available for the AOI between 1992 and 1999. These images are all in descending orbit with a mid-swath 23-degree incidence angle.

#### **Dataset 2:** European Space Agency ENVISAT satellite images

The ASAR sensor image mode was operated on board the European ENVISAT satellite from 2002 to 2011. It consisted of a C-band system with a wavelength of about 5.6cm (i.e. frequency ~5.3GHz) and

a revisit time of 35 days. A total of 11 images are available for the AOI between 2003 and 2006. These images are all in descending orbit with a mid-swath 23-degree incidence angle.

**Dataset 3:** Japan Aerospace Exploration Agency ALOS-PALSAR satellite images

The PALSAR sensor is operating on board the Japanese ALOS (DAICHI) satellite. It is an L-band system with a wavelength of about 23.6cm (i.e. frequency ~1.3GHz) and a revisit time of 46 days. A total of 84 images are available for the AOI between 2006 and 2011. These images are all in ascending orbit with a mid-swath 39-degree incidence angle.

**Dataset 4:** Canadian Space Agency RADARSAT-2 satellite images

The RADARSAT-2 is a Canadian sensor operating in C-band with a wavelength of about 5.5cm (i.e. frequency ~5.3GHz) and a revisit time cycle of 24 days. There are 43 RADARSAT-2 images available for the AOI between 2012 and 2014. These images are all in ascending orbit with a 20-50 degree incidence angle.

Among these datasets the ALOS-PALSAR, with a longer wavelength (23.6cm against 5.3cm), is more accurate than either of the European satellites and less susceptible to vegetation interferences because of its frequency, as L-band is less affected by vegetation biomass and water content than higher frequencies. Consequently, only ALOS data were used to quantify the surface deformation field associated with this part of the Surat Basin. For this purpose, the SBAS methodology [[Berardino et al., 2002](#)] was used to analyze the temporal evolution of surface displacements by inverting a sequence of interferograms to form a deformation time series.

In order to remove the topographic phase noise component in the interferometric processing chain, the Shuttle Radar Topography Mission (SRTM) detailed DEM with 90m spatial resolution and ASTER DEM with 30m resolution were used as ancillary dataset for the data processing. Accessing a very limited amount of multi-temporal SAR data, especially before 2006, was one of the reasons for getting faint surface deformation signals using C-band satellite images (ERS-1/2 and ENVISAT). Due to the scarcity in high precision and multi-look observations, it was not possible to apply more sophisticated data processing techniques, such as MSBAS, to extract horizontal and vertical components of surface deformation.

### 3.5 Chapter Summary

This chapter provides an overview of surface and subsurface geology in the Surat Basin along with available in situ geophysical, petrophysical, and geodetic measurements. From a subsurface perspective, the Surat Basin includes a multi-layer system comprising recognised aquifers within sandstone formations separated with low permeable aquitards. The degree of anisotropy in the complex stratigraphy of this basin is not properly known and the data for the subsurface physical properties and structure are very limited. According to the stratigraphic section, the deeper Walloon Subgroup has significant potential for CSG reserves and is the target for unconventional gas

developments, while the shallower Gubberamunda and Springbok sandstones are already being exploited extensively for their groundwater supplies, meaning that it is important to obtain more detailed information on the actual subsurface conditions.

Although the structure of the Surat Basin is relatively simple there are some regional faults with up to tens of meters displacement propagating into the shallower and younger formations. There are different and controversial viewpoints regarding the role of these faults as hydraulic barriers to lateral groundwater flow.

From a hydrological perspective, the major surface water system in the Surat Basin is the Central Condamine Alluvium encompassing the Condamine River and its tributaries that originate from the mountainous eastern margin of the basin. Thus, as part of Condamine Catchment, the Surat Basin contains highly fertile soils for urban and agriculture developments. The sub-tropical climate of the basin, with recent impacts of climate change, as well as intensive groundwater extraction after the 1960s and poor recovery of the surface water system have caused aquifer storage depletion and imbalance in the reservoir.

According to the above field information and reported gas leakages in the proximity of Chinchilla, different satellite SAR observations with a range of microwave wavelengths were collected for long-term ground deformation monitoring and identifying the areas with high risk of failure. Consequently, Chapter 4 will provide an in-depth description of the interferometric SAR processing results in this region. This is followed by an interpretation of the deformation signals and an evaluation of their causes.

## 4 Advanced Interferometric SAR Processing

In this chapter, the outcomes of advanced *Differential* Interferometric SAR (DInSAR) processing to detect and analyze ground surface behaviour due to man-made interactions are presented. An improvement was achieved in the temporal resolution and accuracy by using a unique combination of both C-band and L-band SAR satellite acquisitions with different temporal and spatial baselines. The two alternate DInSAR methodologies were applied on the north-eastern part of the Surat Basin in which there is no long-term ground-based geodetic observations for surface deformation. The work in this chapter has been published [[Fouladi Moghaddam et al., 2015](#)].

### 4.1 Background

Coal Bed Methane (CBM) is the methane gas captured and released from coal seams around the world, with the highest production in China and the United States, followed by Russia, Australia, Ukraine and India. This underground resource has drawn attention for being both a greenhouse gas (GHG) and an environmentally friendly fuel compare to a conventional gas resources [[Karacan et al., 2011](#)]. Over the past decade, the CBM industry in Australia has experienced substantial growth by commercial production of coal seams in a vast extent of the Surat and Bowen Basins in southern Queensland. These basins contain 95 percent of the known Australian reserves. The targeted shallow (i.e. 200-600m below surface), low-rank coal layers with high permeability have justified low-cost and viable extraction of CBM over the past years, to meet growing domestic and international demands for energy supply [[Hamilton et al., 2012](#); [Papendick et al., 2011](#)].

Underground coal seams extending through impermeable geological layers hold natural gas, mostly dominated by biogenic methane. Under natural conditions this gas, which is attached to the coal layers and held in place by hydrostatic pressure of the water in the coal beds, can be extracted simultaneously by removing some of the formation water and drawing the reservoir pressure down to a level that allows the gas to desorb. In other words, CBM production does not dewater the aquifers but only extracts 200 GL/year estimated peak of saline water from the coal formations, to depressurize the coal seams [[DNRM, 2012](#)]. Approximately 35-40m drop in the water level above the gas producing coal seams will result in the essential rate of depressurization for gas production. The volume of produced water, which is relatively high compared to the volume of gas in the early stages of production, is subsequently reinjected into an underground formation or is discharged to the surface [[CSIRO, 2012](#); [Veil et al., 2004](#)]. The rate of water withdrawal from coal layers is about 18,000 ML/year, which is far greater than that during conventional hydrocarbon production [[APLNG, 2010](#)]. Consequently hydrogeological assessment has indicated that long-term CSG mining and accompanied

groundwater extraction put a number of fresh water storages under progressive depletion and head decline [Tan et al., 2010]. Potential changes in pressure and stress conditions within the subsurface and surrounding geology, induced by these anthropogenic activities, can be projected onto the surface as deformation after considerable compaction or expansion of the subsurface reservoir [Dzurisin, 2007; Galloway et al., 1998].

Ground surface deformation resulting from oil and gas production and geothermal activities [Bürgmann et al., 2000; Fielding et al., 1998], groundwater extraction [Chaussard et al., 2014; Massonnet and Feigl, 1998] and mining developments [Deguchi et al., 2007; Samsonov et al., 2013] can be used to better identify the geomechanical and geological properties of a reservoir, and to mitigate the operation risk throughout the CO<sub>2</sub> storage procedure [Vasco et al., 2010]. Consequently, a number of monitoring techniques to measure surface (tilt meter, levelling, GPS, InSAR) and subsurface (extensometer, 4D seismic surveys) changes have emerged to detect the extent of the deformation and to quantify the rate of the deformation over extraction or injection sites. Some of these techniques have limited and sparse data sampling (i.e. seismic lines or boreholes) while others fail to map geological properties directly [Brown et al., 2014]. However, among the various geodetic measurement tools, InSAR (a remote sensing tool) can not only be used to constrain the geophysical parameters of the reservoir [Sambridge, 1999], but its cost-effective and high temporal resolution data acquisition can also complement other traditional measurements such as GPS [Zhu et al., 2014] and subsurface images captured by seismic surveys [Ramirez and Foxall, 2014]. Moreover, compared to geophysical surveys, InSAR observations have demonstrated the potential for mapping the underlying subsurface structure by detecting long-term deformation patterns on the surface due to changes in subsurface volume and pressure [Anderssohn et al., 2009; Vasco et al., 2010]. These studies suggest that the deformation patterns might also be an indication for the subsurface structural properties which are usually captured for the rock mass by geophysical measurements [Amelung et al., 1999; Hatherly, 2013].

Measuring ground displacement using satellite SAR interferometry and its integration with GPS survey data have been performed in Australia for underground mining operations [Featherstone et al., 2012; Ng et al., 2012; Zahiri, 2012] and for earthquake risk assessment [Dawson et al., 2008]. But for the Surat Basin, the CSG authorities initiated a ground motion baseline program. Their objective was to report any high motion with reference to natural or anthropogenic characteristics [QGC, 2013b]. From their analysis, advanced InSAR technology – PSI with about 600 permanent scatterers per km<sup>2</sup> - did not show any large scale pattern of ground motion between 2006 and 2011, thus reporting to be in the stable condition with less than 8 mm ground deformation per year [Dura et al., 2012]. For the same area, Geoscience Australia conducted an independent study to describe the capabilities and limitations of an analytical model to predict surface deformations caused by fluid volume changes. Based on their analysis, maximum potential for surface deformation was predicted to be less than 0.2 m. assuming that the regional drawdown is around 300m. InSAR observations were suggested to be

examined as a valuable tool to constrain the parameter space, and to develop a surface deformation prediction [Brown *et al.*, 2014].

Taking into account the previous studies, this research presents an interferometric analysis across the same region within the Surat Basin (Figure 4-1), for which surface deformation of an area between Miles and Dalby was reported through in situ observations [DNRM, 2012]. These field surveys, which contradict previous InSAR results, were considered as the starting point for verifying results using this new multi-temporal and high resolution SAR analysis from C-band (ERS-1/2, ENVISAT and RADARSAT-2) and L-band (ALOS-PALSAR) microwave sensors, together with an alternative processing approach.

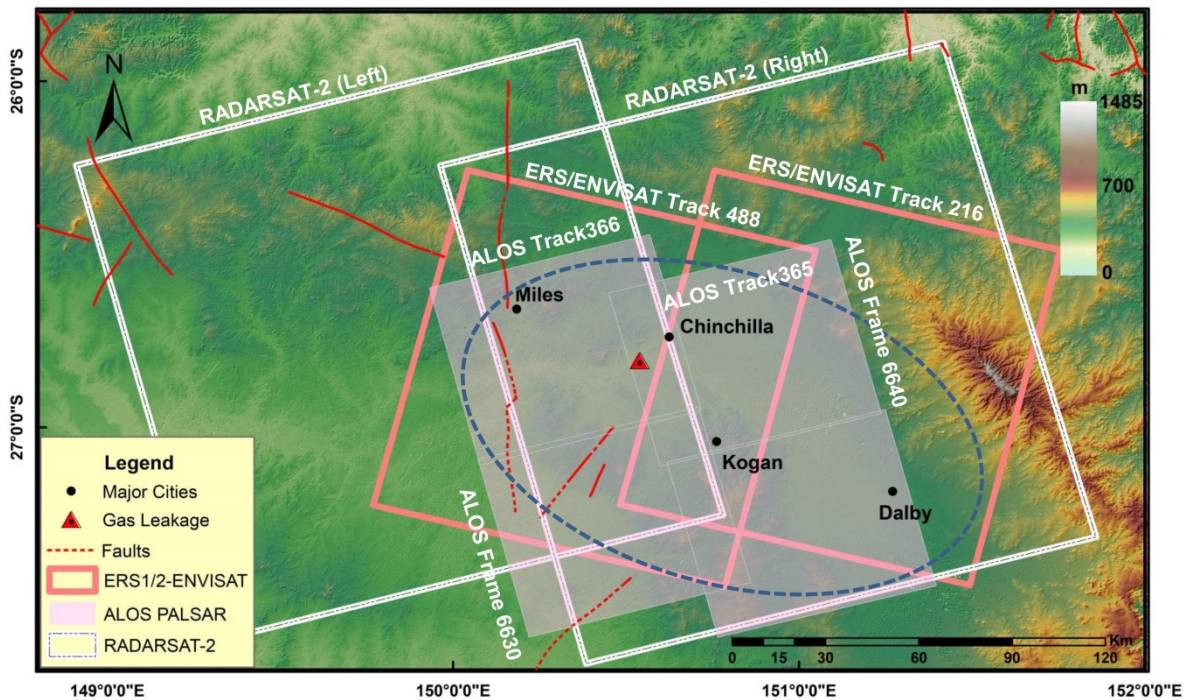


**Figure 4-1: Location map of the study area in the Surat Basin showing C-band (ERS/ENVISAT, RADARSAT-2) and L-band (ALOS-PALSAR) satellite footprints in image mode over the 90 m SRTM Digital Elevation Model. Four scenes of ALOS-PALSAR (grey squares) and two scenes of RADARSAT-2 (white squares), both in ascending paths, cover the region of interest for 2006-2011 and 2012-2014 respectively. ENVISAT coverage in two scenes is in descending paths. The fault traces are shown in red and the triangle marks the location of reported gas leakage.**

## 4.2 Methodology

By reviewing the characteristics and requirements of the interferometric processing techniques and the satellite observations in Chapter 2, two methods will be used in this study for four different satellite acquisitions in both C-band and L-band microwave wavelengths. Details of each processing technique are described in the following sections.

### 4.2.1 Interferometric Analysis

As previously mentioned in literature review, SAR is a technology that measures the return of an actively emitted microwave signal from a target. Due to the nature of microwave energy as an illuminating source in radar sensors, this technology does not rely on solar irradiation, making it more versatile than traditional passive sensor technologies. More importantly, it suffers only limited disturbance from atmospheric conditions, meaning that it has an all-weather observing capability. Imaging radar sensors emit signals in a specific portion of the chosen electromagnetic spectrum, which is generally based on their operational purpose. The near-polar orbit of these satellites, in combination with the Earth's east-west rotation, theoretically allows observing the same area with different incidence angles from opposite look directions provided by ascending and descending modes. Combining these observations not only mitigates the problems arising due to acquisition geometry and uneven sampling on hilly terrain areas, but can also distinguish between vertical and east-west motions [Ferretti et al., 2007; Simons and Rosen, 2007].

The main principle in SAR interferometry is to compare the phase of two or more radar images which are typically acquired from the same flight track but at different times. This technique, which is known as *Differential InSAR*, is used to determine displacements of the Earth's surface at wavelength scale. SAR satellites observe the ground in a non-vertical LOS direction. In zero-baseline condition, the phase information would only be related to the LOS displacement while in reality a certain baseline is always present making the interferogram sensitive to the topography. By using an external DEM, the topographic phase contribution will be subtracted from the interferogram, leading to a Differential SAR interferogram that can be used to detect subtle changes (e.g. deformation) in the range distance between two acquisitions [Goldstein, 1995; Zebker et al., 1997].

### 4.2.2 Stacking Method for Interferometric Analysis

In order to calculate the ground deformation phase captured by SAR technology, other phase components including orbital ramps, atmospheric artefacts, topographic residuals and thermal noises should be removed or mitigated. Considering the fact that differential interferograms have been successfully unwrapped, orbital ramps corrected, and regions with coherence below the threshold are set to zero, each  $k$  interferogram  $\phi_{obs}^k$  is the sum of deformation  $\phi_{def}^k$  residual topographic  $\phi_{topo}^k$ , and atmospheric  $\phi_{atm}^k$  components:

$$\phi_{obs}^k = \phi_{def}^k + \phi_{topo}^k + \phi_{atm}^k , \quad (4.1)$$

The goal is therefore to estimate and remove the residual topographic  $\phi_{topo}^k$  and atmospheric  $\phi_{atm}^k$  components in order to achieve the best possible accuracy in the calculation of the ground deformation  $\phi_{def}^k$ . For simplification of the atmospheric noise contribution, it is assumed that  $\phi_{atm}^k$  contains all other random noise sources such as atmospheric temperature and water vapor [Tarayre and Massonnet, 1996].

For processing SAR images with the DInSAR technique, a simulated phase of elevation model is used to remove the main topographic phase contribution, but the outcome is still prone to temporal and spatial decorrelation which impacts on the number of useful differential pairs and imposes a phase unwrapping deficiency in rough areas or for complicated ground movements [Gabriel et al., 1989; Zebker and Villasenor, 1992]. It is also possible that particular patterns of subsidence make it difficult to separate between deformation signals and atmospheric artefacts, and this has led to the development of a technique called stacking which is based on a set of interferograms covering the same area within a given time period, reducing the ratio between atmospheric effects and deformation signals [Petrat and Wegmuller, 2003; Sandwell and Price, 1998]. When stacking interferograms, the weighted average of all the deformation velocities within the single interferogram is used to estimate the mean deformation rate for each pixel. These weights are selected based on the corresponding time spans [Sansosti et al., 2010].

As long as the images are sufficiently separated in time, the phase noise in a stacked interferogram will be a factor of  $\sqrt{K}$ , where  $K$  is the number of independent interferograms without common images and the noise will reduce to approximately  $1/\sqrt{K}$ . In this case, the averaged interferogram is less noisy than any of the original interferograms but with reduced amplitude. Stacking is the best processing solution when scarcity in the number of satellite observations prevents the application of advanced techniques, similar to the situation in the Surat Basin for ESA's archived C-band satellite observations [Fouladi Moghaddam et al., 2013]. It is also an acceptable approach if the noise is random and normally distributed. When stacking fails to be an effective technique because the noise in the interferograms is not normally distributed, more advanced processing techniques are required [Williams et al., 1998; Zebker et al., 1997].

### 4.2.3 Small Baseline Subset (SBAS) for Interferometric Analysis

Conversely to stacking, Small Baseline Subset (SBAS) [Berardino et al., 2002; Casu et al., 2008] as an evolution of DInSAR technique uses a cluster of SAR acquisitions. SBAS was developed to create time series of deformation with reduced atmospheric, orbital and thermal signals by increasing the number of ground points, and by reducing the baseline length for each of the data pairs [Hooper et al., 2012; Samsonov et al., 2011]. After ensuring that the image-network has no isolated image cluster (fewer than 5 images) the interferograms are formed. The critical step in this algorithm is the

identification of potentially coherent points using image pairs with estimated correlation above a threshold values (based on the expected rate of de-correlation and data availability for a given region). Moreover, it improves the coherence by producing a large number of small baseline multi-reference interferograms using a Single Value Decomposition (SVD) algorithm by building an optimal set of interferograms having the smallest temporal and baseline decorrelation, and by using several master images [Berardino *et al.*, 2002] .

This technique makes it possible to perform time series analysis and to extract the linear deformation rates from a set of co-registered, unwrapped differential interferograms using a linear least squares inversion. The flowchart in Figure 4-2 presents the processing stages which were completed in this study for C-band and L-band satellite observations with high acquisition frequency over the proposed area. Calculating deformation rates, re-construction of cumulative displacements (time series), and estimating mean and linear deformation rates are the tasks performed by this methodology [Samsonov *et al.*, 2011].

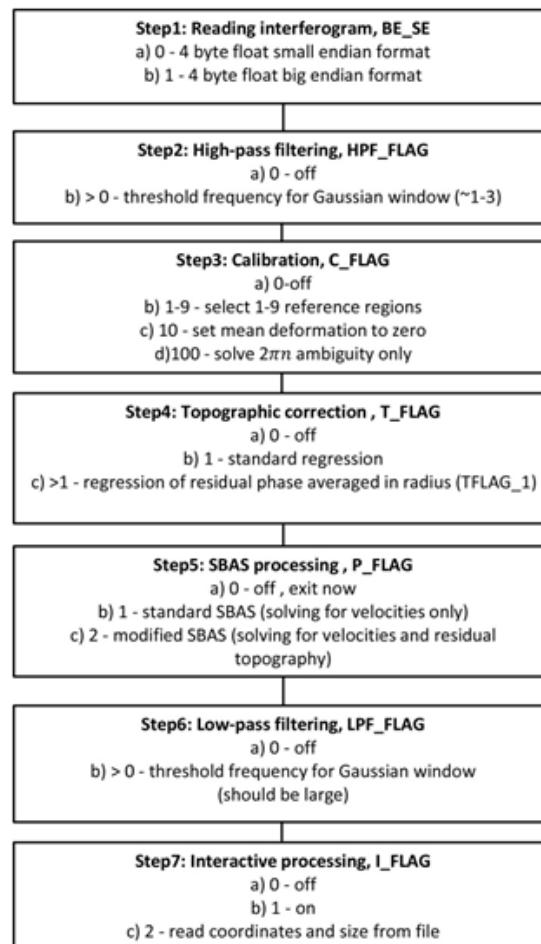


**Figure 4-2: Flow chart diagram of the code used for time series calculation and mean or linear deformation rate estimation in both ALOS-PALSAR and RADARSAT-2 satellite observations. Flags (\_FLAG) specified in a header file are used for controlling processing flow after [Samsonov *et al.*, 2011].**

### 4.3 Data Processing

Assuming that there is no prior information about the exact location of deformation in this part of the Surat Basin, an initial monitoring of the area with large spatial satellite datasets was undertaken to identify potential areas of subsidence or uplift due to underground resource extraction. Performing a standard DInSAR processing for ENVISAT ASAR image mode in four descending tracks and an average revisit frequency of 35 days revealed that two scenes covering the area between Miles and Dalby have captured what appears to be surface deformation, due to consistency in the signal’s phase delay during the time of observation [Fouladi Moghaddam et al., 2013]. Accordingly, the focus of further analysis was on the processing of more high resolution satellite imagery covering the same area with a higher temporal and spatial resolution.

To screen the long-term behaviour of the ground surface and to estimate the rate of deformation in the focal area of the Surat Basin, a standard DInSAR processing including orbit correction, phase unwrapping and geocoding for both C- and L-band SAR images (Table 4-1) with temporal and spatial baseline smaller than the predefined threshold values was performed. This was followed by the stacking technique for interferograms with high coherency and low unwrapping errors, to remove residual orbital ramps and long wave-length atmospheric noise.

**Table 4-1: SAR data used for DInSAR processing in this work: time span (in YYYYMMDD format), azimuth  $\theta$  and incidence angles  $\phi$ , number of available SAR images  $N$  and number of calculated interferograms  $M$ .**

| <i>InSAR Set</i>                         | <i>Time Span</i>  | <i>Resolution (m)</i> | $\theta(^{\circ})$ | $\phi(^{\circ})$ | $N$ | $M$ |
|------------------------------------------|-------------------|-----------------------|--------------------|------------------|-----|-----|
| <i>ERS1, Track 216 (dsc)</i>             | 19920725-19930116 | 7.9 - 4               | -164.45            | 23               | 3   | 3   |
| <i>ERS2, Track 216 (dsc)</i>             | 19951121-19951226 | 7.9 - 4               | -164.45            | 23               | 2   | 1   |
| <i>ERS1, Track 488 (dsc)</i>             | 19920604-19950826 | 7.9 - 4               | -164.45            | 23               | 5   | 5   |
| <i>ERS2, Track 488 (dsc)</i>             | 19960114-19991025 | 7.9 - 4               | -164.45            | 23               | 2   | 1   |
| <i>ENVISAT, Track 216 (dsc)</i>          | 20031209-20051108 | 7.8 - 4               | -164.50            | 23               | 6   | 5   |
| <i>ENVISAT, Track 488 (dsc)</i>          | 20040725-20060101 | 7.8 - 4               | -164.50            | 23               | 5   | 4   |
| <i>ALOS, Track 365, Frame 6630 (asc)</i> | 20070103-20110301 | 4.7 - 3               | -14.66             | 39               | 20  | 37  |
| <i>ALOS, Track 365, Frame 6640 (asc)</i> | 20070103-20110301 | 4.7 - 3               | -14.58             | 39               | 20  | 38  |
| <i>ALOS, Track 366, Frame 6630 (asc)</i> | 20061205-20110131 | 4.7 - 3               | -14.66             | 39               | 22  | 60  |
| <i>ALOS, Track 366, Frame 6640 (asc)</i> | 20061205-20110131 | 4.7 - 3               | -14.58             | 39               | 22  | 61  |
| <i>RADARSAT-2, Right (asc)</i>           | 20120703-20140530 | 12.5 - 12.5           | 345.44             | 35.6             | 22  | 75  |
| <i>RADARSAT-2, Left (asc)</i>            | 20120720-20140429 | 12.5 - 12.5           | 345.44             | 35.6             | 21  | 134 |
| <i>Total</i>                             |                   |                       |                    |                  | 150 | 424 |

In the case of ERS-1/2 (1992-1999), the scarcity of data coverage and the low number of interferograms prevented coherent results being achieved by using stacking, though the stacking stage was slightly successful for the ENVISAT (2003-2006) as shown in Figure 4-3. ENVISAT coverage in two descending tracks (i.e. track 488 and track 216) showed hazy displacement signals around Tara, Chinchilla, and Kogan. Consequently, checking the Japan Aerospace Exploration Agency (JAXA) archive for ALOS-PALSAR indicated that four L-band scenes (T365-F6630, T365-F6640, T366-F6630 and T366-F6640) with approximately 20 images per scene cover the focus areas (Figure 4.1)

between 2006 and 2011. Applying the stacking algorithm over this dataset and at the same time having a sufficient number of interferograms ultimately provided a better cumulative phase delay response with less noise contribution. Stacking results for each scene suggested that among the four ALOS-PALSAR scenes, both T365-F6630 and T366-F6640 have significant deformation signal patterns after 2007 (see Figure 4-4(a) and Figure 4-4(d)).

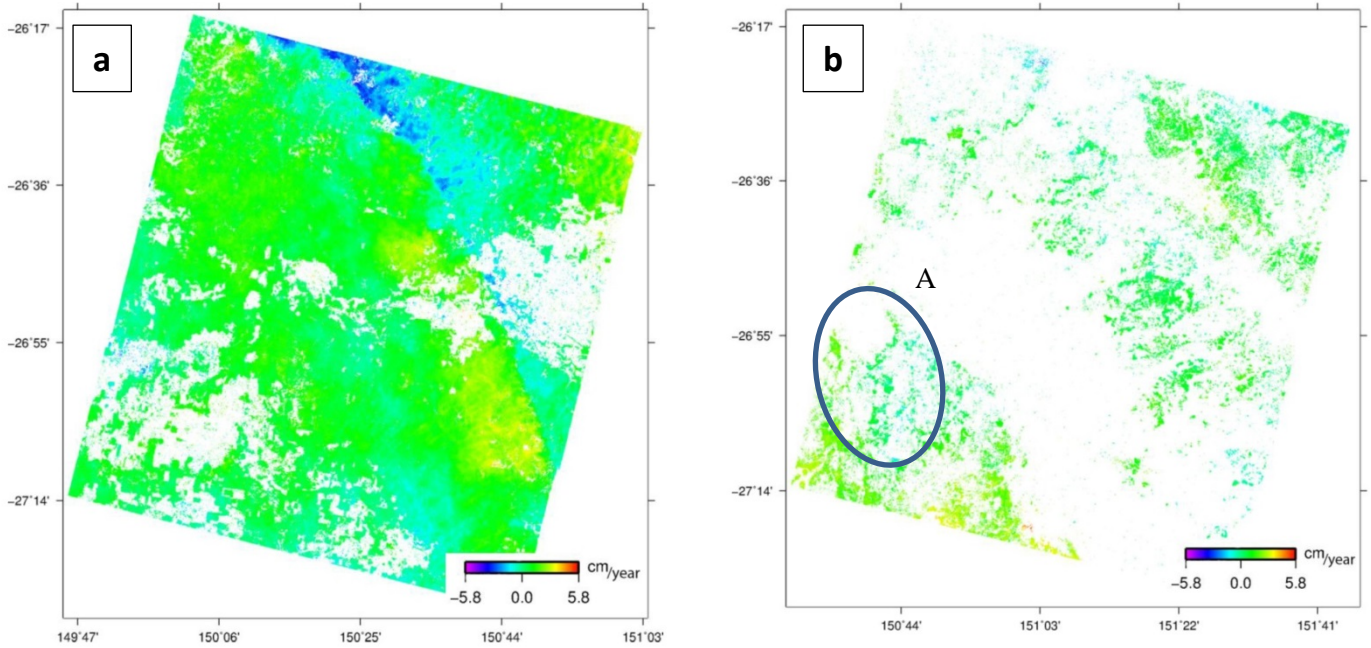


**Figure 4-3: The mean deformation rate in ENVISAT both descending tracks a) T488-F4149 and b) T216-F4149) derived from stacking method in centimetre per year scale. Highlighted location A is the area with likely deformation signals.**

Based on the initial processing results using stacking and predetermined deformation signals in the region, the SBAS code [Samsonov et al., 2011], which functions as an advanced InSAR processing technique to solve for deformation rate and the residual topographic noise simultaneously, was applied for both ALOS-PALSAR archived images and RADARSAT-2 new acquisitions (Table 4-1). The analysis of ALOS-PALSAR observations is from 05 December 2006 through 01 March 2011 and includes different acquisition time frequencies for single (FBS) and for dual beam (FBD) modes. In order to apply the SBAS approach, a parameter file consisting of all interferograms with high coherence, i.e. more than 0.3 was required. The most coherent interferograms for this purpose were selected through calculating the mean coherence of each interferogram. By using such an approach, the linear rate of deformation for both scenes (Figure 4-5(a) and Figure 4-6(a)) and its corresponding error were generated.

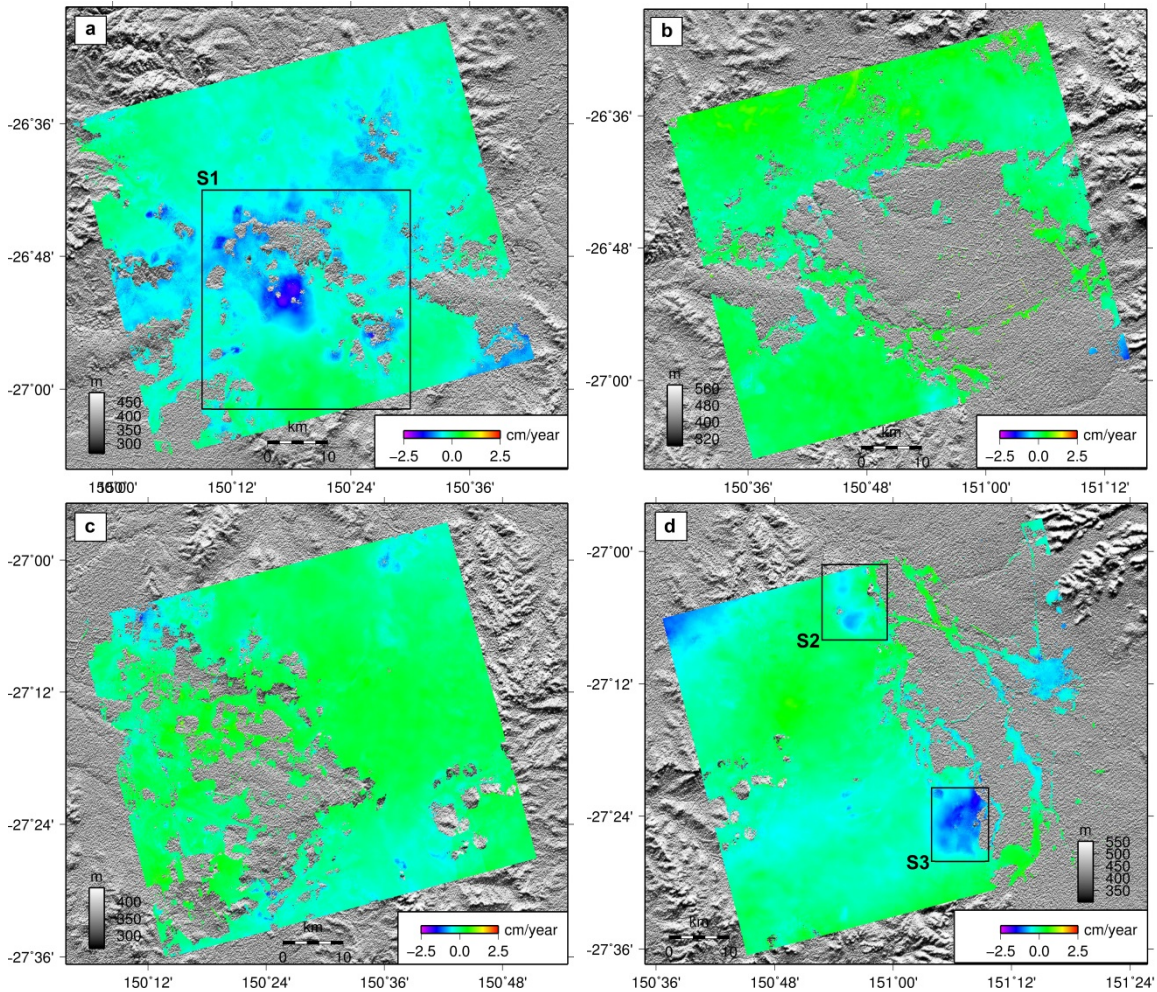


**Figure 4-4: Line of Sight deformation rates (in cm/year) from stacking of ALOS-PALSAR ascending scenes: a) T366-F6640; b) T365-F6640; c) T366-F6630; d) T365-F6630 between 2006 and 2011. Based on the processing results, among four ALOS scenes, significant phase delay responses were detected in a and d, but the other two scenes show no signal of ground movement. Locations S1, S2, and S3 are candidate sites with downward motion, closely aligned to the areas with CSG mining.**

In order to estimate the accuracy of the deformation measurement, LOS linear deformation rates resulting from SBAS for each of the two datasets (assuming here T366-F6640 and T365-F6630 as one set each) were plotted for four different reference points. These points were selected in regions with good coherence (Figure 4-5(a) and Figure 4-6(a); R in green areas on the maps). To test the hypothesis of these points being suitable reference points, the frequency distribution (histogram) of each relative linear deformation rate was plotted and its statistics estimated (i.e. mean, mode and standard deviation) on a cm/year scale. Based on the estimated mode (i.e. the most frequent value of deformation rate in cm/year or stable areas), the values corresponding to the motion greater than the mode of the distribution were selected and the remaining values removed. To produce a Gaussian distribution, the mirrored values of those for which standard deviation ( $\sigma$ ) was estimated ( $\sigma = 0.34$  cm/year for T366-F6640 and  $\sigma = 0.21$  cm/year for T365-F6630) were then added. In this case, the absolute values corresponding to the motion greater than  $2\sigma$  cm/year represent true ground deformation with probability 95 percent were estimated [Casu *et al.*, 2006; Samsonov *et al.*, 2014].

Practically, for T366-F6640 (see [Figure 4-5\(b\)](#)), it could be claimed that true subsidence in LOS was less than -0.68 cm/year while for T365-F6630 ([Figure 4-6\(b\)](#)), it could be claimed that deformation values change between  $\pm 0.42$  cm/year.

Initial time series reconstruction of the linear deformation rates for both scenes has shown seasonal patterns (i.e. grey lines for  $UP_x$  ( $x=1, 2, 3$ )) in both [Figure 4-5\(e\)](#) and [Figure 4-6\(e\)](#) which should be mitigated to extract important statistical properties of a time series including its direction (trend) and its turning. Seasonal pattern can conceal these features by making period-to-period movements in the data [[Statistics-Canada, 2009](#)]. For this purpose, and to extract smoothed cumulative displacements, Gaussian filtering as a separable and low-pass filter was implemented to adjust each observation epoch in the temporal domain. To remove the high frequency component, the shape of the filter was defined as a function of standard deviation in seconds. Smoothing with good localization then resulted from using a Gaussian filter with  $3\sigma$  window size in each direction making it possible to interpret the ground surface deformation signals and to extract the trend in the selected points (i.e. colorful lines for both [Figure 4-5\(e\)](#) and [Figure 4-6\(e\)](#)).

Time series analysis of T366-F6640 ([Figure 4-5\(e\)](#)) demonstrates that in S1 region, both P1 and P2 experienced downward motion since 2007 while P3 showed an uplift behaviour. Moreover, the rate of deformation in P1 was slightly larger than that in P2. Both P1 and P2 are located over a CSG mining area called Berwyndale South, close to Condamine while P3, which appeared with an upheaval signal, is in the vicinity of an industrial timber forest. The reason for the upward motion is not injection in this part of region S1, but the shallow depth formations with elasto-plastic properties. The situation brings that P3 went up in order to respond to the adjacent gradual downward motion in areas with subsidence signals.

For T365-F6630 ([Figure 4-6\(e\)](#)), all selected locations in S2 and S3 regions, which are CSG mining districts, display a downward motion since 2007. But their temporal patterns are not similar; while P1 and P2 shift downward gradually with higher rate for P1, P3 seems to sink abruptly after 2008. However by the start of 2009, P3 commenced to recover with an ongoing uplifting. Although the two regions enclosed CSG operation areas, the geological conditions and depth of mining are different in each of these areas.

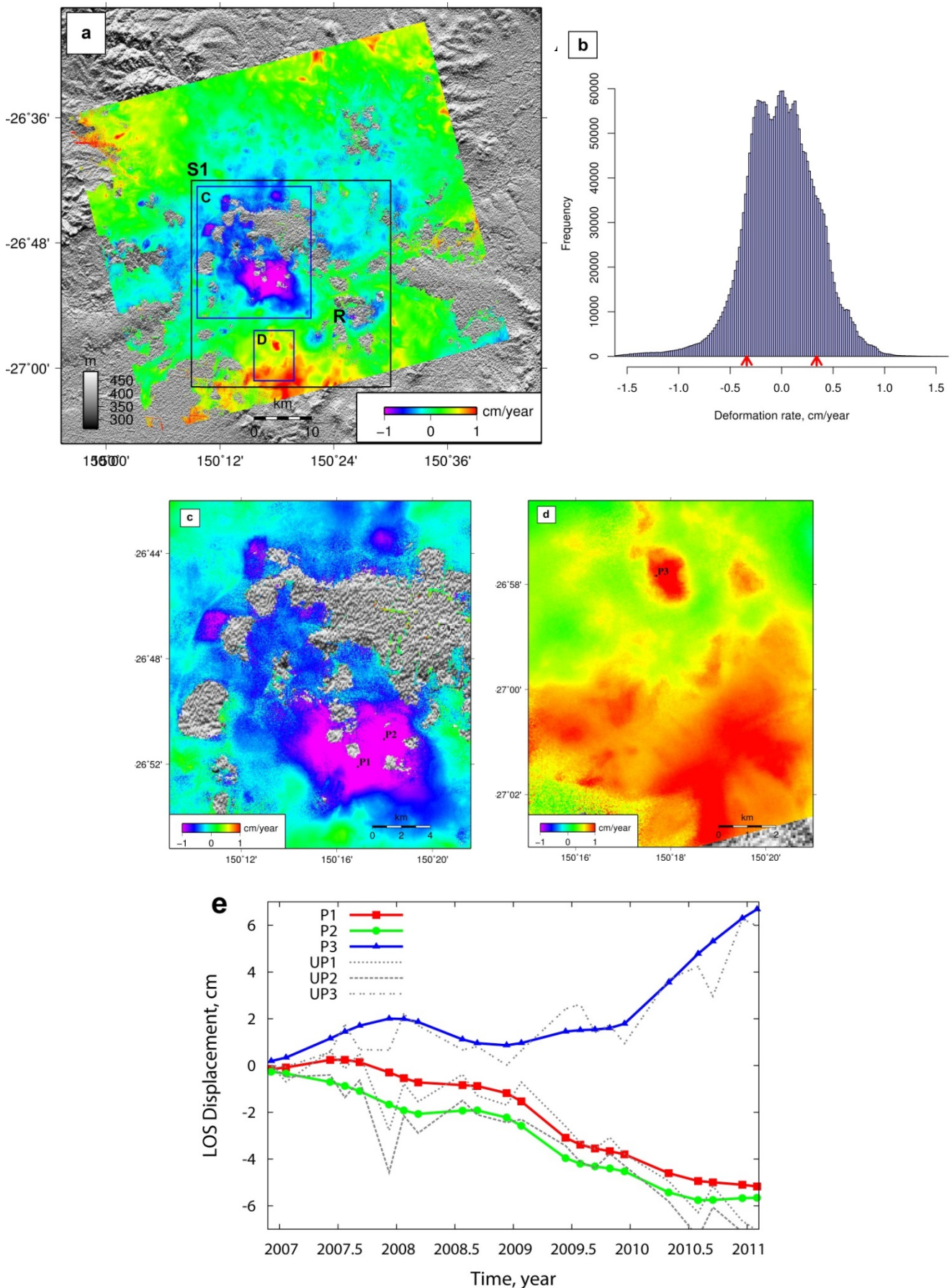


**Figure 4-5: SBAS analysis results for T366-F6640 with 22 ALOS-PALSAR FBS-FBD imagery** a) The rate of deformation (cm/year) in LOS direction b) The frequency distribution of deformation rate for the best reference point (R in 5a) after implementing Gaussian filtering in time domain. c – d) Selected points (P1, P2, and P3) for time series analysis over the areas with downward and adjacent upward motion in candidate region S1. e) Time series of ground surface deformation for selected points relative to the assigned reference in LOS direction before Gaussian filtering (UP<sub>x</sub>) and after filtering (P<sub>x</sub>).

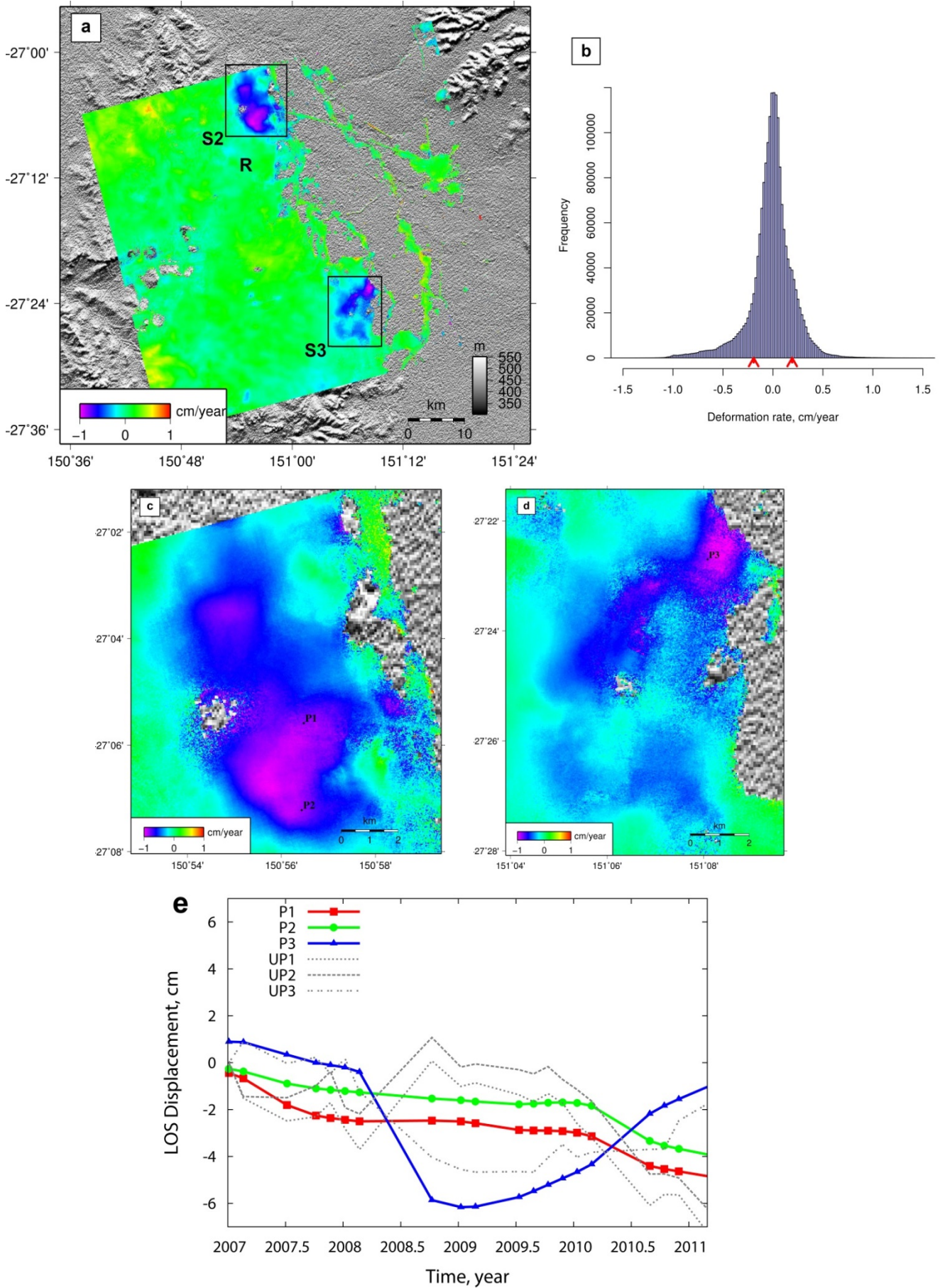


**Figure 4-6: SBAS analysis results for T365-F6630 with 20 ALOS-PALSAR FBS-FBD imagery** a) The rate of deformation (cm/year) in LOS direction b) The frequency distribution of deformation rate for the best reference point (R in 6a) after implementing Gaussian filtering in time domain. c – d) Selected points (P1, P2, and P3) for time series analysis over the areas with downward motion in candidate regions S2 and S3. e) Time series of ground surface deformation for selected points relative to the assigned reference in LOS direction before Gaussian filtering (UPx) and after filtering (Px).

It is worth mentioning that when the proposed area was monitored by recent RADARSAT-2 acquisitions in 2012-2014 (Figure 4-1) using the same processing approach, the results were comparable to the ALOS-PALSAR observations. As shown in Figure 4-7(a) and Figure 4-7(b), the previously mentioned regions S1, S2, and S3 have still retained their gradual settlement to the present day. Due to the swath of the satellite scene, RADARSAT-2 (Left) image did not cover the S2 and S3 regions, but they are covered in the RADARSAT-2 (right) image. Figure 4-7(c) and Figure 4-7(d) depict the frequency distributions of the scenes for the selected reference point (R) after applying Gaussian filtering. Graph 4-7(e) represents the ground surface behaviour in RADARSAT-2 (right)-S1 region for three previously mentioned points before and after Gaussian filtering. For the observation time which was covered by RADARSAT-2 (2012-2014), the ground surface retained its deformation pattern. In other words, P1 and P2 were still experiencing downward motion, while P3 kept shifting upward to present day.

### 4.4 Results

To complement recent field studies conducted in the north-eastern part of the Surat Basin [QWC, 2012] a cost-efficient remote sensing tool with a large spatial extent and high temporal resolution has been used. In depth analysis of the InSAR deformation maps for three candidate regions (S1, S2, and S3) shows substantial ground settlement sites located in the vicinity of extraction areas. In order to interpret these results for further studies including subsurface modelling, the integrity of the mapped deformation signals needs to be verified. As discussed above, most regions have undergone gradual ground settlement since 2007 with increasing downward motion towards 2014. However, the rate of settlement has decreased and even reversed in the period 2008-2009.

Given that levelling or three-dimensional high-frequency measurements of ground motion by a GPS receiver installed at a subsiding site can map the progress of subsidence as a function of time [Hofmann-Wellenhof *et al.*, 2001] and can act as an independent geodetic method to verify the interferometric results [Casu *et al.*, 2006], the availability of continuous geodetic data within the region for our specific observation time (2006-2014) has been checked. The only available GPS time series is from a station located in Dalby (Figure 4-1) between June 2010 and June 2014. However, this station is not useful in this case as the deformation detected from the space borne sensors occurred farther away and is localized. Therefore, the available data on CSG and ground water extraction rate were checked for matching patterns in the surface deformation development.

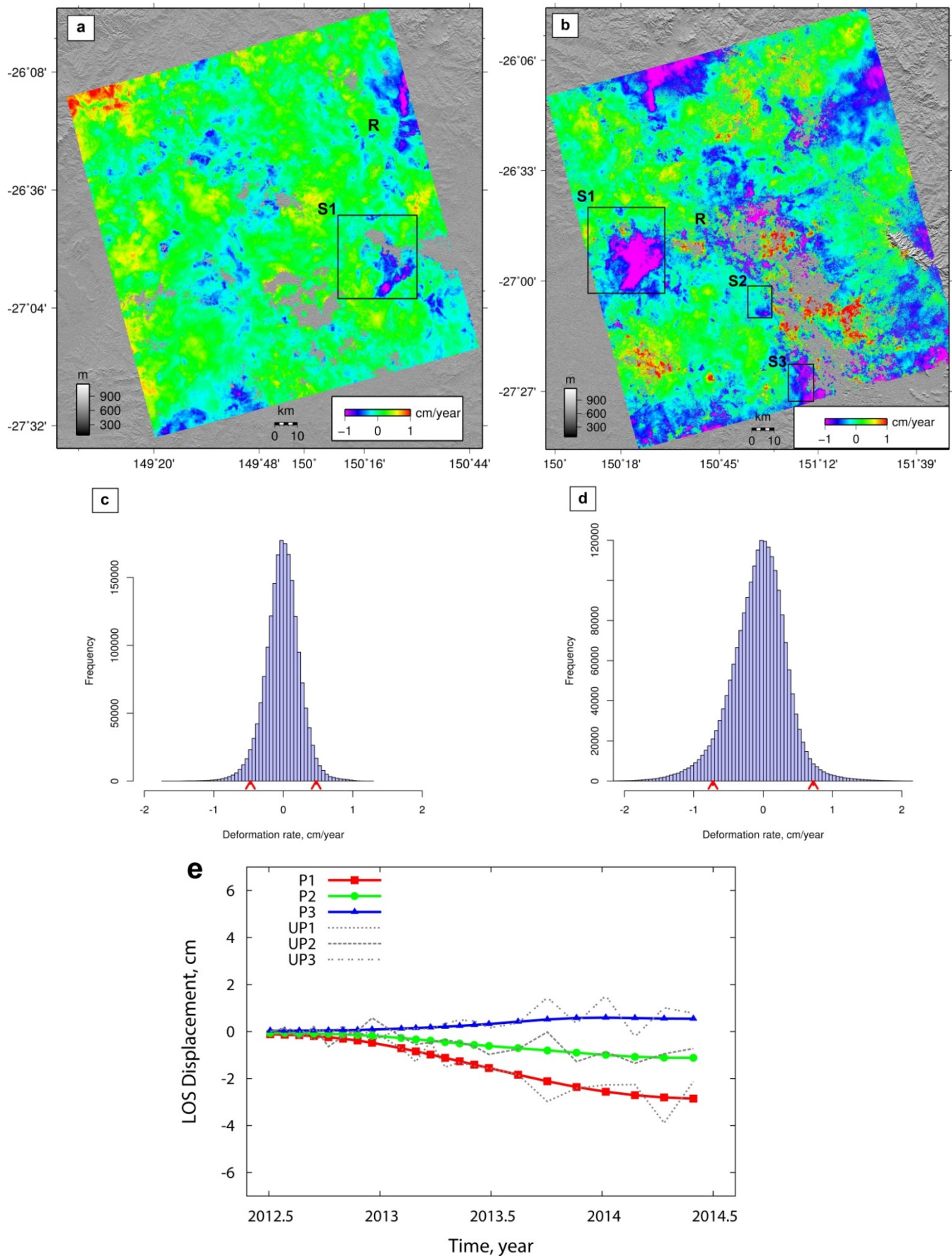


**Figure 4-7: SBAS analysis results for RADARSAT-2. a and b) The rate of deformation (cm/year) in LOS direction for RADARSAT-2 left and right in Figure 4-1 respectively. c and d) The frequency distribution of deformation rate for the best reference points (R in a and b) after implementing Gaussian filtering in time domain. e) Graph illustrates the time series of ground surface deformation for selected points relative to the assigned reference for RADARSAT-2 right.**

From the geological perspective, the Late Jurassic-Early Cretaceous siltstone, mudstone and sandstone along with coal (Jkb) as sedimentary rocks and Late Tertiary-Quaternary clay, silt, sand, gravel and soil (TQr) as alluvium cover the areas with subsidence signal both in NW and SE part of Surat Basin. It is interesting to mention that the rock formations in areas with subsidence are not different to the area with uplift. In other words, surface geology shows that the sedimentary rocks and young-aged alluvium are susceptible to motion but they are not the controlling factors for the deformation signals detected by InSAR.

For the three regions previously identified by InSAR measurements as undergoing deformation spots, the correlation coefficients were calculated to quantify the strength and direction of the relationship between groundwater and CSG extraction, CSG extraction and displacement, and groundwater extraction and displacement (see [Table 4-2](#)).

According to [Figure 4-8\(a\)](#) and [Figure 4-8\(b\)](#) with accompanied [Table 4-2](#), displacement rate per year is highly correlated with CSG extraction. Significant correlation between these two variables with negative value (i.e.  $R = -0.92$  for Daandine (S2) and  $R = -0.84$  for Tipton West (S3)) indicates that more CSG extraction from underground reservoirs resulted in more downward ground surface motion. For both Daandine and Tipton West, the mining operation requires groundwater withdrawal to decrease the pressure on the coal seam for extracting gas. In other words, groundwater extraction in these two fields is accompanied by underground CSG mining with strong correlation i.e.  $R = 0.63$  and  $R = 0.69$  for Daandine and Tipton West correspondingly.

In the other two deformed areas showing surface deformation (i.e. Berwyndale South and Kogan North mining districts) in [Figure 4-8\(c\)](#) and [Figure 4-8\(d\)](#), the scenario is different from that previously examined. As shown in [Table 4-2](#), there is a strong correlation between CSG mining and observed deformation (i.e.  $R = -0.76$  for Berwyndale South (S1) and  $R = -0.86$  for Kogan North (S2), but even with a gradual decrease in groundwater extraction during the observation period, the ground surface deformation still retained its gradual downward trend. Additionally, negative correlation between groundwater and CSG extraction (i.e.  $R = -0.48$  and  $R = -0.81$ ) in the aforementioned sites shows that the nature of CSG mining operations is not related to *direct* depressurization of shallow depth aquifers for both Berwyndale South and Kogan North, despite the fact that there is a report on depressurization in Berwyndale South (S1 in [Figure 4-5\(a\)](#)) from 2005 for domestic groundwater extraction [[QWC, 2012](#)]. In other words, depressurization by groundwater extraction and CSG extraction do not necessarily occur simultaneously or need to have a high temporal correlation in areas with CSG mining. Taking all these observations into account, the role of compaction due to pressure depletion after water/gas pumping cannot be ruled out, and the compaction may have led to surface subsidence because of the viscoelastic response of the subsurface.

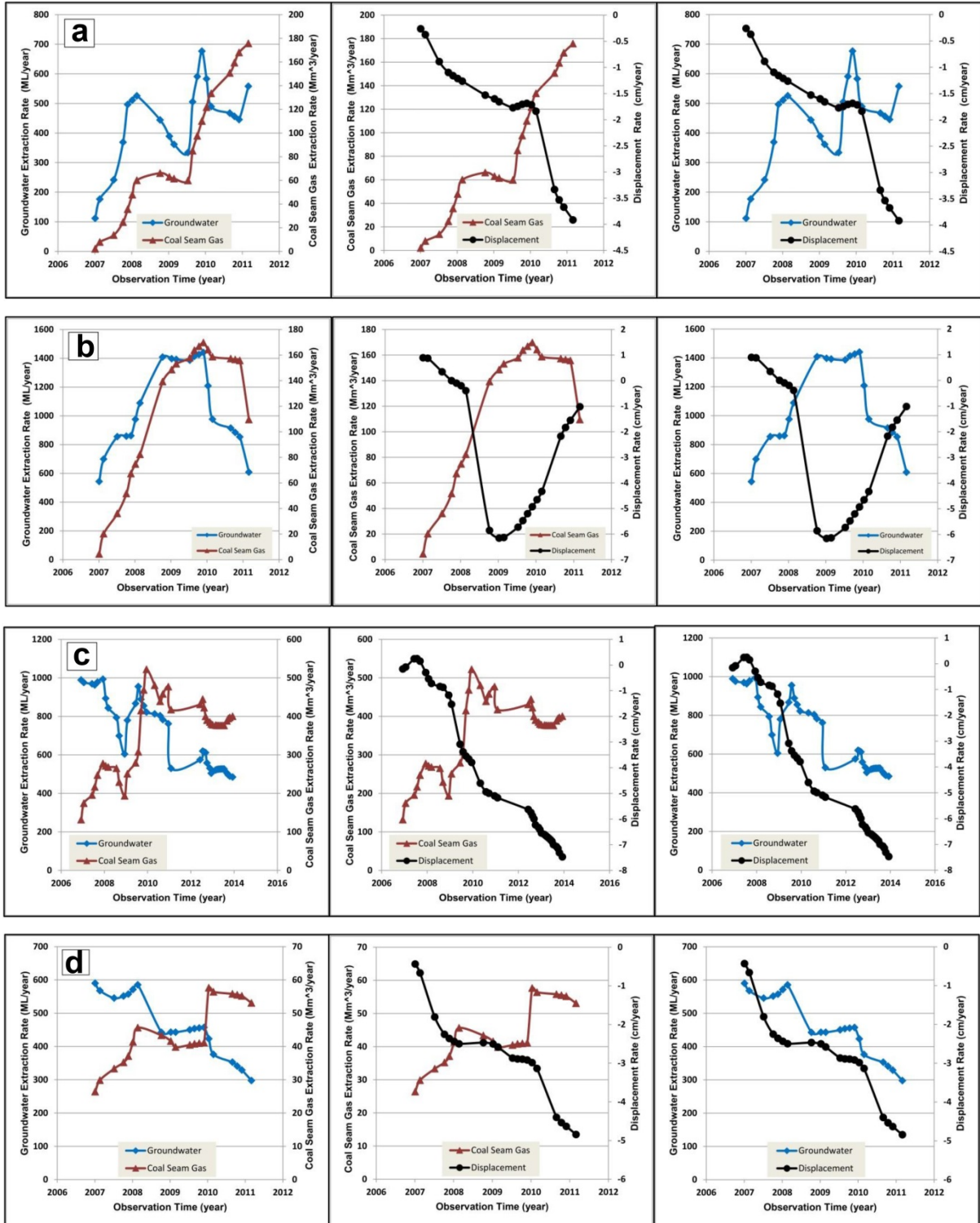


Figure 4-8: Graphs of the CSG and groundwater extraction rates versus ground surface displacement in selected regions S1, S2 and S3. a) Daandine b) Tipton West c) Berwyndale South and d) Kogan North CSG mining districts.

**Table 4-2: Correlation coefficient estimation for each resources extraction site with displacement**

| <b><i>Daandine</i></b> | Deformation | Coal Seam Gas | Groundwater |
|------------------------|-------------|---------------|-------------|
| Displacement           | 1           | -0.92         | -0.46       |
| Coal Seam Gas          | -0.92       | 1             | 0.63        |
| Groundwater            | -0.46       | 0.63          | 1           |

| <b><i>Tipton West</i></b> | Deformation | Coal Seam Gas | Groundwater |
|---------------------------|-------------|---------------|-------------|
| Displacement              | 1           | -0.84         | -0.89       |
| Coal Seam Gas             | -0.84       | 1             | 0.69        |
| Groundwater               | -0.89       | 0.69          | 1           |

| <b><i>Berwyndale South</i></b> | Deformation | Coal Seam Gas | Groundwater |
|--------------------------------|-------------|---------------|-------------|
| Displacement                   | 1           | -0.76         | 0.86        |
| Coal Seam Gas                  | -0.76       | 1             | -0.48       |
| Groundwater                    | 0.86        | -0.48         | 1           |

| <b><i>Kogan North</i></b> | Deformation | Coal Seam Gas | Groundwater |
|---------------------------|-------------|---------------|-------------|
| Displacement              | 1           | -0.86         | 0.88        |
| Coal Seam Gas             | -0.86       | 1             | -0.81       |
| Groundwater               | 0.88        | -0.81         | 1           |

Although the structure of the Surat Basin is relatively simple, according to the Geological Survey of Queensland, the displacement associated with a number of small faults in the shallow formations of the Surat Basin ranges from zero to some tens of meters with only minor propagation into the younger units while regional faults are deeper with less impact on the formations and lateral groundwater flow as a hydraulic barrier [Hodgkinson *et al.*, 2010]. As previously mentioned, for three-year observation period using ALOS-PALSAR, three main subsidence bowls in the north-eastern part of the Surat Basin were detected. The one with maximum downward motion rate is centered on the Berwyndale South CSG mining district and extends in a circular shape with 10 km diameter. From the geological point of view two major faults spatially confine the signals and force them to follow a specific distribution pattern. Interferometric observations show that the deformation signals' distribution is geologically random such as the ones over Daandine, Kogan North, and Tipton West but when faults are in place, subsidence patterns appear to follow the confining structures. These two subsurface structures are Burunga-Leichardt thrust fault and Moonie-Goondiwindi thrust fault that curb the Berwyndale South deformation signal. In combination with three-dimensional structural model obtained from seismic interpretation and wire-line logs with ground surface deformation signals, more detailed information for concealed and localized faults should be obtained in particular for the areas without seismic surveys.

## 4.5 Discussion

Multi-temporal space-borne SAR observations since 1992 to present day have been used to monitor the north-eastern part of the Surat Basin between Miles and Dalby. Interferometric analysis for both C-band (RADARSAT-2) and L-band (ALOS-PALSAR) satellite-based observations were presented between 2006 and 2014 using both stacking and SBAS processing techniques. Contrary to the previous InSAR observation [*Dura et al., 2012*], by using different processing approach for the same dataset, ground surface deformation signals were detected in two out of four ALOS-PALSAR scenes covering the area between Miles and Dalby. These signals showed a subsidence rate in excess of 2 cm/year, particularly for sites located over CSG mining with a large number of groundwater extraction wells. Comparing the space-borne long-term satellite observation to CSG extraction rates, deformation scenarios in different locations have been proposed. This observation suggests that the detected subsidence signal may have resulted from volumetric changes in the subsurface formations and adjacent overburden due to gas extraction and associated strata compaction which can occur due to changes in pore pressure and stresses in rock matrix. As a result of associated aquifer compaction, several centimeters of land subsidence were observed using the InSAR technology. The largest values showed a rate of about 28 mm/year and are in the vicinity of Berwyndale South CSG mining area, which is correlated to large clusters of CSG extraction wells. Subsequent observation of the region with RADARSAT-2 wide frame images in 2012-2014 also confirmed the ongoing land subsidence trend in those areas. Despite implementing aquifer injection in many places around the world, including Australia, there is no record of injecting water into the shallow aquifers of this part of GAB which, incidentally, might be helpful in reversing the downward trend of groundwater supplies associated with detected spots, and in improving the balance in the volume of water withdrawal in the Surat Basin.

Last but not least, multi-temporal SAR observation not only revealed the areas with surface deformation but also facilitated the evaluation of different scenarios responsible for the detected settlement and uplift in this part of the Surat Basin. CSG mining is the prime cause for the downward motion. However, in some areas it has direct impact on shallow-depth aquifer and in some others not. Considering that there is no water or gas injection initiated in the aforementioned region, the area with uplift (*Figure 4-7(d)*) could be due to industrial timber forests or due to elasto-plastic response of overburden layers adjacent to the CBM extraction sites.

The regions undergoing downward motion are located above CSG mining sites with rates up to 28 mm/year. Three scenarios were identified: (i) extensive groundwater extraction from shallow aquifers due to CSG mining, (ii) CSG mining without direct impact on groundwater resources and (iii) patchy uplift over an industrial forest adjacent to a CSG mining district. Contrary to a previous study conducted in this region using the PSI technique which reported stability of the area with insignificant

surface deformation, this study shows that there are considerable deformation signals consistent with resource extraction. Consequently, it is shown that the SBAS approach is superior to PSI for deformation monitoring with focusing on natural distributed scatterers.

### 4.6 Chapter Summary

According to final zonation of deformation signals in the eastern part of the Surat basin, a subset of this information in T366-F6640 of ALOS-PALSAR will be used for 3D subsurface structural modelling and subsequent geophysical inverse modelling. The outcomes of subsurface source modelling and their interpretation are described in the next chapter for better evaluation of the surface deformation mechanism and subsurface structural behaviour in this part of the Surat Basin.

## 5 Subsurface Structural Behaviour

This chapter presents a three-dimensional static geological model of the study area monitored by InSAR for surface deformation, and discussed in Chapter 4. This geo-model, along with extracted property models, replicates subsurface stratigraphic units and structural features including depth and density of underground layers, overburden and reservoir storage. It is hypothesized that integration of elastic properties for each formation with interferometric SAR observations in a stratified elastic medium will lead to a visco-elastic geophysical inverse problem that can be solved for fractional volume change estimation. Moreover, the impact of changing elastic properties of the formations on the rate of surface deformation and its residuals are examined for both real and synthetic deformation maps. While the multi-layer viscoelastic source model has already been tested for conventional hydrocarbon resources such as oil and gas fields in Algeria, it is imperative that it be tested for an unconventional hydrocarbon resource such as CSG field in Australia. The work in this chapter is under preparation for publication.

### 5.1 Background

Modelling subsurface structures and understanding their role in controlling fluid flow at depth is critical in energy production (i.e. conventional and unconventional), CO<sub>2</sub> storage, and groundwater supply conservation. Three-dimensional geological modelling or geo-modelling is a numerical equivalent of a geological map that describes the physical quantities in the domain of interest [Mallet, 2008]. Integration of in situ measurements such as geological, lithological, structural, and geophysical in large and separate datasets with a structured quantitative approach will result in a complete, robust and realistic 3D tool to constrain exploration targets at depth, and to extract valuable information for reservoir management. Although a high-quality, and various dataset with relatively uniform distribution over the entire area is a crucial part of subsurface modelling, the data availability, its density and distribution relative to the working scale and project objectives are also decisive [Fallara *et al.*, 2006]. In general, the structural framework (i.e. resolution and maximum cell size), rock type, reservoir quality (i.e. porosity and permeability), and geostatistics are the components of a static geological model [Ezekwe, 2011]. This model can then be used as a benchmark model for reservoir dynamic modelling or flow simulation.

In this chapter, a range of available datasets for primary geological analysis collated for the domain of interest in the Surat Basin will be discussed. These datasets, including seismic surveys and wire-line logs, are the main components for establishing geological horizons and structural features in three dimensions. Following on the presentation of the datasets, the background concepts and main methodology for constructing subsurface geological models with main boundaries (i.e. horizons,

unconformities, fault and intrusions) as well as the subsequent inverse modelling for volume change calculation are discussed. The developed static subsurface model with various extracted petrophysical models, as the end-result for static structural modelling, are presented in the final section. Consequently, using the subsurface elastic properties resulted from petrophysical modelling, and the geophysical inverse modelling approach, the spatial distribution of fractional volume changes over the mining area with considerable settlement, its trend, and the possible reasons for its particular pattern will be discussed as a new contribution in unconventional hydrocarbon resources.

### 5.2 Data Resources

Reservoir life stage can define the type of data sources required for the development of a geological model. The first stage of a reservoir life is the exploration stage and data sources will be limited to seismic acquisitions, outcrops and comparable reservoir studies. Other subsurface data such as cores, well logs and fluid saturation will be included in the appraisal stage as the second reservoir life stage. At the third stage or development stage, tests such as fluid production or Drill Stem Tests (DST) are designed to assess the extent and potential of the reservoir for production [Ezekwe, 2011].

One of the valuable tools in building a geological model and characterizing the reservoir in a depositional basin such as the Surat Basin is visual description of the subsurface structure and stratigraphy [Wickens and Bouma, 2000]. In addition to site investigation by geoscientists, geophysical measurements such as seismic acquisitions can portray the structure and the stratigraphy of the reservoir by locating available faults and recording the Acoustic Impedance (AI) response of different underground formations [Ezekwe and Filler, 2005; McCarthy et al., 2006]. Together with seismic surveys, well log data are another type of in situ geophysical measurement that provides a petrophysical perspective for a three-dimensional model. Well logs are categorized in various groups such as gamma ray, density, resistivity, neutron, sonic, Nuclear Magnetic Resonance (NMR), and Vertical Seismic Profile (VSP). These provide valuable information on porosity, permeability, water saturation, and formation thickness. Reservoir boundaries, fault locations, and formation pressure tests for reservoir heterogeneity are other types of datasets that can be used to constrain the geological model. For reservoirs in the development stage, performance data such as well production rates, static bottom-hole pressures, production and injection logs can also be integrated to modify the geological model [Ezekwe, 2011].

As described in Chapter 3, the Surat Basin 2D seismic acquisitions, together with down-hole information of selective petroleum and CSG wells, are the only available dataset for three-dimensional modelling. The modelling approach that was used for the Surat Basin characterization was a pixel-based method, for which the important workflow steps will be presented in the following sections.

### 5.2.1 Seismic Data

Understanding subsurface formations and how they can impact on seismic wave propagation and reception are essential for seismic data analysis. Interpretation of seismic data not only provides valuable and basic information about seismic attributes such as amplitude, phase, frequency and travel time of seismic waves, but it also embeds other attributes such as AI with which to examine the petrophysical properties. The AI represents changes of seismic reflections at each lithological boundary due to variations in acoustic properties of rock units as a product of rock density ( $\rho$ ) and seismic velocity ( $V_p, V_s$ ) [Badley, 1985; McCarthy et al., 2006]. To deliver a more tangible meaning for AI concept, hard rocks such as limestone and granite have high acoustic impedance, whereas soft rocks such as clays show low acoustic impedance [Anstey, 1977]. A typical sedimentary basin consists of successive layering with various lithological boundaries, and therefore with various acoustic impedance. The strength of a seismic wave reflection generated at a boundary is quantified as a boundary's reflection coefficient (RC):

$$RC = \frac{AI_2 - AI_1}{AI_2 + AI_1}, \quad (5.1)$$

where  $AI_1$  is acoustic impedance in the upper layer and  $AI_2$  is acoustic impedance in the lower layer. According to the nature of rock sequence i.e. softer rocks overlie harder rocks or vice versa, the reflection coefficient can be positive or negative [Badley, 1985]. Assuming that the velocity of the seismic wave through the rock is known or can be estimated, the travel time of a seismic pulse to the interface and back to the surface (i.e. seismic two-way travel time) can be converted to the depth:

$$depth = \frac{two-way\ time}{2} \times velocity, \quad (5.2)$$

Selection of the proposed region for seismic interpretation was based on the available seismic data, check shots, and their proximity to the deformation signal in S1 (Track 366-Frame 6640) detected by interferometric SAR analysis (Figure 5-1). According to the available dataset (as described in Table 3-4) there are 79 2D seismic lines with a total length of 893 km in the area of interest, while only 50 seismic lines in 10 different seismic surveys had the relevant quality and information (i.e. navigation file and shot point map) for uploading into the seismic interpretation package (i.e. Petrel Schlumberger ©). In addition to 2D seismic acquisition, relevant geological and geophysical reports, as well as Seismic Reference Survey (SRS) were gathered. Generally, migrated seismic lines with spatial and temporal corrections that shift the signal to its originating location of reflectors are more preferable for seismic interpretation; however, in cases that the migrated lines are of poor quality, individual unmigrated lines are ordered and used for better quality interpretation (Figure 5-1). In addition to stratigraphic interpretation, seismic surveys can also be used for structural interpretation such as locating normal faults, strike-slip faults, reverse faults and thrust faults through defining regional stresses in the area of interest.

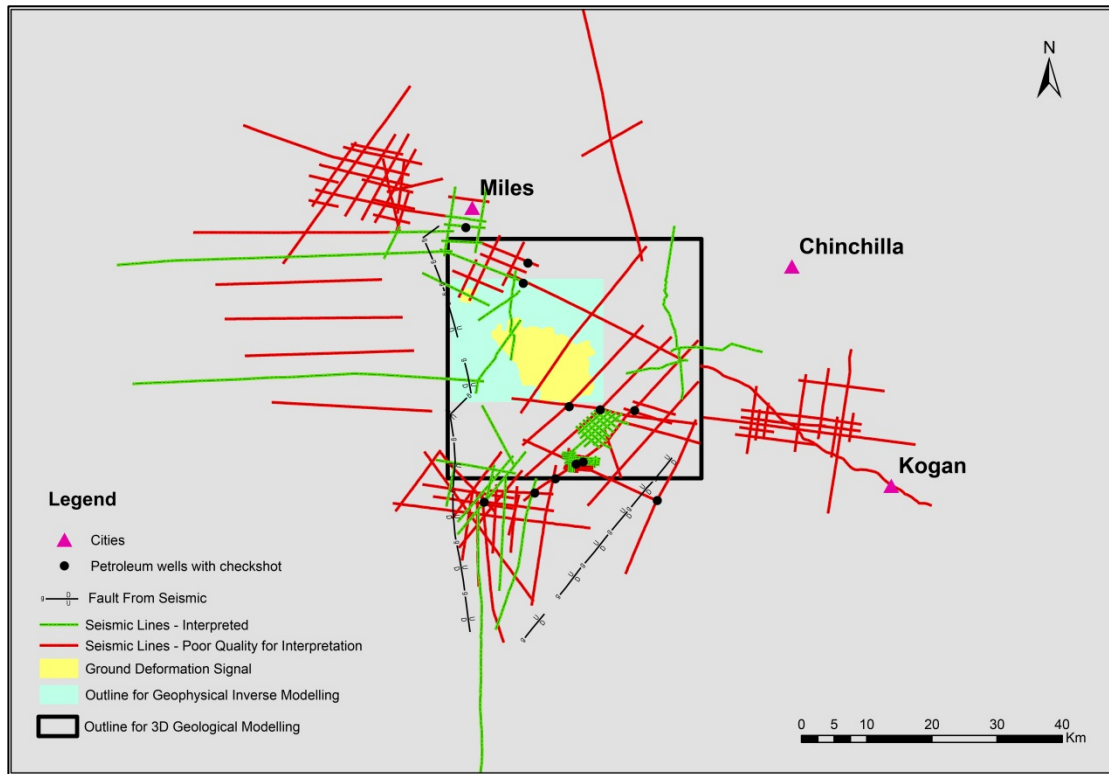


**Figure 5-1: Outline of the area for which the 3D geological modelling and inverse modelling were undertaken (black outline), showing the available seismic dataset (green and red lines). The green seismic lines were in good quality for seismic interpretation but the red ones were in poor quality. The black dot points show the location of petroleum wells with velocity check shots.**

### 5.2.2 Wire-line logs

The analysis of wire-line logs is one of the fundamental methods for reservoir characterization, and understanding the conditions below the surface by measuring the petrophysical properties of rocks. In this study, the information accompanied by well logs will be used for two types of reservoir properties: geophysical and geological. For the first type, such as rock physical properties (elasticity, wave velocity, etc.), formation tops with SRSs will be used to calibrate reflection seismic data, while for the second type, petrophysical properties such as shale volume, water saturation, and porosity will be extracted [Tiab and Donaldson, 2012].

Around 50 available wells in the area of interest have recorded formation tops (Figure 5-1), while 12 of these wells are located within the study area or in the vicinity (<2.5km) and are accompanied by SRSs. These SRSs or velocity check shots are designed as a calibration mechanism for reflection seismic data. Bottom-hole data from the 12 wells penetrating the basement (unconformity horizon) along with 112 CSG wells with wire-line logs and petrophysical information (porosity, density, shear and compressional velocity) were also used. Supplementary data such as well completion reports with accompanying information about exploration well location, measured depths, well casing and the historical status of the operation were also gathered from the Department of Natural Resources and Mines (DNRM) publicly available database in digital format.

Although more than 1600 groundwater bores were registered in the DNRM groundwater database within the 3D geological model domain, only 14 groundwater observation wells provide some temporally sparse information about the groundwater level and conditions of the aquifer. However, their acquisition periods are not continuous enough to cover the missing information in the geo-modelling procedure. Unfortunately, in this project there was no access to core plugs with measurements of porosity, directional permeability, compressibility and grain density for specific wells. In other words, sparse distribution of data in this part of the basin presents a challenge for accurate static modelling. For example the inter-well distance for petroleum wells varies between less than 1km and more than 20km. The following section includes details of the parameters incorporated into subsurface structural modelling and geophysical inverse modelling. All the data sources for model development are listed in **Table 5-1**:

**Table 5-1: List of in situ measurements for 3D geological modelling for the proposed area in the Surat Basin. These data sources are publically available in different scales.**

| Data              | Name                                                  | Source                                                                                                            |
|-------------------|-------------------------------------------------------|-------------------------------------------------------------------------------------------------------------------|
| Surface Elevation | ASTER DEM with 30m resolution S25E148                 | <a href="http://gdem.ersdac.jspacesystems.or.jp/search.jsp">http://gdem.ersdac.jspacesystems.or.jp/search.jsp</a> |
| Surface Geology   | Geological Map of Queensland (2012), scale 1:2,000000 | Geological Survey of Queensland                                                                                   |
| Seismic Surveys   | 50 2D seismic lines in 10 different surveys           | Geological Survey of Queensland                                                                                   |
| Well Logs         | 112 CSG and 12 Petroleum Wells                        | Department of Natural Resources and Mines                                                                         |

### 5.3 Methodology

#### 5.3.1 Subsurface Structural Modelling

This section explains in detail the technical concepts of developing a subsurface structural model. Seismic interpretation, as an initial stage, is followed by structural modelling to build an essential 3D framework for further property modelling.

##### 5.3.1.1 Seismic Interpretation

Extracting major seismic events such as formation boundaries and unconformity, along with chief structural elements such as faults, grabens and dip trends from seismic sections is called seismic

interpretation. Having a good quality seismic section with good vertical resolution provides an initial picture of the main structural features and underlying stratigraphic sequences. Accordingly, the study area in the Surat Basin is categorized as having poor data coverage due to the scarcity of 2D seismic lines, lack of 3D seismic acquisitions, and accompanied noise that obscures the key subsurface reflectors, thus making the interpretation difficult. Consequently, studying seismic sections alone will not be sufficient to identify the lithology, so well-bore information will be required to support the detailed interpretation.

It is known from geophysical acquisition theory that pulses of seismic energy generated by the energy source on the surface travel through the subsurface strata and then are reflected and bounced back towards the receivers on the surface. These recorded seismic wavelets carry the geological information to the surface that can be processed and converted into a zero-phase wavelet for easier and more accurate interpretation, but noise is ever-present component with seismic acquisitions [Zhdanov, 2009].

For detecting subsurface depositional sequence, the formation boundaries with significant AI were automatically or manually traced. These boundaries can be identified by discordant relationships between the reflectors [Badley, 1985]. Discordant relationship in this part of the Surat Basin with underlying Bowen Basin (see Figure 3-7) is very well developed at basin margins and resulted in depositional unconformity. Thorough analysis of the available well data such as check shots was used to calibrate the seismic section to a reference datum. Tying well and seismic data together is an alternative approach to identify the reflectors in seismic time domain for the proposed area. For individual lines in the entire area, time versus depth plots extracted from sonic data and accompanied with check shots were used for correcting any misties between seismic sections and wells (see Figure 5-2).

### 5.3.1.2 Structural Modelling

Static geological modelling to assess the structural properties and characterize shallow depth aquifers in the Surat Basin is critical for having a holistic image of the subsurface with assigned petrophysical properties. It can also be used as a basis for dynamic geo-modelling and fluid flow simulation in the same area. The primary objective in developing such a three-dimensional model is to have a realization of the subsurface that honours the available dataset at known points and makes a robust interpretation between these points for the full extent of the model. This framework can then be improved by inserting petrophysical attributes to define the elastic properties of the subsurface medium for further geophysical inversion using interferometric surface observations.

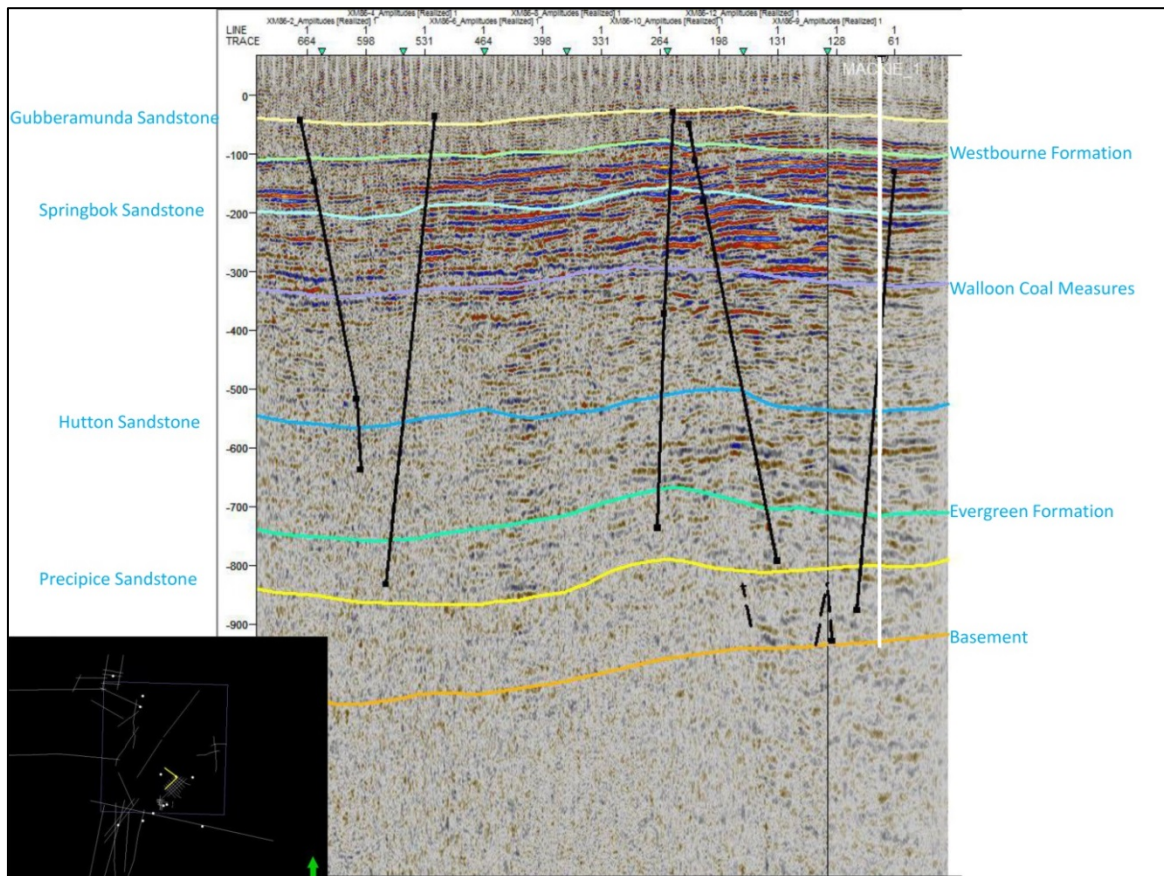


**Figure 5-2: A composite line between XM86-9 and XM86-14 seismic lines as shown in small image on the lower left-hand corner. By overall reviewing of significant events in seismic lines and using SRSs in Mackie\_1, stratigraphic levels and structural features were identified and traced. The image in the background, shows tying Mackie\_1 with seismic and horizon picks. The colourful lines show the traced stratigraphic levels while the black lines are normal and reverse faults both in time domain.**

The boundaries of the model domain were defined based on data availability, i.e. areas where seismic surfaces are available and deformation signals have been observed. The following steps provide a standard mapping workflow for subsurface three-dimensional modelling (Figure 5-3). It will start with importing subsurface data consisting of well tops and digitized seismic events, followed by zone-averaged petrophysical properties and volume calculations.

As shown in Figure 5-3, the following steps were used for building the three-dimensional geological model:

1. Importing and creating seismic data, well tops and well logs
2. Building a 2D structure grid for each horizon
3. Building a structural 3D framework
4. Building average 2D petrophysical grids for each zone
5. Building petrophysical 3D properties
6. Calculating volumes

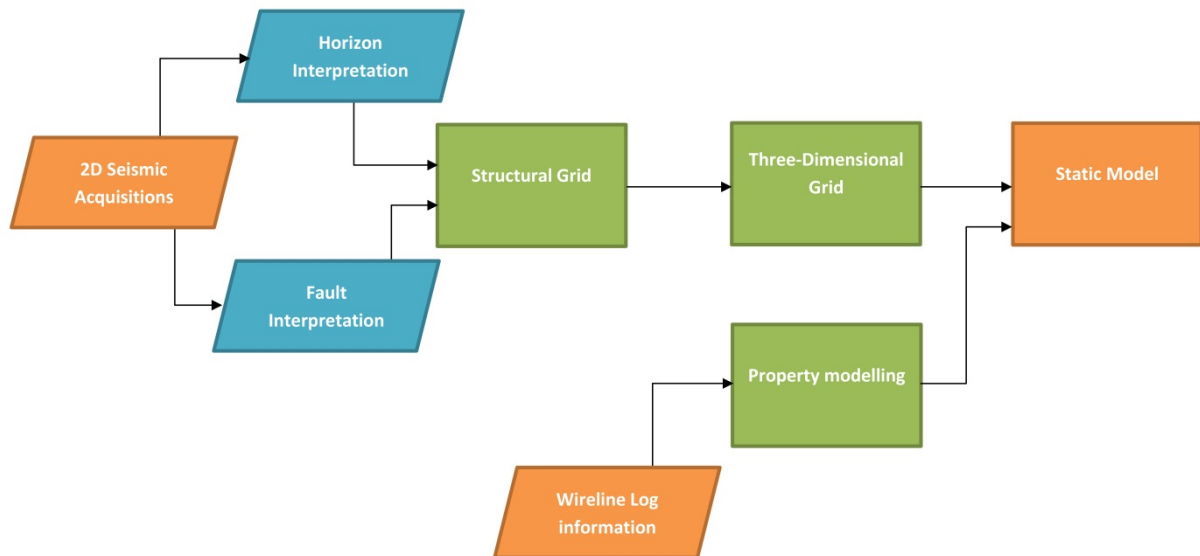


**Figure 5-3: The workflow for interpretation and modelling in the proposed geological modelling package.**

Once digitized subsurface data are imported into the modelling package, producing a simple 2D grid for each horizon that was chosen during the seismic interpretation, and cross-checked with well tops is the next step. To standardise the stratigraphic horizon names, well log data were already verified by revising the lithology of each well in order to identify appropriate stratigraphic units. More than 30 horizons were identified in the study area from which eight common stratigraphic units will be used in the 3D geological modelling, corresponding with those that were formally recognized by Geoscience Australia [*Geoscience-Australia and Australian-Stratigraphy-Commission, 2014*]. The accuracy in choosing eight selected formation surfaces based on seismic interpretation was then evaluated by comparison with the formation tops in well logs. In most cases the surfaces matched with the top of the corresponding stratigraphic unit recorded by the well completion reports, and there were only a few small areas where the reliability of the surfaces is questionable. In the modelling package used here, three stages for static 3D structural modelling using built stratigraphic horizons were available: (a) Geometry Definition; (b) Fault Framework Modelling; and (c) Horizon Modelling.

During the geometry definition, the geometry of the whole structure will be defined by choosing one of the built horizons in the time domain as reference geometry for the framework. The grid cell size increments in the *i* and *j* directions can also be changed, but the software default of 150m × 150m will be accepted. By implementing this part, a new structural framework will be shaped which has three modelling parts: Faults, Horizons and Zones.

When it comes to the fault modelling stage, all faults that are available in the area of interest need to be introduced to this tool in order to build the fault planes over the fault segments that were already picked during the seismic interpretation stage. For the first round of fault modelling, the software defaults for all faults to be active, 500m for grid interval, and 5km for influence radius of fault tops were accepted.

For the horizon modelling part, each stratigraphic surface was built based on seismic interpretation and will be introduced in a sequential manner from top to bottom. Setting up all the stratigraphic surfaces, geological rules will be applied and a zone model will be created for each input horizons. By using geological rules for building a zone model, the stratigraphic rules within the structural framework will be applied to all horizons. Consequently, those horizons that are eroded by another horizon will be correctly visualized.

Sometimes, due to the way faults intersect each other, or the sampling rate for building the geological model, some fault planes might be dismissed. In such conditions, the problematic fault and the particular horizon should be identified and the fault status in that horizon should be changed from active to passive and then model should be re-run. In case that de-activating the problematic fault does not resolve the issue, another approach is possible, limiting the impact of that fault on the modelling through setting a specific impact distance. Using this option, the problematic fault can be active with a specific sampling distance (i.e. 500 per side) and the interpolation will be done to fill the gap in the areas without data.

Before property modelling, domain conversion (i.e. time to depth) of seismic interpretation and the structural model is required. For an effective approach to convert seismic time to depth, the interpreter needs to have an understanding of the nature of velocity fields and their representations. “Poorly positioned wells, miscorrelated horizons, and inconsistent formation tops can distort the implied velocity field and result in false structuring” [*Schlumberger, 2015*]. This critical stage in geological modelling will be discussed in the following section with more details.

### 5.3.1.3 Velocity Modelling

Interpretation of geological horizons and structural faults on 2D seismic acquisitions are done in the time domain, while subsurface geological features are in the depth domain. The bridge between time and depth is through velocity modelling [*Cameron et al., 2006*]. For an adequate interpretation it is important to build a representative velocity model for linking these two domains together, as velocity equates to depth over time.

Once stratigraphic horizons are interpreted and gridded into surfaces based on seismic interpretation in the time domain, there are two approaches to build a geological model in the depth domain. The first method is to build a model in time domain and then convert it with a velocity model into depth domain. The second method is to convert selected horizons and faults directly from time to depth domain using a velocity model and subsequently build a 3D geological model. In this study, both methods were examined, but applying the velocity model directly to convert the previously built structural model in time domain did not work properly and suffered from missing several surfaces because of using the simplistic velocity model that was based on limited velocity information from the wells.

For preparing a velocity model to convert individual horizons into depth maps, the check shot and depth information of four wells spreading over the area of interest were used to extract a polynomial equation (Figure 5-4) as a relationship between time and depth. The interval velocity for each formation is based on averaging the interval velocity of four wells associated with each formation. The estimated interval velocity values based on the time-depth plot (Figure 5-4) is shown in Table 5-2. These values were used for direct conversion of horizons and faults into the depth domain and then producing a structural model.

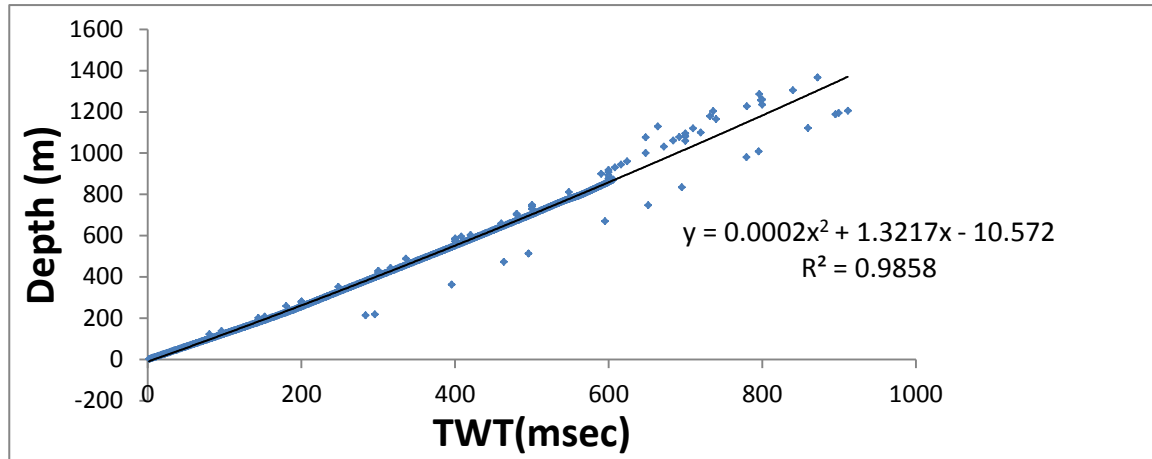


**Figure 5-4: The time-depth plot used to extract the velocity model and to convert horizons in seismic time domain into depth domain. These results based on observed interval velocity of four wells with checkshots i.e. Bulwer\_1, Coloomoola\_1, Picurda\_1, and Xylex\_1 with equal weight in distribution.**

**Table 5-2: Interval velocity for each formation unit estimated based on averaging the down-hole interval velocity measured for the four selected wells.**

|                        |            |                     |            |
|------------------------|------------|---------------------|------------|
| Gubberamunda Formation | 2607 m/sec | Hutton Sandstone    | 3079 m/sec |
| Westbourne Formation   | 2633 m/sec | Evergreen Formation | 3575 m/sec |
| Springbok Formation    | 2811 m/sec | Precipice Sandstone | 3769 m/sec |
| Walloon Coal Measure   | 2927 m/sec | Basement            | 3820 m/sec |

Using the estimated interval velocity ( $V_{Int}$ ) and the assumption  $V = V_0 = V_{Int}$  in which  $V_0$  is constant with no correction applied, resulted in the first model of velocity variations in the proposed outline. Accordingly, to change the seismic datum from two-way seismic time (TWT) into depth equivalent ( $Z$ ), the datum needs to be adjusted from 100m in time (based on the maximum elevation time in the upper level surface, i.e. Gubberamunda Sandstone) to 244m, which is the common datum in depth for the SRSs. Although, averaging the interval velocities resulted in a 3D structural model in the depth domain, a quality check of this model against well top locations across the entire region was

not satisfactory. This might be due to some misties between stratigraphic well tops and seismic horizons in the initial seismic interpretation stage.

To solve this problem another strategy was taken to build a new velocity model for this area. This time, the velocity model was built using three horizons including Walloon Coal Measures, Hutton Sandstone and Basement. This velocity model was corrected by well tops and then modelled using interval velocities between DTM-Walloon, Walloon-Hutton, and Hutton-Basement. For instance, to calculate the interval velocity between DTM (surface) and Walloon Coal Measures, Equation 5.3 may be applied.

$$V_{DTM,WCM} = V_{Int} = \frac{isochore(depth)}{isochron(time)} = \frac{[(DTM,westbourne)+(westbourne,WCM)]}{[(DTM,westbourne)+(westbourne,WCM)]} \quad (5.3)$$

Based on Equation 5.3 the interval velocity ( $V_{Int}$ ) is a ratio between the formation thickness and its correspondent in seismic time. As the surfaces for DTM- Westbourne and Westbourne-Walloon Coal Measures in depth and time domains have already been built, the ratio of their summation can give us the interval velocity between DTM and Walloon Coal Measures.

**Table 5-3: The input box for creating velocity model – this input box includes different horizons that are trended with well tops and modelled by selective interval velocity (Petrel Schlumberger ©).**

| Conversion            | From Two Way Travel Time (TWT) to Depth |                                   |
|-----------------------|-----------------------------------------|-----------------------------------|
| Datum                 | From Surface                            | DTM in TIME Domain                |
|                       | To Surface                              | DTM in DEPTH Domain               |
| Base Horizons         | Well tops for Correction                | Velocity Interval for Modelling   |
| Walloon Coal Measures | Walloon Coal Measure Stratigraphic Tops | DTM_Walloon Interval velocity     |
| Hutton Sandstone      | Hutton Sandstone Stratigraphic Tops     | Walloon_Hutton Interval velocity  |
| Basement              | Basement Stratigraphic Tops             | Hutton_Basement Interval Velocity |

As shown in [Table 5-3](#), to build a velocity model three types of information are needed: base horizons, well tops for correction, and velocity intervals for modelling. The base horizons are the ones that were selected for the three-dimensional modelling. In the present case, different combinations of the eight horizons were tested and the best combination chosen based on trial and error. This optimum combination was between Walloon Coal Measures, Hutton Sandstone, and Basement.

When selecting seismic horizons in time, it needs to be confirmed by the interpreter that the extracted surfaces are properly matched with the well tops which are already in place. Therefore, as pre-processing constrains to make surfaces seismic horizons will be trended with stratigraphic well tops in two-way time domain. Then for the correction as shown in [Table 5-3](#), the trended surfaces of the Walloon Coal Measures, Hutton Sandstone, and the Basement will be introduced to correct the base horizons and adjust the final model. Finally, the interval velocity between DTM\_ Walloon,

Walloon\_ Hutton, and Hutton \_Basement estimated by Equation 5.3 will be given. For the datum, time-depth conversion will be performed from DTM in time domain into resampled DTM in depth domain. The resampled DTM is a coarser version of ASTER DTM with 200m spatial resolution.

By introducing the velocity model to the three-dimensional grid in time, a three-dimensional grid in depth is generated. Horizons of this 3D depth grid will be converted to structured horizons and then will be used to produce surfaces which are compatible with previously mentioned three-step geological modelling embracing the provided fault model with 32 fault segments.

### 5.3.1.4 Property Modelling

The central objective of property modelling is to distribute continuous petrophysical properties between available wells to realistically preserve the reservoir heterogeneity. There are two main steps to do property modelling for a depth-converted 3D structural model: (a) scaling up the well logs and (b) petrophysical modelling. In the first stage a new property layer will be made based on the wire-line log information of all selected wells and it will be scaled up to assign this property to all structural zones using the statistical Gaussian Random Function Simulation (GRFS) method. The available wire-line logs that were used for property modelling were Sonic (DT), Neutron Porosity (NPOR), Density (DEN), Gamma Ray (GR), and Spontaneous Potential (SP). Digital format of these wire-line logs was imported and then their quality was checked before petrophysical analysis. Quality control involved checking the unit consistency and accuracy, depth shifting, and any errors in scaling or digitization. Using an arithmetic average for upscaling wire-line logs, for instance, density is determined based on the well log information as input and then will be scaled up to assign this property to all structural zones.

The homogenous nature of petrophysical properties across scales is an initial assumption for property modelling. Accordingly, an experimental variogram with isotropic distribution will be used to determine the range and the nugget of the specific petrophysical attribute that is going to be modelled. The extracted information based on specific variogram are critical input parameters for property estimation and stochastic simulation [[Schlumberger, 2010](#)]. For petrophysical modelling in the Surat Basin with spatially variable petrophysical properties across the field, the spherical variogram was used and the property estimation was conducted using the default variogram distribution ([Table 5-4](#)).

**Table 5-4: Setting up variogram analysis for petrophysical modelling**

| Variogram Analysis for Petrophysical Modelling |                                     |
|------------------------------------------------|-------------------------------------|
| Analysis method for Zones                      | Gaussian Random Function Simulation |
| Variogram Type                                 | Spherical                           |
| Variogram Total Sill                           | 1.0                                 |
| Variogram Nugget                               | 0.0001                              |
| Anisotropy Range                               | Major Direction : 17700 m           |
|                                                | Minor Direction : 17700 m           |
|                                                | Vertical Direction: 357.5 m         |
| Major Direction Orientation                    | Azimuth: 0 and Dip : 0              |

### 5.3.2 DInSAR Geophysical Inverse Modelling

In order to interpret the surface deformation in terms of volume change at depth, a model of the elastic structure in which the reservoir is embedded is required. The following sections explain the fundamental concepts of the deformation source model and its parameters in more detail.

#### 5.3.2.1 Deformation Source Model

As discussed in the literature review, the PSGRN/PSCMP source model shows several advantages compare to other previously mentioned source modelling tools. First and foremost, in this numerical model there is no restriction on the number of layers that can be used as an input for a multi-layer subsurface medium. The Green's functions database in this model is computed once and can be used repeatedly for deformation modelling with different scenarios as long as the Earth model remains unchanged. By using an orthonormalised propagator algorithm in the PSGRN program, the loss of precision due to the Thomson-Haskell propagator algorithm [[Haskell, 1953](#); [Thomson, 1950](#)] will be avoided. The computation efficiency is increased by using a convergence accelerator technique and the numerical accuracy of the inverse Laplace transform will be improved by using Fast Fourier Transform (FFT). The PSGRN/PSCMP numerical model can be used for complicated geometries with a number of rectangular fault planes with gravity effects included. Ultimately, deformation components and changes at the surface or at a given depth can be extracted in the form of time-series and/or snapshots.

To calculate viscoelastic deformations based on a layered half-space Earth model, two separate programs are executed: PSGRN and PSCMP [[Wang et al., 2006](#)]. The first program is an elastic model that calculates all fundamental time-dependent Green's functions of the given multi-layered half space as an input for the second program. PSCMP performs the convolution integrations and computes the time-dependent deformation, geoid and gravity changes with extended fault planes. The outputs are three displacement components, six stress components, and radial and tangential tilt components, rotation of the horizontal plane, geoid and gravity changes. Together these two programs estimate the fractional volume change for the grid blocks of the model using the least square inversion.

Using geo-mechanical modelling, the surface deformation can be projected into pressure changes within the reservoir [Hodgson *et al.*, 2007; Vasco and Ferretti, 2005]. It is also possible to estimate reservoir properties such as permeability directly from estimated pressure changes [Vasco *et al.*, 2003; Vasco and Ferretti, 2005; Vasco *et al.*, 2001]. However, in this research an alternative approach which is relatively insensitive to the geo-mechanical properties within the reservoir and their heterogeneity will be used to investigate the subsurface structural behaviour in terms of volume change in the Surat Basin, across locations that showed significant surface deformations.

### 5.3.2.2 Model Parameters

Compared to other source models with elastic half-space and constant properties, the PSGRN model is a layered overburden structure that needs compressional velocity (P-velocity), Shear velocity (S-velocity), and density ( $\rho$ ), all extracted from seismic observations (see Table A-7 in Appendix A2). A “layered overburden”, otherwise known as flat elastic layers framework, is assumed to be present. P-velocity ( $V_p$ ) can be extracted from the sonic logs, and S-velocity ( $V_s$ ) can be extracted from P-velocity ( $V_p$ ) according to an experimental relationship ( $V_p = \sqrt{3}V_s$ ), whereas density wire-line logs will be used to estimate an approximate density in each layer. The transient viscosity ( $\eta_1$ ), steady-state viscosity ( $\eta_2$ ), and ratio between the effective and the unrelaxed shear modulus ( $\alpha$ ) will be assumed constant for all subsurface layers.

For the PSCMP program, the parameters for a rectangular sub-fault are introduced in Table A-8 in Appendix A2. Uniform regional principal stresses  $\sigma_1, \sigma_2$  and  $\sigma_3$  are the outcomes of this program by assuming that the master fault is optimally oriented according to the Coulomb failure criterion. The displacement, stress and tilt components, being outcomes of PSCMP, are time series with the time window similar to the one that was used for the Green’s function. Each of these outcomes is assigned to their specific Green’s function.

The first stage in the modelling procedure (Figure 5-5) is to extract the equations for the elastic boundary-value problem. Then, partial differential equations governing the deformation field are converted into a set of ordinary differential equations in the wave number domain using the Hankel transform [Piessens, 2000]. Consequently, in wave number domain, the problem will be solved by the Thomson-Haskell propagator algorithm after satisfying the source and boundary conditions, and subsequently, the deformation field in the spatial domain will be extracted from the inverse Hankel transform. By calculating the Green’s functions for four different dislocation centres (i.e. the strike-slip, the dip-slip, the compensated linear vertical dipole (CLVD), and the point inflation) at different depths, any finite dislocation can be modelled using linear superposition. Except for inverse Hankel transform all calculations are based on analytical methods while in practice, both procedures are carried out numerically.

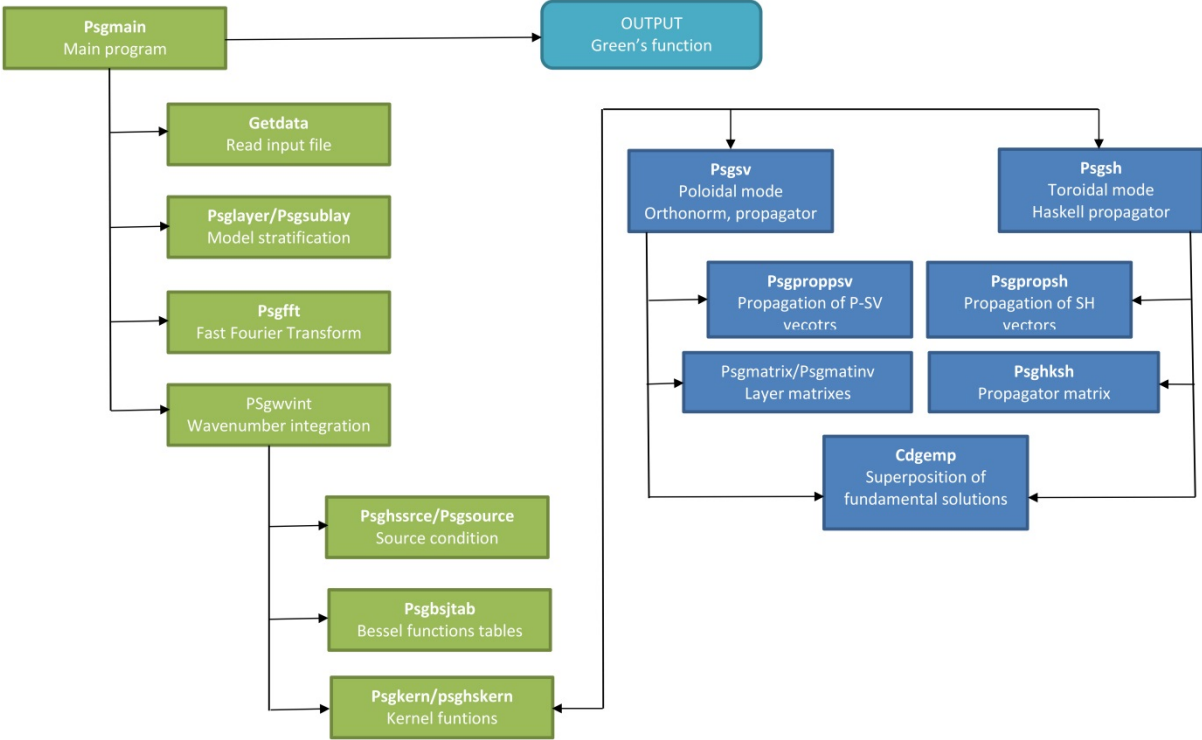


Figure 5-5: The flowchart of major subroutines in PSGRN program [after Lorenzo-Martin 2006]

In the static elastic case, the Thomson-Haskell propagator algorithm can be adopted to compute the spectral Green’s functions, and then the Fast Fourier Transform (FFT) can be used to estimate the time-dependent inelastic Green’s functions. Coupling between the surface deformation and the Earth’s gravity field can be performed in this source model resulting in extracting deformation components (displacement, stress, and tilt) and gravity-geoid changes [Lorenzo-Martin, 2006]. In sum, this tool can be used to determine the surface and subsurface time-dependent deformation (Figure 5-6), as well as changes in the geoid and gravity, produced by dislocation sources embedded in a mixed elastic or inelastic layered half-space.

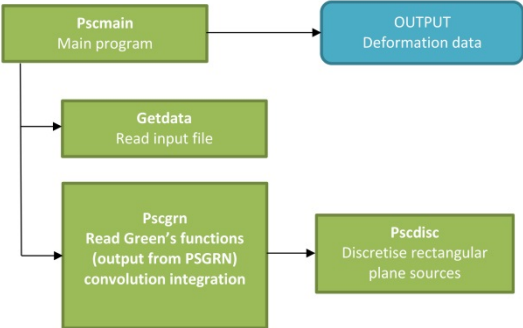


Figure 5-6: The flowchart of major subroutines in PSCMP program[after Lorenzo- Martin 2006]

The inverse problem is solved by the “linear least square” approach and its outcome is the fractional volume change of each grid block within the layer that will lead to the observed surface

deformation. The fractional volume change model attempts to represent the source as a grid, either two or three dimensional, with rectangular blocks that undergo variable volume change. This approach works best if the source of volume change like the coal layer is two dimensional. There is also an option for regularizing this model by setting grid blocks intersected by injection and production wells to implement the volume of fluids.

To estimate volume changes, the reservoir layer will be divided into grid blocks. For each element, a vector that relates volume changes of that grid block to all the measurement points will be generated. Then volume change can be inferred by solving a linear system for each grid block element as a matrix. For an elastic overburden, the relationship between the displacement vector  $u_h$  (quasi vertical) and the volume changes in the grid blocks  $v$  will be formulated as follows with the certain constraint:

$$\begin{aligned} u_h &= G_h v, \\ v &\geq 0, \end{aligned} \tag{5.4}$$

where  $G_h$  is the vertical Green's function and the condition is for injection [Vasco *et al.*, 1988]. The layered model that is used here is the same as the elastic model plotted in Vasco *et al.* [2010] that can be used for both uplift and subsidence. To solve the inverse problem for fluxes in the reservoir volume, the reflective Newton's method [Coleman and Li, 1996] was used with the minimization of a quadratic function subject to inequality constraint  $v \geq 0$  [Rucci *et al.*, 2010; 2013].

According to previous investigation using this source model [Rucci *et al.*, 2013], the sensitivity of the surface deformation to a dislocation source within the Earth is a strong function of its depth. In other words, surface observations are most strongly influenced by the aperture and volume changes closest to the surface. According to Rucci *et al.* [2010], due to data distribution, data uncertainty, Green's function, and distance weighting in the regularization, the largest errors associated with model parameters occur near the injection wells and are extended along the reservoir layer. In addition, the layered velocity structure and large variations in elastic properties impose larger errors at or below the reservoir depth and in the horizontal direction with significant impact on the surface deformation [Vasco *et al.*, 2010].

## 5.4 Results

### 5.4.1 Subsurface Structural Modelling

In this section, the results of subsurface structural modelling including depth map of each subsurface formation that extracted from seismic interpretation and converted from time to depth by using the velocity model, calculated isopach (thickness) map, and the 3D view of the geological

model with structural faults included will be presented. Using wire-line logs and property modelling, the spatial distribution of compressional velocity, shale formation, density, and porosity is shown.

### 5.4.1.1 Depth and Isopach Maps

In structural geology, thickness maps represent variations and trends for given stratigraphic units. These maps are grouped into two different types: isochore and isopach maps. An isochore map is a contour map that connects points with the same vertical thickness, while isopach maps show contours that connect points with equal true thickness measured perpendicular to the bedding.

When working with seismic surveys and wire-line logs in the Surat Basin, formation vertical thickness can be estimated through measured True Vertical Depth (TVD) in the well. Figure 5-7(a) shows the Gubberamunda Sandstone depth map resulted from seismic interpretation and velocity modelling along with isopach map between Gubberamunda Sandstone and Westbourne Formation (both in metric units) that is presented in Figure 5-7(b).

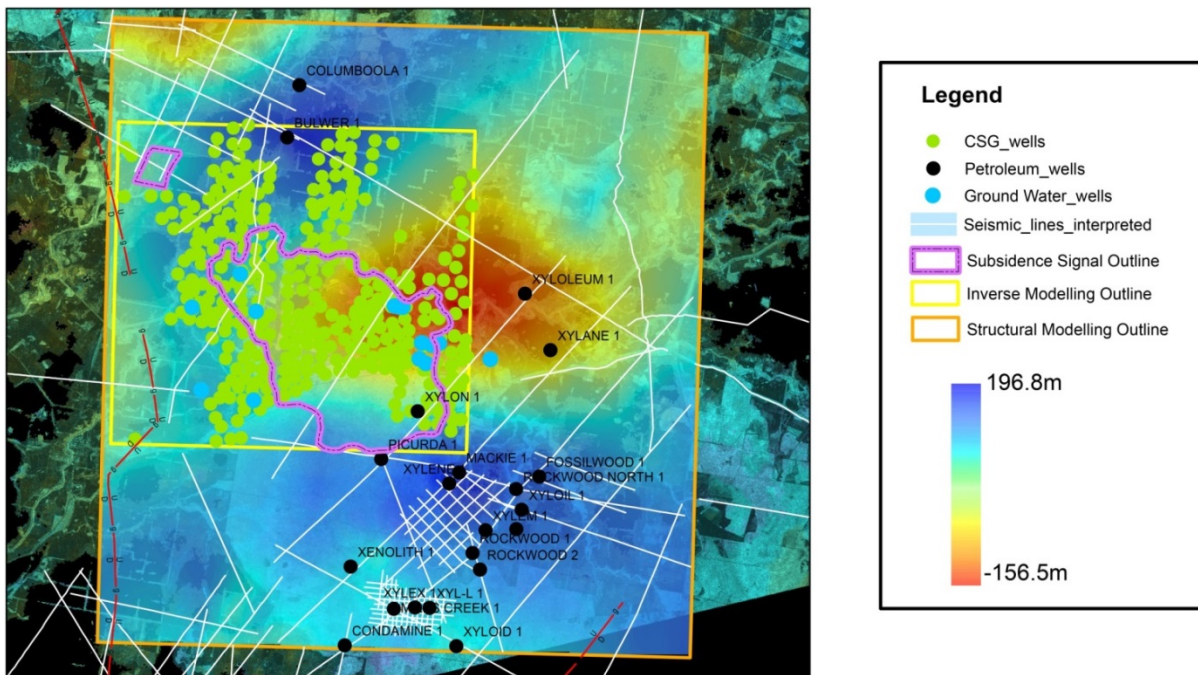


**Figure 5-7(a): Vertical depth map of the Gubberamunda Sandstone formation in the study area. This map was extracted from seismic interpretation and velocity modelling steps.**

The depth maps show the depth variations in the subsurface formations from Gubberamunda Sandstone as the top layer to Basement as the very lowest formation. As shown, both Hutton Sandstone and Evergreen Formation are deep layers in the region with settlement while other formations in the study area are shallow. In order to evaluate the thickness maps in the modelling outline over the deformation area, two zones, i.e. Springbok Sandstone-Walloon Coal Measures and

Precipice Sandstone-Basement have the largest thicknesses while the thickness in other zones varies only slightly.

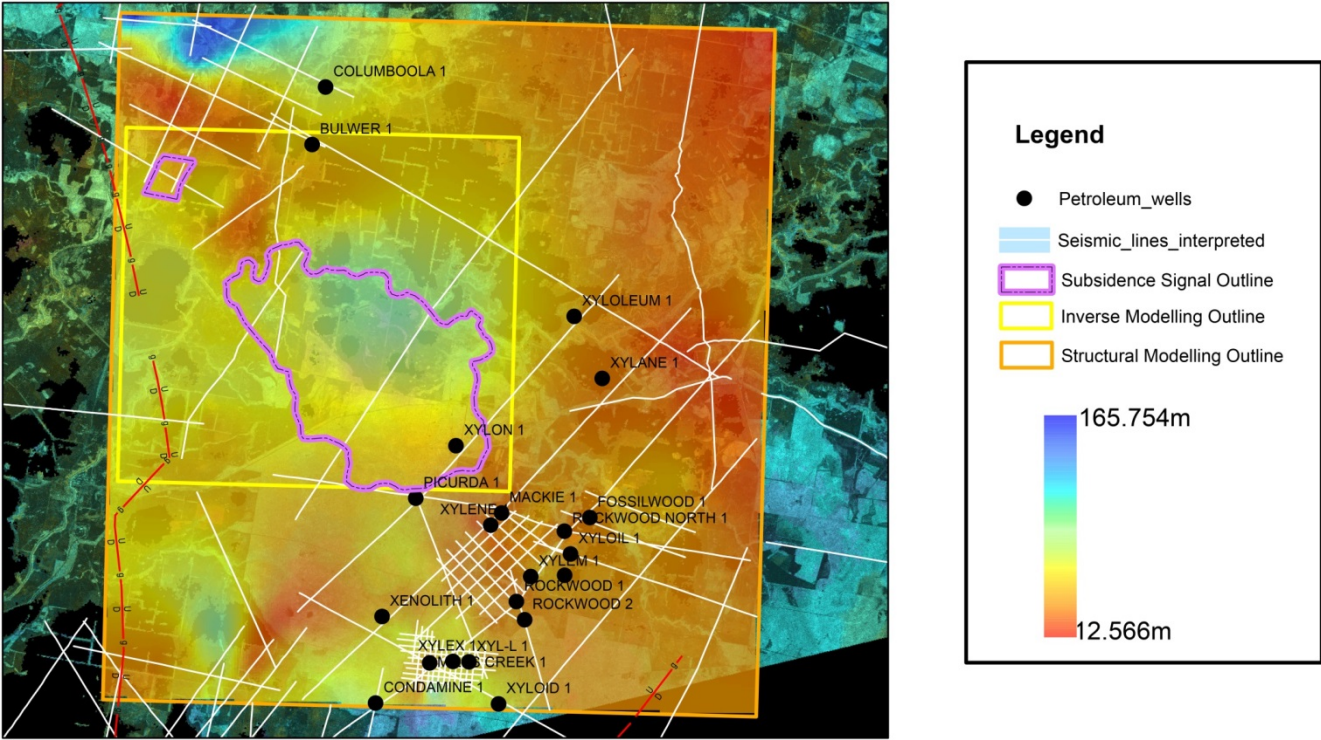
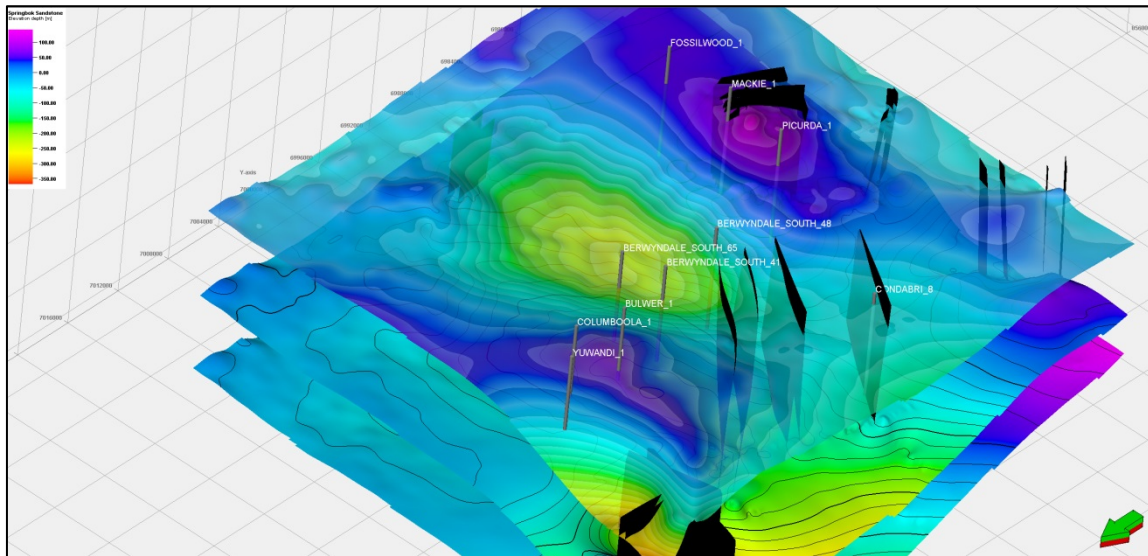


Figure 5-7(b): Isopach map for the Gubberamunda Sandstone and Westbourne Formation in the study area. This map is extracted from seismic depth conversion.

5.4.1.2 Three-dimensional Structural Model

It is necessary to establish a boundary for the model and internal horizons before starting to make a structural modelling framework. For the proposed area the boundary was selected based on available seismic dataset and well information and covers an area of 35 km by 35 km (1274 sq.km) in the north-western part of the region that was previously monitored by ALOS-PALSAR satellite images. For three-dimensional modelling, early Cretaceous Gubberamunda Sandstone as well as early to late Jurassic Westbourne Formation, Springbok Sandstone, Walloon Coal Measures, Hutton Sandstone, Evergreen Formation, Precipice Formation, and Basement were set as the fundamental eight horizons for the model. Creating Cartesian stratigraphic grids provides the geostatistical framework for subsequent property and petrophysical modelling. For this study, the x and y cell dimensions were assigned to 150 × 150 m<sup>2</sup> for sustaining both computational constraints of modelling and providing reasonable geological continuity. All available datasets, such as wire-line logs and seismic data, were then conditioned to this Cartesian grid. In a three-dimensional model to define the boundary surfaces for each stratigraphic unit, developing a surface for the top of each stratigraphic unit is essential and the base of this unit will be the top of the underlying unit [Raiber et al., 2012]. By assessing the

distribution in each cross section, well logs and seismic surfaces were loaded and a digitization process carried out, which assessed the distribution of each stratigraphic unit from the base (Basement) to the top (Gubberamunda Sandstone), as well as the distribution of the main structures such as faults. In addition, for vertical layering, the gridded eight layers were divided evenly into seven zones.



**Figure 5-8: Three-dimensional view of the entire region with structural faults (black colour) that were traced on seismic sections.**

As shown in Figure 5-9, the three-dimensional grid in depth is generated from a three-dimensional grid in time using the pre-defined velocity model. This 3D grid is then converted to the data presented in Figure 5-10, which is the result of three-steps in geological modelling using available stratigraphic horizons and fault modes with 32 fault segments.

Primary limitations in this three-dimensional geological model are due to uncertainties that are propagated throughout the model. The major sources of these uncertainties are data quality and distribution, interpolation method, and model constraints. Sparse data distribution in the proposed area of the Surat Basin can result in less precise interpolated values for the areas that lie between known values. Based on the chosen interpolation method, the resulting values will vary. In the current three-dimensional geological model, as presented in Figure 5-10, two zones of low confidence in certainty have been identified. One is located near the north-eastern corner of the model domain and the other is in the central part of the model domain where limited well control data and seismic section exist. The second area also corresponds to the region that shows maximum surface deformation in ALOS-PALSAR interferometric analysis.

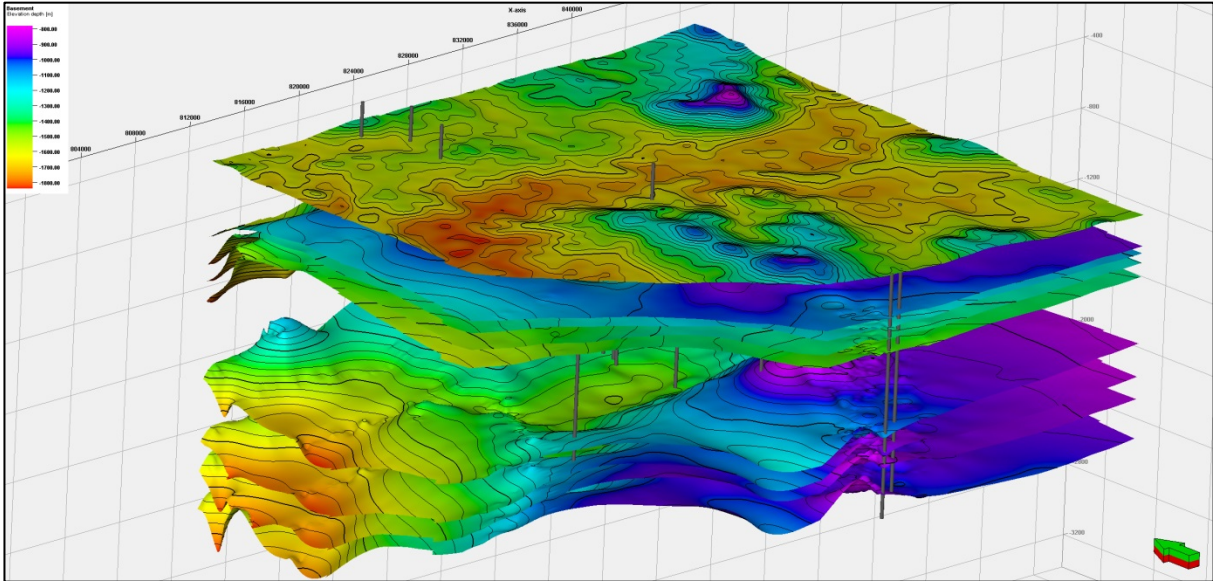


Figure 5-9: 3D view of eight horizons in depth domain converted by using the velocity model and well-bores that were involved for subsurface down-hole information.

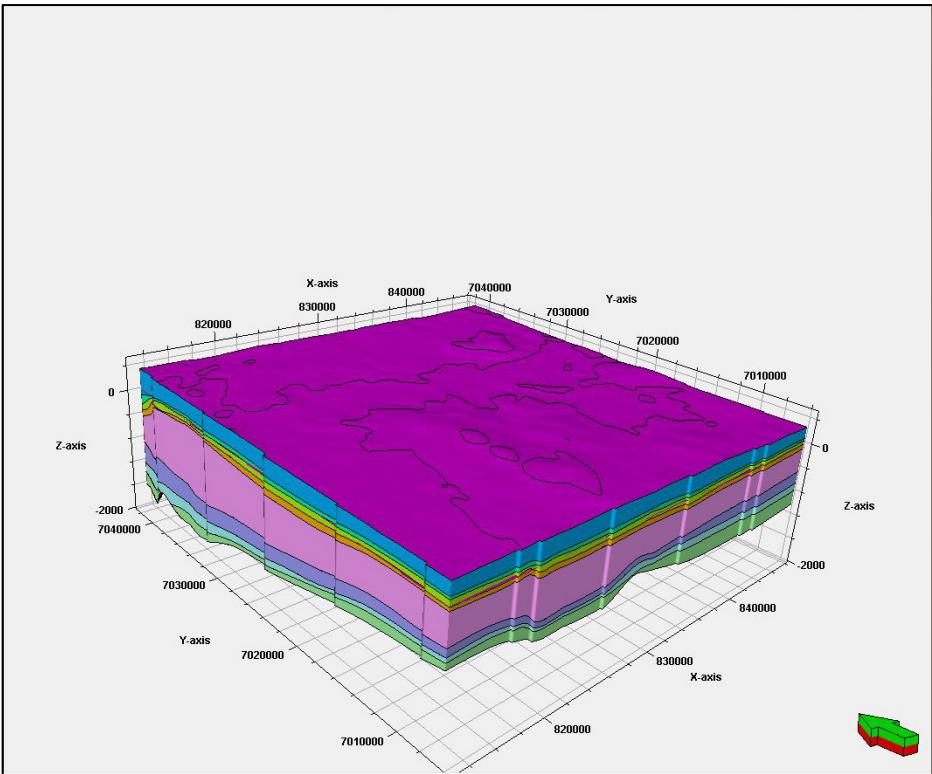


Figure 5-10: Three-dimensional view of the structural model based on available seismic interpretation and well log data trended with stratigraphic well tops in depth domain.

### 5.4.1.3 Property Modelling Based on Well-bore Data

A number of formation properties will be estimated in the following sections using available wire-line log information for the proposed modelling outlined in the Surat Basin. Kriging is a standard geostatistical method for deterministic simulation of the distribution of these properties. It relies on the spatial relationship in the dataset that can be recognized through variogram data analysis. The goodness of fit for Kriging in geostatistics is highly dependent on sufficient knowledge of the modelling subject, and on the context of the data to minimize the uncertainty at the unsampled locations. These criteria were not well satisfied with the available data for the Surat Basin, but it could capture the heterogeneity of the system as a viable petrophysical modelling option.

#### 5.4.1.3.1 Sonic Logs and Seismic Velocity Distribution

Acoustic or Sonic logs which are lowered on a cable into a borehole are designed for measuring formation porosity and compressional wave velocity of the adjacent rock units. Such logs show the velocity variation in individual beds as a crude depiction of vertical variability of the rock sequences. The unit for sonic compressional wave slowness is microseconds per feet with high apparent porosity values in coal seams, with about 120msec/ft. ( $\sim 39.97 \times 10^{-5}$  sec/m in SI units).

As shown in [Figure 5-11](#) and [Figure 5-12](#) the spatial distribution of compressional velocity ( $V_p$ ) in the proximity of Condabri 8, 9 is very low (i.e. 0.2 m/sec) while in the deformation area the values range from 0.6 to 0.9 m/sec. The sonic distribution changes abruptly in the area of interest, but it is compatible with  $V_p$  distribution. The values with low range between 94 and 102msec/ft ( $\sim 31.30 \times 10^{-5}$  sec/m and  $33.97 \times 10^{-5}$  sec/m in SI units) are showing formations with coal.

#### 5.4.1.3.2 Porosity Estimation

Several well logs such as sonic, density, and neutron wire-line data can be used for quantitative estimation of porosity. Although it is assumed that acoustic methods such as sonic logs are more sensitive to porous formations, and neutron and density logs can estimate total porosity and the sensitivity of sonic logs in carbonate lithologies is not completely confirmed. For deep saline aquifers with 100% water saturation, resistivity logs might be more useful for quantitative estimation of porosity [[Eisinger and Jensen, 2009](#)].

In [Figure 5-13](#) the spatial distribution of neutral porosity estimated from neutron wire-line logs is shown within the Walloon Coal Measures. Except for the north and south parts of the region with high porosity formations, most of the region is covered with medium to low porosity. Within the area with settlement signal, the porosity values range is 31 to 37 PU (porosity unit) equivalents to 31 to 37 percent indicating fair porous formations.

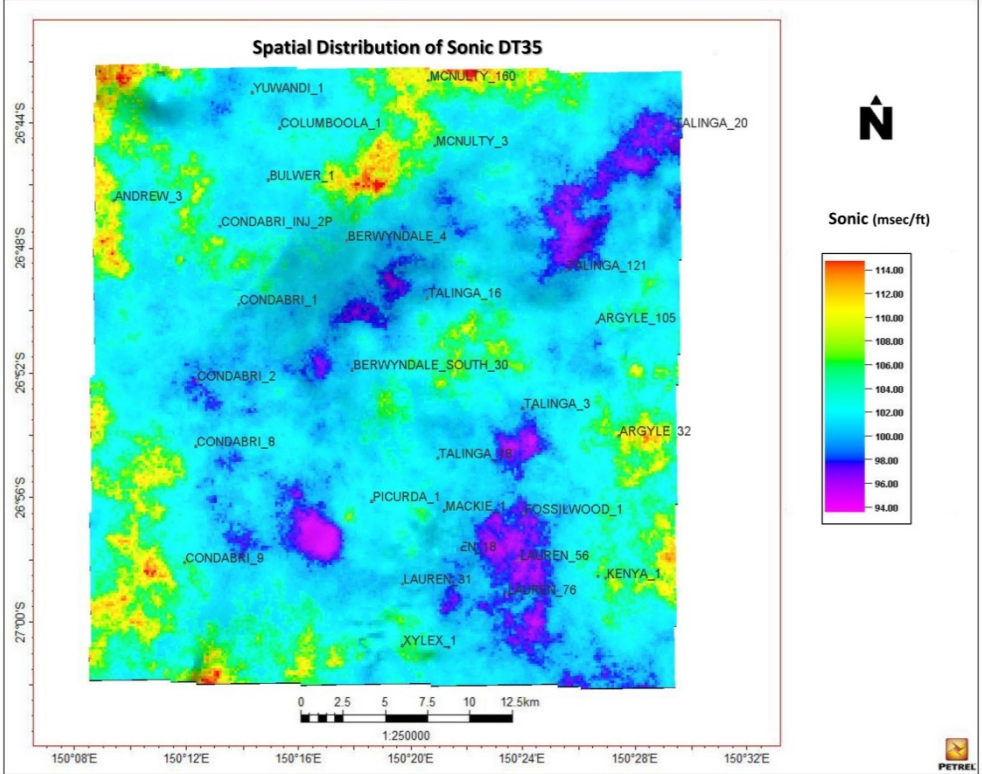
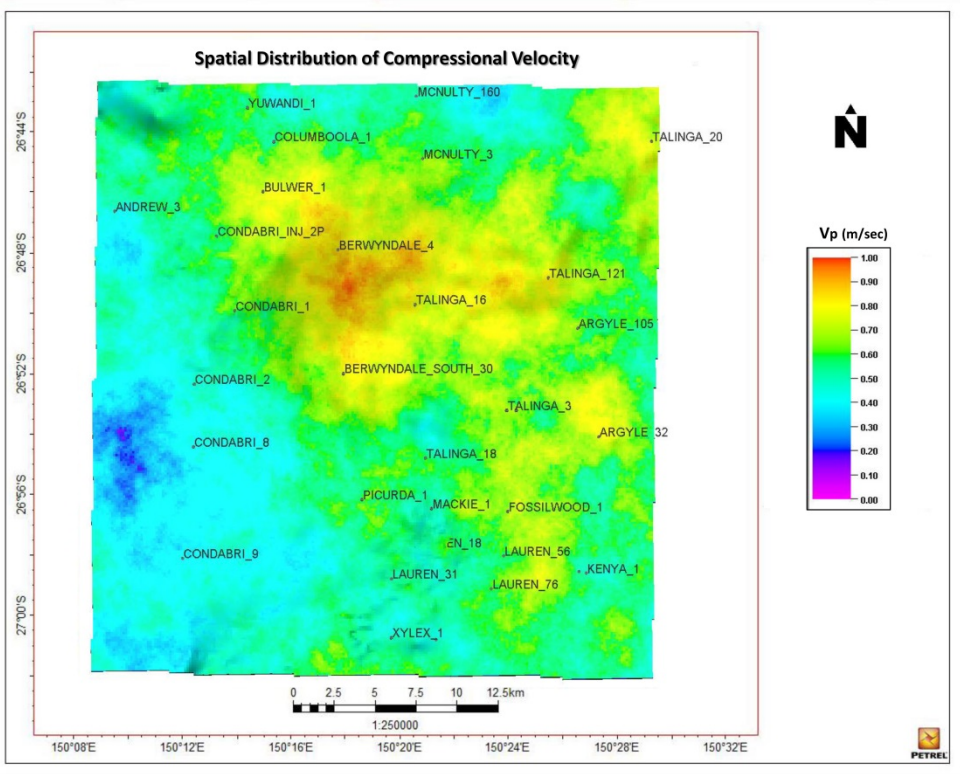


Figure 5-11: Spatial distribution of compressional velocity over the entire modelling region within the Walloon Coal Measures layer. As it is shown the compressional velocity has the lowest value in the south-western part of the study area, but over the deformation area the values are quite high.

Figure 5-12: Spatial distribution of sonic log over the entire region within the Walloon Coal Measures layer. As it is shown the values are the lowest in the proximity of the deformation region and change abruptly from south to north.

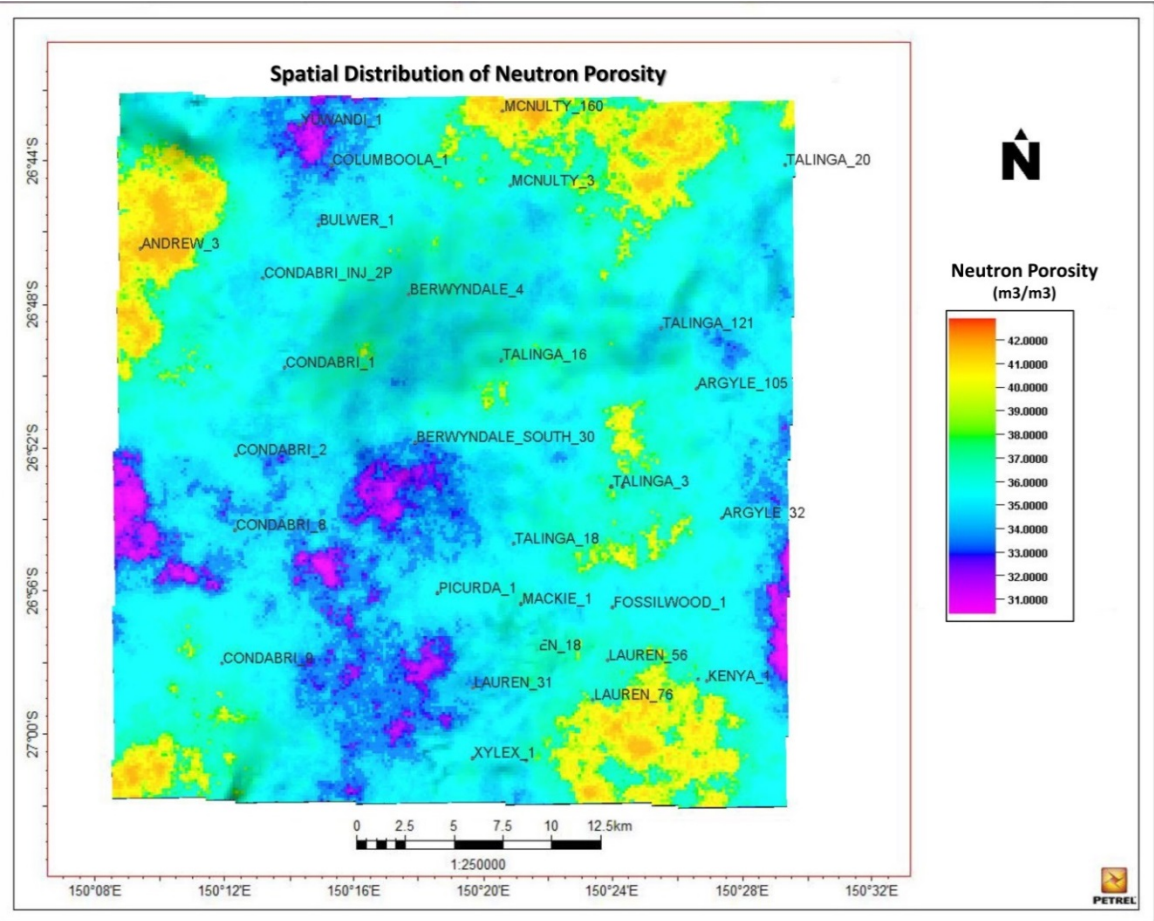


Figure 5-13: Spatial distribution of neutral porosity over the entire outline for geological modelling. While the majority of study area covered with medium neutral porosity formations, the area with deformation signal shows both high and medium porous formations.

5.4.1.3.3 Gamma Ray Distribution

The Gamma Ray (GR) log is one of the primary geophysical logs, measured in American Petroleum Institute (API) units. These logs are calibrated based on the limestone gamma ray emission. The primary use of GR logs is to distinguish reservoir rocks from shales [Scholes and Johnston, 1993]. Generally, GR has a high signal over shaly formations while sandstone has low GR footprints. The siltstone is a type of formation that presents with medium GR signal. Shales with little or no permeability cannot produce fluids and they will have higher radiation than other rocks with developed pore space.

As shown in Figure 5-14, areas with green colour show medium to high GR response and represent the shale. These shaly formations are located over the areas with surface deformation that were detected by InSAR previously. However, areas with blue colour correspond to the low GR response or reservoir rocks such as sandstone with high permeability.

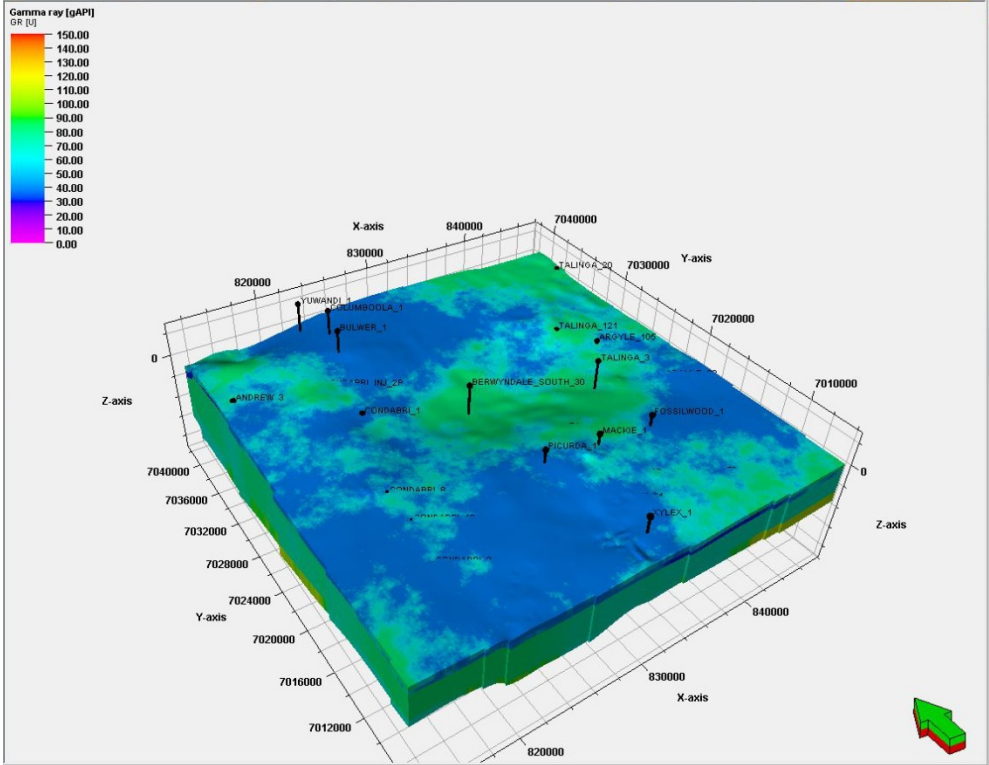


Figure 5-14: Spatial distribution of gamma ray response in three-dimensional view. It is shown that the GR values in area with deformation vary between 60 and 100 gAPI.

5.4.1.3.4 Density Estimation

A formation density log is a qualitative indicator of the relationship between the geological formation penetrated by the well and the equivalent seismic section. The primary objective of using density logging is to measure the traditional formation porosity, but it can also identify coals. Because of the low density of coals, density logs read low density and very high apparent porosity in coal seams [Scholes and Johnston, 1993]. Density logs can also be used for estimating overburden stress. As these logs are not usually recorded at shallow depth, some empirical methods can be employed to calculate the rock density at shallow depth.

In situ stress measurements show that there is a linear relationship between vertical stress (MPa) and depth (m) as follows [Peng and Zhang, 2007]:

$$\sigma_v = (1.9 \pm 1.26) + (0.0266 \pm 0.0028)z, \tag{5.5}$$

$$\sim \sigma_v = 0.027z,$$

Figure 5-15 shows that the density values change between 1.8 and 2.4 g/cm<sup>3</sup> with yellow to red colour in the centre of the region with deformation signal. These values are in the range of compacted shale density. Compared to these dense areas, the concentration of coal seams is higher in the

surrounding areas with low density values and high apparent porosity in the southwestern corner of the image.

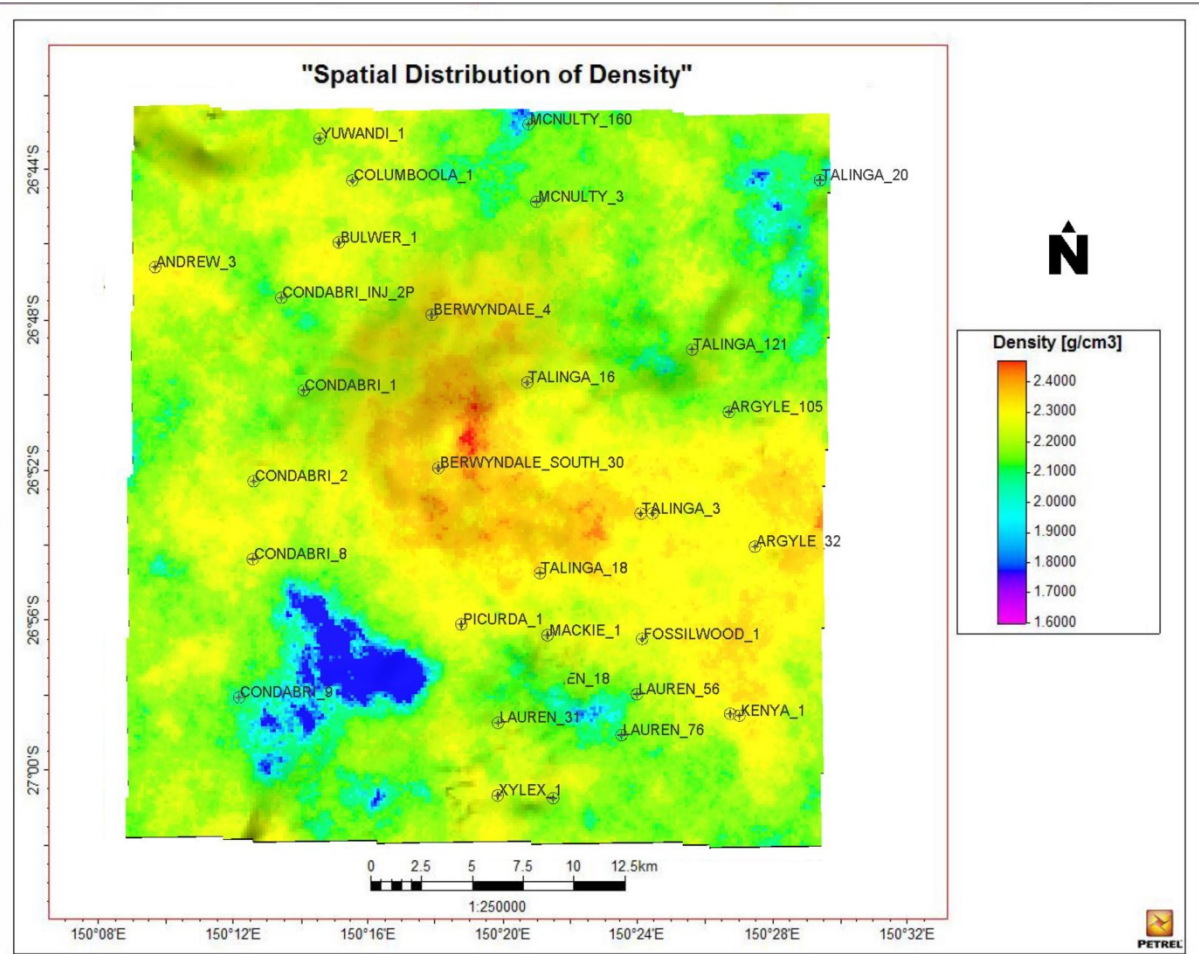


Figure 5-15: Spatial distribution of density over the modelling area at Walloon Coal Measures depth (~ -400m) in g/cm<sup>3</sup> upscaled for the well-bore column in the subsurface model.

5.4.1.3.5 Spontaneous Potential (SP) Distribution

Spontaneous Potential or self-potential log (SP) is one of the well logs to characterise lithology. This log measures small electric potentials in millivolts between the reference voltage at the surface and voltage at different depths in the borehole. The SP tool is one of the simplest logging measures that can be used to define the formation boundaries, to locate permeable formations and to estimate the formation-water resistivity. Under right conditions, SP with great values of water resistivity ( $R_w$ ) in the formation can be a source to identify the presence or absence of hydrocarbon-bearing formations [Scholes and Johnston, 1993].

Figure 5-16 shows that the SP values show an even distribution in the northern and southern parts of the deformation signals with the values changing from -200mV up to 300mV. Conversely, the SP values drop significantly to zero at the center of the study area where Berwyndale South\_30 CSG well

is located. This indicates that there is an east-west trend for the presence of hydrocarbon bearing formations in the area and that trend is located either over or close to the deformation districts.

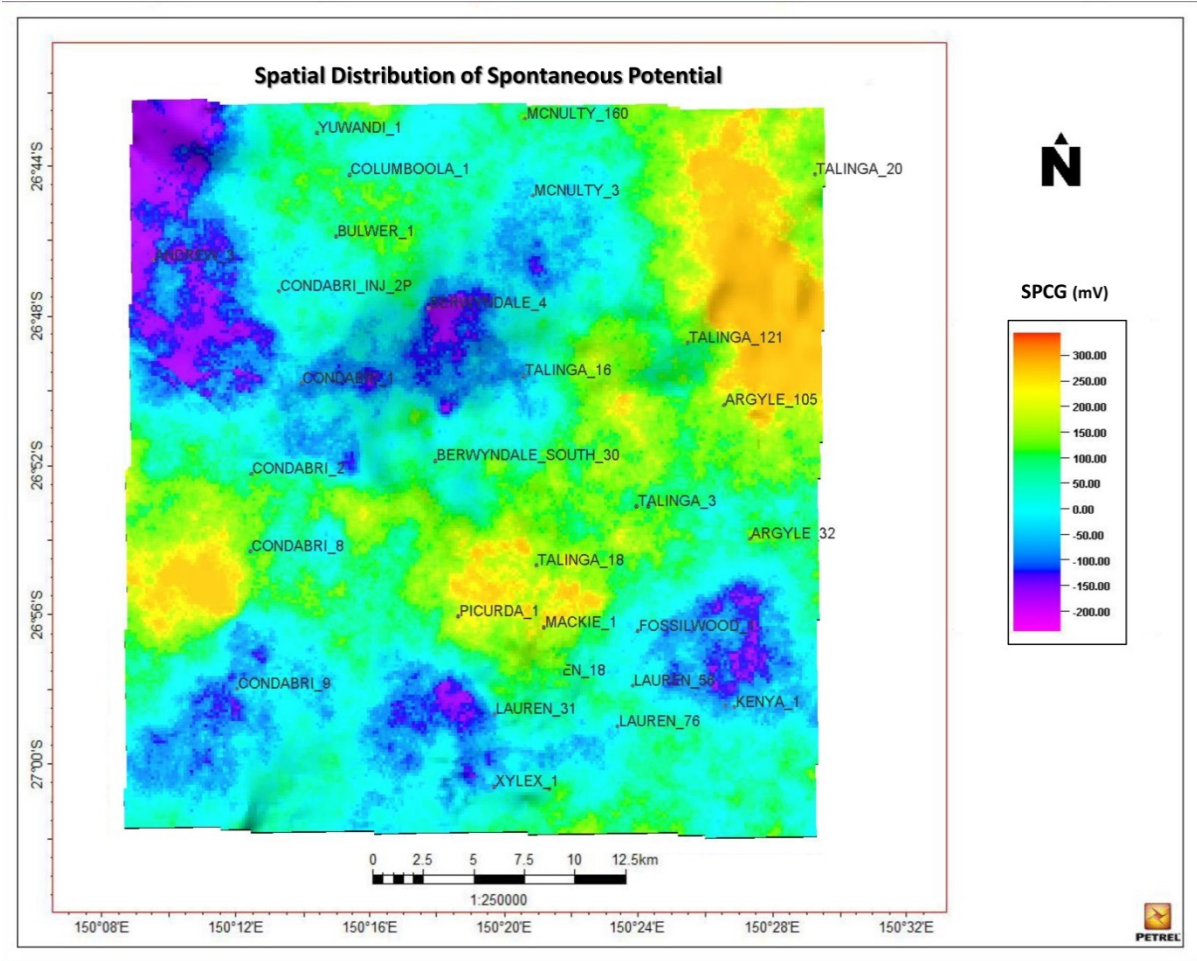


Figure 5-16: Spatial distribution of Spontaneous Potential (SP) over the outline of modelling with the highest values in the proximity of Condabri\_8, Picurda\_1, and Talinga\_121 within the Walloon Coal Measures.

5.4.1.3.6 Pressure Data Analysis

Pore pressure in a formation is part of overburden pressure and it is not supported by the rock matrix, but by gas or fluid in the pore spaces. Normal pore pressure at a specific depth is the hydrostatic pressure of a water column from that depth to the surface. If the pore pressure is less than the hydrostatic pressure, the formation will be sub normally pressured while if the pore pressure is higher than hydrostatic pressure, the formation will be abnormally pressured. Normal hydrostatic pressure typically corresponds to reservoir original pressure, i.e. the pressure that existed before any disturbance due to production. Therefore, any deviation from the pressure normal trend is called abnormal pressure. Formation pressure is pressure acting upon fluids in the pore space of the formation. When formation pressure ( $\cong$  pore pressure) is lower than hydrostatic pressure, the

formation is in sub-pressure status while for over pressurized reservoirs the formation pressure is higher than hydrostatic pressure.

In Figure 5-17 the pressure-depth plot extracted from CSIRO’s PressureQC™ system is shown to evaluate the petroleum formation pressure data in detail and to interpret the consequent impact of each data point in the geomechanical model results. Although for evaluation of reservoir system, pressure data can be supplemented with formation water analyses and formation temperature but in the Surat Basin the lack of these measurements is significant. As it is shown the overall pressure-depth trend of the available downhole measurements in the Surat Basin (solid purple line) is less than the hydrostatic pressure gradient (9 kPa) and lithostatic (overburden) pressure gradient (2.25 kPa).

In other words, the formations including reservoir in the Surat Basin is sub-pressure and the selected wells for 3D modelling (Bentley\_1, Cooloomala\_1, Mackie\_1, Xylex\_1) follow this general trend (red dots). Deviation from the hydrostatic pressure gradient as it is shown in Figure 5-17 may be natural, but is more likely to be induced by anthropogenic activities, either related to pumping (i.e. groundwater use or CSG production) or injection. Although in the Surat Basin, ten petroleum wells have formation pressure tests in more than one formation to examine vertical communication between the aquifers, and eight of these wells have significant differences in the hydraulic head values in each formation [Hodgkinson et al., 2010], the majority of these wells are out of the study area and therefore, are not going to be discussed further.

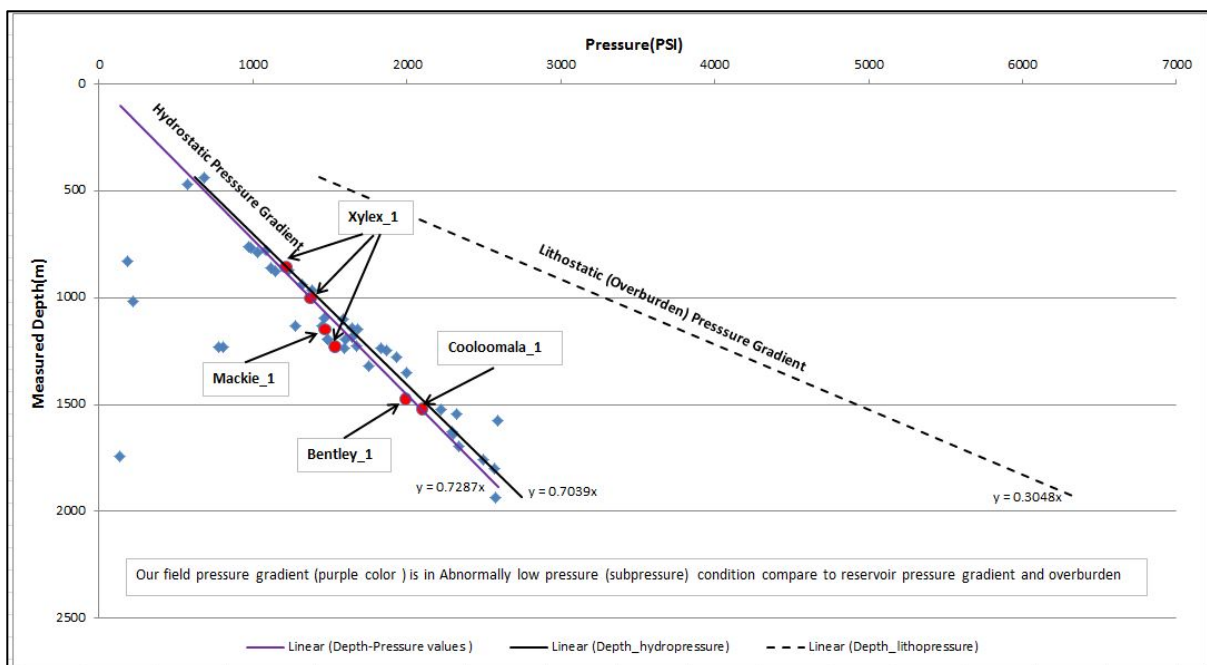


Figure 5-17: Pressure – Depth gradient plot for 31 petroleum wells available in the entire Surat Basin (solid purple line) and its comparison with standard hydrostatic pressure and lithostatic pressure gradients in a reservoir.

### 5.4.2 DInSAR Geophysical Inverse Modelling

In situ geophysical dataset integration with geological and petrophysical information, resulted in a 3D subsurface structural framework comprising stratigraphic layers, structural faults and petrophysical properties such as depth, density, compression velocity and shear velocity of each subsurface formation in the area of interest. The subsurface layer undergoing volume change has elastic properties and is embedded in a layered elastic medium. In order to estimate fractional volume change, the medium elastic properties estimated from the 3D subsurface structural modelling along with surface deformation will be inverted.

Before more discussion on the subsurface structural behaviour and estimation of flux in reservoir volume (i.e. Walloon Coal Measure), major steps of source modelling method are outlined in [Figure 5-18](#). It is shown that the elastic multi-layer model consists of two packages: an inverse and forward modelling package. The inverse modelling part is used for inverting overburden deformation detected by SAR interferometric observation and estimating volume change within the reservoir while the forward modelling part uses the previously estimated volume change to approximate surface deformation. Another outcome of the forward modelling is an impulse response to a volume change in a particular cell (i.e. `pscmp.insar.calc`). It is written out for quality control purposes when computing the sensitivity matrix. In both packages the elastic properties of the subsurface medium attained from 3D structural modelling are as inputs to estimate the Green's functions in PSGRN program while for PSCMP program previously calculated Green's functions as well as available fault properties were used.

For the inverse modelling within the Surat Basin, the model is subdivided into a 30×30 grid of cells with boundaries from 0 to 21 km in both directions (the area for inverse modelling is 21 by 21 km so size of each grid is 700m by 700m). The layers extend from surface to 10 km in depth. Each cell may undergo distinct volume change and the relationship between volume change and surface deformation is given by the system of constraints.

#### 5.4.2.1 Subsurface Structural Behaviour

The elastic properties such as formation depth, formation density, compressional velocity and shear velocity are input parameters to inverse modelling package that are extracted from the three-dimensional structural model. In order to determine the sensitivity of the model to its parameterization, but also to investigate whether this model is suitable for use with SAR data, a synthetic study was undertaken. To examine the impact of changing elastic properties on surface deformation, two synthetic tests were executed. For the first test ([Figure 5-19](#)) the depth of Walloon Coal Measure was changed from 380m in the synthetic deformation map to 780m with increment steps of 100m. For the second set, the density of the WCM was changed in the range between

1526kg/m<sup>3</sup> and 1885.8kg/m<sup>3</sup> (see Figure 5-20). Through these two synthetic tests, it was shown that increasing the density values gradually impacts on the subsidence values in a reverse manner but changing the depth will increase the downward motion. In both sets of images, *range change data* is the real InSAR observations over the area of interest with the maximum downward movement in the centre of the image, and *Forward layer.degrees.calc* is the synthetic deformation map extracted from forward modelling (Figure 5-18).

To interpret the outcome of these two synthetic tests, the residual maps of both sets are shown in Figure 5-21 and Figure 5-22. When varying the depth, the absolute residual values in the centre and lower right corner of the image increased, while the centre of the image displays negative residuals and the lower right corner has positive residuals (Figure 5-21). On the other hand, a variation in the density of coal formation resulted in positive residuals in the lower right corner of the image indicating that an increase in formation density decreases the surface deformation rate (Figure 5-22). According to these two tests and their residual maps, it can be concluded that changing the density and depth of the coal layer (as a reservoir) in the model will not change the resultant deformation map (from forward modelling) significantly. Consequently, the source model at this stage is not sensitive enough for using with interferometric SAR maps only, as an independent source from seismic data to derive the subsurface structure.

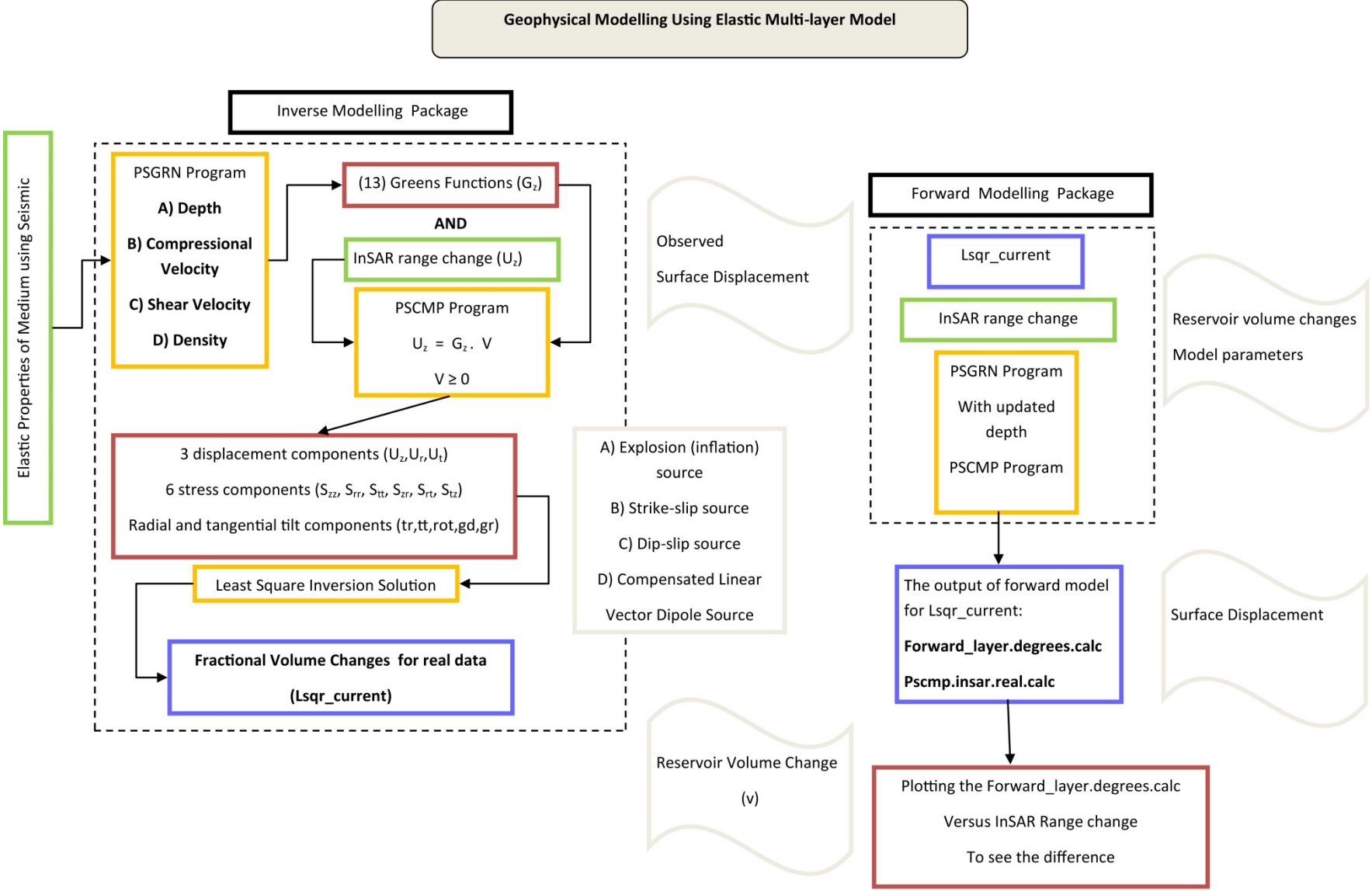
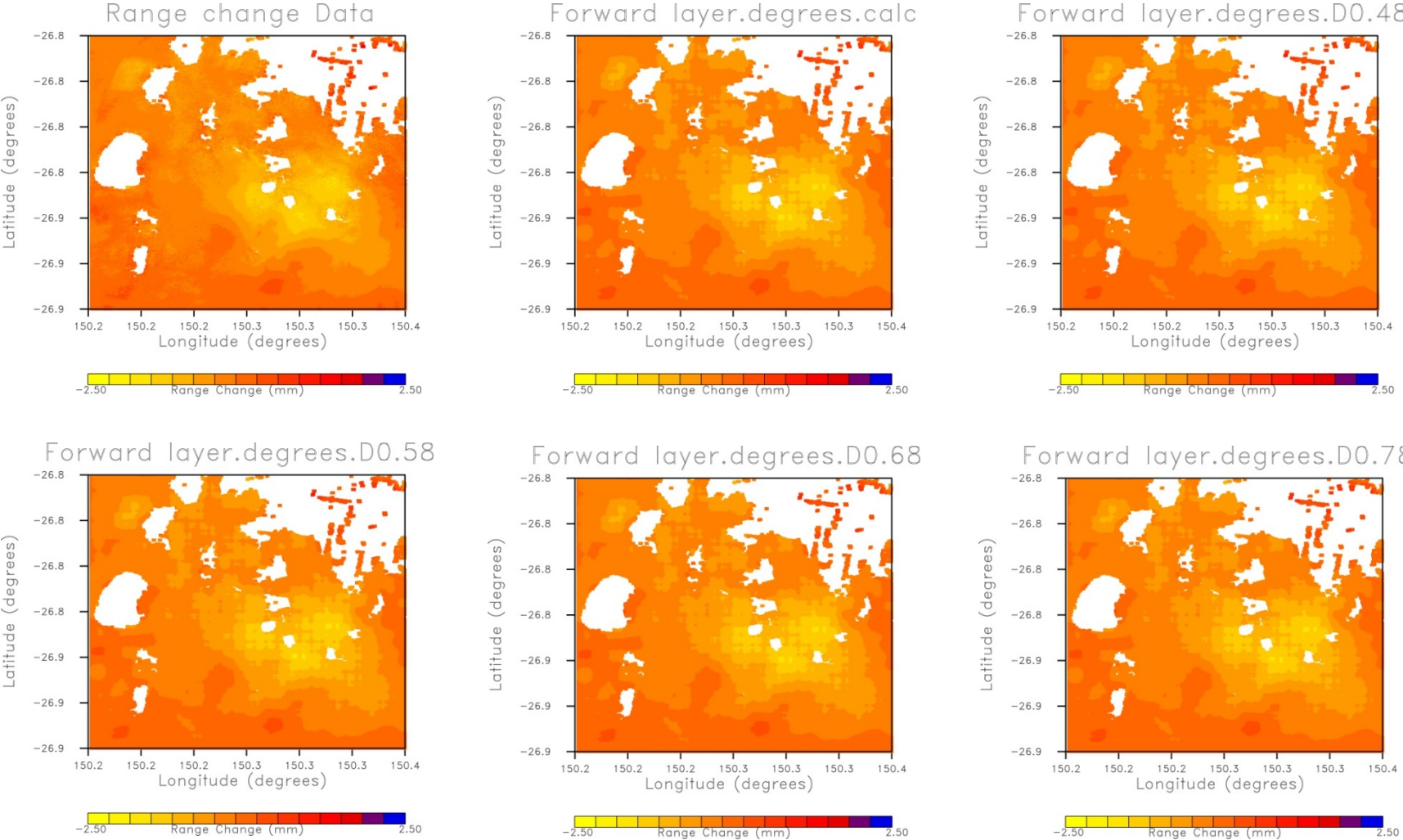


Figure 5-18: Flowchart of the inverse and forward modelling packages to estimate the synthetic data and to calculate the fractional volume change.



**Figure 5-19: The impact of different depths of Walloon Coal Measures (CSG reservoir) on the rate of surface deformation recovery. Range change data is surface deformation observation by SAR interferometry (truth) while others are the outcomes of forward modelling (simulated).**

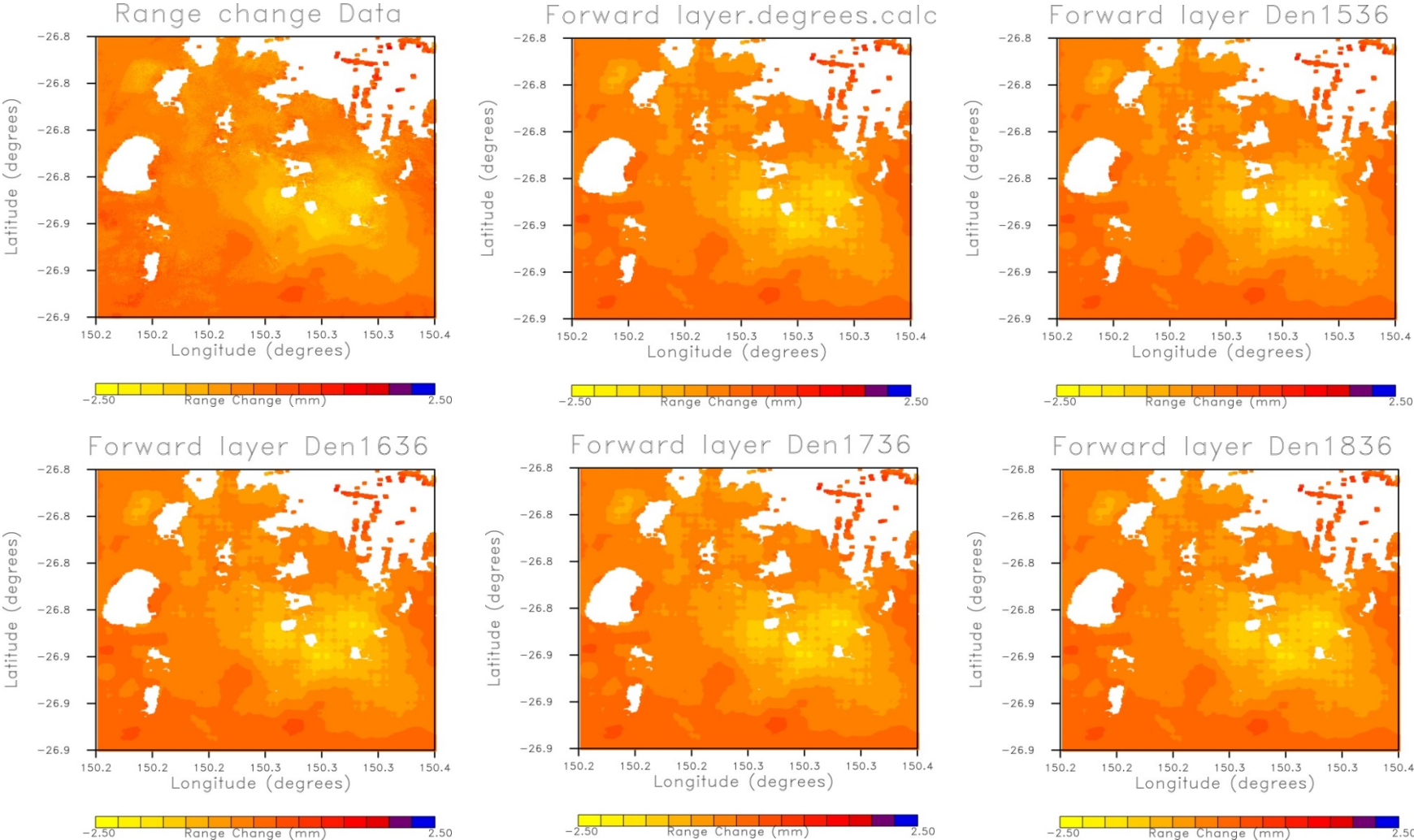
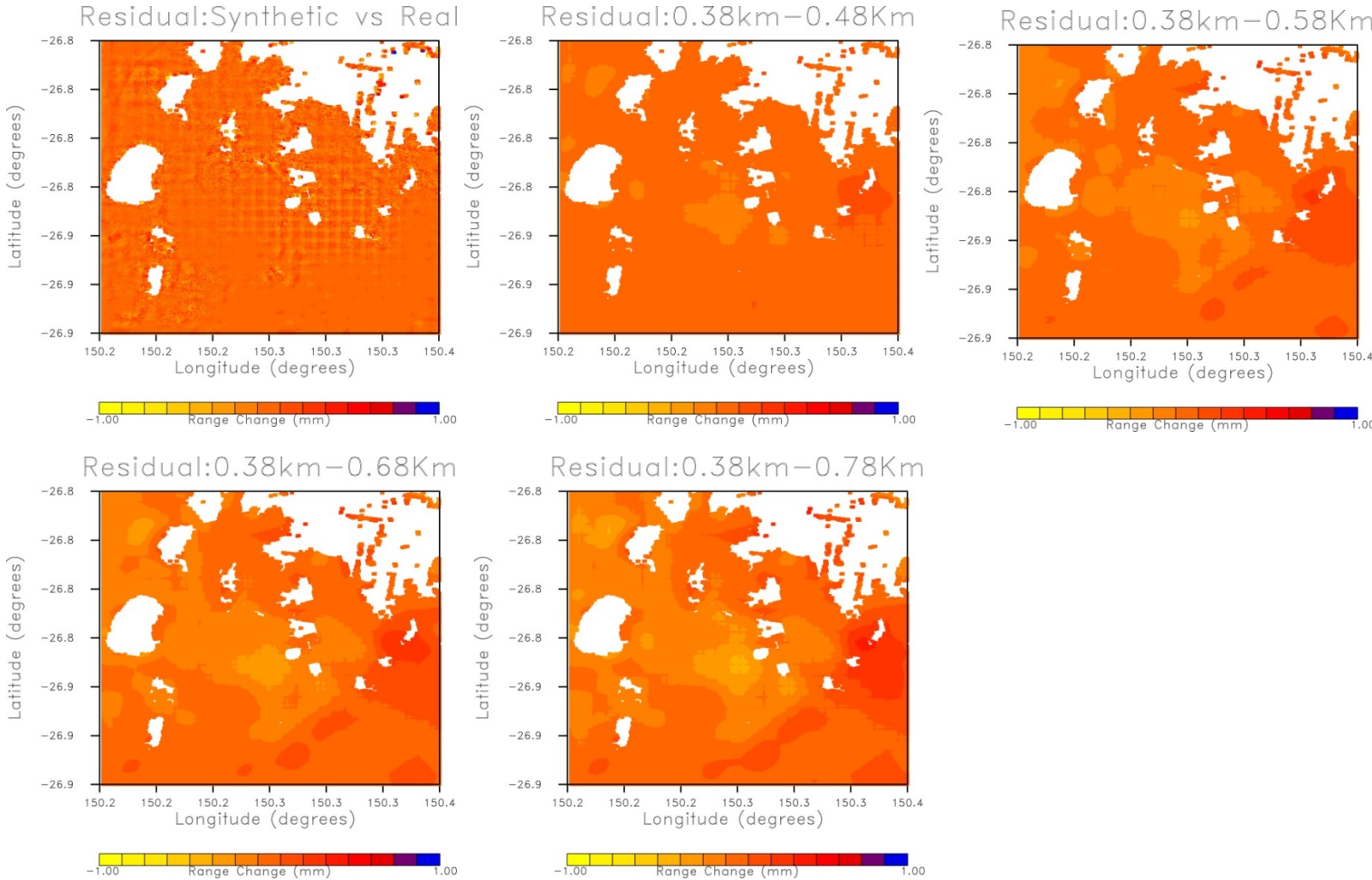
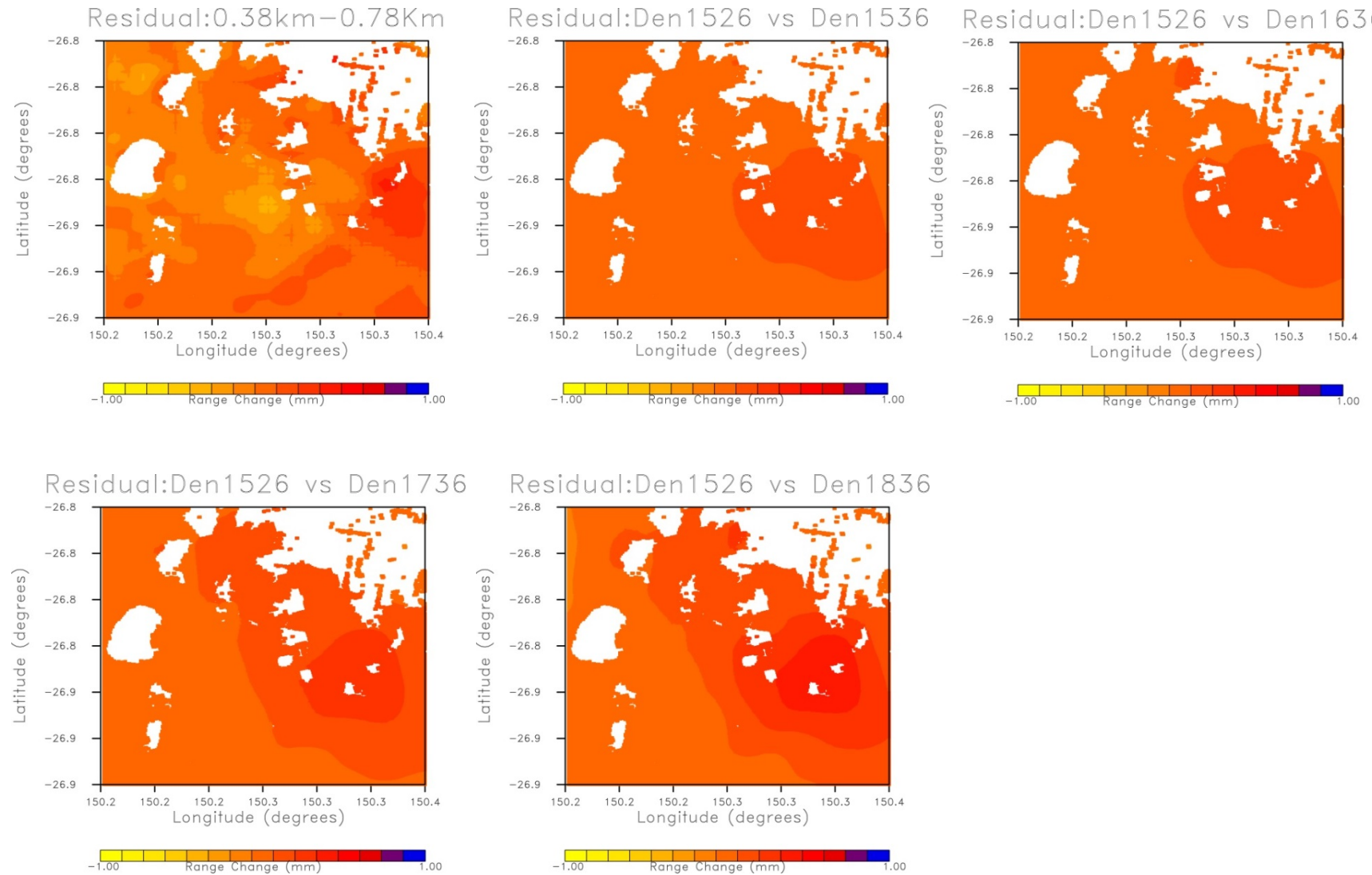


Figure 5-20: The impact of different formation density of Walloon Coal Measures (CSG reservoir) on the rate of surface deformation recovery. Range change data is surface deformation observation by SAR interferometry (truth) while others are the outcomes of forward modelling (simulated).



**Figure 5-21: Residual values between synthetic deformation maps at different depths of Walloon Coal Measure source layer. Based on seismic interpretation and 3D modelling, Walloon Coal Measure is located at 380m.**

## Subsurface Structural Behaviour



**Figure 5-22: Residual values between synthetic deformation maps for different densities of Walloon Coal Measure source layer. Based on seismic interpretation and 3D modelling, density of Walloon Coal Measure changes between 1526(kg/m<sup>3</sup>) and 1885.8 (kg/m<sup>3</sup>).**

### 5.4.2.2 Reservoir Volume Change Calculation

The amount of fluid that is extracted or injected from/to a reservoir leads to pressure and volume changes within the reservoir formation, stress changes in the region surrounding the reservoir, and deformation within the overburden. The reservoir layer undergoes a fractional volume change due to changes in fluid pressure. Therefore, once volume changes are computed, they can be mapped into pressure changes through linear transformation.

Figure 5-23 shows the fractional volume change calculated for the Walloon Coal Measures as an underground layer that having been mined out. The positive fractional volume change is probably the result of noise in the observation, due to the atmosphere, or ground motion due to shallow processes such as groundwater flow. By imposing inequality constraints in the inversion, only negative volume change can be allowed. According to the source of deformation, which in the case of the Berwyndale South area is CSG mining, this volume change is due to the creation of a cavity at an unknown depth at the centre of image. There is also a NW-SE trend for the volume change over the area with a settlement that is quite stable by changing the depth of source layer.

This particular trend that can also be seen on the surface deformation maps might be due to the configuration of the extraction wells and the rate of production or underlying structural faults. Unfortunately, due to the lack of seismic lines in the centre of deformation, the latter assumption cannot be verified, but the effects of a distinct fracture or fault can be clearly observed in the middle of the deformed area. As shown in Figure 5-23, the maximum volume change in the centre of the image is divided into two lobes by a narrow conduit. The eastern lobe has a smaller extent of fractional volume change than the western lobe. The number of CSG wells on the eastern lobe is far more than the western lobe and will strongly contradict with this assumption that the density of extraction wells or production rate resulted in this particular pattern of volume change. Furthermore, from the seismic interpretation and structural modelling it was already known that the general slope of the formations in this part of the Surat Basin is towards the South-West. The setting of stratigraphic formations and their slope could be an indication for the distinctive pattern of estimated volume change in the western part of the deformation area that needs to be investigated in more detail.

Although, the majority of volume change occurred in the centre of the image with maximum surface deformation rate, there is a linear pattern of volume change happening along the Burunga-Leichhardt thrust fault that is in the proximity of the displacement area. This pattern confirms the initial assumption that the structural faults are the controlling factor for the deformation signal distribution.

Inverse modelling of deformation field extracted from interferometric observation for volume change showed promising estimation of the location and behaviour of subsurface structures such as faults that were not mapped previously using field observations or seismic interpretation. Although,

sensitivity analysis disclosed that the source model for reservoir volume change is not sensitive enough for a change in reservoir depth or formation density with substantial overburden, there is still a valuable potential in this estimation that can be used as a large-scale map for extracting concealed faults or structural apertures at the reservoir level for which seismic surveys are blind to detect.

### 5.5 Discussion on Modelling Results

This chapter used a numerical method to mimic subsurface stratigraphic units and structural features. This static geological model comprised eight stratigraphic surfaces that can be fed into a dynamic model such as fluid flow or geomechanical simulation package.

Extracting subsurface stratigraphic layers was mainly based on interpolating between the available seismic sections tied with petroleum well tops. For property modelling, CSG wire-line information was sufficient to run the petrophysical analysis. According to the properties which were modelled in the proposed area, the deformation signal is located over a porous medium composed of shale or shaly formation that has the potential to bear hydrocarbon and not that much coal. In addition, the compressional velocity in areas with deformation is low compare to other areas in the outline.

Figure 5-7(a) and (b) show the depth and isopach maps of different subsurface layers draped over the area, with the surface settlement detected by interferometric SAR shown. Visual interpretation of depth maps in different formations shows that in the proximity of the region with subsidence, all formations except Hutton Sandstone and Evergreen Formation have shallow depth (Table A-9 in Appendix A2). The isopach (thickness) map of different formations for this specific area is significantly variable from medium to high thickness in Precipice Sandstone - Basement zone to very low in Evergreen formation - Precipice Sandstone zone (Table A-10 in Appendix A2).

Using the depth and isopach maps extracted from the 3D geological model, we can understand that from the surface up to the Walloon Coal Measures, a major reservoir for unconventional mining, the layers are shallow and their thickness is variable, which is compatible with the aquifer-aquitard nature of the subsurface in this particular area of the Great Artesian Basin. Theoretically, it is expected that by increasing depth and thickness of an overburden from top to bottom (Gubberamunda Sandstone to Basement), the vertical component of subsidence decreases. To verify this assumption, multiple tests were conducted by changing depth and density values in the reservoir layer. Following three-dimensional structural modelling, physical properties of the subsurface media such as depth, density, compression velocity and shear velocity of each underlying layers were used along with surface deformation map to demonstrate the subsurface structural behaviour in terms of volume change. Assuming that the reservoir (Walloon Coal Measures) layer is embedded in a stratified elastic medium, the fractional volume change was estimated using a viscoelastic geophysical inverse model. Synthetic surface deformation maps in satellite LOS direction resulted from forward modelling of real InSAR observations were used to test the impact of changing elastic properties of the formations on

the rate of surface deformation and its residuals. The residual maps show that slight changes in depth of the source formation will increase the absolute residual values both in downward and upward motions, but variations in density of this layer resulted in declining surface deformation rate due to compaction. However, the magnitude of these variations is not significant enough to allow an accurate retrieval of the model parameters using SAR data.

Interpretation of inverse modelling results reveal that there are three sources that might explain the way that the reservoir's volume has been changed throughout the three-year observation time: (a) Formation properties including depth, density and slope of the formations, (b) Tectonic framework and structural faults, and (c) Resource extraction and density of wells.

Although extracted fractional volume change for different depths of the source layer did not change significantly, the pattern indicates an opening or cavity at the centre of the image. Moreover, the NW-SE trend of volumetric flux in the region represents the effect of a probable underlying fracture and/or fault controlling the reservoir geo-mechanical behaviour by dividing the flux into two distinct lobes. The asymmetric size of these lobes indicates that the slope of the formations in this part of the Surat Basin might be a liable reason for such a pattern when there is no CSG well available over the western part of the volumetric change. [Figure 5-24\(b\)](#) shows the result of inversion using interferometric deformation map and elastic properties in [Figure 5-23](#) over the depth map at Walloon Coal Measures as a reservoir layer in [Figure 5-24\(a\)](#). As it is clear, without using the local faults, the volumetric change estimation using InSAR inversion was able to define the location of available faults. Moreover, it displays that the use of surface data such as interferometric measurement of deformation rate will help to resolve uncertainties of imaging geology at depth where poor seismic data coverage exist.

According to the results obtained from deformation mapping using satellite observations, three-dimensional structural modelling and geophysical inverse modelling for extracting volume change, the elastic properties (depth and density) of the source layer are not considered as the ruling factor for the volumetric variation in the reservoir, but the slope of the formation can be responsible. This slope can impact on the strength of the formation underneath, in response to the stress and strain variations. Nevertheless, we cannot negate the impact of available or perceived faults or fractures as constraining barriers inside and around the area with settlement such as the Burunga-Leichhardt thrust fault on the left corner of the image. Resource extraction with a dense network of CSG wells on the eastern side of the volumetric change is suggested as a reliable cause for the detected surface settlement and the subsequent volume change. But for the western side, tectonic elements are a more likely factor in controlling the signal.

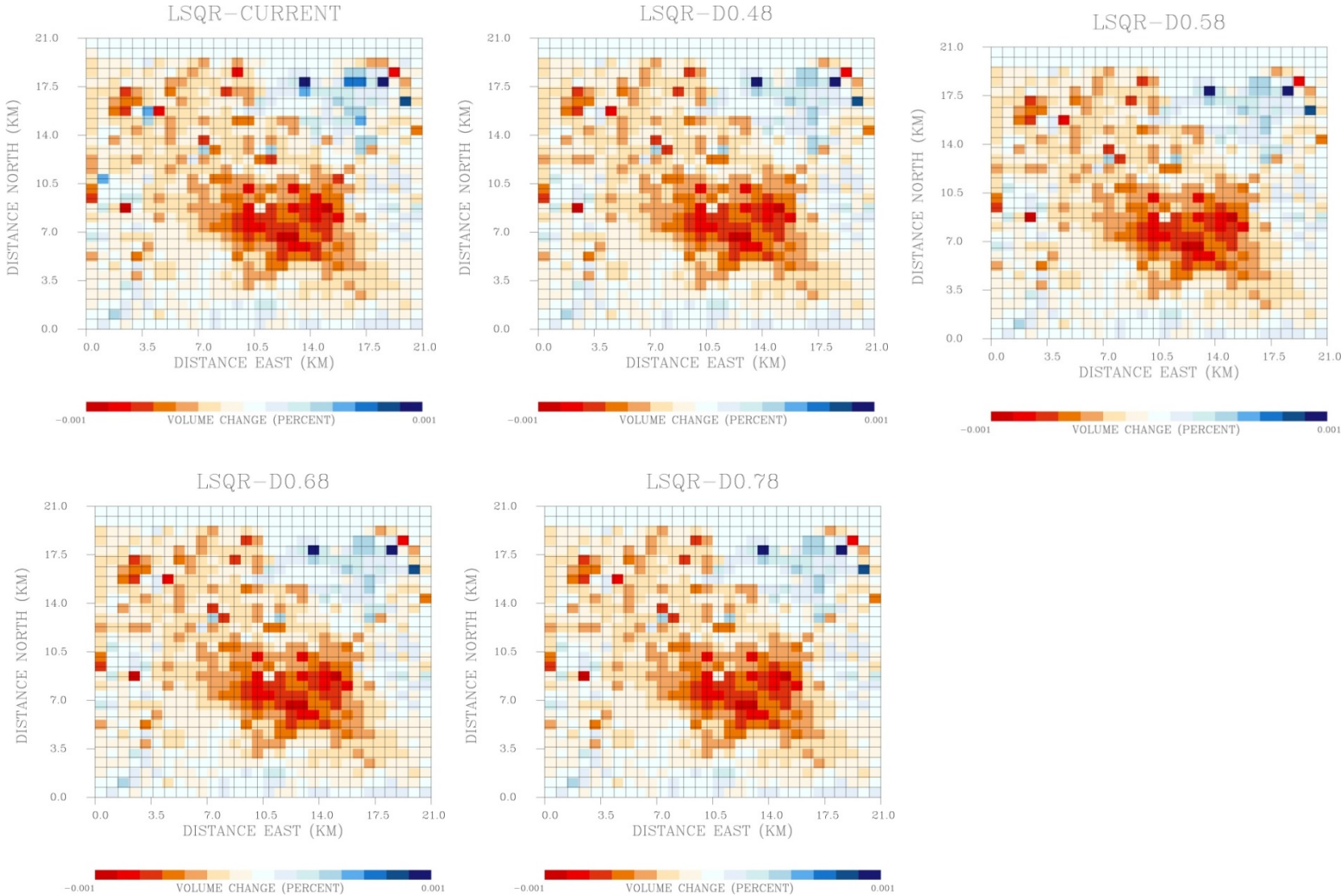


**Figure 5-23: Result of modelling as a fractional volume change (equates to change in volume over initial volume) represents the source as a grid that undergoes variable volume changes. As it is shown changing in the depth of reservoir (Walloon Coal Seam) from 0.38 km to 0.78 km did not impact on the amount of volume flux significantly.**

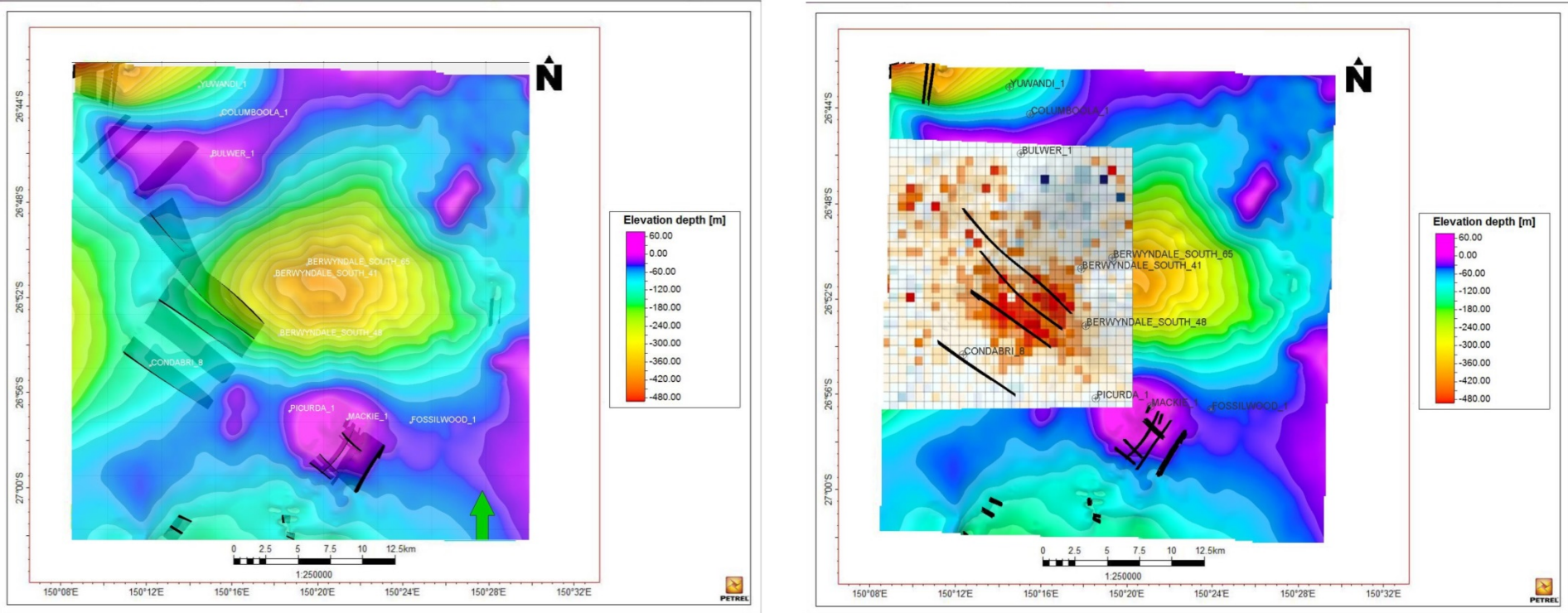


Figure 5-24: (a) Location map of structural faults intersected with Walloon Coal Measure reservoir layer at approximately 400 m depth. (b) The result of geophysical inverse modelling using InSAR surface observation superimposed on the Walloon Coal Measure depth map in (a).

### 5.6 Chapter Summary

Following the satellite observation for ground surface deformation illustrated in Chapter 4 with subsequent interpretation of the settlement signals, this chapter presented a three-dimensional structural model and accompanied reservoir property model. The outcomes of the property modelling such as density and compressional velocity were used as input for geophysical source modelling to demonstrate the rate of volume change and stress components in the area with limited seismic acquisition and well logs but substantial ground deformation.

Applying viscoelastic multi-layer model to an unconventional hydrocarbon reservoir i.e. coal seam gas (CSG) and evaluating the role of volume change in detecting subsurface structural features such as faults are the new contribution of this research to knowledge.

## 6 Conclusions and Future Work

This chapter addresses the research hypotheses that were discussed in Chapter 1. After collecting archived and new acquisitions of the SAR datasets across two decades over a sedimentary basin with intense CSG resource extraction, a non in situ ground surface deformation technique called interferometric SAR was applied. This remote sensing analysis was applied to various SAR sensors using two different processing algorithms to extract the most accurate elevation change maps.

Deformation rate maps highlighted areas with significant risk of ground failure over a three-year observation period. The SAR information was then meant to be used to increase the efficiency in building a three-dimensional geological model by interpreting the most relevant seismic acquisitions tied to down-hole wire-line information. This static 3D model was then improved by means of an extensive dataset of petrophysical information from both petroleum and CSG wells to define the formation properties at each depth level. Elastic properties of each subsurface formation as well as InSAR surface deformation maps were then combined to estimate the variation in reservoir volume and to define the subsurface structural behaviour at the local scale.

### 6.1 Remote Sensing of Surface Deformation

The objective of this research was to test the use of remotely sensed ground surface deformation that resulted from subsurface resource extraction and mining developments to characterize in a better manner the geological structure of the subsurface strata and to deduce the production risk associated with the reservoir development phase. Existing interferometric SAR processing algorithms, including stacking and SBAS [Berardino *et al.*, 2002], were used to derive subsidence maps from archived ALOS-PALSAR and new acquisitions of RADARSAT-2 SAR imagery for the study area that was reported for considerable toxic gas leakages into fresh-water reserves [QGC, 2013b]. The proposed region of interest was previously monitored by using another algorithm based on PSI method [Dura *et al.*, 2012]. However, the processing results showed no substantial downward motion with a deformation rate of 8mm/yr. Therefore, the main contribution of this research was to provide an additional estimate of the ground subsidence in a part of the Surat Basin, Australia, by using multiple SAR observations (L-band and C-band) and an advanced interferometric processing technique with significant improvement in both temporal and spatial resolutions. As the literature review suggested, PSI is generally expected to lack accuracy in an area such as the Surat Basin, due to the sparsity of natural or artificial corner reflectors; therefore, the SBAS algorithm was used in this context as it showed that SBAS results in other publications were more accurate than PSI for the same case studies and with limited SAR data coverage [Agram, 2010]. The High-resolution deformation maps presented

in Chapter 4 showed that the results from the SBAS processing algorithm in this research provided a solid suggestion on the preferred approach when applied to the basin-wide cases with sparse or no stable persistent scatterers or corner reflectors. In this algorithm, time series of ground deformation with mitigated atmospheric, orbital and thermal noises were extracted for each ground point by reducing the baseline length for each SAR pairs, and taking advantage of the whole cluster of SAR images. Finally, this research project tested the viscoelastic multi-layer source [Vasco *et al.*, 2008] model for coal seam gas reservoirs to estimate the amount of volume change at the reservoir depth and to analyse the sensitivity of the source model to a controlled change in depth and density of the producing formation. This model was previously applied for both earthquake epicenters and for conventional hydrocarbon resources such as oil and gas, but has never been tested for stratified layers such as shallow coal seam gas reservoirs.

### 6.1.1 Surface Deformation Retrieval from SAR

At first the exact locations of the ground deformation in the Surat Basin were not evident. As the literature review suggested [Crosetto *et al.*, 2005], low-cost screening over large areas with nominal low spatial resolution SAR images (i.e. 25-30m) such as those obtained from ERS-1/2 and ENVISAT ASAR is the first strategy to define areas with signals that are more likely to be a deformation signal than noise components. By using several historical C-band SAR images of ERS-1/2 and ENVISAT for the period 1992 to 2006 and employing a stacking algorithm in an area without reliable long-term geodetic measurements, the interferometric SAR analysis was initiated. As it was presented in Chapter 4, the mean deformation rate extracted from a stack of ENVISAT descending observations, showed a small area in the southwestern side of the scene susceptible to surface deformation. Following this primary observation and considering the fact that there were no C-band SAR acquisitions in this region after 2006, the InSAR monitoring was changed to use higher-resolution ALOS-PALSAR images collected at L-band that have a larger surface penetration and lower sensitivity to ground surface foliage.

The large coverage of PALSAR data in both single and dual beam modes on its ascending track provided the opportunity not only to monitor the area of interest after 2006, but it also allowed for the implementation of advanced processing algorithms such as SBAS. The SBAS algorithm increases the number of interferograms and reduces atmospheric noise levels, leading to more reliable subsidence maps, with extracted deformation rate time series for each ground measurement point. Contrary to a previous study [Dura *et al.*, 2012] in the Surat Basin that also covered the sub-basin in this research with analogous L-band ALOS-PALSAR dataset, but different methodology, ground surface deformation signals were detected in two out of four ALOS-PALSAR scenes. Testing different reference points for extracting the most accurate time series of deformation for each selected ground point as well as removing the seasonal effects on the deformation signal due to the different surface

conditions in the time of image acquisition resulted in two separate surface deformation maps that showed three regions with significant downward ground motion up to 28mm/yr and one area with upward movement. Consequently, processing new acquisitions of RADARSAT-2 wide frame images in ascending tracks (2012-2014) with the SBAS algorithm, but different processing parameters, also confirmed the ongoing land subsidence trend in those pre-defined areas. While areas with subsidence were detected in the vicinity of CSG mining districts, initially suggesting a causal link, the area with uplift is located over a timber forest with no evidence of fluid injection, but some possibility of elasto plastic response to the nearby subsidence region or probable residual atmospheric effects.

### 6.1.2 Interpretation of Remotely Sensed Deformation Maps

In order to interpret the deformation signals identified by the InSAR measurements, the available in situ resources were identified and checked. From a surface geology perspective, all three regions with downward motion are located over sedimentary rocks and young-aged alluvium that is similar to the rest of the sub-basin without deformation signals. In other words, soil materials and geological formations on the surface are not the controlling factors for the deformation signals detected by InSAR. The next stage to uncover the cause for deformation signals was using geodetic measurements available in the area of interest. As presented in Chapter 3, there are four GNSS CORS stations and one CGPS station in this region. The GNSS CORS observations have been available since 2010, but Dalby is the only station that showed seasonal patterns of movement on the ground surface between 2010 and 2014. This station is also equipped with CGPS, but because the deformation signal detected from space-borne sensor occurred farther away and is localized, Dalby CGPS is not of much use. Therefore, the available data on CSG and ground water extraction rate were checked for matching patterns in the surface deformation development. For the regions previously identified by InSAR measurements as undergoing deformation spots with four CSG mining sites, correlation coefficients were calculated to quantify the strength and direction of the relationship between groundwater and CSG extraction, CSG extraction and displacement, and groundwater extraction and displacement.

According to correlation coefficients estimated in Chapter 4, there is a strong correlation between CSG mining and observed displacement rate per year in all four mining regions, which indicates that more CSG extraction from underground reservoirs resulted in more land subsidence. However, two different scenarios are available for the relationship between mining operations and groundwater extraction. There is a positive correlation between CSG and groundwater withdrawal in the Daandine and Tipton West mining sites. Therefore, by decreasing resource extraction in these regions, the rate of deformation can be reduced. The other two deformed areas i.e. Berwyndale South and Kogan North represent another scenario. Production rate analysis show that even with a gradual decrease in groundwater extraction during the observation period, the ground surface deformation still retained its gradual downward trend. There is also a negative correlation between groundwater extraction and

CSG mining in these two regions showing that the mining operations are not related to the direct depressurization of shallow aquifers. Among these four mining sites with deformation signals, Berwyndale South with maximum downward motion and an ongoing ground settlement is located between two regional thrust faults that spatially confine the signals and force them to follow a specific distribution pattern. Taking all these in situ and remote observations into account, the role of compaction due to pressure depletion after pumping cannot be ruled out, which may have resulted in compaction and subsequent surface subsidence. Moreover, the role of structural features such as thrust faults are clear in this part of the Surat Basin; therefore, a viscoelastic source model with a multi-layer framework and input parameters from both subsurface formations and nearby faults will be used to calculate the fractional volume change, and to define the role of subsurface structures as a barrier for deformation signal distribution.

### 6.2 Subsurface Modelling

For the subsurface modelling stage of this research, it is hypothesized that elastic properties of each underlying formation in a stratified medium (e.g. CSG reservoir) integrated with InSAR surface observation will lead to a visco-elastic geophysical inverse problem that can be solved for fractional volume change estimation at reservoir depth. However, to define the elastic properties, a comprehensive geological model based on in situ seismic acquisitions and well-logging with property modelling was required. To determine the sensitivity of the model to changes in its initial states, elastic properties of the reservoir strata were changed and used for extracting the surface deformation rate its residuals for both real and synthetic deformation maps.

#### 6.2.1 Subsurface Model Retrieval from in situ Measurements

To assess the structural features such as faults and characterize shallow depth formation properties, a static geological model of the Surat Basin was developed. This three-dimensional model was developed by interpreting available 2D seismic surveys in time domain that then were tied to well-log depth measurements. This static geological framework was then converted from time to depth domain by using a suitable velocity model, and was improved by inserting petrophysical attributes to make a more realistic representation of the elastic properties of the subsurface medium for further geophysical inversion using InSAR surface deformation.

Consequently, for a quantitative interpretation of the underground source responsible for these localized signals and estimation of its volume change due to coal excavation, a proper geophysical source model is required. Considering the fact that the proposed area is located in a low relief region, with several stratified layers and viscoelastic medium, a source model with the assumption of a flat earth and multi-layer viscoelastic body was chosen [Vasco *et al.*, 2008]. During its subsequent

inversion using SAR interferometric observations, subsurface properties such as compressional velocity, shear velocity, depth and density were extracted from the static geological model. This geological model consisted of eight subsurface stratigraphic units with intersecting structural features. According to the extracted property model for each formation, the area with the maximum rate of surface deformation is located over a porous medium with low compressional seismic velocity. Using structural model and petrophysical properties to integrate with surface deformation map in the multi-layer source model was then not only solved for fractional volume change at reservoir depth but also used for demonstrating the role of structural features for the specific pattern of deformation.

### 6.2.2 Interpretation of Subsurface Modelling and Sensitivity Analysis

The primary results of subsurface structural modelling were a depth map of each subsurface formation, a calculated isopach map for each horizon with regard to its underlying horizon, and a 3D view of the geological model with structural faults that were extracted from seismic interpretation. As shown in Chapter 5, Hutton Sandstone and Evergreen Formation are the deep layers in the area with a deformation signal while the shallow Springbok Sandstone-Walloon Coal Measures zone and the deep Precipice Sandstone-Basement zone have the largest thicknesses. Using the depth and isopach maps, it can be shown that the subsurface layers from the surface up to the Walloon Coal Measures, are shallow and their thickness is variable demonstrating the aquifer-aquitard nature of the area in Great Artesian Basin. On the other hand, petrophysical modelling including distribution of formation density, its porosity and compressional velocity is the secondary outcome of the 3D static geological modelling in this research.

Assuming that the reservoir layer is embedded in a stratified elastic medium, the fractional volume change was estimated by using geophysical inverse modelling. Theoretically, it is expected that by increasing depth and thickness of a reservoir layer, the vertical component of subsidence would decrease. To verify this assumption, two synthetic tests were conducted by changing depth and density values in the reservoir layer. The residual maps show that slight changes in depth of the CSG layer will increase the absolute residual values both in downward and upward motions, but variations in density of this layer resulted in declining surface deformation rate due to compaction. However, the magnitude of these variations is not significant enough to allow an accurate retrieval of the model parameters using SAR data.

Analyzing the inverse modelling results also revealed that three causes might be responsible for such reservoir volume changes throughout the observation time. Resource extraction with a dense network of CSG wells is the most prominent reason, while the impact of structural faults and tectonic framework as constraining barriers cannot be excluded. Formation properties such as depth, density, and formation slope were also proposed as a third cause but testing the impact of changing these properties on the rate of deformation in three years and its residuals suggested otherwise. Although

residual maps revealed that the marginal change in source depth will increase the absolute residuals, and variations in density will have a reverse effect on deformation rate, the magnitude of these impacts was found to be not sufficiently significant for the extracted fractional volume change. Another outcome of the geophysical source inversion was the pattern of volumetric change in the proposed region. As shown in Chapter 5, the modelling activity showed the NW-SE trend of volumetric flux and its two-lobe pattern over the Walloon Coal Measure depth map supporting the controlling effect of an underlying fracture or fault for reservoir behaviour. In addition, it shows that the inversion of interferometric SAR deformation map for source parameters is able to resolve the uncertainties with seismic interpretation.

### 6.3 Conclusion

In summary, this study shows that using multi-temporal SAR observations for interferometric SAR analysis is a cost-efficient and reliable tool for historical analysis of ground surface deformation and associated scenarios, where in situ measurements are not available or sparse. It also illustrates that for subtle deformation rates in a large basin without long-term geodetic measurements, having access to a large stack of satellite observations and choosing the suitable processing algorithm can make a significant difference in signal detection and accuracy of the results. In this particular study area, coal seam gas mining activities turned out to be the main cause for the detected downward motion that might be accompanied by direct depressurization of groundwater supplies in some regions. The surface deformation maps have also proved to be a valuable tool to estimate volume fluxes at reservoir depth and an indicator for subsurface structures that seismic interpretation cannot detect them either because of seismic resolution or because of lack of seismic acquisition in the remote region. Therefore, using surface deformation observation and fractional volume change can also be used for planning future seismic acquisitions by uncovering the concealed structural faults or change in the slope of underlying formations.

### 6.4 Future Directions

For further research, a number of improvements are suggested following the current investigation in the Surat Basin:

1. Although interferometric SAR emerged as a non in situ remote sensing technique to support the geodetic observation network in the Surat Basin, obtaining reliable and absolute ground surface velocities from InSAR requires planning for the location of corner reflectors to ensure that the SAR-derived observations can help to constrain the local geodetic and geophysical source models. To address this, government authorities or private operational companies

should start designing a geodetic network for InSAR using corner reflectors or transponders to extract absolute displacement of scatterers on the field.

2. Historical analysis of surface deformation in the mining districts has been conducted in the north eastern part of the Surat Basin using both C-band (ERS-1/2, ENVISAT, and RADARSAT-2) and L-band (ALOS-PALSAR) since 1992. However, ERS-1/2 and ENVISAT coverage was not sufficient to establish a good baseline, while regular observations were provided by ALOS-PALSAR and RADARSAT-2. Emerging new satellite observations such as ALOS-2 and Sentinel-1 covering the same region with both ascending and descending paths should be considered for further baseline observations. These new acquisitions will make it possible to use multi-temporal SBAS algorithm for more accurate deformation monitoring and prediction in the region. But, in particular, Sentinel-1 C-band images would need some work, in spite of being radiometrically more accurate with higher resolution to verify whether their interferometric SAR maps are comparable to L-band observations.
3. One of the potential requirements in the petroleum industry is to calibrate and validate geomechanical models and to improve decisions and de-risk exploration, development and production activities. Developing a cost-efficient method to retrieve subsurface elastic properties by using interferometric surface observations in a region without seismic acquisitions or down-hole logging could be another field that needs further attention. In order to use InSAR to calibrate elastic properties, a reservoir model needs to be available. Having no access to a reservoir model with down-hole formation properties of specific wells located in the area with settlement was the main limiting factor in this study. Moreover, extracting the properties of the overburden and volume change of the reservoir involves a trade-off and a non-unique solution simply because the nature of the trade-off was not understood properly. Exploring this trade-off in more detail is one possibility to improve the current state of this research.
4. The fractional volume change is an approximation of compaction or expansion in the rock matrix and the accompanying fluid. In the CSG case, it is the coupled impact of pressure change in both the coal layer and the fresh-water shallow aquifers. Increasing the overburden pressure on a relatively thin coal layer can be projected as a ground deformation on the surface. Accordingly, a comprehensive geomechanical model to differentiate these causative effects needs to be built to define explicitly the impact of each potential cause in the region (i.e. groundwater extraction, CSG mining, fluid migration and soil shrinkage) that might be responsible for the reported rate of deformation, and the subsequent volume change at reservoir depth.

## References

### A

Abdulraheem, A., M. Zaman, and J. C. Roegiers (1993), Numerical simulation of a compacting reservoir, *International Journal of Rock Mechanics and Mining Sciences & Geomechanics Abstracts*, 30(7), 1299-1302.

Adeoti, L., N. Onyekachi, O. Olatinsu, J. Fatoba, and M. Bello (2014), Static reservoir modelling using well log and 3D seismic data in a KN Field, offshore Niger Delta, Nigeria, *International Journal of Geosciences*, 5, 93-106.

Agram, P. S. (2010), *Persistent Scatterer Interferometry in Natural Terrain*, 144 pp, Stanford University.

Amelung, F., D. L. Galloway, J. W. Bell, H. A. Zebker, and R. J. Laczniaik (1999), Sensing the ups and downs of Las Vegas: InSAR reveals structural control of land subsidence and aquifer-system deformation, *Geology*, 27(6), 483-486.

Anderssohn, J., M. Motagh, T. R. Walter, M. Rosenau, H. Kaufmann, and O. Oncken (2009), Surface deformation time series and source modeling for a volcanic complex system based on satellite wide swath and image mode interferometry: The Lazufre system, central Andes, *Remote Sensing of Environment*, 113(10), 2062-2075.

Anstey, N. A. (1977), *Seismic Interpretation: the physical aspects*, IHRDC Press.

APLNG (2010), Australian Pacific LNG Project Environmental Impact Statement, *Open File Groundwater Technical Rep. Gas Field*, 5(21).

AUSPOS (2015), Online GPS Processing Service, Geoscience Australia, <http://www.ga.gov.au/scientific-topics/positioning-navigation/geodesy/auspos> , accessed on : 15.06.2015.

### B

Badley, M. E. (1985), *Practical Seismic Interpretation*, 257 pp., Prentice Hall, NJ, USA.

Baer, G., U. Schattner, D. Wachs, D. Sandwell, S. Wdowinski, and S. Frydman (2002), The lowest place on Earth is subsiding—An InSAR (interferometric synthetic aperture radar) perspective, *Geological Society of America Bulletin*, 114(1), 12-23.

Bajkowski, J. (2014), Queensland Government Hits Underground Coal Gasification with Environmental Damage Charges, *Clean Energy, Environment, Law, State Open File Rep.*

Bakon, M., D. Perissin, M. Lazecky, and J. Papco (2014), Infrastructure Non-linear Deformation Monitoring Via Satellite Radar Interferometry, *Procedia Technology*, 16, 294-300, doi:<http://dx.doi.org/10.1016/j.protcy.2014.10.095>.

Barrett, D., N. Kunz, C. Moran, and S. Vink (2008), Scoping Study: Groundwater Impacts of Coal Seam Gas Development – Assessment and Monitoring, *Open File Rep.*, Centre for Water in the Minerals Industry (CWIMI), Brisbane, Queensland.

- Battaglia, M., P. F. Cervelli, and J. R. Murray-Muraleda (2013), Modelling crustal deformation-A catalogue of deformation models and modeling approaches, *Open File Rep.*, U.S. Geological Survey Techniques and Methods , pp. 96.
- Bell, M. (2008), Modelling post seismic deformation, *Open File Rep.*, 6 pp.
- Berardino, P., G. Fornaro, R. Lanari, and E. Sansosti (2002), A new algorithm for surface deformation monitoring based on small baseline differential SAR interferograms, *IEEE Transactions on Geoscience and Remote Sensing*, 40(11), 2375-2383.
- Biggs, J., E. Y. Anthony, and C. J. Ebinger (2009), Multiple inflation and deflation events at Kenyan volcanoes, East African Rift, *Geology*, 37(11), 979-982.
- Bjørlykke, K. (2015), introduction to petroleum Geology, in *Petroleum Geoscience, from sedimentary environment to rock physics*, p. 637, Springer press, Department of Geoscience, University of Oslo, Norway.
- Bradshaw, B. E., L. K. Spencer, A. C. Lahtinen, K. Khider, D. J. Ryan, J. B. Colwell, A. Chirinos, and J. Bradshaw (2010), *An assessment of Queensland's CO2 geological storage prospectivity - The Queensland carbon dioxide geological storage atlas*, CO2 Geological Storage Solutions Pty.Ltd., Australia.
- Brooke-Barnett, S., S. K. Naidu, P. K. Paul , T. Flottman , E. Kirk-Burnnand, and S. Buseti (2013), Influence of in Situ Stresses on Fracture Stimulation in the Surat Basin, Southeast Queensland, in *SPE Unconventional Resources Conference and Exhibition-Asia Pacific (SPE 167064)*, Brisbane, Australia.
- Brown, N. J., A. W. Woods, J. A. Neufeld, and C. Richardson (2014), Constraining surface deformation predictions resulting from coal seam gas extraction, *Rep. Record 2014/14*, Geoscience Australia, Canberra.
- BRS, and NRM (2003), Groundwater Recharge in the Great Artesian Basin Intake Beds, *Open File Technical Rep.*, Queensland Department of Natural Resources and Mines, Brisbane.
- Bruno, M. S., and C. A. Bovberg (1992), Reservoir compaction and surface subsidence above the Lost Hills field, California, paper presented at Symp. on Rock Mechanics 33, Santa Fe, NM.
- Buis, A., and J. D. Harrington (2014), That sinking feeling *Rep.*, JPL, Caltech, No. 2014-073, <http://www.jpl.nasa.gov/news/news.php?release=2014-073>.
- Burbey, T. J. (2008), Stress-strain analysis for aquifer-system characterization, *Ground Water*, 39(1), 128-136.
- Bürgmann, R., P. A. Rosen, and E. J. Fielding (2000), Synthetic Aperture Radar Interferometry to Measure Earth's Surface Topography and Its Deformation, *Annual Review of Earth and Planetary Sciences*, 28(1), 169-209.
- ## C
- Cadman, S. J., and L. Pain (1998), Bowen and Surat Basins, Clarence-Moreton Basin, Gunnedah Basin, and other minor onshore basins, Queensland, NSW and NT. , *Australian Petroleum Accumulations Rep.11 Rep.*, Bureau of Resource Sciences, Canberra.

- Cameron, M., S. Fomel, and J. Sethian (2006), Seismic velocity estimation and time to depth conversion of time-migrated images paper presented at SEG Annual Meeting New Orleans, USA.
- Capasso, G., and S. Mantica (2006), Numerical Simulation of Compaction and Subsidence Using ABAQUS, paper presented at 2006 ABAQUS Users' conference, Cambridge, MA, USA.
- Carnec, C., and C. Delacourt (2000), Three years of mining subsidence monitored by SAR interferometry, near Gardanne, France, *Journal of Applied Geophysics*, 43(1), 43-54.
- Castleden, R. (1988), Interpretation Report ATP 378P, *Open File Rep. CR17284A*, Surat Basin, Queensland, Beach Petroleum N.L.
- Casu, F., M. Manzo, and R. Lanari (2006), A quantitative assessment of the SBAS algorithm performance for surface deformation retrieval from DInSAR data, *Remote Sensing of Environment*, 102(3-4), 195-210.
- Casu, F., M. Manzo, A. Pepe, and R. Lanari (2008), SBAS-DInSAR Analysis of Very Extended Areas: First Results on a 60,000 km<sup>2</sup> Test Sites, *Geoscience and Remote Sensing Letters, IEEE*, 5(3), 438-442.
- Cervelli, P., M. H. Murray, P. Segall, Y. Aoki, and T. Kato (2001), Estimating source parameters from deformation data, with an application to the March 1997 earthquake swarm off the Izu Peninsula, Japan, *Journal of Geophysical Research: Solid Earth*, 106(B6), 11217-11237.
- Chaussard, E., R. Bürgmann, M. Shirzaei, E. J. Fielding, and B. Baker (2014), Predictability of hydraulic head changes and characterization of aquifer-system and fault properties from InSAR-derived ground deformation, *Journal of Geophysical Research: Solid Earth*, 119(8), 6572-6590.
- Chen, C. W., and H. A. Zebker (2002), Phase unwrapping for large SAR interferograms: statistical segmentation and generalized network models, *Geoscience and Remote Sensing, IEEE Transactions on*, 40(8), 1709-1719.
- Chin, L., R. R. Boade, J. H. Prevost, and G. H. Landa (1993), Numerical simulation of shear-induced compaction in the ekofisk reservoir, *International Journal of Rock Mechanics and Mining Sciences & Geomechanics Abstracts*, 30(7), 1193-1200.
- Choudhury, J., and B. Bell (1984), Bennett and Bennett Detail Seismic Survey Final Report, ATP 244P Block D, Surat Basin, Queensland, *Open File Rep. CR12812*, Tenneco oil and minerals of Australia Inc., Australia.
- Cigna, F., B. Osmanoglu, E. Cabral-Cano, T. H. Dixon, J. A. Ávila-Olivera, V. H. Garduño-Monroy, C. DeMets, and S. Wdowinski (2012), Monitoring land subsidence and its induced geological hazard with Synthetic Aperture Radar Interferometry: A case study in Morelia, Mexico, *Remote Sensing of Environment*, 117, 146-161.
- Clewett, J. F., N. M. Clarkson, D. A. George, S. H. Ooi, D. T. Owens, I. J. Partridge, and G. B. Simpson (2003), Rain man Stream Flow version 4.3: a comprehensive climate and streamflow analysis package on CD to assess seasonal forecasts and manage climate risk, *Open File Rep. QI03040*, Queensland Department of Primary Industries, Brisbane.
- Cloude, S. (2009), *Polarization: Applications in Remote Sensing*, Oxford Univ. Press. ISBN 978-0-19-956973-1, Oxford, UK.
- Coleman, T. F., and Y. Li (1996), A Reflective Newton Method for Minimizing a Quadratic Function Subject to Bounds on Some of the Variables, *SIAM Journal on Optimization*, 6(4), 1040-1058.

Colesanti, C., S. L. Mouelic, M. Bennani, D. Raucoules, C. Carnec, and A. Ferretti (2005), Detection of mining related ground instabilities using the Permanent Scatterers technique—a case study in the east of France, *International Journal of Remote Sensing*, 26(1), 201-207.

Commonwealth-of-Australia (2014), Monitoring and management of subsidence induced by coal seam gas extraction,, *Open File Knowledge Rep.*, Coffey Geotechnics for the Department of the Environment, Canberra.

Crosetto, M., B. Crippa, and E. Biescas (2005), Early detection and in-depth analysis of deformation phenomena by radar interferometry, *Engineering Geology*, 79(1–2), 81-91.

CSIRO (2008), Water availability in the Condamine-Balonne, A report to the Australian Government from CSIRO Murray-Darling Basin Sustainable Yields Project, *Open File Rep.*, 169 pp.

CSIRO (2011), Basin resource management for carbon storage - A literature review, *Open File Rep.*, 70 pp, Australian National Low Emissions Coal Research and Development (ANLEC R&D), Curtin Univ. Press, Perth.

CSIRO (2012), Coal seam gas-produced water and site management *Rep.*, <http://www.csiro.au/news/coal-seam-gas#FactSheets>, accessed on 5.10.2013.

Cunha, L. B. (2004), Integrating static and dynamic data for oil and gas reservoir modelling, *Journal of Canadian Petroleum Technology*, 43(3).

Currenti, G., A. Bonaccorso, C. Del Negro, F. Guglielmino, D. Scandura, and E. Boschi (2010), FEM-based inversion for heterogeneous fault mechanisms: application at Etna volcano by DInSAR data, *Geophysical Journal International*, 183(2), 765-773.

## D

Da Silva, F. W., G. F. Debande, C. A. Pereira, and B. Plischke (1990), Casing collapse analysis associated with reservoir compaction and overburden subsidence, paper presented at Society of Petroleum Engineers, 20953, pp.7.

Davis, P. M. (1986), Surface deformation due to inflation of an arbitrarily oriented triaxial ellipsoidal cavity in an elastic half-space, with reference to Kilauea volcano, Hawaii, *Journal of Geophysical Research: Solid Earth*, 91(B7), 7429-7438.

Dawson, J., P. Cummins, P. Tregoning, and M. Leonard (2008), Shallow intraplate earthquakes in Western Australia observed by Interferometric Synthetic Aperture Radar, *Journal of Geophysical Research: Solid Earth*, 113(B11).

Deguchi, T., M. Kato, H. Akcin, and H. S. Kutoglu (2007), Monitoring of mining induced land subsidence using L- and C-band SAR interferometry, paper presented at Geoscience and Remote Sensing Symposium, 2007. IGARSS 2007. IEEE International, 23-28 July 2007.

Densmore, J., K. Ellett, J. Howle, M. Carpenter, and M. Sneed (2010), Measuring land-surface deformation on Bicycle Lake playa, Fort Irwin, California, USA, paper presented at Land subsidence, associated hazards and the role of natural resources development (EISOLS 2010), IAHS Publ. 339, Wallingford, UK.

DNRM (2012), [www.mines.industry.qld.gov.au](http://www.mines.industry.qld.gov.au). accessed regularly : 2013- 2015.

Draper, J. J., and C. J. Boreham (2006), Geological controls on exploitable coal seam gas distribution in Queensland *APPEA Journal*, 46, 343-366.

Du, A. Aydin, and P. Segall (1992), Comparison of various inversion techniques as applied to the determination of a geophysical deformation model for the 1983 Borah Peak earthquake, *Bulletin of the Seismological Society of America*, 82(4), 1840-1866.

Du, and J. E. Olson (2001), A poroelastic reservoir model for predicting subsidence and mapping subsurface pressure fronts, *Journal of Petroleum Science and Engineering*, 30(3-4), 181-197.

Duncan, E. E., J. S. Kuma, and G. Avane (2010), Surface deformation monitoring in the Goldfields Ghana limited area, *The Electronic Journal on Information Systems in Developing Countries*, 42(6), 1-7.

Dura, J., D. Albiol, and J. Sabater (2012), Baseline report on InSAR monitoring on the Surat-Bowen Basin, *Rep. AL-051212*.

Duro, J., D. Albiol, O. Mora, and B. Payas (2013), Application of advanced InSAR techniques for the measurement of vertical and horizontal ground motion in long wall mining, paper presented at Coal Operators' Conference, The Univ. of Wollongong, Australia.

Dzurisin, D. (2007), *Volcano Deformation: New Geodetic Monitoring Techniques*, Springer, Washington, USA.

### *E*

Eisinger, C. L., and J. L. Jensen (2009), Data integration, petrophysics and geomodelling: Wabaman area CO<sub>2</sub> sequestration project (WASP) static earth model, *Open File Rep.*, Institute for Sustainable Energy, Environment and Economy (ISEEE), University of Calgary.

Ellis, L., and P. Mather (2011), Geology, Landform and Soils Study, Arrow Energy Surat Project EIS Surat Basin, Queensland, *Open File Rep. ENAUBRIS07040AC-9097\_GLS\_Rev4*, 339 pp, Coffey Geotechnics Pty. Ltd., Brisbane.

Engelbrecht, J., and M. Inggs (2013), Differential interferometry techniques on L-band data employed for the monitoring of surface subsidence due to mining, *South African Journal of Geomatics*, 2(2), 82-93.

Esterle, J. S., S. K. Hamilton, V. Ward, S. Tyson, and R. Sliwa (2013), Scales of geological Heterogeneity within the Walloon Subgroup and its Coal Measures, Final report of Activity 1.3 of the Healthy Head Waters Coal Seam Gas Water Feasibility Study, *Open File Rep.*, Department of Natural Resources and Mines, Brisbane.

Exon, N. F. (1974), The geological environment of the southern Taroom Trough and the overlying Surat Basin, *Australian Petroleum Exploration Association Journal*, 14, 50-58.

Exon, N. F. (1976), Geology of the Surat Basin in Queensland, *Rep. Bulletin 166*, Bureau of Mineral Resources, Geology and Geophysics, Australia.

Ezekwe, J. N. (2011), *Petroleum Reservoir Engineering Practice* 816 pp., Prentice Hall, Upper Saddle River, NJ, USA.

Ezekwe, J. N., and S. L. Filler (2005), Modelling Deepwater Reservoirs in *Annual Technical Conference and Exhibition*, SPE 95066, Dallas, TX, USA.

**F**

Faegh-Lashgary, P., M. Motagh, M.-A. Sharifi, and M.-R. Saradjian (2012), Source Parameters of the September 10, 2008 Qeshm Earthquake in Iran Inferred from the Bayesian Inversion of Envisat and ALOS InSAR Observations, in *VII Hotine-Marussi Symposium on Mathematical Geodesy*, edited by N. Sneeuw, P. Novák, M. Crespi and F. Sansò, pp. 319-325, Springer Berlin Heidelberg.

Fallara, F., M. Legault, and O. Rabeau (2006), 3-D Integrated Geological Modelling in the Abitibi Subprovince(Quebec, Canada): Techniques and Applications, *Exploration and Mining Geology*, 15(1-2), 27-41.

Featherstone, W. E., M. Filmer, N. Penna, L. Morgan, and A. Schenk (2012), Anthropogenic land subsidence in the Perth Basin: challenges for its retrospective geodetic detection, *Journal of the Royal Society of Western Australia* 95(1), 53-62.

Fennell, J., P. C. Smith, T. J. F. Cook, J. Sweeney, G. Wilcox, E. Haak, and S. Honicke (2012), Spatial analysis of coal seam gas water chemistry, Healthy Headwaters, Coal Seam Gas Water Feasibility Study, *Final Rep.*, Worley Parsons resources and Energy, Australia.

Ferretti, A. (2014), *Satellite InSAR data: reservoir monitoring from space*, EAGE Publication., DB Houton, The Netherlands.

Ferretti, A., A. Fumagalli, F. Novali, C. Prati, F. Rocca, and A. Rucci (2011a), A New Algorithm for Processing Interferometric Data-Stacks: SqueeSAR, *Geoscience and Remote Sensing, IEEE Transactions on*, 49(9), 3460-3470.

Ferretti, A., A. Monti Guarnieri, C. Prati, and F. Rocca (2007), InSAR principles: guidelines for SAR Interferometry processing and interpretation, *Rep.*, ESA Publication, The Netherlands.

Ferretti, A., C. Prati, and F. Rocca (2001), Permanent scatterers in SAR interferometry, *Geoscience and Remote Sensing, IEEE Transactions on*, 39(1), 8-20.

Ferretti, A., A. Tamburini, F. Novali, A. Fumagalli, G. Falorni, and A. Rucci (2011b), Impact of high resolution radar imagery on reservoir monitoring, *Energy Procedia*, 4, 3465-3471.

Fialko, Y., Y. Khazan, and M. Simons (2001), Deformation due to a pressurized horizontal circular crack in an elastic half-space, with applications to volcano geodesy, *Geophysical Journal International*, 146(1), 181-190.

Fialko, Y., and M. Simons (2000), Deformation and seismicity in the Coso geothermal area, Inyo County, California: Observations and modeling using satellite radar interferometry, *Journal of Geophysical Research: Solid Earth*, 105(B9), 21781-21793.

Fielding, R. G. Blom, and R. M. Goldstein (1998), Rapid subsidence over oil fields measured by SAR interferometry, *GEOPHYSICAL RESEARCH LETTERS*, 25(17), 3215-3218.

Fielding, A. R. G. Gray, G. I. Harris, and J. A. Salomon (1990), The Bowen Basin and overlying Surat Basin, In Finlayson D.M. (ed) *The Eromanga-Brisbane Geoscience Transect: A guide to basin development across Phanerozoic Australia in southern Queensland* *Rep. Bulletin* 232, 105-116 pp, Bureau of Mineral Resources, Australia.

Fokker, P. A., K. Visser, E. Peters, G. Kunakbayeva, and A. G. Muntendam-Bos (2012), Inversion of surface subsidence data to quantify reservoir compartmentalization: A field study, *Journal of Petroleum Science and Engineering*, 96-97, 10-21.

Fouladi Moghaddam, N., C. Rudiger, S. Samsonov, J. P. Walker, and M. Hall (2013), An assessment of DInSAR potential for simulating geological subsurface structure, in *20th International Congress on Modelling and Simulation*, edited by J. Piantadosi, R. S. Anderssen and J. Boland, pp. 3099-3105, Adelaide, Australia.

Fouladi Moghaddam, N., S. Samsonov, C. Rüdiger, J. P. Walker, and M. Hall (2015), Multi-Temporal SAR Observations For Deformation Scenario Evaluation Associated with Man-made Interactions, *Environmental Earth Sciences*, 75(4),281-296.

Fujiwara, S., P. A. Rosen, M. Tobita, and M. Murakami (1998), Crustal deformation measurements using repeat-pass JERS 1 synthetic aperture radar interferometry near the Izu Peninsula, Japan, *Journal of Geophysical Research: Solid Earth*, 103(B2), 2411-2426.

## G

GABCC (2000), Great Artesian Basin Strategic Management Plan, *Open File Rep.*, Great Artesian Basin Consultative Council, Department of the Environment, Canberra.

Gabriel, A. K., R. M. Goldstein, and H. A. Zebker (1989), Mapping small elevation changes over large areas: Differential radar interferometry, *Journal of Geophysical Research: Solid Earth*, 94(B7), 9183-9191.

Galloway, D. L., and T. J. Burbey (2011), Review: Regional land subsidence accompanying groundwater extraction, *Hydrogeology Journal*, 19(8), 1459-1486.

Galloway, D. L., K. W. Hudnut, S. E. Ingebritsen, S. P. Phillips, G. Peltzer, F. Rogez, and P. A. Rosen (1998), Detection of aquifer system compaction and land subsidence using interferometric synthetic aperture radar, Antelope Valley, Mojave Desert, California, *Water Resources Research*, 34(10), 2573-2585.

Garner, C., and R. Coffman (2014), Remote Sensing Methods for Monitoring Ground Surface Deformation of Compacted Clay Test Sections, in *Geo-Congress 2014 Technical Papers*, pp. 963-978.

Garthwaite, M. C., M. Hazelwood, S. Nancarrow, A. Hislop, and J. H. Dawson (2015), A regional geodetic network to monitor ground surface response to resource extraction in the northern Surat Basin, Queensland, *Australian Journal of Earth Sciences*, 62(4), 469-477.

Gas-field-Commission (2013), Hydrogeology of the Surat Basin, in [www.gasfieldscommissionqld.org.au](http://www.gasfieldscommissionqld.org.au), accessed on 08.05.2013.

Ge, L., and X. Li (2014), Trial of satellite radar interferometry (InSAR) to monitor subsidence along the Gippsland coast, *Open File Rep.*, Victorian Government Department of Environmental and Primary Industries, Melbourne, Australia.

Gens, R. (2003), Two-dimensional phase unwrapping for radar interferometry: Developments and new challenges, *International Journal of Remote Sensing*, 24(4), 703-710.

Gens, R., and J. L. Van Genderen (1996), Review Article SAR interferometry—issues, techniques, applications, *International Journal of Remote Sensing*, 17(10), 1803-1835.

Geoscience-Australia (2010), Australia's Identified Mineral Resources 2010, in [http://www.ga.gov.au/corporate\\_data/71584/71584.pdf](http://www.ga.gov.au/corporate_data/71584/71584.pdf), accessed on 05.02.2015.

Geoscience-Australia, and Australian-Stratigraphy-Commission (2014), Australian Stratigraphic Units Database,  
<http://www.ga.gov.au/products-services/data-applications/reference-databases/stratigraphic-units.html>.

GolderAssociates (2009), QGC Groundwater Study Surat Basin, Queensland, Coal seam gas field component for Environment Impact Statement, *Open File Rep. 087633050-016-Rev.1*.

Goldstein, R. (1995), Atmospheric limitations to repeat-track radar interferometry, *GEOPHYSICAL RESEARCH LETTERS*, 22(18), 2517-2520.

Green, P. M., D. C. Carmichael, T. J. Brain, C. G. Murray, J. L. Mckeller, J. W. Beeston, and A. R. G. Gray (1997), Lithostratigraphic units in the Bowen and Surat Basins, Queensland, in *The Surat and Bowen Basins, South-East Queensland. Queensland Minerals and Energy Review Series*,, edited by P. M. Green, pp. 31-108, Queensland Department of Mines and Energy.

Grigg, K. M. (2012), Using InSAR technology and groundwater pumping data to model land subsidence from Coal Bed Methane production in the Power River Basin, Wyoming, Paper No. 21-5, paper presented at 64th Annual Meeting, Geological Society of America Rocky Mountain section, Albuquerque, New Mexico.

## H

Habermehl, M. A. (1980), The Great Artesian Basin, Australia, *BMR Journal of Australian Geology and Geophysics*, 5, 9-38.

Habermehl, M. A. (1982), Springs in the Great Artesian Basin, Australia - Their Origin and Nature, *Australian Government Publishing Services*.

Habermehl, M. A. (2002), Hydrogeology, Hydrochemistry and Isotope Hydrology of the Great Artesian Basin, *Open File Rep.*, Bureau of Rural Sciences, Water Science Program, Canberra.

Hamilton, N. Desassis, J. S. Esterle, and S. Tyson (2013), Lithofacies transition probabilities within the Walloon Subgroup and its coal measures, *Open File Rep.*, School of Earth Sciences, University of Queensland for Queensland Department of Natural Resources and Mines, Brisbane.

Hamilton, J. S. Esterle, and S. D. Golding (2012), Geological interpretation of gas content trends, Walloon Subgroup, eastern Surat Basin, Queensland, Australia, *International Journal of Coal Geology*, 101, 21-35.

Hamilton, A. V. Maller, and M. D. Prins (1992), Subsidence-induced shear failures above oil and gas reservoirs, paper presented at 33rd U.S. Symposium on Rock Mechanics 33, Santa Fe, NM, USA.

Hanssen, R. F. (2001), *Radar interferometry: Data interpretation and error analysis*, 159 pp., Kluwer Academic Publishers, ISBN 0-7923-6945-9.

Hanssen, R. F. (2005), Satellite radar interferometry for deformation monitoring: a priori assessment of feasibility and accuracy, *International Journal of Applied Earth Observation and Geoinformation*, 6(3-4), 253-260.

Harris, P. S., A. J. W. Biggs, and B. J. Stone (1999), Central Darling Downs Land Management Manual (MCD), *Open File Rep. DNRQ990102*, Queensland Department of Natural Resources, Australia.

- Haskell, N. A. (1953), The dispersion of surface waves on multi-layered media, *Bull.Seism.Soc.Am.*, 43, 17-34.
- Hatherly, P. (2013), Overview on the application of geophysics in coal mining, *International Journal of Coal Geology*, 114, 74-84.
- Henning, A. (2005), A summary of the Hydrogeology of the Southern Eromanga and Surat Basins of the Great Artesian Basin, *Open File Rep. RPT05-0024, CO2CRC*.
- Hodgkinson, J., A. Hortle, and M. McKillop (2010), The application of hydrodynamic analysis in the assessment of regional aquifers for carbon geostorage: Preliminary results for the Surat Basin, Queensland, paper presented at APPEA Conference 2010, Brisbane.
- Hodgkinson, J., M. Preda, A. Hortle, M. McKillop, and L. Foster (2009), The Potential Impact of Carbon Dioxide Injection on Freshwater Aquifers: The Surat and Eromanga Basins in Queensland, *Open File Rep.*, Department of Employment, Economic Development and Innovation, Brisbane.
- Hodgson, N., C. MacBeth, L. Duranti, J. Rickett, and K. Nihei (2007), Inverting for reservoir pressure change using time-lapse time strain: Application to the Genesis field, Gulf of Mexico, *The Leading Edge*, 26(5), 649-652.
- Hoffmann, K. L., J. M. Totterdell, O. Dixon, G. A. Simpson, A. T. Brakel, A. T. Wells, and J. L. McKellar (2009), Sequence stratigraphy of Jurassic strata in the lower Surat Basin succession, Queensland, *Australian Journal of Earth Sciences*, 56(3), 461-476.
- Hofmann-Wellenhof, B., H. Lichtenegger, and J. Collins (2001), *GPS Theory and Practice*, Springer-Verlag, Wien.
- Holland, J. H. (1973), Genetic algorithms and the optimal allocation of trials, *SIAM Journal on Computing*, 2(2), 88-105.
- Hooper, A. (2008), A multi-temporal InSAR method incorporating both persistent scatterer and small baseline approaches, *GEOPHYSICAL RESEARCH LETTERS*, 35(16).
- Hooper, A. (2010), Bayesian inversion of wrapped InSAR data for geophysical parameter estimation, ESA SP-686, paper presented at ESA living planet symposium, Bergen, Norway, 28 June-2 July.
- Hooper, A., D. Bekaert, K. Spaans, and M. Arkan (2012), Recent advances in SAR interferometry time series analysis for measuring crustal deformation, *Tectonophysics*, 514–517, 1-13.
- Hooper, A., and T. R. Wright (2009), Comparison of Monte Carlo methods for model probability distribution determination in SAR Interferometry, ESA-SP-677, paper presented at Fringe workshop, Frascati, Italy.
- Hooper, A., H. Zebker, P. Segall, and B. Kampes (2004), A new method for measuring deformation on volcanoes and other natural terrains using InSAR persistent scatterers, *GEOPHYSICAL RESEARCH LETTERS*, 31(23).
- Hosseini, S. A., H. Lashgari, J. W. Choi, J.-P. Nicot, J. Lu, and S. D. Hovorka (2013), Static and dynamic reservoir modeling for geological CO<sub>2</sub> sequestration at Cranfield, Mississippi, U.S.A, *International Journal of Greenhouse Gas Control*, 18, 449-462.

**I**

ICSM (2014), Standard for the Australian survey control network - SP1 – Version 2.1, *Open File Rep.*, Inter-governmental Committee on Surveying and Mapping ,  
[URL:http://www.icsm.gov.au/publications/sp1/Standard-for-Australian-Survey-Control-Network\\_v2.1.pdf](http://www.icsm.gov.au/publications/sp1/Standard-for-Australian-Survey-Control-Network_v2.1.pdf).

IESC (2014), Coal Seam Gas and Large coal mining development, subsidence from coal seam gas extraction, *Fact Sheet Rep.*, 4 pp, Australia.

IPCC (2005), Special report on Carbon Dioxide Capture and Storage, *Open File Rep.*, Cambridge Univ. Press, New York.

**J**

Johnson, J. R. L., and S. Mazumder (2014), Key Factors Differentiate the Success Rate of Coalbed Methane Pilots Outside of North America - Some Australian Experiences, International Petroleum Technology Conference.

Jones, G. D., and R. B. Patrick (1981), Stratigraphy and coal exploration geology of the northeastern Surat Basin, *Journal of Coal Geology* 1(4), 153-163.

Jonsson, S., H. A. Zebker, P. Segall, and F. Amelung (2002), Fault slip distribution of the 1999 M7.1 Hector mine, California, Earthquake, Estimated from satellite Radar and GPS measurements, *Bulletin of the Seismological Society of America*, 92(4), 1377-1389.

Jung, H. C., S.-W. Kim, H.-S. Jung, K. D. Min, and J.-S. Won (2007), Satellite observation of coal mining subsidence by persistent scatterer analysis, *Engineering Geology*, 92(1–2), 1-13.

**K**

Kampes, B. M., and R. F. Hanssen (2004), Ambiguity resolution for permanent scatterer interferometry, *Geoscience and Remote Sensing, IEEE Transactions on*, 42(11), 2446-2453.

Karacan, C. O., F. A. Ruiz, M. Cote, and S. Phipps (2011), Coal mine methane: A review of capture and utilization practices with benefits to mining safety and to greenhouse gas reduction: Review Article, *International Journal of Coal Geology*, 86, 121-156.

Katzenstein, K. W. (2012), InSAR identifies subsidence resulting from coalbed methane production in the San Juan Basin, Colorado and New Mexico, paper presented at 64th Annual Meeting, Geological Society of America Rocky Mountain Section, Paper No. 34-14 Albuquerque, New Mexico.

King, N. E., et al. (2007), Space geodetic observation of expansion of the San Gabriel Valley, California, aquifer system, during heavy rainfall in winter 2004-2005, *Journal of Geophysical Research B: Solid Earth*, 112(3).

Klohn-Crippen-Berger (2012), Central Condamine River Alluvium (CCRA) Injection Study *Rep.*, Healthy Headwaters, Coal Seam Gas water feasibility study, Australia.

Korsch, R. J., C. J. Boreham, J. M. Totterdell, R. D. Shaw, and M. G. Nicoll (1998), Development and petroleum resource evaluation of the Bowen, Gunnedah and Surat basins, eastern Australia, *APPEA Journal*, 38, 199–236.

Korsch, R. J., J. M. Totterdell, T. Fomin, and M. G. Nicoll (2009), Contractual structures and deformational events in the Bowen, Gunnedah and Surat Basins, eastern Australia, *Australian Journal of Earth Sciences*, 56(3), 477-499.

## L

Lanari, R., O. Mora, M. Manunta, J. J. Mallorqui, P. Berardino, and E. Sansosti (2004), A small-baseline approach for investigating deformations on full-resolution differential SAR interferograms, *Geoscience and Remote Sensing, IEEE Transactions on*, 42(7), 1377-1386.

Lane, W. B. (1979), Progress Report on Condamine Underground Investigation to December 1978Rep., Queensland Water Resources Commission, Brisbane, Queensland.

Lauknes, T. R. (2004), Long-term surface deformation mapping using small-baseline differential SAR interferograms, 88 pp, University of Tromsq.

Le Toan, T., et al. (2011), The BIOMASS mission: Mapping global forest biomass to better understand the terrestrial carbon cycle, *Remote Sensing of Environment*, 115(11), 2850-2860.

Leva, D., G. Nico, D. Tarchi, J. Fortuny-Guasch, and A. J. Sieber (2003), Temporal analysis of a landslide by means of a ground-based SAR Interferometer, *Geoscience and Remote Sensing, IEEE Transactions on*, 41(4), 745-752.

Lillesand, T. M., R. W. Kiefer, and J. W. Chipman (2008), *Remote Sensing and Image Interpretation*, John Willey & Sons, Hoboken, NJ, USA.

Linc-Energy (2011), UCG Underground Coal Gasification, <http://www.lincenergy.com/overview.php>, accessed on: 08.05.2015.

Liu, P. (2012), InSAR observations and modelling of earth surface displacement in the yellow river delta (China), 195 pp, Univ. of Glasgow, UK.

Lorenzo-Martin, F. (2006), Time-dependent Crustal Deformation after Strong Earthquakes – Rheological Model Calculations, 128 pp, Ruhr University Bochum, Germany.

Lu, N., and W. J. Likos (2004), *Unsaturated Soil Mechanics*, 584 pp., Wiley, Hoboken, NJ, USA.

## M

Mallet, J. L. (2008), *Numerical Earth Models (EET 3)*, EAGE Publications.

Martin (1981), Deposition of the Precipice Sandstone and the evolution of the Surat Basin in the Early Jurassic, 21(1), 16-23.

Martin, M. Wakefield, M. K. MacPhail, T. Pearce, and H. E. Edwards (2013), Sedimentology and stratigraphy of an intra-cratonic basin coal seam gas play: Walloon Subgroup of the Surat Basin, eastern Australia, *Petroleum Geoscience*, 19(1), 21-38.

Massonnet, D., and K. L. Feigl (1998), Radar interferometry and its application to changes in the Earth's surface, *Reviews of Geophysics*, 36(4), 441-500.

Massonnet, D., M. Rossi, C. Carmona, F. Adragna, G. Peltzer, K. Feigl, and T. Rabaute (1993), The displacement field of the Landers earthquake mapped by radar interferometry, *Nature*, 364(6433), 138-142.

Matusik-Property-Insights (2011), Chinchilla, Miles, and the Surat Basin *Rep.*, Matusik Market Overview Report, accessed on : 25.06.2015

[URL:https://www.google.com/?gws\\_rd=ssl#q=Chinchilla%2C+Miles+and+the+Surat+Basin+Matusik+Market+Overview+%C2%A9+Report](https://www.google.com/?gws_rd=ssl#q=Chinchilla%2C+Miles+and+the+Surat+Basin+Matusik+Market+Overview+%C2%A9+Report).

McCandless, S. W., and C. R. Jackson (2004), Principles of synthetic Aperture Radar - Chapter 1, N.S. manual, edited by NOAA, pp. 1-24.

McCarthy, P., J. Brand, B. Paradiso, J. N. Ezekwe, N. Wiltgen, A. Bridge, R. Willingham, and M. Bogaards (2006), Using Geostatistical Inversion of Seismic and Borehole Data to Generate Reservoir Models for Flow Simulations of Magnolia Field, Deepwater Gulf of Mexico, in *6th International Conference & Exposition on Petroleum Geophysics*, pp. 573-576, Kolkata.

McTigue, D. F., and P. Segall (1988), Displacements and tilts from dip-slip faults and magma chambers beneath irregular surface topography, *GEOPHYSICAL RESEARCH LETTERS*, 15(6), 601-604.

Megorden, M. P., H. Jiang, and P. J. D. Bentley (2013), Improving Hydraulic Fracture Geometry by Directional Drilling in Coal Seam Gas Formation, in *SPE Unconventional Resources Conference and Exhibition-Asia Pacific (SPE 167053)*, Brisbane, Australia.

Mogi, K. (1958), Relations between the eruptions of various volcanoes and the deformation of the ground surfaces around them, *Open File Rep. Bull. Earthquake Research Institute* 36, 99-134 pp.

Murphy, G. (2008), Management of Groundwater – Condamine River and Tributary Alluvium: Information Paper for Groundwater licensees and users (Central Condamine River Alluvium), *Open File Rep.*, Groundwater Assessment and Planning Group, Water Services, South West Region, Department of Natural Resources and Water, Brisbane.

## N

Nagel, N. B. (2001), Compaction and subsidence issues within the petroleum industry: From wilmington to ekofisk and beyond, *Physics and Chemistry of the Earth, Part A: Solid Earth and Geodesy*, 26(1-2), 3-14.

Neeff, T., L. V. Dutra, J. R. dos Santos, C. d. C. Freitas, and L. S. Araujo (2005), Tropical Forest Measurement by Interferometric Height Modeling and P-Band Radar Backscatter, *Forest Science*, 51(6), 585-594.

Ng, A. H.-M., L. Ge, K. Zhang, and X. Li (2012), Estimating horizontal and vertical movements due to underground mining using ALOS PALSAR, *Engineering Geology*, 143-144, 18-27.

Normand, J. C. L., and E. Heggy (2015), InSAR Assessment of Surface Deformations in Urban Coastal Terrains Associated With Groundwater Dynamics, *Geoscience and Remote Sensing, IEEE Transactions on*, 53(12), 6356-6371.

## O

Okada, Y. (1985), Surface deformation due to shear and tensile faults in a half-space, *Bulletin of the Seismological Society of America*, 75(4), 1135-1154.

Ostermeier, R. M. (1995), Deep water gulf of Mexico turbidites - compaction effects on porosity and permeability, paper presented at Society of Petroleum Engineers Formation Evaluation, 10(2), 26468-PA, <http://dx.doi.org/10.2118/26468-PA>.

## P

Papendick, S. L., K. R. Downs, K. D. Vo, S. K. Hamilton, G. K. W. Dawson, S. D. Golding, and P. C. Gilcrease (2011), Biogenic methane potential for Surat Basin, Queensland coal seams, *International Journal of Coal Geology*, 88(2–3), 123-134.

Peng, S., and J. Zhang (2007), In-situ stress and pore pressure, in *Engineering Geology for Underground Rocks*, p. 319, Springer Press, Berlin.

Perissin, D., Z. Wang, and T. Wang (2011), The SARPROZ InSAR tool for urban subsidence/manmade structure stability monitoring in China, paper presented at ISRSE 2011, Sydney, Australia.

Perski, Z., R. Hanssen, A. Wojcik, and T. Wojciechowski (2009), InSAR analyses of terrain deformation near the Wieliczka Salt Mine, Poland, *Engineering Geology*, 106(1–2), 58-67.

Perski, Z., and D. Jura (2003), Identification and measurement of mining subsidence with SAR interferometry: potentials and limitations, paper presented at 11th FIG Symposium on Deformation Measurements, Santorini, Greece.

Petrat, L., and U. Wegmuller (2003), Simulation of abandoned mining induced surface movements for estimating DInSAR detection limits, paper presented at Geoscience and Remote Sensing Symposium, 2003. IGARSS '03. Proceedings. 2003 IEEE International, 21-25 July 2003.

Piessens, R. (2000), The Hankel Transform, in *The transforms and applications handbook* edited by A. D. Poularikas, Boca Raton, CRC Press, LLC.

Plischke, B. (1994), Finite element analysis of compaction and subsidence - Experience gained from several chalk fields, in *Proceedings of EUROCK '94*, pp. 795-802.

Poland, J. F., and G. H. Davis (1969), Land subsidence due to withdrawal of fluids, *Reviews in Engineering Geology* 2, 187- 269.

Power, P. E., and S. B. Devine (1970), Surat Basin, Australia – subsurface stratigraphy, history, and petroleum, *Open File Rep. American Association of Petroleum Geologists, Bulletin* 54, 2410 – 2437 pp.

Prati, C., A. Ferretti, and D. Perissin (2010), Recent advances on surface ground deformation measurement by means of repeated space-borne SAR observations, *Journal of Geodynamics*, 49(3–4), 161-170.

Preston, R., P. Lawson, and T. Darbas (2007), Landholder practices, attitudes, constraints and opportunities for change in the Condamine Alliance region, *Open File Rep.*, Condamine Alliance and Department of Natural Resources and Water, Toowoomba.

Pritchard, M. E., and M. Simons (2004), An InSAR-based survey of volcanic deformation in the central Andes, *Geochemistry, Geophysics, Geosystems*, 5(2).

**Q**

QCGI (2009), Potential for carbon geostorage in the Taroom Trough, Roma Shelf and the Surat, Eromanga and Galilee Basins, Preliminary Report, *Open File Rep.*, 311 pp, Geological Survey of Queensland Carbon Geostorage Initiative, Brisbane.

QGC (2013a), The conceptual model of groundwater flow in the Surat Basin, *Open File Rep.*, 70-86 pp, Brisbane.

QGC (2013b), Approval Conditions 49 to 64: Stage 3 CSG Water Monitoring and Management Plan, *First Revision Open File Rep.*, 414 pp, Brisbane.

QGC (2013c), Ground motion monitoring and management plan, Part 10.0, *Open File Rep.*, 112-123 pp, Queensland Mines and Energy, Queensland's coal seam gas overview - industry update 2012.

QGC (2013d), Report for QWC-17-10 (Stage 3 WMMP): CSG water monitoring and management plan, *Open File Rep.*, accessed on : 05.02.2015.

Queensland-Mines-and-Energy (2012), Queensland's coal seam gas overview - industry update. (<http://mines.industry.qld.gov.au/assets/qld-mining-update/csg.pdf>), 05.02.2015.

QWC (2012), Underground Water Impact Report for the Surat Cumulative Management Area, *Open File Rep.*, Coal Seam Gas Water, Queensland Water Commission, [www.qwc.qld.gov.au](http://www.qwc.qld.gov.au).

QWC (2013), Surat Underground Water Impact Report- Summary, *Open File Rep.*, Brisbane.

**R**

Radke, B. M., J. Ferguson, R. G. Creswell, T. R. Ransley, and M. A. Habermehl (2000), Hydrochemistry and implied hydrodynamics of the Cadna-owie-Hooray aquifer Great Artesian Basin *Rep.*, 229 pp, Bureau of Rural Science, Canberra.

Raiber, M., P. A. White, C. J. Daughney, C. Tschritter, P. Davidson, and S. E. Bainbridge (2012), Three-dimensional geological modelling and multivariate statistical analysis of water chemistry data to analyse and visualise aquifer structure and groundwater composition in the Wairau Plain, Marlborough District, New Zealand, *Journal of Hydrology*, 436–437, 13-34.

Ramirez, A., and W. Foxall (2014), Stochastic inversion of InSAR data to assess the probability of pressure penetration into the lower caprock at In Salah, *International Journal of Greenhouse Gas Control*, 27, 42-58.

Raucoules, D., C. Maisons, C. Carnec, S. Le Mouelic, C. King, and S. Hosford (2003), Monitoring of slow ground deformation by ERS radar interferometry on the Vauvert salt mine (France): Comparison with ground-based measurement, *Remote Sensing of Environment*, 88(4), 468-478.

Rayner, B. L. (1987), ATP 247P Technical Review, Beach Petroleum N.L., accessed on: 17.05.2015.

Rosen, P. A., S. Hensley, I. R. Joughin, K. L. Fuk, S. N. Madsen, E. Rodriguez, and R. M. Goldstein (2000), Synthetic aperture radar interferometry, *Proceedings of the IEEE*, 88(3), 333-382, doi:10.1109/5.838084.

Rothman, D. H. (1985), Nonlinear inversion, statistical mechanics, and residual statics estimation, *Geophysics*, 50(12), 2784-2796.

Rucci, A., D. W. Vasco, and F. Novali (2010), Fluid pressure arrival-time tomography: Estimation and assessment in the presence of inequality constraints with an application to production at the Krechba field, Algeria, *Geophysics*, 75(6), O39-O55.

Rucci, A., D. W. Vasco, and F. Novali (2013), Monitoring the geologic storage of carbon dioxide using multicomponent SAR interferometry, *Geophysical Journal International*.

## S

Sambridge, M. (1999), Geophysical inversion with a neighbourhood algorithm—I. Searching a parameter space, *Geophysical Journal International*, 138(2), 479-494.

Sambridge, M., and K. Mosegaard (2002), MONTE CARLO METHODS IN GEOPHYSICAL INVERSE PROBLEMS, *Reviews of Geophysics*, 40(3), 3-1-3-29.

Samsonov, S., N. d'Oreye, P. J. González, K. F. Tiampo, L. Ertolahti, and J. J. Clague (2014), Rapidly accelerating subsidence in the Greater Vancouver region from two decades of ERS-ENVISAT-RADARSAT-2 DInSAR measurements, *Remote Sensing of Environment*, 143, 180-191.

Samsonov, S., and N. d'Oreye (2012), Multidimensional time-series analysis of ground deformation from multiple InSAR data sets applied to Virunga Volcanic Province, *Geophysical Journal International*, 191(3), 1095-1108.

Samsonov, S., N. d'Oreye, and B. Smets (2013), Ground deformation associated with post-mining activity at the French–German border revealed by novel InSAR time series method, *International Journal of Applied Earth Observation and Geoinformation*, 23, 142-154.

Samsonov, S., M. van der Kooij, and K. Tiampo (2011), A simultaneous inversion for deformation rates and topographic errors of DInSAR data utilizing linear least square inversion technique, *Computers & Geosciences*, 37(8), 1083-1091.

Sandwell, D. T., and E. J. Price (1998), Phase gradient approach to stacking interferograms, *Journal of Geophysical Research: Solid Earth*, 103(B12), 30183-30204.

Sansosti, E., F. Casu, M. Manzo, and R. Lanari (2010), Space-borne radar interferometry techniques for the generation of deformation time series: An advanced tool for Earth's surface displacement analysis, *GEOPHYSICAL RESEARCH LETTERS*, 37(20).

Schlumberger (2005), Eclipse Reference Manual , accessed on : 27.10.2014.

Schlumberger (2010), Petrel E&P technical manual.

Schlumberger (2015), Oilfield

Glossary, <http://www.glossary.oilfield.slb.com/en/Terms.aspx?LookIn=term%20name&filter=abnormal+pressure>.

Scholes, P. L., and D. Johnston (1993), Coalbed Methane Applications of Wireline Logs, in *Hydrocarbons from Coal*, edited by B. E. Law and D. D. Rice, p. 400, AAPG, Tulsa, Oklahoma, USA.

Scott (1999), Improving Coal Gas Recovery with Microbially Enhanced Coalbed Methane, in *Coalbed Methane: Scientific, Environmental and Economic Evaluation*, edited by M. Mastalerz, M. Glikson and S. Golding, pp. 89-110, Springer Netherlands.

- Scott (2002), Hydrogeologic factors affecting gas content distribution in coal beds, *International Journal of Coal Geology*, 50, 363-387.
- Scott, B. Anderson, P. Crosdale, J. Dingwall, and G. Leblang (2004), Revised Geology and Coal Seam Gas Characteristics of the Walloon Sub-group, paper presented at PESA Eastern Australasian Basins Symposium II, Adelaide.
- Scott, B. Anderson, P. Crosdale, J. Dingwall, and G. Leblang (2007), Coal petrology and coal seam gas contents of the Walloon Subgroup - Surat Basin, Queensland, Australia, *International Journal of Coal Geology* 70, 209-222.
- Segall, P. (1992), Induced stresses due to fluid extraction from axisymmetric reservoirs *Pure & Applied Geophysics* 139(3-4), 535-560.
- Segall, P. (2010), *Earthquake and volcano deformation*, 456 pp., Princeton Univ. Press, ISBN 9780691133027.
- Shirvany, R. (2012), Estimation of the degree of polarization in polarimetric SAR imagery: Principles and Applications, 116 pp, Univ. of Toulouse, France.
- Shirzaei, M., and T. R. Walter (2009), Randomly iterated search and statistical competency as powerful inversion tools for deformation source modeling: Application to volcano interferometric synthetic aperture radar data, *Journal of Geophysical Research: Solid Earth*, 114(B10).
- Simons, M., and P. A. Rosen (2007), Interferometric synthetic aperture radar geodesy, *Treatise on Geophysics, Geodesy*, 3, 391- 446.
- Sliwa, R., and J. Esterle (2008), Re-evaluation of structure and sedimentary packages in the eastern Surat Basin, in *Eastern Australasian Basins Symposium III, Petroleum Exploration Society of Australia, Special Publication*, edited by J. E. Blevin, p. 527.
- SRK (2008), Bowen and Surat Basins Regional Structural Framework Study.
- Statistics-Canada (2009), Seasonal adjustment and trend-cycle estimation, Statistics Canada Quality Guideline, 5th edition, Catalogue no. 12-539-X, <http://www.statcan.gc.ca/pub/12-539-x/2009001/seasonal-saisonnal-eng.htm>, accessed on 15.01.2015.
- T**
- Tan, P. L., et al. (2010), Tools for water planning: lessons, gaps and adoption, *WaterlinesRep. Part 3*, National Water Commission, Canberra.
- Tarayre, H., and D. Massonnet (1996), Atmospheric Propagation heterogeneities revealed by ERS-1 interferometry, *GEOPHYSICAL RESEARCH LETTERS*, 23(9), 989-992.
- Teatini, P., L. Tosi, T. Strozzi, L. Carbognin, G. Cecconi, R. Rosselli, and S. Libardo (2012), Resolving land subsidence within the Venice Lagoon by persistent scatterer SAR interferometry, *Physics and Chemistry of the Earth, Parts A/B/C*, 40-41, 72-79.
- Telioni, E. (2006), Ground Surface Settlements due to Underground Works, in *Geodetic Deformation Monitoring: From Geophysical to Engineering Roles*, edited by F. Sansò and A. Gil, pp. 285-292, Springer Berlin Heidelberg.
- Thomson, W. T. (1950), Transmission of elastic waves through a stratified medium, *Journal of Applied Physics*, 21, 89-93.

Tiab, D., and E. C. Donaldson (2012), *Petrophysics: theory and practice of measuring reservoir rock and fluid transport properties*, Third ed., Gulf professional publishing.

## V

Van Zyl, J., and Y. Kim (2010), *Synthetic Aperture Radar Polarimetry*, 309 pp., John Wiley and Sons, ISBN 978-1-118-11511-4, JPL, Caltech.

Vasco, D. W. (2008), Estimating permeability from quasi-static deformation: Temporal variations and arrival time inversion.

Vasco, D. W., A. Datta-Gupta, R. Behrens, P. Condon, and J. s. Rickett (2003), Seismic imaging of reservoir flow properties: Time-lapse amplitude changes.

Vasco, D. W., and A. Ferretti (2005), On the use of quasi-static deformation to understand reservoir fluid flow, *Geophysics*, 70(4), O13-O27.

Vasco, D. W., A. Ferretti, and F. Novali (2008), Estimating permeability from quasi-static deformation: Temporal variations and arrival-time inversion, *Geophysics*, 73(6), O37-O52.

Vasco, D. W., L. R. Johnson, and N. E. Goldstein (1988), Using surface displacement and strain observations to determine deformation at depth, with an application to Long Valley Caldera, California, *Journal of Geophysical Research: Solid Earth*, 93(B4), 3232-3242.

Vasco, D. W., K. Karasaki, and K. Kishida (2001), A coupled inversion of pressure and surface displacement, *Water Resources Research*, 37(12), 3071-3089.

Vasco, D. W., A. Rucci, A. Ferretti, F. Novali, R. C. Bissell, P. S. Ringrose, A. S. Mathieson, and I. W. Wright (2010), Satellite-based measurements of surface deformation reveal fluid flow associated with the geological storage of carbon dioxide, *GEOPHYSICAL RESEARCH LETTERS*, 37(3).

Veil, J. A., M. G. Puder, D. Elcock, and R. J. Redweik, Jr. (2004), A white paper describing produced water from production of crude oil, natural gas, and coal bed methane *Rep. Under Contract W-31-109-Eng-38*, U.S. Department of Energy, National Energy Technology Laboratory.

## W

Wang, R., F. Lorenzo-Martín, and F. Roth (2006), PSGRN/PSCMP—a new code for calculating co- and post-seismic deformation, geoid and gravity changes based on the viscoelastic-gravitational dislocation theory, *Computers & Geosciences*, 32(4), 527-541.

White, I., K. Burry, G. Baldwin, P. Tan, D. George, and J. Mackenzie (2010), National Water Commission- Water lines- Part 3- Condamine groundwater from over allocation to sustainable extraction, *Open File Rep.*, 187-282 pp.

Wickens, H. D., and A. H. Bouma (2000), The Tanqua Fan Complex, Karoo Basin, South Africa- Outcrop Analog for Fine-Grained, Deepwater Deposits, in *Fine-Grained Turbidite Systems*, edited by A. H. Bouma and C. G. Stone, pp. 153-163, AAPG Memoir 72/SEPM Special Publication.

Williams, S., Y. Bock, and P. Fang (1998), Integrated satellite interferometry: Tropospheric noise, GPS estimates and implications for interferometric synthetic aperture radar products, *Journal of Geophysical Research: Solid Earth*, 103(B11), 27051-27067.

Woods, P. H., G. R. Walker, and G. B. Allison (1990), Estimating groundwater discharge at the southern margin of the Great Artesian Basin near Lake Eyre, South Australia, paper presented at Proceedings of the International Conference on Groundwater in Large Sedimentary Basins, Australian Water Resources Counsel Conference Series, No. 20, p.298-309, Perth, Australia, 9-13 July.

Worley-Parson (2010), Spatial Analysis of Coal Seam Water Chemistry, Task1 : Literature Review, *Open File Rep. 301001-012102Z1001A*, 62 pp.

Wright, and R. Stow (1999), Detecting mining subsidence from space, *International Journal of Remote Sensing*, 20(6), 1183-1188.

Wright, T., E. Fielding, and B. Parsons (2001), Triggered slip: Observations of the 17 August 1999 Izmit (Turkey) Earthquake using radar interferometry, *GEOPHYSICAL RESEARCH LETTERS*, 28(6), 1079-1082.

## Y

Yague-Martinez, N., M. Eineder, C. Xiao Ying, and C. Minet (2012), Ground Displacement Measurement by TerraSAR-X Image Correlation: The 2011 Tohoku-Oki Earthquake, *Geoscience and Remote Sensing Letters, IEEE*, 9(4), 539-543.

Yang, X.-M., P. M. Davis, and J. H. Dieterich (1988), Deformation from inflation of a dipping finite prolate spheroid in an elastic half-space as a model for volcanic stressing, *Journal of Geophysical Research: Solid Earth*, 93(B5), 4249-4257.

## Z

Zahiri, H. (2012), Integration of Synthetic Aperture Radar Interferometry (InSAR) and Geographical Information Systems (GIS) for monitoring mining induced surface deformations, Curtin University.

Zebker, H. A., P. A. Rosen, R. M. Goldstein, A. Gabriel, and C. L. Werner (1994), On the derivation of coseismic displacement fields using differential radar interferometry: The Landers earthquake, *Journal of Geophysical Research: Solid Earth*, 99(B10), 19617-19634.

Zebker, H. A., P. A. Rosen, and S. Hensley (1997), Atmospheric effects in interferometric synthetic aperture radar surface deformation and topographic maps, *Journal of Geophysical Research: Solid Earth*, 102(B4), 7547-7563.

Zebker, H. A., and J. Villasenor (1992), Decorrelation in interferometric radar echoes, *Geoscience and Remote Sensing, IEEE Transactions on*, 30(5), 950-959.

Zektser, S., H. A. Loáiciga, and J. T. Wolf (2005), Environmental impacts of groundwater overdraft: selected case studies in the southwestern United States, *Env Geol*, 47(3), 396-404.

Zhang, K., A. H.-M. Ng, L. Ge, Y. Dong, and C. Rizos (2010), L-Band and C-Band Combined Interferometric Monitoring of the Wenchuan Earthquake, in *Advances in Earth Observation of Global Change*, edited by E. Chuvieco, J. Li and X. Yang, pp. 239-253, Springer Netherlands, Dordrecht.

Zhdanov, M. S. (2009), Geophysical Electromagnetic Theory and Methods, in *Methods in Geochemistry and Geophysics 43*, Utah, USA.

Zhu, Q.-L. Wang, Y.-L. Shi, and D.-X. Cui (2008), Modelling Pressurized Deformation Source for Changbaishan Volcano with Homogenous Expansion Point Source, *Chinese Journal of Geophysics*, 51(1), 89-96.

Zhu, Q. Zhang, X. Ding, C. Zhao, C. Yang, F. Qu, and W. Qu (2014), Landslide monitoring by combining of CR-InSAR and GPS techniques, *Advances in Space Research*, 53(3), 430-439.

# Appendix A1

## Depth and Isopach Maps

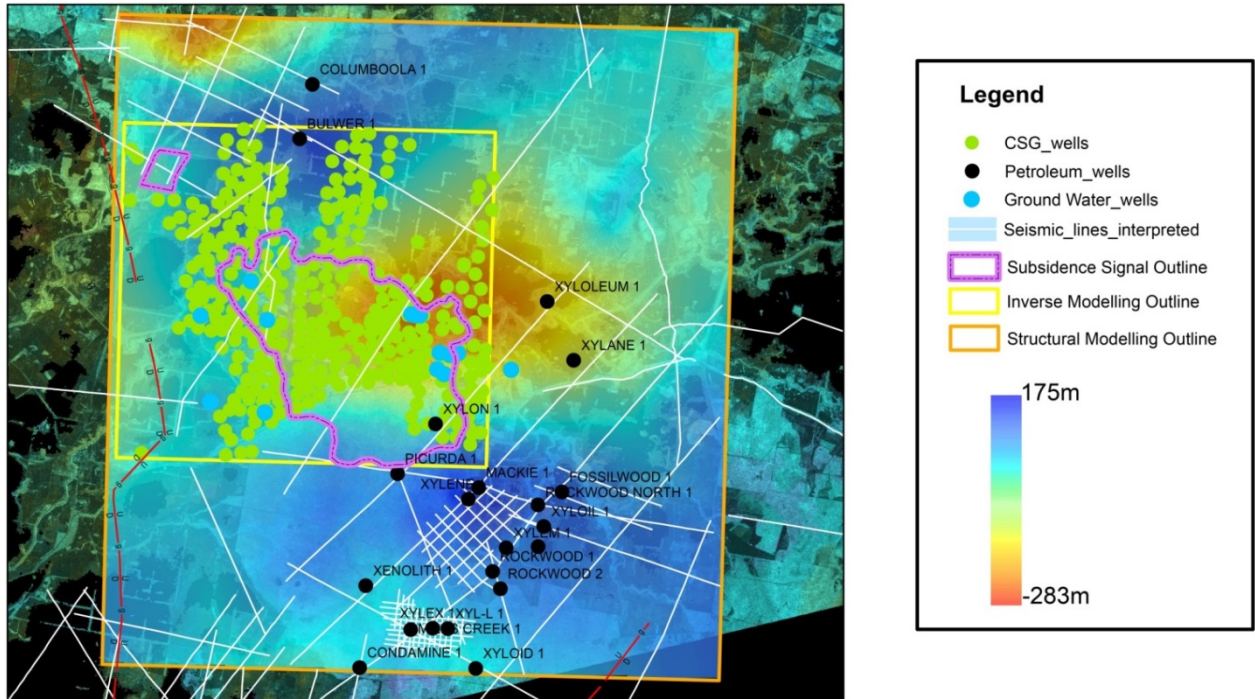


Figure A-1: Westbourne Formation depth map extracted from seismic depth conversion

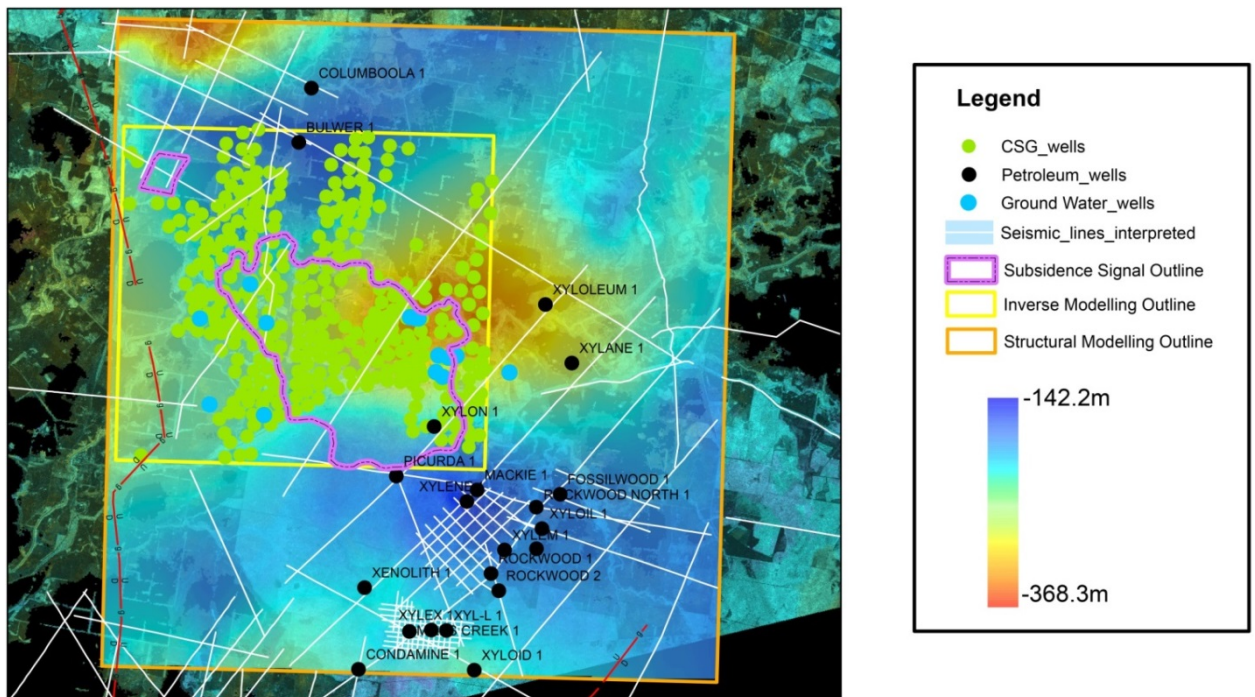


Figure A-2: Springbok Sandstone depth map extracted from seismic depth conversion.



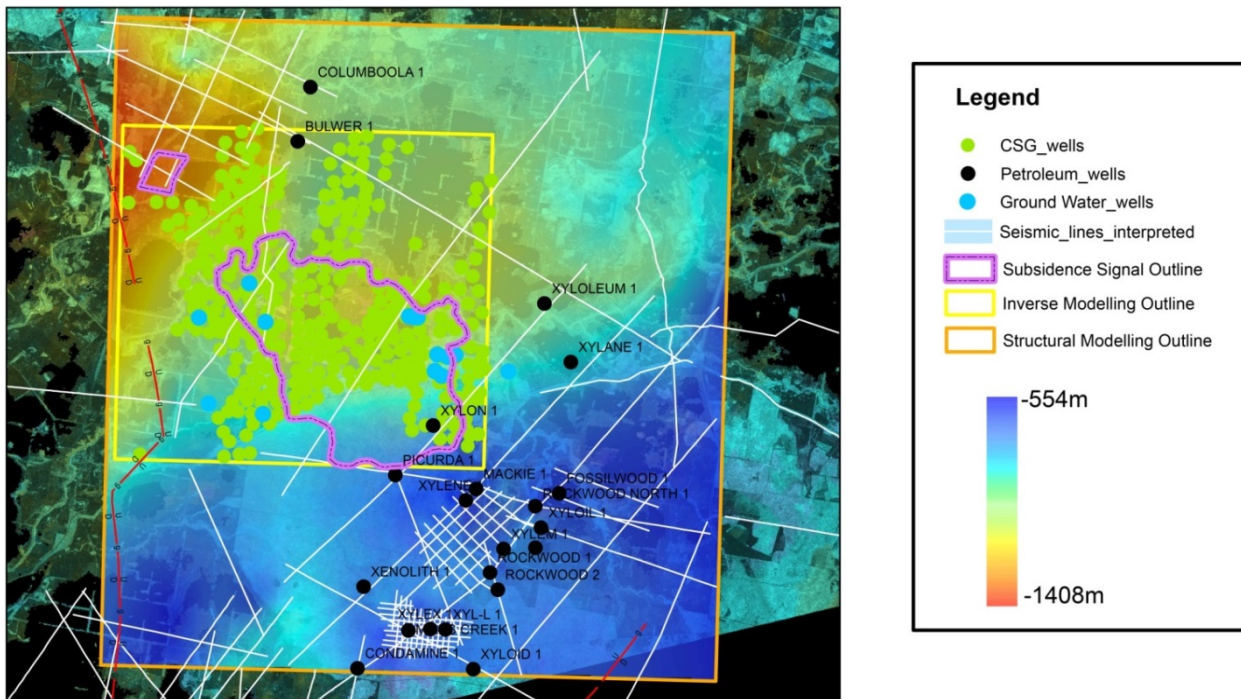


Figure A-5: Evergreen Formation depth map extracted from seismic depth conversion.

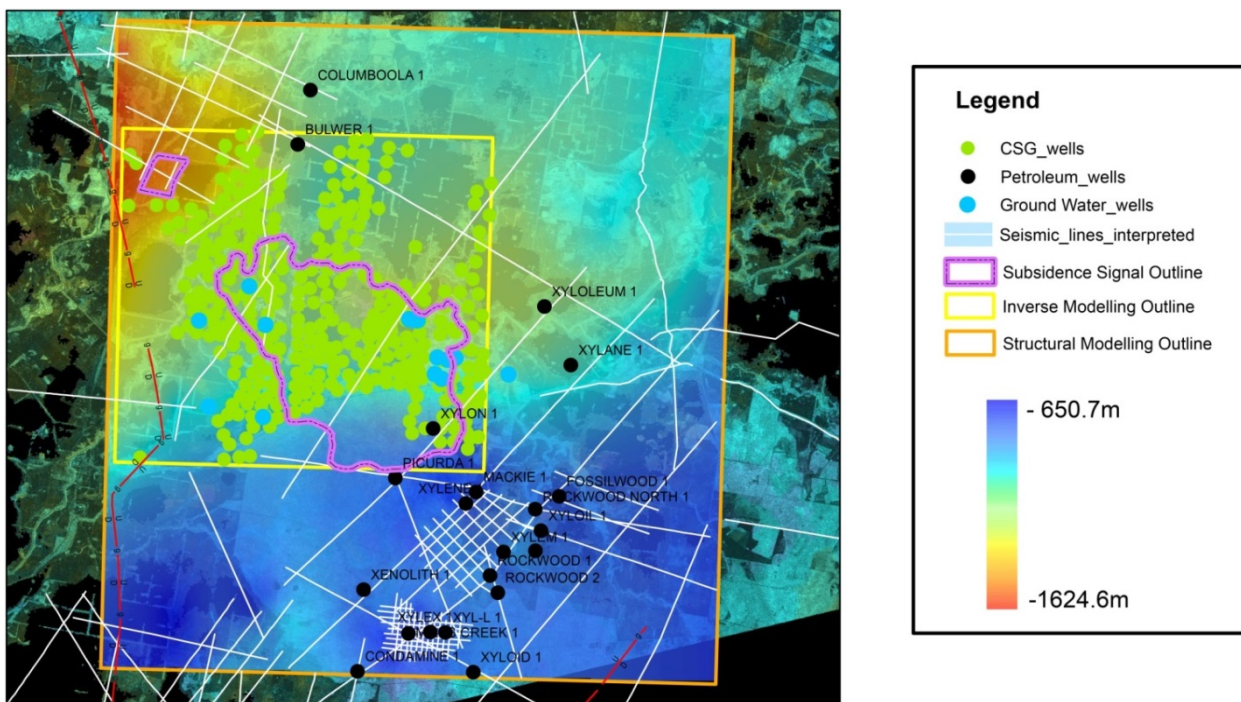


Figure A-6: Precipice Sandstone depth map extracted from seismic depth conversion.

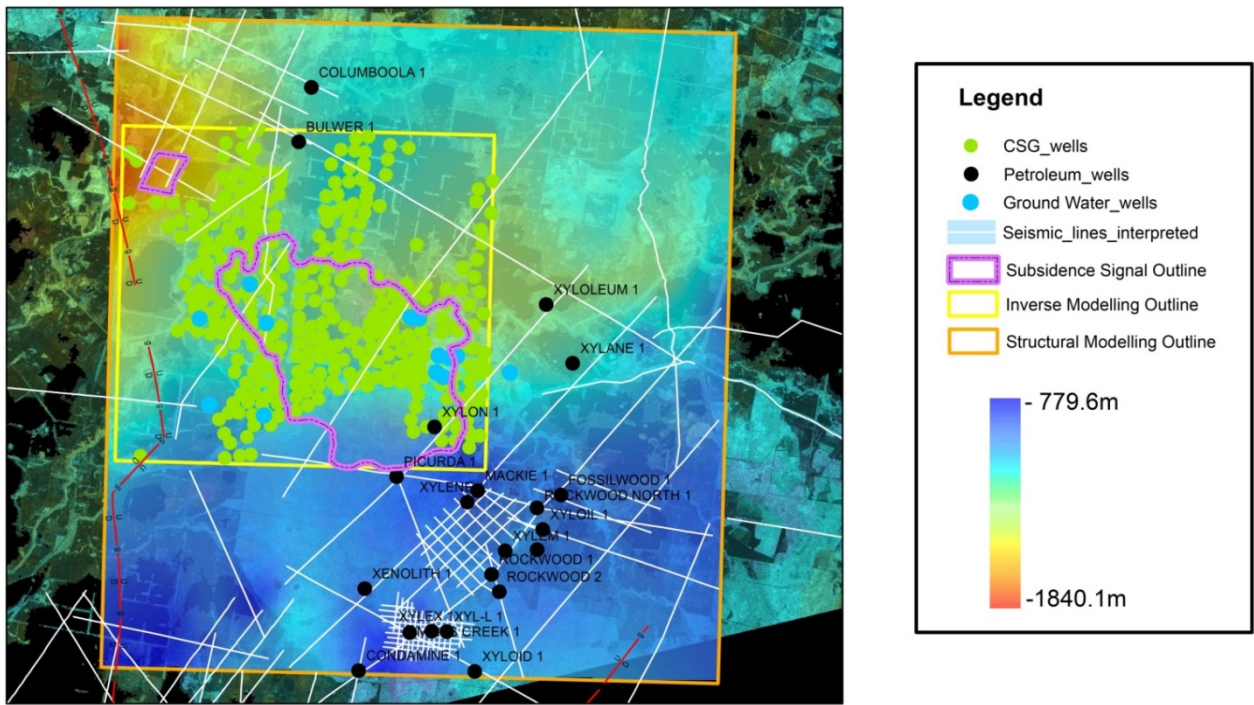


Figure A-7: Basement depth map extracted from seismic depth conversion.

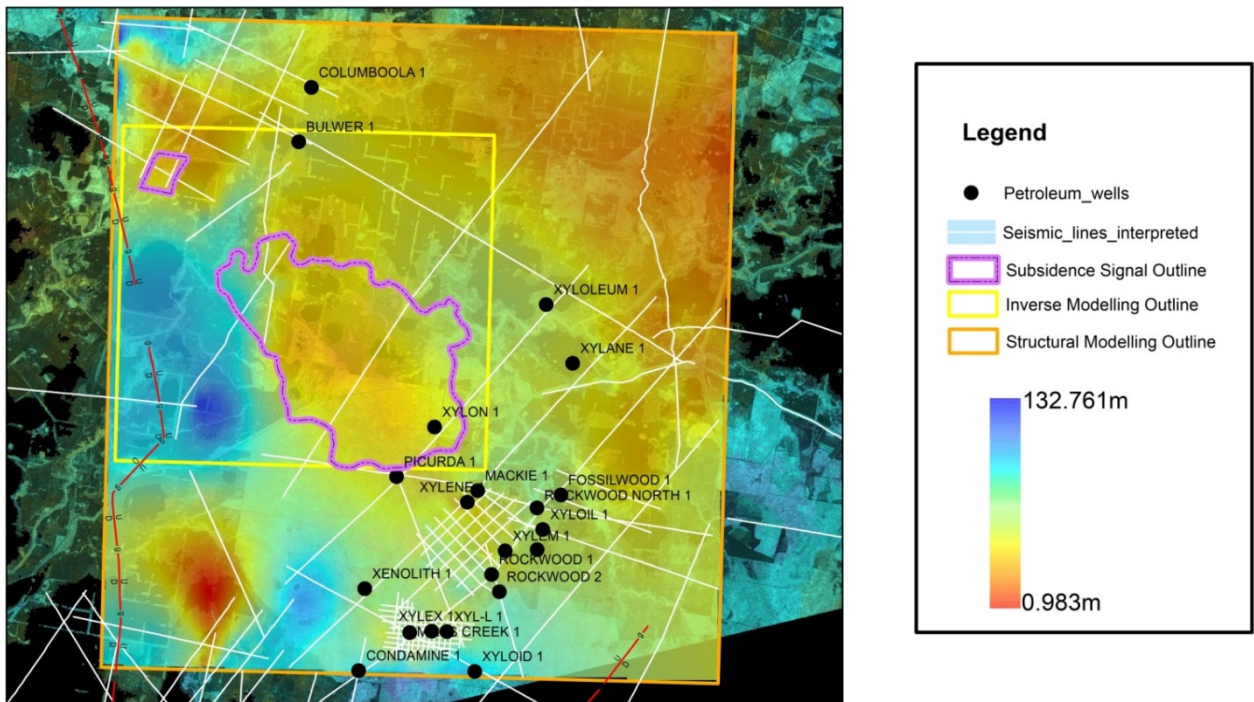
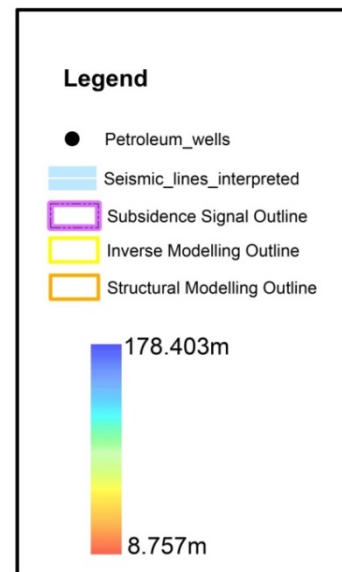
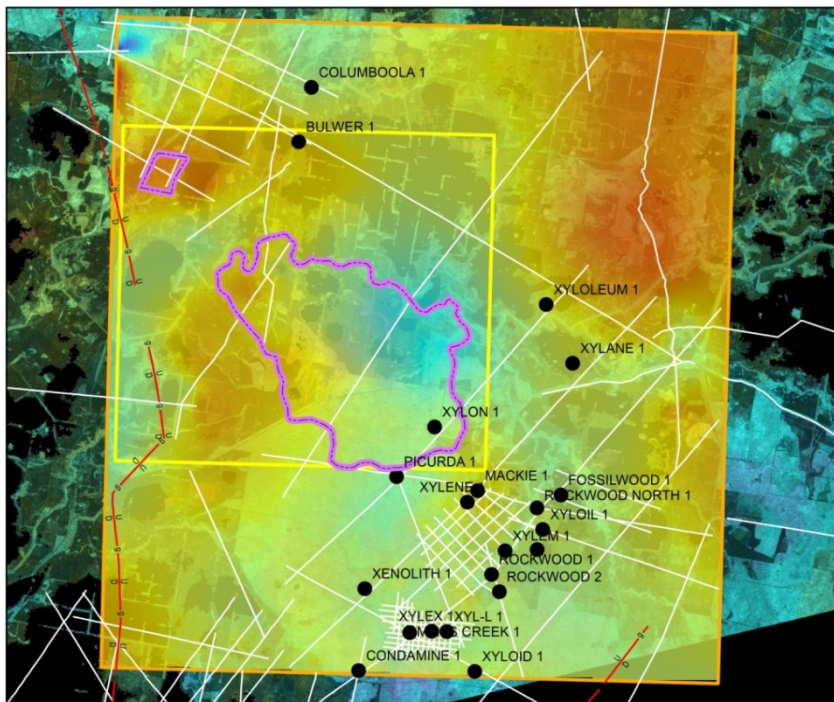
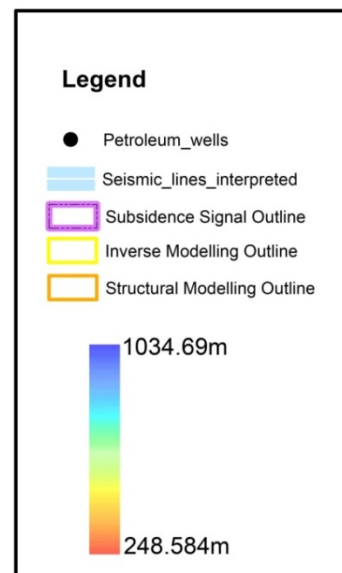
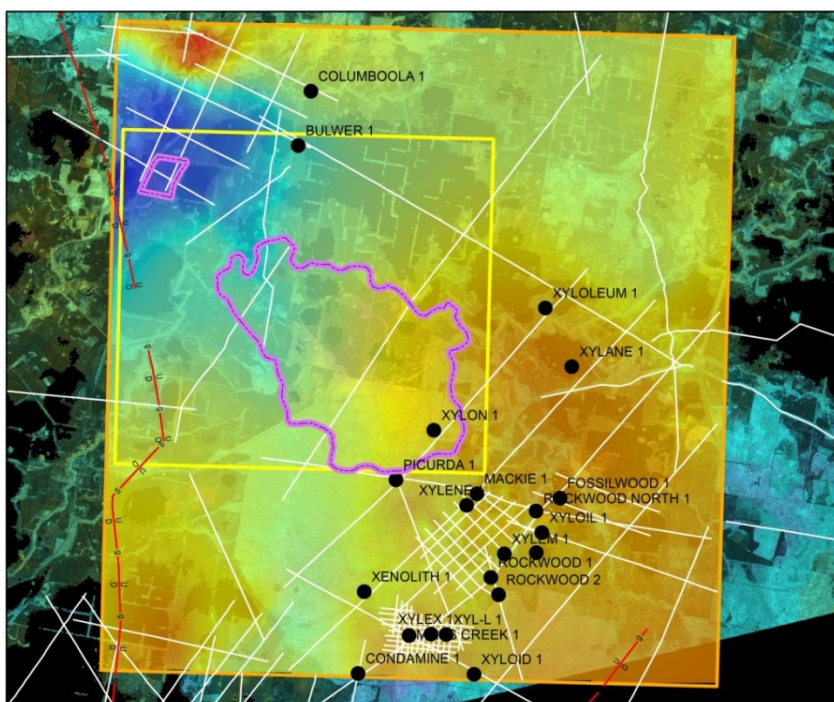


Figure A-8: Westbourne Formation – Springbok Sandstone isopach map extracted from seismic depth conversion.



**Figure A-9: Springbok Sandstone – Walloon Coal Measures isopach map extracted from seismic depth conversion.**



**Figure A-10: Walloon Coal Measures – Hutton Sandstone isopach map extracted from seismic depth conversion.**

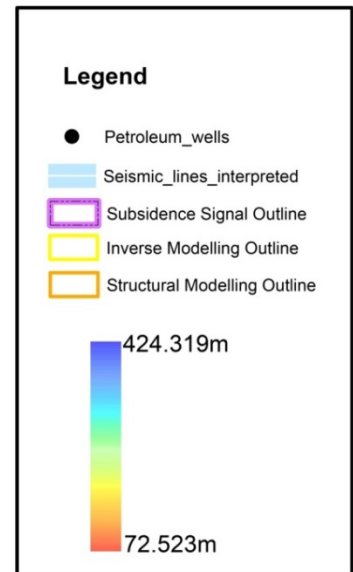
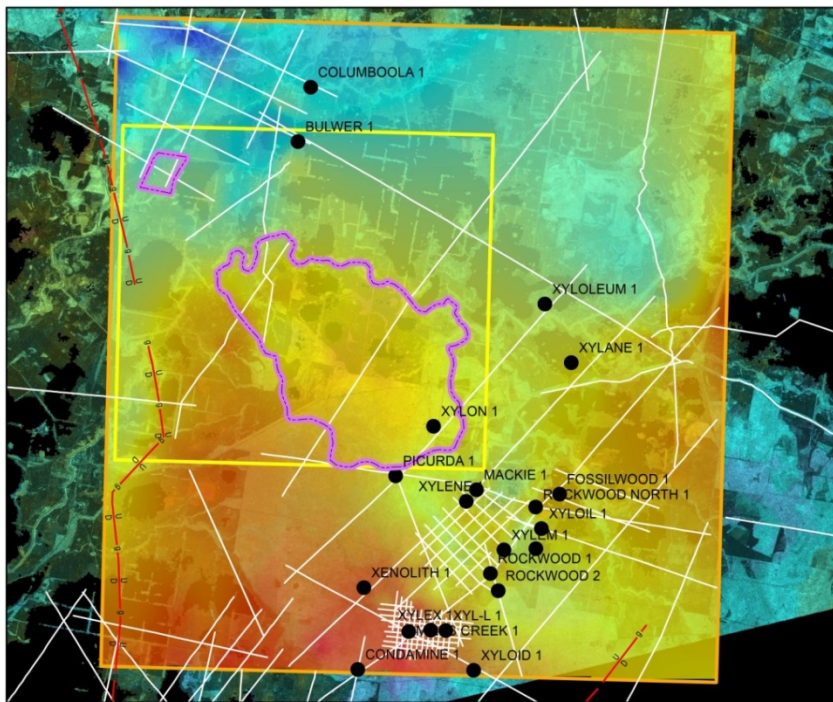


**Figure A-11: Hutton Sandstone – Evergreen Formation isopach map extracted from seismic depth conversion.**

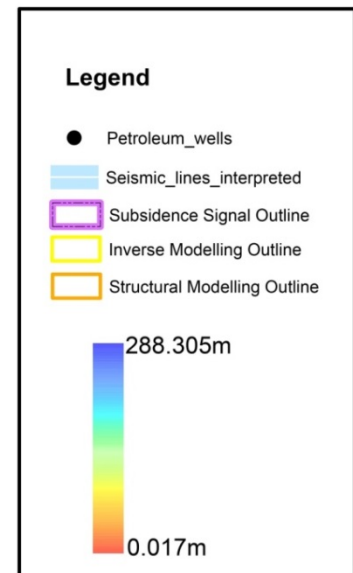
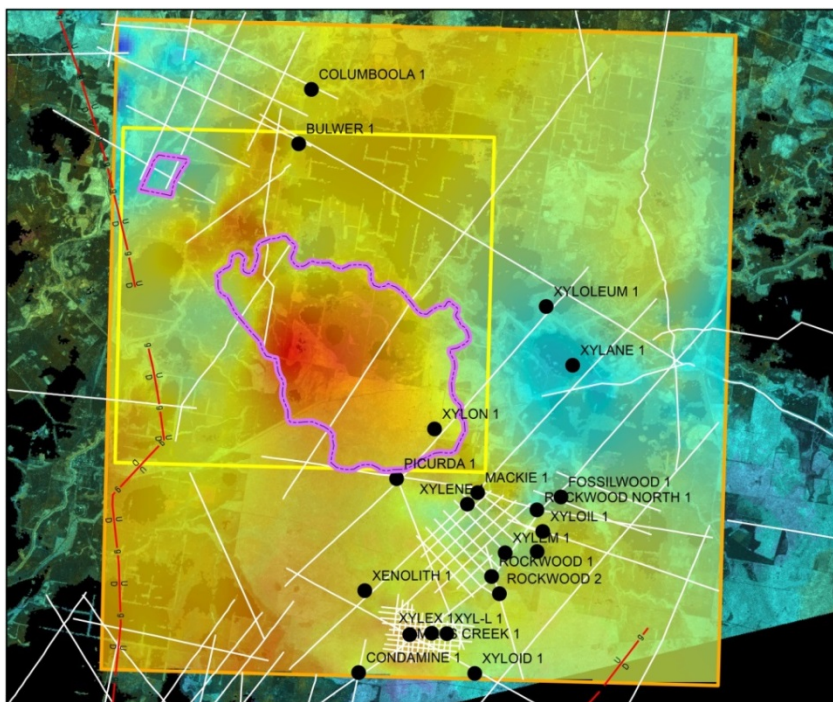


**Figure A-12: Evergreen Formation – Precipice Sandstone Isopach Map Extracted from Seismic Depth Conversion.**

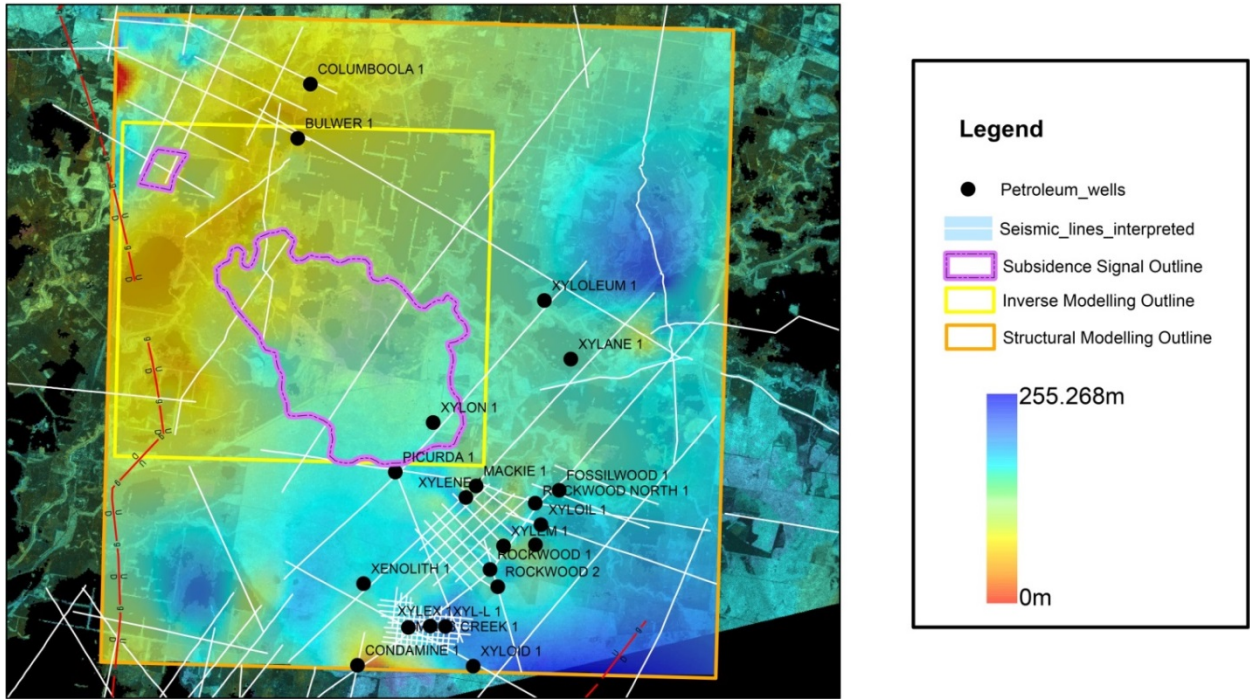


Figure A-13: Precipice Sandstone – Basement Isopach Map Extracted from Seismic Depth Conversion.

## Appendix A2

### Tables

Table A-1: List of lines with good quality for further seismic interpretation and analysis.

|          |           |          |         |         |
|----------|-----------|----------|---------|---------|
| 80-H36   | H81BN-35  | MS87B-35 | XM86-4  | XX85-5  |
| 80-H37   | H82BN-103 | MS87B-37 | XM86-5  | XX85-7  |
| 80-H39   | OW05-101  | MS87B-39 | XM86-6  | XX85-8  |
| AT92-03  | OW05-102  | OO07-3   | XM86-7  | XX85-10 |
| AT92-04  | OW05-103  | OO07-4   | XM86-8  | XX85-12 |
| AT92-05  | MS87B-12  | OO07-5   | XM86-9  | XX85-14 |
| AT92-06  | MS87B-14  | PR81-12A | XM86-10 | XX86-1  |
| H79-3    | MS87B-16  | PR81-12B | XM86-12 | XX86-16 |
| H81BN-15 | MS87B-31  | XM86-2   | XM86-14 | XX86-18 |
| H81BN-17 | MS87B-33  | XM86-3   | XX85-3  | XX86-25 |

Table A-2: List of fault names that were detected in the area of interest by interpreting seismic lines.

|             |              |           |
|-------------|--------------|-----------|
| OW05-F1     | MS87B-37-F7  | XM86-F8   |
| OW05-F2     | MS87B-37-F10 | XM86-F10  |
| OW05-F3     | XX85-F1      | XM86-F11  |
| OW05-F4     | XX85-F2      | XM86-F12  |
| OW05-F5     | XX85-F3      | H81BN-F1  |
| MS87B-F1    | XM86-F1      | H81BN-F4  |
| MS87B-F2    | XM86-F2      | H81BN-F5  |
| MS87B-F3    | XM86-F3      | H81BN-F6  |
| MS87B-37-F4 | XM86-F4      | OO07-4-F5 |
| MS87B-37-F5 | XM86-F5      | OO07-4-F6 |
| MS87B-37-F6 | XM86-F7      |           |

Table A-3: List of wells in the area outlined for modelling and with available formation tops. Among these wells only 8 reached the basement beneath the Surat Basin. Arlington\_1 is the deepest well and penetrated to the precipice Sandstone (1997 m MD).

|                     |                |                 |                 |                     |                |              |
|---------------------|----------------|-----------------|-----------------|---------------------|----------------|--------------|
| ABERDEEN_PARK_1     | BRAEMAR_1      | DAVIDSON_1      | KOGAN_1         | MALARA_1            | ROGERS_1       | WIEAMBILLA_1 |
| ALICK_CREEK_1       | BULWER_1       | DEEP_CROSSING_1 | KOGAN_SOUTH_1   | MILES_CREEK_1       | TARA_1         | WILLARA_1    |
| ARLINGTON_1         | CABAWIN_2      | DEVON_PARK_1    | KUMBARILLA_1-1A | PADDY_CREEK_1       | TARA_SOUTH_1   | XYLEX_1      |
| BENNETT_1           | CABAWIN_EAST_1 | DOGWOOD_1       | LAWSON_1        | PADDY_CREEK_SOUTH_1 | TEATREE_1      |              |
| BENNETT_2           | COBBAREENA_1   | FOSSILWOOD_1    | LEICHHARDT_1    | PAGET_1             | TEY_1          |              |
| BENNETT_NORTH_1     | COLUMBOOLA_1   | GREEN_SWAMP_1   | LEICHHARDT_2    | PICURDA_1           | UNDULLA_1      |              |
| BENTLEY_1           | CONDAMINE_1    | GUMS_1          | LORRAINE_1      | PIEBALD_1           | WAMBO_CREEK_1  |              |
| BERWYNDALE_SOUTH_30 | COOLOOMALA_1   | HUMBUG_CREEK_1  | MACKIE_1        | ROCK_CREEK_1        | WEST_BRAEMAR_1 |              |

Table A-4: List of wells with velocity check shots. Among these wells Bentley\_1 was the deepest with 1484 m MD reached to the Precipice Sandstone.

|              |              |               |
|--------------|--------------|---------------|
| BENTLEY_1    | COOLOOMALA_1 | MILES_CREEK_1 |
| BULWER_1     | DOGWOOD_1    | PICURDA_1     |
| COLUMBOOLA_1 | FOSSILWOOD_1 | WIEAMBILLA_1  |
| CONDAMINE_1  | MACKIE_1     | XYLEX_1       |

Table A-5: List of different formation horizons which were picked in seismic interpretation over the entire modelling outline. The formation in bold was selected as dominant horizons for further analysis.

|                       |                    |                                  |                                         |
|-----------------------|--------------------|----------------------------------|-----------------------------------------|
| Roma                  | Disconformity      | Oralla Formation                 | <b>Springbok Sandstone</b>              |
| Bundamba              | Eurombah Formation | Bungil Formation                 | <b>Walloon Coal Measure</b>             |
| Tangalooma Sandstone  | Wandoan Sandstone  | Mooga Sandstone                  | <b>Hutton Sandstone</b>                 |
| Snake Creek Mudstone  | KIANGA             | Evergreen Resistivity Marker     | <b>Evergreen Formation</b>              |
| Rewen Group           | Blythesdale        | Evergreen Formation (lower unit) | <b>Precipice Sandstone (upper unit)</b> |
| Moolayember Formation | CABAWIN            | Precipice Sandstone (Lower unit) | <b>Basement</b>                         |
| Buffel Formation      | Blackwater Group   | <b>Gubberamunda Sandstone</b>    |                                         |
| Volcanics             | Black Creek Group  | <b>Westbourne Formation</b>      |                                         |

Table A-6: Making property layer by inserting available wire-line information for all wells.

| <b>Making Property Map for Density</b> |                   |
|----------------------------------------|-------------------|
| Input                                  | Density Well Logs |
| Average Method                         | Arithmetic        |
| Treat Log                              | As points         |
| Method                                 | Neighbour Cell    |

Table A-7: PSGRN Parameters for each formation extracted from seismic interpretation and property modelling.

| No. | Depth [km] | Vp[km/sec] | Vs[km/sec] | rho[kg/m <sup>3</sup> ] | eta1[pa*s] | eta2[pa*s] | alpha1 | Formation              |
|-----|------------|------------|------------|-------------------------|------------|------------|--------|------------------------|
| 1   | 00.0       | 2.9310     | 1.6922     | 1709.5                  | 0.0E+00    | 0.0E+00    | 1.000  | Surface                |
| 2   | 0.20       | 2.9310     | 1.6922     | 1709.5                  | 0.0E+00    | 0.0E+00    | 1.000  | Gubberamunda Sandstone |
| 3   | 0.20       | 2.7223     | 1.5717     | 2106.1                  | 0.0E+00    | 0.0E+00    | 1.000  | Gubberamunda Sandstone |
| 4   | 0.22       | 2.7223     | 1.5717     | 2106.1                  | 0.0E+00    | 0.0E+00    | 1.000  | Westbourne Formation   |
| 5   | 0.22       | 2.8891     | 1.6680     | 1913.7                  | 0.0E+00    | 0.0E+00    | 1.000  | Westbourne Formation   |
| 6   | 0.34       | 2.8891     | 1.6680     | 1913.7                  | 0.0E+00    | 0.0E+00    | 1.000  | Springbok Sandstone    |
| 7   | 0.34       | 2.9633     | 1.7108     | 1526.0                  | 0.0E+00    | 0.0E+00    | 1.000  | Springbok Sandstone    |
| 8   | 0.38       | 2.9633     | 1.7108     | 1526.0                  | 0.0E+00    | 0.0E+00    | 1.000  | Walloon Coal Measures  |
| 9   | 0.38       | 3.7635     | 2.1728     | 1885.8                  | 0.0E+00    | 0.0E+00    | 1.000  | Walloon Coal Measures  |
| 10  | 0.83       | 3.7635     | 2.1728     | 1885.8                  | 0.0E+00    | 0.0E+00    | 1.000  | Hutton Sandstone       |
| 11  | 0.83       | 4.0356     | 2.3300     | 1847.7                  | 0.0E+00    | 0.0E+00    | 1.000  | Hutton Sandstone       |
| 12  | 1.05       | 4.0356     | 2.3300     | 1847.7                  | 0.0E+00    | 0.0E+00    | 1.000  | Precipice Sandstone    |
| 13  | 1.05       | 3.7170     | 2.1460     | 2480.3                  | 0.0E+00    | 0.0E+00    | 1.000  | Precipice Sandstone    |
| 14  | 10.0       | 3.7170     | 2.1460     | 2480.3                  | 0.0E+00    | 0.0E+00    | 1.000  | Basement               |

\* Vp: Compressional Velocity, Vs: Shear Velocity, rho: Formation Density, eta1: transient viscosity (Kelvin-Voigt body), eta2: steady-state viscosity (Maxwell body), alpha1: ratio between the effective and the unrelaxed shear modulus=  $\mu_1/(\mu_1+\mu_2)$

Table A-8: Fault parameters in PSCMP based on approximate location of Burunga-Leichhardt thrust fault.

| O_lat[deg] | O_lan[deg] | O_depth[Km] | Length[Km] | Width | Strike[deg] | Dip[deg] | Start_time | Pos_s[Km] | Pos_d[Km] | Slp_stk[m] | Slp_stk[m] | Open[m]    |
|------------|------------|-------------|------------|-------|-------------|----------|------------|-----------|-----------|------------|------------|------------|
| -26.88600  | 150.770000 | 2.5000      | 15.00      | 15.00 | 0.00        | 0.00     | 0.00       | 0.00      | 0.00      | 0.000      | 0.000      | 1.0000E-03 |

Table A-9: List for depth maps for sub-surface formations in the Surat Basin from top to bottom

|                               |                   |
|-------------------------------|-------------------|
| <b>Gubberamunda Sandstone</b> | Shallow Depth     |
| <b>Westbourne Formation</b>   | Shallow Depth     |
| <b>Springbok Sandstone</b>    | Shallow Depth     |
| <b>Walloon Coal Measure</b>   | Shallow Depth     |
| <b>Hutton Sandstone</b>       | Significant Depth |
| <b>Evergreen Formation</b>    | Significant Depth |
| <b>Precipice Sandstone</b>    | Shallow Depth     |
| <b>Basement</b>               | Shallow Depth     |

Table A-10: List of isopach maps in the Surat basin with their thickness evaluation over the area with deformation signal

|                                 |                |
|---------------------------------|----------------|
| <b>Gubberamunda- Westbourne</b> | Low to Medium  |
| <b>Westbourne- Springbok</b>    | Low            |
| <b>Springbok- Walloon</b>       | Medium to High |
| <b>Walloon-Hutton</b>           | Medium to Low  |
| <b>Hutton- Evergreen</b>        | Low            |
| <b>Evergreen-Precipice</b>      | Very Low       |
| <b>Precipice-Basement</b>       | Medium to High |